Onboard Orbit Determination Using GPS Measurements for Low Earth Orbit Satellites

by

Ning Zhou

B.S., Nanjing University, People's Republic of China, 1997
M.S., Nanjing University, People's Republic of China, 2000

A THESIS submitted to
the Faculty of the Built Environment and Engineering
in partial fulfilment of
the requirement for the degree of
Doctor of Philosophy

Cooperative Research Centre for Satellite Systems
Queensland University of Technology
GP.O. Box 2434, QLD 4001, Australia
December 2004

Abstract

Recent advances in spaceborne GPS technology have shown significant advantages in many aspects over conventional technologies. For instance, spaceborne GPS can realize autonomous orbit determination with significant savings in spacecraft life cycle, in power, and in mass. At present, the onboard orbit determination in real time or near-real time can typically achieve 3D orbital accuracy of metres to tens metres with Kalman filtering process, but 21st century space engineering requires onboard orbit accuracy of better than 5 metres, and even sub-metre for some space applications. The research focuses on the development of GPS-based autonomous orbit determination techniques for spacecraft. Contributions are made to the field of GPS-based orbit determination in the following five areas:

Techniques to simplify the orbital dynamical models for onboard processing have been developed in order to reduce the computional burden while retaining full model accuracy. The Earth gravity acceleration approximation method was established to replace the traditional recursive acceleration computations. Results have demonstrated that with the computation burden for a 5×5 spherical harmonic gravity model, we achieve the accuracy of a 70×70 model. Efforts were made for the simplification of solar & lunar ephemerides, atmosphere density model and orbit integration. All these techniques together enable a more accurate orbit integrator to operate onboard.

Efficient algorithms for onboard GPS measurement outlier detection and measurement improvement have been developed. In addition, a closed-form single point position method was implemented to provide an initial orbit solution without any a priori information.

The third important contribution was made to the development of sliding-window short-arc orbit filtering techniques for onboard processing. With respect to the existing Kalman recursive filtering, the short-arc method is more stable because

more measurements are used. On the other hand, the short-arc method requires less accurate orbit dynamical model information compared to the long-arc method, thus it is suitable for onboard processing. Our results have demonstrated that by using the 1 ~ 2 revolutions of LEO code GPS data we can achieve an orbit accuracy of 1 ~ 2 metres. Sliding-window techniques provide sub-metre level orbit determination solutions with 5~20 minutes delay.

A software platform for the GPS orbit determination studies has been established. Methods of orbit determination in near-real time have been developed and tested. The software system includes orbit dynamical modelling, GPS data processing, orbit filtering and result analysis modules, providing an effective technical basis for further studies.

Furthermore a ground-based near-real time orbit determination system has been established for FedSat, Australia's first satellite in 30 years. The system generates 10-metre level orbit solution with half-day latency on an operational basis. This system has supported the scientific missions of FedSat such as Ka-band tracking and GPS atmosphere studies within the Cooperative Research Centre for Satellite System (CRCSS) community. Though it is different from the onboard orbit determination, it provides important test-bed for the techniques described in previous section.

This thesis focuses on the onboard orbit determination techniques that were discussed in Chapter 2 through Chapter 6. The proposed onboard orbit determination algorithms were successfully validated using real onboard GPS data collected from Topex/Poseidon, CHAMP and SAC-C satellites.

Table of Contents

List of Figures

List of Tables

List of Symbols

The symbols used in this work are listed in the table below. Note that certain symbols may have several meanings depending on the particular context. In many cases, the symbols are explained separately under each formula where they appear.

1σ	one sigma value
3σ	three sigma value
α	elevation cut-off angle
α	regularization parametre
α, δ	equator latitude and equator longitude
$\overline{\alpha}$	mean orbital elements
ξ, ϑ, z	presession angles
γ	the angle between the solar panel surface normal unit vector and satellite velocity vector
γ	the angle between the solar panel surface normal unit vector and satellite-Sun unit vector
γ	the parameterised post-Newtonian parametre
ν	the eclipse factor
η	reflectivity coefficient of the satellite
η_p	the surface normal unit vector of the solar panel
$\Delta P^{k,j}$	pseudo-range single difference between two GPS satellite k and j
$\Delta\rho_{rel}$	range total correction for the special relativity
$\Delta\rho_{srel}$	range correction for the special relativity
$\Delta\rho_{grel}$	range correction for the general relativity
$\Delta\rho_{ant}$	spacecraft GPS antenna phase centre offset
$\Delta\rho_{gps\_ant}$	GPS satellite antenna phase centre offset
$\Delta\mathbf{x}_0$	vector of corrections
δt	GPS / receiver clock bias
$\delta\Delta\psi, \delta\Delta\varepsilon$	celestial pole offsets
$\Delta\psi, \Delta\varepsilon$	nutation angles
Δt	integrator step size
$\delta\phi$	time-differenced carrier phase measurement
ε	error tolerance

ε	equation of equinox
$\boldsymbol{\varepsilon}$	measurement random noise
θ	angular distance
λ	longitude
λ	wavelength of the carrier signal
ρ	total mass density of the Earth atmosphere
ρ	geometric distance between GPS satellite and receiver
σ_x	standard deviation of vector x
$\boldsymbol{\Phi}$	linearized state transition matrix
ϕ_i	carrier phase measurement in cycles signal frequency i
φ	latitude
ω	argument of perigee of the satellite
$\boldsymbol{\Theta}$	coordinate transformation matrix from ITRF to ICRF
$\boldsymbol{\Delta}$	position vector
Ω	ascending node angle
$\mathbf{a}_x$	acceleration acted on satellite from source x
A	the cross-sectional area of the satellite body perpendicular to velocity direction
A	the cross-sectional area of the satellite normal to the Sun
A_p	the solar panel's area
B	ballistic coefficient
B	process noise transition matrix
a_e	radius of the Earth
$\mathbf{c}$	Earth pseudo-centre vector
C	light speed in vacuum
C_1, C_2	the once-per-revolution density correction coefficients
C_x	covariance matrix
C_{dp}	the drag coefficient for the solar panel
C_D	the drag coefficient for the satellite
$C_d A/m$	ballistic coefficient
$\overline{C}_{lm}, \overline{S}_{lm}$	normalized spherical harmonic coefficients of degree l and order m
$Cov()$	covariance matrix function
E( )	expect function
F^*	diurnal variation factor
dt	clock

e	orbit eccentricity
f	state transition function
f_1	frequency of the primary carrier L_1
f_2	the frequency of the secondary carrier L_2
G	geometrical straight-line path length
GM_e	the gravitational constant of the Earth
H	linearized measurement design matrix
H	state transition matrix considering only two body forces
H	height above the ellipsoid
H	receiver hardware delay for range
H_0	height of site above sea level
h	satellite altitude in ICRF
I	identity matrix
J	Jacobian magnitude
J_i	Earth gravity zonal coefficient of order i
K	Kalman filter gain
l	mean anomaly
L_i	phase measurement in metres at signal frequency i
L_w	wide-lane combination
L_1	GPS L_1 signal
L_2	GPS L_2 signal
L_5	GPS L_5 signal
m	mass of the satellite
mas	milli-arcseconds
M	mean anomaly of the satellite
N	ambiguity
$\mathbf{O}$	the antenna phase centre offset in satellite body fixed coordinate system
P	the momentum flux due to the Sun
P	pseudo-range measurement
P_1	pseudo-range measurement at L_1
P_2	pseudo-range measurement at L_2
P_{IF}	ionosphere-free code combination
$\overline{P}_{lm}$	the normalized associated Legendre function of degree l and order m
p, q	orbit dynamic constants

$\mathbf{P}$	covariance of unknown vector
$\hat{\mathbf{P}}$	estimated covariance of unknown vector
$\tilde{\mathbf{P}}$	apriori estimation of covariance of unknown vector
$\mathbf{Q}$	covariance matrix of process noise
r	radial distance, magnitude of $\mathbf{r}$
$\mathbf{r}$	positional vector
$\dot{\mathbf{r}}$	velocity vector
$\mathbf{R}$	covariance matrix of measurement noise
$\mathbf{R}_x$	rotation matrix along x axis
$\mathbf{R}_y$	rotation matrix along y axis
$\mathbf{R}_z$	rotation matrix along z axis
t	the true anomaly of satellite
t	time tag
T	julian centuries
T	tropospheric delay
$\mathbf{u}$	random process noise vector
U	gradient of potential force
V	vector of residuals
v	velocity
W	weight matrix
x_p, y_p	polar motion
$\mathbf{x}$	unknown vector
$\hat{\mathbf{x}}$	estimated unknown vector
$\tilde{\mathbf{x}}$	apriori estimation of unknown vecor
$\mathbf{Y}$	measurement residual vector
$\mathbf{z}$	GPS measurement vector

List of Acronyms

3D	Three dimensions
3DRMS	Three dimensional root mean square
AS	Anti-spoofing
BIRD	Bi-spectral infra-red detection satellite
C/A	Coarse/acquisition code
C/N	Signal-to-noise ratio
CEP	Celestial Ephemeris Pole
CHAMP	CHAllenging Minisatellite Payload
CPR	One-cycle-per-orbit-revolution
CRCSS	Cooperative Research Centre for Satellite Systems, Australia
DE405	JPL Development Ephemeris 405
DGPS	Differential GPS
DORIS	Doppler Orbitography and Radiopositioning Integrated by Satellite
DTM	Drag temperature model
EC	European Community
ECEF	Earth-centred earth-fixed coordinate system
EGM	The NASA GSFC and NIMA Joint Geopotential Model
EGNOS	The European Geostationary Navigation Overlay Service
EKF	Extended Kalman filter
EOP	Earth orientation parametres
EPS	Satellite Earth-Probe-Sun system
FEDSAT	Australian Federal Government Satellite
FODT	FedSat orbit determination and tracking software
GEO	Geostationary Earth Orbit
GFZ	GeoForschungsZentrum Potsdam, Germany
GIPSY	JPL GPS-Inferred Positioning SYstem
GIS	Geographic Information System
GMST	Greenwich Mean Sidereal Time
GNSS	Global Navigation Satellite Systems
GPS	Global Positioning System
GPST	GPS system time
GSFC	NASA Goddard Space Flight Centre
GTO	Geostationary Transfer Orbit
HCL	Satellite Height-Crosstrack-Alongtrack system
HEO	High Elliptical Orbit
IAU	International Astronomical Union

ICRF	International Celestial Reference Frame
IERS	International Earth Rotation Service
IGP	IGS predicted orbits, predicted for 24 up to 48 hours
IGR	IGS rapid orbits, delivered with a latency of 2 days
IGS	International GPS Service for Geodynamics
IGS	IGS final orbits, delivered with a latency of 2 weeks
IGU	IGS ultra-rapid orbits
ITRF	International Terrestrial Reference Frame
JD	Julian Date
JGM3	Joint Gravity Model 3
JPL	Jet Propulsion Laboratory
LEO	Low-earth orbiter, satellite with small orbit altitude (500-1000 km)
LOS	Line of sight
MCS	Master control station
MEO	Medium-earth orbiter, satellite with medium orbit altitude (>20,000km)
MIT	Massachusetts Institute of Technology
MSIS86	Mass-Spectrometre-Incoherent-Scatter model 1986
NASA	National Aeronautics and Space Administration, USA
NEOS	US National Earth Orientation Service
NIMA	US National Imagery and Mapping Agency
NRT	Near-real-time
OASIS	JPL Orbit Analysis Simulation Software
OD	Orbit determination
OI	Orbit integrator
ONS	GPS Onboard navigation solution
PDOP	Position dilution of precision
POD	Precise orbit determination
PPP	Precise Point Positioning
PRN	Pseudo-random noise
QUT	Queensland University of technology
RAM	Random access memory
RDT	Reduced dynamic tracking
RINEX	Receiver-independent exchange format
RK	Runge-Kutta integrator
RMS	Root mean square
ROM	Read only memory
RTG	Real time GIPSY
SA	Selective availability
SAC-C	Agentine Satélite de Aplicaciones Científicas mission C
SGP4	Simplified general perturbations model 4

SLR	Satellite Laser Ranging system
SPP	Single point positioning
SPS	Standard positioning system
ST	Sidereal time
STEC	Slant Total Electron Content
SVD	Singular value decomposition
T/P	TOPEX/POSEIDON satellite
TAI	International atomic time
TDB	Barycentric dynamical time
TDT	Terrestrial dynamical time
UTC	Coordinated universal time
UT1	Coordinated universal time format 1
VLBI	Very long baseline interferometry
WAAS	Wide area augmentation system
WADGPS	Wide area differential GPS
WGS84	World Geodetic System 1984

Statement of Authorship

The work contained in this thesis has not been previously submitted for a degree or diploma at this or any other higher education institution. To the best of my knowledge and belief, the thesis contains no material previously published or written by another person except where due reference is made.

Signature: _____

Date: _____

Acknowledgements

Words cannot explain how grateful I am to the many people who directly and indirectly contributed to this work. First of all I would like to thank my supervisor, Dr. Yanming Feng, for directing me towards this research topic and providing me with excellent advice and guidance. Moreover, he has consistently helped me to stay motivated, especially in the darkest days when the deadline loomed.

I thank my associate supervisor, A/Prof. Werner Enderle, for his support and guidance; thank Prof. Miles Moody for his grateful support throughout my studies at QUT; Yi Zheng and Zhengdong Bai for their discussions and friendship. Thanks go to everybody else at CRCSS I didn't mentioned. I am fortunate to have had access to such an excellent facility and staff.

Special thanks go to the Australian Government for the International Postgraduate Research Scholarship (IPRS) which covers the tuition fee and oversee student health cover for me. Thanks also go to the Faculty of the Built Environment and Engineering, Queensland University of Technology (QUT) and the Cooperative Research Centre for Satellites Systems (CRCSS), QUT node, for the Living Allowance Scholarship and Top-up Scholarship.

Finally, I want to thank my parents, for raising me to believe that I could achieve anything I set my mind do, for encouraging me to take the more challenging path, and for their unwavering support during my study and my life so far.

Special thanks go to my dear partner, Ms. Xiaowen Lei. Know that I could not have finished without you, thank you for your love and constant support.

Chapter 1
Introduction

In this chapter a brief overview of Global Positioning System (GPS) based orbit determination is given, followed by an introduction to onboard orbit determination for Low Earth Orbiters (LEO). The objectives and scope of the research will be outlined, and the structure of the thesis is provided in the last section.

1.1 GPS-based Orbit Determination for LEO Spacecraft

1.1.1 Main Attractions of Spaceborne GPS

Over the last two decades there has been tremendous advancement in GPS technology for a variety of applications. Spaceborne GPS is revolutionizing future spacecraft systems [*Munjal, et al.*, 1992]. It has a combined capability of determining spacecraft trajectory and attitude, relative positioning between space vehicles, sounding the atmosphere, and delivering precise time synchronization to spacecraft electronics. The use of GPS receivers in Low Earth Orbit spacecraft systems has been quite common for both engineering and scientific purposes. In the relatively new applications, such as navigation in Geostationary Earth Orbit (GEO) [*Christian*, 2001], Geostationary Transfer Orbit (GTO), High Elliptical Orbit (HEO), space rendezvous, maneouvres and atmospheric re-entry, GPS receivers are the preferred navigation sensors, even though GPS–based navigation is, in many cases, still in the experimental phase or under development. The main applications of space GPS receivers include, but are not limited to, the following aspects.

Real time orbit information for tracking and navigation applications*:* A spacecraft collecting GPS data with an onboard receiver can compute its 3D position and velocity in a diversity of ways, depending in part on the orbit and mission

requirements. The real time orbit state information can benefit both ground-station operation and onboard uses: simplifying ground tracking and operations, and significantly improving space vehicle autonomy [*Potti, et al.*, 1995].

Precise timing applications*:* In addition to position and velocity, the GPS receiver can also provide accurate reference time synchronized to UTC to better than 1μs. This accuracy can be useful for telecommunications and observations, and also for time synchronization between satellites and ground stations [*Klepczynsk*, 1996].

Attitude determination applications*:* Using three or four GPS antennas, the receiver can determine real time attitude information of the spacecraft to an accuracy of 0.5 degree or better via processing carrier phase measurements [*Lightsey*, 1996]. Limitations of the separation of antennas and multipath effects on the spacecraft structure limit the achievable `

Scientific applications*:* Recorded raw dual-frequency measurements can be downloaded to ground stations for post-processing, which may lead to precise orbit solutions of the spacecraft required for scientific observation missions, including remote sensing. Raw data may also be used for earth science studies, such as gravity recovery, GPS atmosphere sounding and GPS ocean reflection [*Bertiger, et al.*, 1998].

Among these applications what appears most remarkable is the capability of spaceborne GPS to provide accurate and/or autonomous satellite orbit determination, which serves for both space-engineering and scientific purposes, and finds applications in spacecraft tracking and navigation from near Earth to beyond geostationary altitudes. Orbit accuracy requirements can range from hundreds of metres to metres for engineering purposes, from one metre to a few centimetres for scientific applications.

Spacecraft tracking and navigation requirements can include:

- Real time state knowledge and active control during launch and orbit insertion, during re-entry and landing;

- Real time relative navigation between vehicles during rendezvous;
- Autonomous station keeping;
- Near-real time orbit knowledge for operations and orbit maintenance, rapid post-maneouver orbit recovery; and
- After-the-fact precise orbit determination for scientific applications.

This PhD research is concerned with the applications of using Global Positioning System (GPS) receivers for spacecraft tracking and navigation applications: ground- and space-based orbit determination approaches in general, addressing the particular challenges posed in GPS-based real time and near-real time onboard orbit determination. The next section presents the objective and scope of this research.

1.1.2 Ground-based Precise Orbit Determination

The techniques involved in these applications can be classified into *direct* GPS-based orbit determination, and *differential GPS* precise orbit determination (POD). As illustrated in Figure 1, in the former case only flight GPS measurements are used for orbit tracking and/or autonomous navigation, achieving orbit accuracy of a few to hundreds of metres. In the latter case, the data collected at a global GPS tracking network of tens of stations are processed along with the flight data to achieve the orbit accuracy of better than 10 centimetres. Figure 1.1 illustrates the concepts of GPS-based satellite POD with a global differential GPS network.

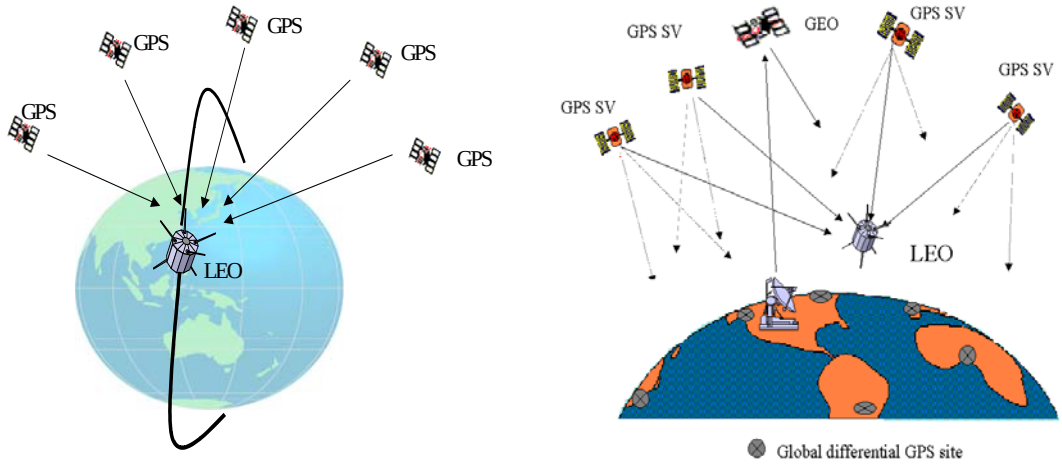

Figure 1.1 Concepts of standalone (left) and global GPS orbit determination (right).

The potential of GPS to provide accurate and autonomous satellite orbit solution was noted early in its development. Early studies of direct GPS-based tracking can be found in a number of references [*Farr*, 1979], which addressed the applications from near-Earth to beyond geosynchronous orbit. *Van Leeuween & Carrier* [1997] examined GPS tracking of the Space Shuttle and *Tapyley* [1987] focused on autonomous near-Earth navigation. The recent studies and applications include those in *Gill, et al.* [2001], which reported the BIRD satellite mission as a milestone towards GPS-based autonomous navigation; and *Christian* [2001] which examined the GPS receiver architecture and expected performance for autonomous navigation in High Elliptical Orbits (HEO). The first reported results from relative GPS navigation were those of the ETS-VII autonomous rendezvous using relative GPS navigation [*Kawano*, 1999], which achieved the accuracy of relative navigation of 10m in position and 3cm/s in velocity. Further information can be found in the website [*Spaceborne GPS mission directory*, 2004, see Appendix B], which is a GPS mission directory, chronologically listing the space missions that have included a GPS receiver, or receivers, for any number of reasons. It is a comprehensive directory of missions that have been cited in the scientific literature, although it may not be an all-inclusive listing of spaceborne GPS missions flown. Mission descriptions, the capacity that the GPS receiver or receivers had, the model of GPS receiver, and references citing the mission are also given.

Direct GPS orbit determination can meet the most stringent of the accuracy needs for spacecraft tracking and navigation for the most dynamically unpredictable vehicles. The orbit computation may be conducted onboard spacecraft in real time or at a ground-station in near-real time, or in both ways. There are two ways to obtain the orbit solutions: GPS navigation solutions (point positioning) and orbit filter/improvement solutions. GPS standard point positioning is as accurate in low orbit as on the ground: theoretically 10 to 20 metres with zero Selective Availability. Any orbit below 3000km is considered Low Earth Orbit (LEO) in this context. Below 3000km altitude, signals from 10 or more GPS satellites are typically received by an upward-looking antenna with the current GPS constellation, reaching the receiver with nearly uniform power levels and geometric distribution above the horizon. Above 3000km altitude, the condition for receiving GPS signals becomes much less favourable [*Mehlen*, 2000]. Received signal power typically decreases

because: (1) the transmitted power of some signals drops off as a result of the attenuation pattern of the transmitting GPS satellite and (2) the ranges to many of the visible satellites increase. As a result, the number of visible or receivable satellites by an up-looking antenna drops dramatically in orbits above 3000km. The flight data from an onboard receiver would have difficulty generating a single-point solution above 3000km. In any orbit there is also a not uncommon problem: some onboard GPS receivers cannot operate all the time, due to reasons such as limitations of the onboard power supply. As a result, a continuous supply of navigation solutions is not always possible.

An orbit filter procedure can provide better orbit solutions, meeting the stringent orbit accuracy requirements for GPS tracking and navigation services to satellites in different orbits, ranging from above the Earth surface, below 3000km, 3000km to 20,000km, Geosynchronous and High Elliptical Orbits. The orbit filter (OF) uses the GPS measurements or navigation solutions (measurements normally sampled at rates of seconds to minutes) over a data arc of tens of minutes to hours in length, to estimate the state vector for each epoch state. Functioning along with the orbit filter is an orbit integrator (OI), which propagates the state between state update epochs, and hours to days forward for real time tracking when required. In general, an orbit filter provides smooth and continuous orbit solutions, achieved with an additional piece of software. The early studies of using GPS flight data for precise real time LEO navigation testing were reported in *Bertiger, et al.* [1998], which demonstrated that the 3D RMS orbit error of 4 ~ 6 metres was achieved after cold start of 4 hours, using broadcast GPS orbits and non-zero SA signals for Topex/Poseidon at 1340km altitude. The recently reported results [*Da Kuang, et al.*, 2001] from filtering processing of T/P flight data with zero SA indicates that orbit positional accuracy at the 1 to 2 metre level is achievable, while the results from processing of GPS/MET flight data with zero SA indicates the 3D orbit accuracy of 6 to 8 metres.

Differential GPS Precise Orbit Determination (POD) can meet the requirements for orbit accuracies ranging from 1 metre down to a few centimetres. POD techniques with differential GPS was initially developed for non-real time applications, which can tolerate the delay of 24 hours to several days after data collection. But later on near-real time processing of GPS tracking data could routinely provide LEO orbit

determination accuracy at the level of 5cm to 10cm with delay of 10 hours by the Jet Propulsion Laboratory (JPL) and other space organizations. Recent improvements in JPL's GIPSY-OASIS II processing system have enabled turn around at the 1-hour level or better for such precise orbit determination. Further development will allow real time orbit determination with NASA's global differential GPS correction signals broadcast via communication satellites. The concept is also shown in Figure 1.1 (right).

The key to achieving near-real time and real time POD is to implement a highly automated procedure to collect and process the global GPS tracking data for precise GPS orbits and clocks, then distribute the solutions to users (onboard or on the ground) in a few tens of minutes to hours (near-real time) or seconds to minutes (real time). Studies for real time orbit determination have shown that with precise GPS orbits and clocks, the RMS accuracy at the decimetre level for radial and cross-track components can be achieved a few hours after an initial cold start for T/P, and the RMS accuracy was 20cm to 70cm for GPS/Met satellite, which has lower orbit (700km) for which the drag and gravitational forces are less well modelled.

There are three basic strategies presently in use to determine precise LEO orbits with GPS. They are the dynamic, the kinematic or non-dynamic, and the hybrid or reduced-dynamic strategies.

1.1.3 Onboard Orbit Determination

Onboard Orbit Determination invariably performs orbit computations in the receiver or onboard the electronics in real time. The techniques involved in this application also include *direct* GPS-based orbit determination, and *differential GPS* precise orbit determination (POD). The choices depend on the signals available for the receiver in orbit to use: standalone GPS signals and differential messages. For instance, a normal space GPS receiver can only perform direct GPS-based OD determination with standalone GPS signals, while a GPS/WAAS or GPS/EGNOS capable receiver can choose to use the differential techniques for improved onboard orbit solutions. In any case, in addition to onboard navigation solutions (ONS) directly obtained from the space GPS receiver, the central point of onboard OD is the implementation of the

above OD capability on the orbit electronics for improved or precise orbit solutions. Due to significant differences in computing resources and requirements for orbit information between onboard and on the ground, this implementation is challenging both engineering and science. The focus of this work is to develop efficient models and algorithms for onboard orbit determination, mainly addressing the scientific challenges, instead of the engineering ones.

In contrast to onboard OD, a closely related concept is the ground-based POD and ground-based autonomous LEO tracking for real time orbit information using GPS measurements and ground-based satellite tracking and orbit determination. Table 1.1 summarizes the characteristics of these concepts, showing the similarity and differences of these methods. It is seen that onboard OD makes use of limited resources to achieve the orbit accuracy for advanced space engineering and certain scientific applications.

1.2 The Objectives and Main Contributions of the Study

1.2.1 Major Research Objectives

The overall objective of this research is to develop a robust and accurate onboard orbit determination (OD) algorithm for Low Earth Orbiting (LEO) spacecraft with onboard GPS facility. The goal is to autonomously process GPS pseudo-ranges, in real time, to produce orbit estimates with RMS accuracy at metre levels for satellites. “Real time” here means that the orbit state with the given accuracy is made available within seconds to tens of minutes after the last observation is made. In particular, the research will address a number of scientific challenges for onboard orbit determination, in order to achieve the overall objective.

Table 1.1 Summary of GPS-based orbit determination.

	Ground-based Precise Orbit Determination (Ground-based POD)	**Ground-based real time LEO tracking or Real time Orbit Determination (RT OD)**	**Onboard LEO Orbit Determination (Onboard OD)**
Observations available	All GPS measurements and others such as SLR and precise GPS orbits	Standalone or DGPS measurements and other sources of ground tracking data	Standalone GPS code measurements and phase smoothed GPS code measurements
Mission objectives	Provide post-fitted orbit solutions as accurately as possible, with delay hours to days	Provide predicted LEO orbit knowledge for real time tracking and ground-based spacecraft operation application	Provide accurate orbit knowledge on board spacecraft for autonomous operation and navigation in real time or near real time in space
Methods	Differential GPS POD, with data from global GPS tracking network or precise GPS orbits from the networks	Direct GPS orbit estimation, with GPS broadcast orbits or precise predicted orbits	Direct GPS orbit estimation, with GPS broadcast orbits from GPS or Geostationary satellites
Degree of autonomy	Desirable, but not required	Required	Required
Orbital positional accuracy (3D RMS)	Centimetres to sub-metre	Metres to tens of metres	Typically metres to ten metres, moving towards sub-metre
Orbital velocity accuracy (3D RMS)	Typically 0.1mm/s to mm/s	Typically cm/s	Typically m/s to cm/s
Applications	Geosciences, ocean altimetres, gravity recovery, imagery satellites	Satellite tracking, and operation	Autonomous navigation, orbit knowledge for space engineering in future

- Develop techniques to simplify the orbital dynamical models for onboard processing, in order to reduce the computing burden, which is critical for onboard computing, while possibly retaining full model accuracy. One focus is the Earth gravity acceleration approximation, aiming to achieve the accuracy of a 70×70 spherical harmonic model with the computational load of a 5×5 gravity model. Simplification of the solar & lunar ephemerides, atmosphere density model and orbit integrator will also be discussed. All these techniques together enable a precise accuracy onboard orbit integrator.
- Examine and implement efficient quality control and improvement algorithms for onboard GPS measurements, for instance, outlier detection and phase smoothing, which will also lead to reduction of data points from seconds to minutes for more efficient onboard computations.

- Develop and test the short-arc orbit filtering techniques for onboard orbit determination. With respect to the existing Kalman recursive filtering, the short-arc method is more stable because more measurements are used. On the other hand, short-arc methods require less orbit dynamical model information compared to long-arc methods. The goal is to achieve a few metres orbit accuracy with data arc as short as a few revolutions of LEO orbits, using code GPS data.
- Establish a software platform to test and implement the above algorithms and ground-based FedSat orbit determination. The software system includes orbit dynamical modelling, GPS data processing and result analysis modules, providing an effective technical basis for further studies. It also routinely provides orbit determination service to the FedSat project, which gives tens of metres positional accuracy with a half-day delay.

1.2.2 Benefits of the Research

Recent advances in spaceborne GPS technology have shown significant advantages in many aspects the conventional technologies. On the one hand, accurate and autonomous spaceborne orbit determination onboard spaceborne can result in significant savings in spacecraft life cycle cost, in power, and in mass. The 21st century space engineering requires onboard orbit accuracy of better than 5 metres. On the other hand, it is desirable that sub-metre accuracy is achievable onboard for scientific and engineering applications, such as in the case of imaging satellites. The research focuses on the development of precise GPS-based autonomous orbit determination techniques for space engineering and science applications. This topic has attracted significant attention [*Ashkenazi, et al.*, 1997; *Gold, et al.*, 1994a; *Hart, et al.*, 1996; *Lichten, et al.*, 1995a; *Pradines, et al.*, 1993; *Spardley*, 1993; *Tu, 1990*]. With GPS Selective Availability (SA) being turned off on 2 May 2000, it has become more attractive for space engineering. Space mission planners need very accurate states of the satellites, i.e., position, velocity and/or attitude information, in real time or near-real time at an accuracy of centimetres to tens of metres, while minimizing dependence on ground-based tracking assets [*Cruickshank,* 1998]. In addition, it is desirable to perform OD in real-time, onboard an Earth orbiting

satellite, where accurate position, velocity and attitude information are made available for other satellite instruments [*Hart, et al.*, 1996].

Several onboard orbit determination systems have been developed in previous years. They will be discussed in detail in Chapter 2. We proposed an onboard orbit determination method addressing both the accuracy and stability problems of current methods.

1.2.3 Scope of the Research

This research focuses on software aspects of the onboard GPS orbit determination problem. As the computation will need to take time to complete after each data output, strictly speaking, this is a near-real time solution. However, by prediction, the system can provide real time precise orbit knowledge to cover the delay due to the computation, which can be several to tens of minutes. In addition, although the techniques have been thoroughly tested using real LEO GPS data, additional efforts are needed to implement the algorithms into a real hardware platform. Issues of computing speed; memory usage and power consumption must be re-visited from the point of view of software and hardware engineering. To reach an optimal performance, revisions to the proposed methods are also required for optimal portability to the actual computing system.

1.3 Organization of the Thesis

This thesis is organized as follows:

Chapter 1 gives a brief overview of the Global Positioning System (GPS), followed by an introduction to GPS-based orbit determination for Low Earth Orbiters (LEO). The objectives and scope of the research are outlined, and the structure of the thesis is provided.

Chapter 2 summarizes the principles of existing onboard orbit determination techniques. A review of LEO missions using GPS for tracking and navigation is

given first. Next, the performance of the onboard orbit solutions in these missions is discussed. Following this, we introduce three existing algorithms for onboard orbit determination: extended dynamic filter, phase-connected kinematics filter and onboard SGP4 filter. Finally, we outline the ideas of the short-arc orbit filter to be studied in this thesis.

Chapter 3 first gives a detailed review of the orbit dynamical models. Considering the limitations of power and computing capacity onboard a spacecraft, a full dynamical model is not possible, especially on small LEO satellites. Model simplification is discussed to make the onboard least squares filter feasible. In this chapter, different schemes for orbit model simplification are examined and new simplification methods are proposed.

Chapter 4 continues the study of orbital model simplifications and describes an alternative method to calculate the Earth gravity acceleration. An Earth gravity acceleration approximation method was developed. Instead of calculating the harmonic coefficients using recursive algorithm, an Earth pseudo-centre grid was generated on the ground and a simple two-step interpolator was used to recover the gravity acceleration on-the-fly. The results show that the computational burden of the method is equivalent to that of a 5×5 gravity model with the accuracy of a 70×70 model.

Chapter 5 deals with quality control and improvement of onboard GPS measurements and navigation solutions, which are normally worse than those obtained on the ground due to the harsh observation conditions in space. This mostly concerns the issue of outlier detection. In addition, the chapter develops phase smoothing procedures to allow clean and compacted GPS data for efficient onboard orbit estimation.

Chapter 6 discusses the least square filter techniques. The orbit dynamics of LEO satellites will be analyzed. An effort is made to test the simple, but robust, dynamic method- a short-arc batch estimation, in order to address both orbit accuracy and computational burden issues for onboard orbit determination with GPS code measurements. Furthermore, the sliding-window short-arc method is implemented to

fulfill the requirement for near-real time orbit determination. It updates the processing arc every 5 ~ 40 minutes, and generates the orbit solution in 10~40 minute delays with metre-level accuracy.

Chapter 7 presents strategies and results of the Australian Federal Government Satellite (FedSat) orbit determination. The requirement for FedSat orbit determination will be outlined and its onboard GPS receiver operation limitations analyzed. The orbit determination results with different methods are presented and discussed. The research effort finally leads to the establishment of a ground-based autonomous orbit determination system.

Finally, Chapter 8 summarizes the main findings of this thesis and gives suggestions for future research.

This thesis focuses on the onboard orbit determination techniques that were discussed in Chapter 2 through Chapter 6. The proposed onboard orbit determination algorithms were successfully validated using real onboard GPS data collected from Topex/Poseidon, CHAMP and SAC-C satellites. On the other hand, Chapter 7, addressing the ground-based orbit determination for FedSat project, has been included this thesis because this part of research work is very important during author's PhD study, and this part of work provided a basis, and test bed for the onboard orbit determination development. Furthermore, the software package for ground-based orbit determination is very helpful to the onboard research work.

Chapter 2
A Review of Onboard Orbit Determination Using GPS

In this chapter, a review for Low Earth Orbit satellite missions using GPS for tracking and navigation is presented. Next, performance of the onboard orbit solutions in these missions is discussed. Following this, four existing algorithms for onboard orbit determination are introduced: onboard navigation solution, extended dynamic filter, phase-connected kinematics filter and onboard SGP4 filter. The last section outlines the concepts of the short-arc orbit filter to be developed in this thesis.

2.1 Overview of GPS-based LEO missions and Onboard Orbit Determination Systems

2.1.1 Missions Overview

Space missions that have included a GPS receiver or receivers for any number of reasons are listed in Appendix B extracted from detailed information (Space Mission Directory, 2004). Our interest is the onboard orbit determination in real time or near-real time. Real time, in-orbit OD results are referred to sparingly in the following list of literature. For convenience of analysis, Table 2.1 summarises the representative missions that have GPS-based onboard orbit determination capacity in support of the space engineering and scientific applications. According to this analysis, we make the following observations:

- Although there have been over 100 missions that included a GPS receiver (or receivers), only some of the missions since 1996 have had the onboard orbit determination capability.

- According to the results reported for many of the missions, the GPS-based onboard navigation solutions are apparently worse than those achievable on the ground. The onboard orbit filtering accuracy is not necessarily always better than that of the onboard navigation solution, but a filter provides continuous solutions;
- The high-accuracy onboard orbit results were often obtained only for the high-cost space missions, and
- The existing onboard orbit determination algorithms mostly use an Extended Kalman filter (EKF).

2.1.2 Onboard OD Software System

There are several real time onboard software systems used in the above missions. Examples are JPL's Real time GIPSY [*Lichten*, *et al.*, 1995b], the Microcosm autonomous Navigation System (MANS) [*Collins & Conger*, 1994], the Brazilian National Institute of Space Research's (INPE's) ORBesT [*Lopes & Kuga*, 1997] and GSFC's GEODE [*Hart, et al*., 1997b]. Also, the University of Nottingham's Institute of Engineering Surveying & Space Geodesy (IESSG) developed another unnamed system [*Ashkenazi*, *et al.*, 1997]. There is currently no published information on space qualified (actually flown in space) precise, real time OD software.

JPL's Real time GIPSY (RTG)

RTG is an ANSI C version of GOA-II created by JPL to accommodate high data rates (1 Hz) and improve portability to systems other than UNIX. JPL's goal is to incorporate all the precise models from GOA-II, make it suitable for embedded systems such as GPS receivers and make it capable of real time processing [*Bertiger*, 1998]. Compiler options in RTG allow it to be scaled down to meet various processor load requirements. To provide the best accuracy, RTG is to be used in conjunction with a global Wide Area Augmentation System (WAAS) or a Wide Area Differential GPS (WADGPS) system. Without WAAS or WADGPS, RTG has shown 3D RMS values in the 4~6 meter range when used to process T/P data with

the broadcast GPS ephemeris and SA on [*Bertiger*, *et al.*, 1998]. The following is a summary of the characteristics of RTG [*Hurst*, 2004]:

- Precise dynamic models for orbiting receivers: arbitrary-sized gravity fields, drag model, empirical spacecraft accelerations, general-purpose variable step integrator;
- General relativity and light time calculations;
- General purpose factorized Kalman filter: current state or epoch state, process noise on any parametre, prediction residual test for outlier detection ;
- Minimized load size (400 Kbytes) with fast throughput for flight CPUs;
- Efficient CPU utilization: RTG will use ~ 0.1% of 99 MHz HP 9000/735 workstation for LEO flight GPS data processing (at 0.03 Hz data rate) and RAD6000 (RISC) flight processors are about 2.5 times slower load size ~ 400 Kbytes (currently);
- Other platforms include PowerPC 603e chip (RISC).

GEODE at GSFC

The GSFC-developed GEODE is a real time software analysis package [*Hart*, *et al.*, 1997b]. GEODE is highly modular, programmed in ANSI C and has been targeted to UNIX and PC systems as well as the RAD6000 RISC microprocessor. It requires a modest 400 Kbytes of computer RAM. GEODE was originally designed as experimental software to fly on the SSTI Lewis satellite contracted by NASA to TRW [*Hart*, *et al.*, 1997a]. GEODE is implemented with an Extended Kalman Filter (EKF), which feeds a real time state propagator. GEODE is designed to be hosted on either a spacecraft flight computer, or in a GPS receiver's processing unit. Pre-launch orbit determination studies using GEODE indicate that 1σ orbit accuracy of 10m in position, and 0.01m/s in velocity may be attained in the presence of SA. Below is a summary of relevant information concerning GEODE [*Lee & Long*, 1999]:

Table 2.1 Summary of onboard GPS-based orbit determination missions and results.

Missions	Orbit Determination Method	Accuracy achieved
Space Flyer Unit (SFU), March 1995, [*Ichikawa*, *et al.*, 1995]	Onboard navigation solution (ONS) and extended Kalman filter (EKF)	positional error of 200m and velocity error of 0.5m/s for both ONS and EKF;
The Extreme Ultraviolet Explorer (EUVE), June 1992, [*Gold*, *et al*., 1994a, 1994b]	EKF with Reduced Dynamic Tracking (RDT) and single frequency Group and Phase Inonospheric Calibration (GRAPHIC) techniques. The truncated Earth gravity model is also used.	Produced real time total position accuracies of about 60m (1σ) and velocity accuracies of 1.5m (1σ), with occasional spikes of over 500m and 5m/s for the position and velocity, respectively
PoSAT-1, September 1993, [*Unwin*, 1993, *Unwin & Sweeting* 1994,1995]	Onboard navigation solution (ONS) and onboard SGP4 filter. The receiver was turned on for only one orbit per day.	100m accuracy for ONS, and 1.5km for onboard SGP4.
The U.S. Advanced Research Projects Agency (ARPA) SATellite (DARPASAT), March 1994, [*Cubbedge* & *Higbee* 1994; *Nicastri*, 1992; *Mitchell*, *et al.* 1996]	Onboard navigation solution (ONS)	Accuracy of 350m. The navigation solution was however compared to radar range vectors
GPS/MET, April 1995, [*Hajj*, *et al.,* 1995]	Onboard navigation solution (ONS)	A receiver navigation solution accuracy of 46m was achieved in one test.
Wake Shield Facility-02, November 1996, [*Schltz*, *et al.*, 1995]	Onboard navigation solution (ONS)	Produced a solution accuracy of 62.6m with a post-processed least squares fit of an orbit to a navigation solution.
SSTI Lewis, August 1997, [*Hart*, *et al.*, 1996, 1997a]	Onboard GEODE flight software using an EKF.	Proposes real time total one sigma position and velocity accuracy of 20m and 0.03m/s, respectively
Bi-spectral Infra-Red Detection (BIRD), October 2001, *[Gill, et al.*, 2001]	Onboard navigation solution, Onboard EKF filter and SGP4 filter. Simplified orbital model is used. Furthermore, an advanced numerical integration scheme (RKF4R) was implemented.	The ONS generates a 40m accuracy solution. A peak error of 25m and a filter standard deviation of 5.6m can be achieved with EKF, and the orbit can be predicted for 30 minutes with the error of 90m.
FedSat, December 2002, [*Feng*, *et al.*, 2003]	Onboard navigation solution (ONS)	A 3D positional RMS error of 56m was achieved for ONS solution.

- JGM-2 30×30 spherical harmonic gravity model;
- Solar and Lunar point mass 3rd body force model;
- Harris-Priester atmospheric drag model;
- Geometrical editing of measurements with high ionospheric errors;
- Broadcast GPS ephemerides used;

- Extended Kalman Filter (EKF) implemented;
- UDU factorized state error covariance;
- Uplink of polar motion coefficients, accurate a priori state information and a priori state error and process noise covariance terms;
- Processes pseudo-range measurements only.

During one test using the GPS/MET data it took less than one minute to process the entire 24 hours of data on a 450 MHz Pentium II with 128 Mbytes RAM. The filter converged after about two hours of data and yielded a converged 3D RMS error of 11.61m [*Hart*, *et al.*, 1997b].

The University of Nottingham's Study

In a study for the UK Defense and Evaluation Research Agency (DERA), The Institute of Engineering Surveying & Geodesy (IESSG) at the University of Nottingham developed an extended Kalman filter, using Reduced Dynamic Tracking (RDT), to generate real time satellite position estimates with a radial RMS error of 1.08m 1σ and a 3D RMS error of 3.95m 1σ [*Ashkenazi*, *et al.*, 1997]. IESSG used real and simulated Standard Positioning System (SPS) data from T/P. They reported the filter converged after approximately five hours [*Chen*, 1998]. They used a JGM-2 45×45 gravity field, a simplified drag model (due to the T/P's relatively high orbit), and broadcast GPS ephemerides. The application required approximately 500 Kbytes of computer memory and the code could produce solutions within one minute of recording an observation. A trade study between microprocessor was also performed finding a military standard 1750A microprocessor (8086 equivalent) to be more than capable of producing the solutions each minute [*Ashkenazi*, *et al.*, 1997].

2.1.3 LEO Missions Used in the Simulation Experiments

To this end we have introduced four LEO missions using onboard GPS data in their experimental tests. Their orbit characteristics are summarized in Table 2.2. These missions are described below. The data sets collected from these missions will be used in this thesis for experiments and analysis.

Table 2.2 Summary of CHAMP, SAC-C, T/P and FedSat orbit characteristics.

	CHAMP	**SAC-C**	**T/P**	**FedSat**
Mean Orbit Altitude (kilometre)	474	703	1340	802.92
Inclination (degree)	87.27	98.25	66	98.673
Eccentricity	0.00396	0.000655	0.000	0.002
Orbit Period (minutes)	94	99	112	100.9

Topex/Poseidon (T/P)

T/P is a joint project between the National Aeronautics and Space Administration (NASA) and the French Space Agency, Centre National d'Etudes Spatiales (CNES). The T/P satellite carries a 6-channel Motorola Monarch Receiver, GPS demonstration receiver (GPSDR), which is capable of collecting dual-frequency (L_1 / L_2) data when the GPS anti-spoofing (AS) function is inactive.

CHAMP

The CHAMP satellite was launched in July 2000 into a circular orbit of 450 kilometres to support geoscientific and atmospheric research. The mission is managed by GFZ in Germany. The GPS payload consists of a JPL BlackJack receiver with 3 antennas, the one facing up provides data for precise orbit determination services, the one facing down is for GPS altimeter studies and there is a limb antenna for atmospheric sounding.

SAC-C

SAC-C is an international cooperative mission between NASA and the Argentine Commission on Space Activities (CONAE). SAC-C will provide multi-spectral imaging of terrestrial and coastal environments. It carries a TurboRogue III GPS and four high gain antennas developed by the JPL. It is capable of automatically acquiring selected GPS transmissions that are refracted by the Earth's atmosphere and reflected from the Earth's surface.

FedSat

FedSat is an Australian scientific micro-satellite mission, a 50cm cube weighing approximately 58 kg. It was launched in December 2002 by Japan's National Space Development Agency. Its purposes are: to establish Australian capability in micro-satellite technologies; to develop expertise necessary for sustaining those industries and profiting from them; to test and develop Australian-developed intellectual property; and to provide a research platform for Australian space-science, communication and GPS studies. FedSat is being developed by the Cooperative Research Centre for Satellite Systems (CRCSS), which combines the resources and skills of 12 Australian organizations. Contributions from each of the partner organizations are doubled by the Commonwealth Government, under its Commonwealth Government's Cooperative Research Centre's Program.

2.2 Onboard GPS Navigation Solutions

The direct orbit solutions that a GPS receiver onboard a spacecraft shall provide are the onboard navigation solutions (ONS), also called “Single Point Positioning (SPP)”solutions. The positioning accuracy was better than 100 metres in the horizontal components, and better than 156 metres in the vertical component (at the 95% confidence level) when Selectivity Availability (SA) was the dominant source of error for SPP solutions (introduced on 25 March 1990). After SA was turned off on 1 May 2000, the improvement in instantaneous accuracy of GPS-SPP is clearly seen for the period immediately before and after SA was ‘switched off’. Figure 2.2 shows this change for a terrestrial GPS receiver. Onboard stand-alone GPS navigation solutions are as accurate in low earth orbit as solutions on the ground. Currently a RMS positional accuracy of 10 to 20 metres is achieved by using the civilian broadcast GPS signals. This provides the simplest way for the onboard orbit determination. The results of previous LEO missions show a consistent accuracy, normally tens to one hundred metres accuracy were achieved when the SA was active, and tens metres accuracy in the absence of SA.

Although the ONS solution can satisfy many space applications, dynamical filtering techniques are still required in the following circumstances:

- when a higher orbit accuracy, for instance, at the metre or even sub-metre level, is needed to satisfy advanced space engineering applications, including satellite flying formation and docking, etc [*Da Kuang*, *et al.*, 2001];
- where continuous and predicted orbit information is required, but GPS navigation solutions are only available at discrete time epochs, especially when onboard GPS operates intermittently. For instance, the Australia Federation satellite - FedSat operates 2-by-10 minutes per orbit period, because of the restrictions of the on-board power supply [*Feng*, 1999];
- where visible satellites are sometimes less than four, resulting in onboard navigation solutions not being provided on a regular basis.

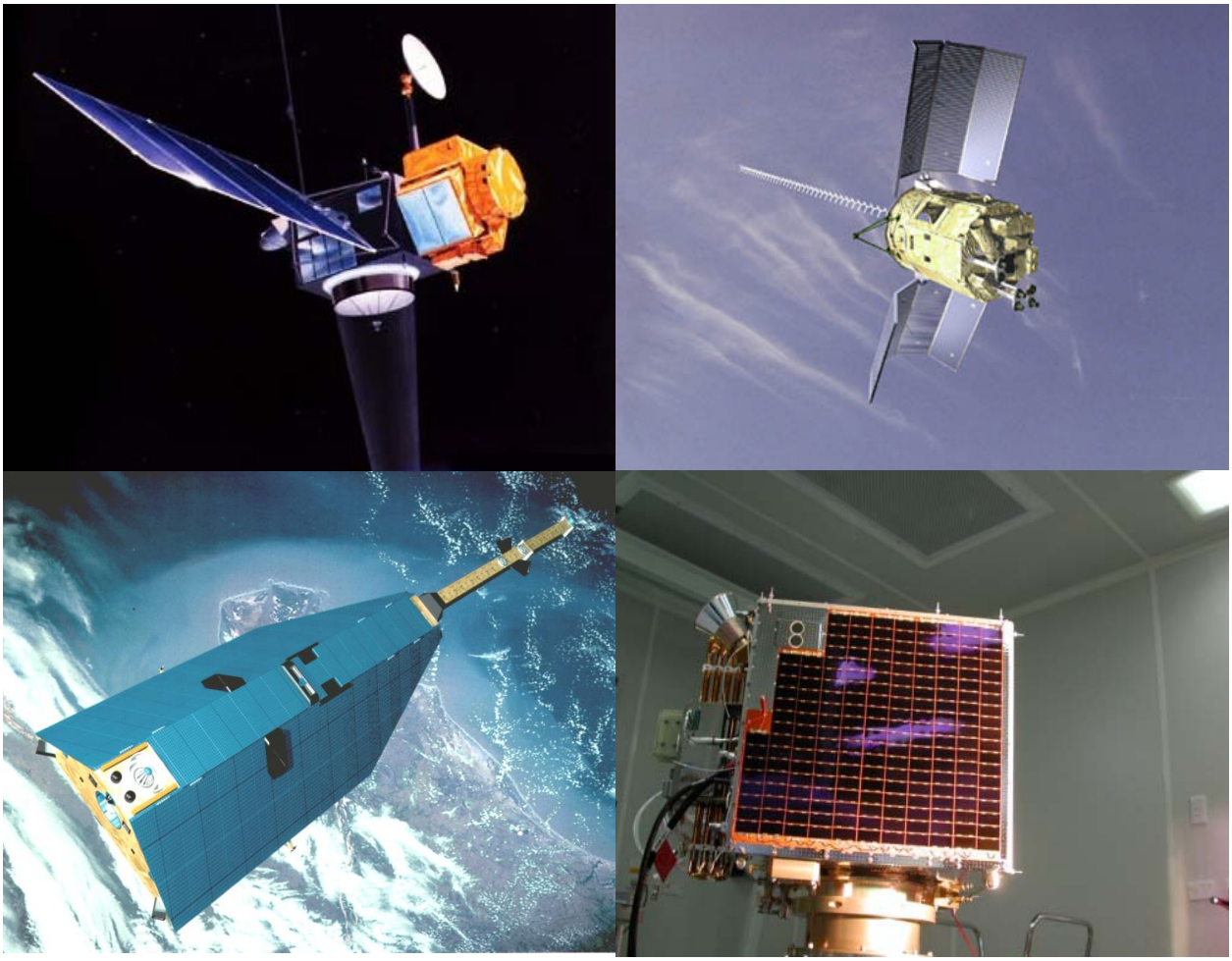

Figure 2.1 T/P (upper-left), SAC-C (upper-right), CHAMP (lower-left) and FedSat (lower-right), respectively.

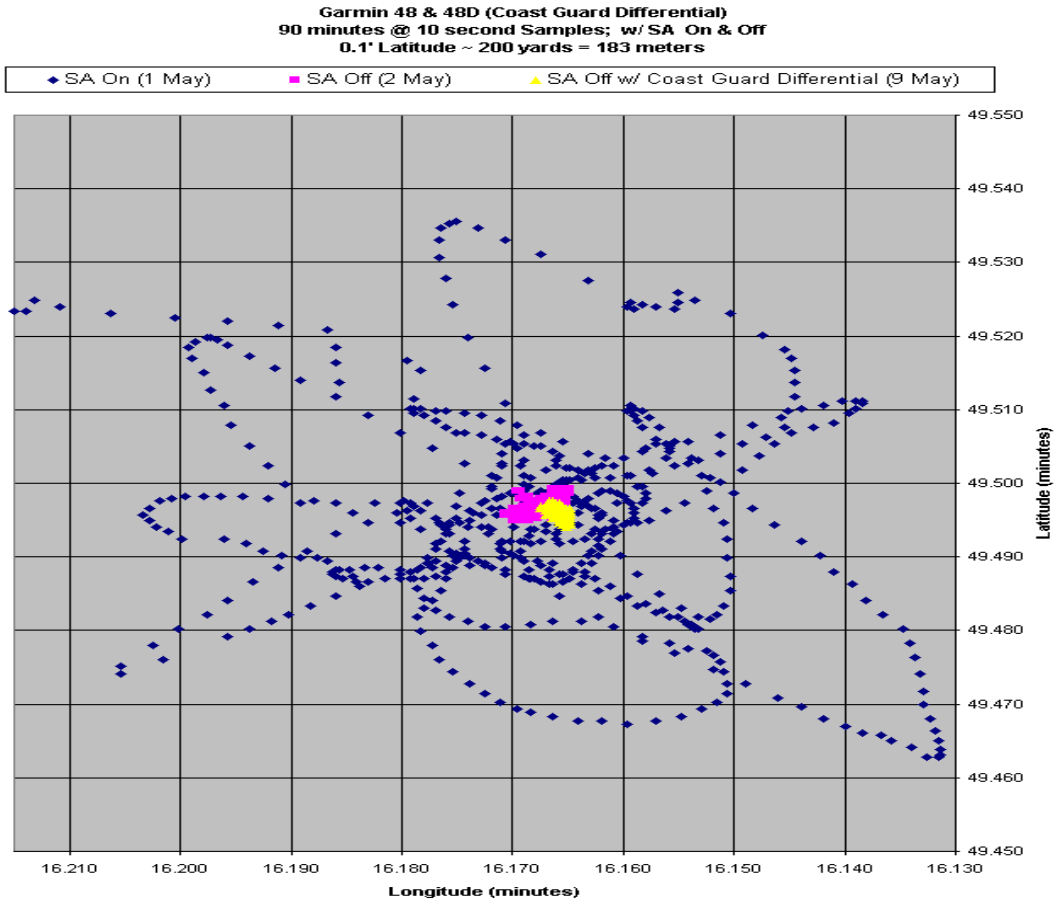

Figure 2.2 GPS Single Point Position (SPP) accuracy before and after the SA "switched off" for a terrestrial GPS receiver. [*Hydraulics laboratory*, 2004].

A positional accuracy of 10 ~ 20 metres satisfies most engineering requirements, and this requirement may be satisfied by the ONS without any additional effort, Indeed, ONS is the simplest OD strategy available, and desirable if the requirement can be met. In reality, it seems that most onboard orbit determination applications do not rely on the ONS solutions from the GPS receiver. To ensure robust and continuous onboard orbit solutions, some kind of filtering process is needed. The following sections will review different filtering strategies.

2.3 Extended Kalman Filter

An Extended Kalman filter provides a well established means for LEO orbit determination, and is a popular algorithm choice for most onboard OD applications due to its emphasis on both computing simplicity and accuracy. A Kalman filter-

based orbit determination process generates estimates of the instantaneous spacecraft state vector at discrete time steps that usually coincide with the arrival of new measurements. It operates in a sequential manner and does not demand the storage of previous measurements. However, it can properly use previous measurements and orbital information through the adjustment of the Kalman Gain. The system model errors can also be compensated for by means of process noise. These good characteristics make it a good choice for onboard data processing.

2.3.1 The Observation Models

Typically, numerical methods of varying complexity are applied to propagate the state vector between measurements. The satellite dynamical model is necessary for this purpose. Due to the limit of onboard memory and computing capability, most onboard applications use a simplified orbital model. This includes a truncated or simplified Earth gravitational model, which omits higher order spherical items. By reviewing the available onboard OD systems, a practical orbit model can be described as:

- Using a truncated Earth gravitational model by considering only up to spherical harmonic degree and order of 10, depending on different requirements. Some missions even use a pre-tuned specific gravitation model.
- Only considering the Earth rotation matrix when transforming from Earth-fixed frame to the inertial celestial frame (ICRF). This means the nutation, precession effects are neglected.
- Ignoring the drag and solar radiation pressure, as well as the gravitational perturbations from the Sun and the Moon.
- Using a simple Runge-Kutta 4(5) order integrator.

Of course, this only illustrates a general dynamical model for the onboard filter, and some missions use a more complicated model. Some even use a Keplerian one.

For the onboard orbit determination problem, the linear continuous state propagation equation and the observation state equation can be generally represented as:

$$\begin{cases} x_t = \Phi_{t,t-1} x_{t-1} + \mathbf{B}_t \mathbf{u}_t \\ z_t = \mathbf{H}_t x_t + \boldsymbol{\varepsilon}_t \end{cases} \quad (2.1)$$

where $\Phi_{t,t-1}$ and $\mathbf{B}_t$ are known functions of time. The noise term $\mathbf{u}_t$ is a random process with specified mean and covariance, i.e.,

$$E(\mathbf{u}_t) = \tilde{\mathbf{u}}_t, \quad E(\mathbf{u}_t \mathbf{u}_t^T) = \mathbf{Q}_t \quad (2.2)$$

Similarly, the measurement noise term $\boldsymbol{\varepsilon}_t$ is statistically described as:

$$E(\boldsymbol{\varepsilon}_t) = 0, \quad E(\boldsymbol{\varepsilon}_t \boldsymbol{\varepsilon}_t^T) = \mathbf{R}_t \quad (2.3)$$

The following Extended Kalman Filter is based on these basic equations and assumptions [*Kalman,* 1960*; Kalman & Bucy,* 1961].

2.3.2 The Extended Kalman Filter

The major difference between the traditional Kalman algorithm and the Extended Kalman filter lies in the fact that the latter does not keep the reference trajectory constant, but updates it based on the new estimate of $\mathbf{x}$ [*Minkler*, 1993]:

Given the following parametres:

- An a priori estimate of $\mathbf{x}$, $\hat{\mathbf{x}}_{t-1}$;
- The associated covariance matrix for $\hat{\mathbf{x}}_{t-1}$, $\hat{\mathbf{P}}_{t-1}$;
- Observation $\mathbf{z}_t$ at time t with associated observational error covariance matrix $\mathbf{R}_t$.

If the process noise $\mathbf{u}_t$ is not considered, the extended sequential computational algorithm for the optimal estimate of $\mathbf{x}$ at any time t is here summarized. Integrate or propagate numerically from $t-1$ to t:

1. Giving the following parametres:

$$\dot{\tilde{\mathbf{x}}} = f(\tilde{\mathbf{x}}, t), \quad \tilde{\mathbf{x}}_{t-1} = \hat{\mathbf{x}}_{t-1} \quad (2.4)$$

$$\dot{\boldsymbol{\Phi}}_{t,t-1} = \mathbf{H}_t \boldsymbol{\Phi}_{t,t-1}, \quad \boldsymbol{\Phi}_{t-1,t-1} = \mathbf{I} \quad (2.5)$$

2. Propagate (time update):

$$\tilde{P}_k = \tilde{\boldsymbol{\Phi}}_{t,t-1} \hat{P}_{t-1} \boldsymbol{\Phi}_{t,t-1}^T \quad (2.6)$$

3. Compute the linearized measurements:

$$\mathbf{Y}_t = \mathbf{z}_t - \mathbf{G}(\tilde{\mathbf{x}}_t, t) \tag{2.7}$$

$$\mathbf{H}_t = \left[\frac{\partial G(\tilde{\mathbf{x}}_t, t)}{\partial \tilde{\mathbf{x}}_t} \right] \tag{2.8}$$

4. Compute the measurement updates:

$$\mathbf{K}_t = \mathbf{P}_t \mathbf{H}_t^T \left[\mathbf{H}_t \tilde{\mathbf{P}}_t \mathbf{H}_t^T + \mathbf{R}_t \right]^{-1} \tag{2.9}$$

$$\hat{\mathbf{P}}_t = \left[\mathbf{I} - \mathbf{K}_t \mathbf{H}_t \right] \tilde{\mathbf{P}}_t \tag{2.10}$$

$$\hat{\mathbf{x}}_t = \tilde{\mathbf{x}}_t + \mathbf{K}_t \mathbf{Y}_t . \tag{2.11}$$

2.3.3 Process Noise and Measurement Noise

To observe unmodelled motion, we model the time-varying satellite force as the sum of a deterministic component (our standard dynamic model) and a stochastic component. The latter is often called a process noise model. Augmenting a Kalman filter with a process noise model is a way of telling the filter that the state transition information in $\Phi_{t,t-1}$ is incomplete—that there is another component that the filter cannot predict, but that it can try to observe in the data and estimate at each time step [*Yunck,* 1996].

In the context of orbit determination this means that at each time step, in addition to applying the standard dynamic updates, the filter will examine the discrepancy between the dynamic state estimate and the apparent state as indicated geometrically by the measurements. From that discrepancy it will estimate a local correction to the dynamic model, valid only over the update interval $t_{k-1} \sim t_k$. When added to the dynamic model that correction will reduce the disagreement between the observations and the solution trajectory at time t_i . As it proceeds through the data, the filter will generate a sequence of local force model corrections, one at each update time, bringing the solution trajectory into better agreement with the observations [*Feng*, 1998]. That may be good or bad, depending on the quality of the observations and the accuracy of the models. We must, therefore, take care to hinder the local corrections from "chasing after" bad measurements. In other words, we must consider the effects of the measurement outliers.

Because the kinematic correction is geometric, it is vulnerable to weak geometry. Momentary data outages or large position dilution of precision (PDOPs) will cause the error to grow or the solution to fail. The kinematic solution, moreover, makes no use of dynamic information—it is an empirical result constructed from the measurements. Often, however, dynamic information is at hand which, if properly treated, can improve the result. When geometry weakens or fails, dynamic information can then "carry" the solution with little loss of accuracy.

In current practice, the strategy is to achieve a balance of dynamic and geometric information in the orbit solution by imposing a judicious constraint on the process noise parametres. In an optimal solution (under the assumption of a Gauss-Markov process noise model), the time constant will reflect the actual correlation time of dynamic model errors, and the steady-state variance, the actual error in the dynamic model. The geometric corrections will not be free to "follow" the measurements wherever they lead, but will be bound by the constraint to the dynamic model. The relative weight will, in fact, shift back and forth between dynamic and geometric information as the observing strength varies. When geometry is weak, the process noise constraint will hold the correction close to the dynamic solution; if there are no observations at all, no correction can be computed and the dynamic solution is produced. This optimised technique is known as *reduced dynamic* orbit determination.

In the dynamic solution, random error is minimized (because the fewest parametres are adjusted), while dynamic error is fully expressed. This is reversed in the kinematic solution as many parametres are adjusted, amplifying the effect of data noise while absorbing dynamic error. The reduced dynamic solution seeks the optimal balance to minimize overall errors.

This raises the question of how we choose the process noise weighting. Often there is some prior knowledge of the quality of the force models in use and the consequent position error expected. Computer simulations or covariance analysis can then suggest a reasonable a priori weighting. When real data become available, a variety of strategies for tuning the reduced dynamic constraints become possible. One approach is to observe the magnitude of the process noise corrections; if they

approach the constraints, the constraints should be relaxed; if they fall well short, then the constraints can be tightened. Another technique is to compare orbit solutions on short overlapping segments and tune the constraints to minimize the discrepancy.

2.3.4 Discussion

Many available onboard orbit determination systems show that positional accuracy of metres to tens of metres can be achieved, with a convergence time of around several hours. This is satisfactory for most applications. One of the difficulties of the extended sequential algorithm is that the reference (nominal) trajectory integration (propagation) needs to be restarted at every step. On the other hand, the reference trajectory update might still lead to divergence. This is especially true if the update of the nominal trajectory is performed from the beginning using estimates of $\mathbf{x}_t$ that might still be far from the true state. This algorithm, as was the case with the previous sequential algorithm, has the problem of divergence caused by the asymptotically approach to zero of the covariance matrix [*Van Dierendonck*, 1992]

2.4 Phase-connected Kinematic Filter

Alternatively, a complete geometric approach for onboard orbit determination has been devised [*Bisnath & Langleg,* 2001]. It does not use any dynamic model but requires both code and phase measurements. The strategy relies on combining the time-continuous measurement strength of the pseudo-range and carrier-phase observables.

2.4.1 Phase-connected Point Positioning Filter

The use of only GPS measurements for satellite positioning can be achieved in a number of different ways ranging from pseudo-range point positioning to some form of combined pseudo-range and carrier-phase positioning. The latter approach is used in this strategy and its basic form can be attributed to the seminal work of *Hatch* [1982]. The crux of carrier and pseudo-range combination is the use of averaged noisy code-phase range measurements to estimate the ambiguity term in the precise

carrier-phase range measurements. The longer the pseudo-range averaging, the better the carrier-phase ambiguity estimate.

The carrier/pseudo-range averaging periods are typically short in spaceborne applications due to the relatively fast motion of the LEO, necessitating frequent changing of GPS satellites being tracked by the receiver. Such a situation does not allow for the highest precision of the technique to be attained. However by performing the averaging in the position rather than the range domain, previous position solutions can be used for estimating present and future position solutions. In essence, the pseudo-ranges provide coarse position estimates and the relative carrier-phase measurements provide precise positioning change estimates. The position-change estimates are used to map all of the position estimates to one epoch for averaging.

2.4.2 Filter Models and Solution

The liberalized filter observation model in matrix form is:

$$\begin{bmatrix} P_t - P_t^0 \\ \delta\phi_t - \delta\phi_t^0 \end{bmatrix} = \begin{bmatrix} \mathbf{0} & \mathbf{H}_t \\ -\mathbf{H}_{t-1} & \mathbf{H}_t \end{bmatrix} \begin{bmatrix} \delta\mathbf{x}_{t-1} \\ \delta\mathbf{x}_t \end{bmatrix} + \begin{bmatrix} \boldsymbol{\varepsilon}^{p}{}_{t} \\ \boldsymbol{\varepsilon}^{\phi}{}_{t,t-1} \end{bmatrix} \tag{2.12}$$

where P_t and P_t^0 are the pseudo-range measurement and computed value, respectively; $\delta\phi_t$ and $\delta\phi_t^0$ are the time-differenced carrier-phase measurement and predicted value, respectively; $\delta\mathbf{x}_{t-1}$ and $\delta\mathbf{x}_t$ are the estimated corrections to the LEO receiver position and clock at epochs *t-1* and *t*, respectively; $\mathbf{H}_{t-1}$ and $\mathbf{H}_t$ are the measurement partial derivatives with respect to the LEO receiver position and clock estimates for epochs *t-1* and *t*, respectively; $\boldsymbol{\varepsilon}^{p}{}_{t}$ and $\boldsymbol{\varepsilon}^{\phi}{}_{t,t-1}$ are the measurement errors associated with P_t and $\delta\phi_t$, respectively; and $\mathbf{C}_P$ and $\mathbf{C}_\phi$ are the covariance matrices for P_t and $\delta\phi_t$, respectively.

The best solution for Equation (2.12), in a least squares sense, is:

$$\begin{bmatrix} \hat{\mathbf{x}}_{t-1} \\ \hat{\mathbf{x}}_t \end{bmatrix} = \begin{bmatrix} \mathbf{x}_{t-1}^0 \\ \mathbf{x}_t^0 \end{bmatrix} - \begin{bmatrix} \mathbf{H}_{t-1}^T\mathbf{C}_\phi^{-1}\mathbf{A}_{t-1} + \mathbf{C}_{\mathbf{x}_{t-1}}^{-1} & -\mathbf{H}_{t-1}^T\mathbf{C}_\phi^{-1}\mathbf{H}_t \\ -\mathbf{H}_t^T\mathbf{C}_\phi^{-1}\mathbf{H}_{t-1} & \mathbf{H}_t^T(\mathbf{C}_p^{-1} + \mathbf{C}_\phi^{-1})\mathbf{H}_t \end{bmatrix}^{-1} \times$$

$$\begin{bmatrix} -\mathbf{H}_{t-1}^{T}\mathbf{C}_{\phi}^{-1}\mathbf{w}_{\phi} \\ \mathbf{H}_{t}\mathbf{C}_{p}^{-1}\mathbf{w}_{p} + \mathbf{H}_{t}\mathbf{C}_{\phi}^{-1}\mathbf{w}_{\phi} \end{bmatrix} \tag{2.13}$$

where $\hat{\mathbf{x}} = \mathbf{x}_0 + \delta\mathbf{x}$; $\mathbf{w}_p$ and $\mathbf{w}_\Phi$ are the misclose vectors for the pseudo-ranges and time-differenced carrier-phases, respectively; and $\mathbf{C}^{-1}{}_{x_{t-1}}$ is the LEO receiver position and clock covariance based on the last epoch's observations.

The position estimate at the previous epoch, *t-1*, is used as an approximate value to estimate the position at epoch *t* and so on for the moving LEO. Equation (2.13) represents a kinematic, sequential least squares filter. This type of filter is a subset of the general Kalman filter.

2.4.3 Discussion

Theoretically this geometric method utilizes the full potential of the GPS measurements, and makes use of the readily available GPS data products. The dynamics-free nature makes it a very simple and efficient orbit determination method for LEO. On the other hand, it demands good GPS geometry as well as sufficient phase connection arc length.

Some ground-based simulation results have been reported. The results suggest an overall 100cm 3D RMS accuracy for T/P [*Bisnoth & Langley*, 2001], and for periods of good geometry, the accuracy can be improved considerably to the 30cm level. Report [*Bisnath & Langley*, 2002] also suggests that 40cm in radial component and 30cm in each of the along-track and cross-track components have been achieved for CHAMP. But these results were obtained from IGS orbital products and precise GPS satellite information, such as the GPS satellite phase wind-up modelling, sub-diurnal variations in the Earth rotation, etc. It is estimated that metre level accuracy could be achievable if using the broadcast ephemerides and less complex satellite model information.

2.5 Onboard Simplified General Perturbations- SGP4 Filter

In a typical onboard Extended Kalman Filter the disadvantage of numerical orbit prediction may be overcome by the use of analytical orbit models, which can be evaluated at arbitrary times and do not require a step-wise integration of the trajectory. This allows offline predictions over mid- and long-term time scales (multiple revolutions to multiple days) at the expense of decreased short-term (<1 revolution) accuracy. The Simplified General Perturbations- SGP4 model [*Hoots & Rochrich*, 1980] is a common choice because of its widespread application for near-circular, low altitude satellites, and its high communality with existing ground equipment and commercial off-the-shelf software products. The onboard SGP4 filter is formulated for the direct estimation of the SGP4 mean orbital parametres from the onboard GPS measurements.

2.5.1 SGP4 Model Overview

Developed in 1970 by NORAD, the SGP4 (Simplified General Perturbations) model is based on the analytical theory of Brouwer and accounts for the Earth gravitational field through zonal terms J_2, J_3, J_4 and the atmospheric drag through a power density function assuming a non-rotating spherical atmosphere. Short periodic perturbations, however, are only modelled to first order (J_2). The SGP4 model, which is denoted here by the symbol **S** in the sequel, relates the spacecraft state vector as:

$$y_t = \begin{pmatrix} \mathbf{r}_t \\ \dot{\mathbf{r}}_t \end{pmatrix} \approx \mathbf{S}_t(\overline{\alpha}_0, B) \tag{2.14}$$

at time *t* to a set of mean elements:

$$\overline{\alpha}_0 = (\overline{a}_0, \overline{e}_0, \overline{i}_0, \overline{\Omega}_0, \overline{\omega}_0, \overline{M}_0) \tag{2.15}$$

at epoch t_0 and a ballistic coefficient $B = C_D A / m$ describing the effective satellite area-to-mass ratio. The SGP4 orbit model comprises the computation of secular and long-periodic perturbations of the orbital elements from which a preliminary state vector is computed. Upon adding the short-periodic perturbations, an approximate osculating state vector is obtained. In total the SGP4 model is considered a 6-

dimensional, continuous and differentiable function of time, dependant on seven dynamic parameters. A detailed description of the SGP4 model is given in [*Hoots & Rochrich*, 1980].

2.5.2 Osculating to Mean Elements Conversion

A different parametreization of the SGP4 model is required for the adjustment of orbital parametres from observations. The so-called 'mean SGP4 state vector concept' can be expressed as the mean state vector at epoch t_0 [*Herman*, 1998]:

$$\bar{y}_0 = \mathbf{K}(\bar{\alpha}_0) \tag{2.16}$$

where $\bar{\alpha}_0$ denotes the SGP4 mean elements at the same epoch. The expression:

$$y_t \approx \mathbf{S}(\mathbf{K}^{-1}(\bar{\mathbf{y}}_0), B) = \mathbf{s}_t(\mathbf{x}) \tag{2.17}$$

which relates the osculating state vector for a given time *t* to the combined parametre vector $\mathbf{x} = (\bar{y}_0, B)$ via the composite function **s**. Compared to the original formulation, **s** is non-singular even for circular or equatorial orbits and the partial derivatives of *s* with respect to the orbital parametres are well defined throughout the phase space of interest.

For epoch t_0 and a given ballistic coefficient B, we can get:

$$\bar{y}_0^{(0)} = \mathbf{y}_0, \quad \bar{y}_0^{(i+1)} = \bar{y}_0^{(i)} + (y_0 - \mathbf{s}(\bar{y}_0^{(i)}, B), t_0) \tag{2.18}$$

This provides a useful point-to-point conversion from osculating to mean state vectors.

2.5.3 SGP4 Elements Estimation from GPS Measurements Using Kalman Filter

A classical Kalman filter, estimating the instantaneous state vector, is likewise undesirable due to the non-trivial mapping of osculating to mean orbit information. As a solution to this problem, an extended epoch state filter is considered, which processes all the measurements sequentially (and only once) to update an a priori value of the mean state vector at epoch, as well as its covariance. In contrast to the classical Kalman filter the epoch state filter does not include a state update, since propagation of the estimated state to the measurement epoch is not required. Instead it consists of a measurement update only, which comprises the computation of the

Kalman Gain, correction of the current parametre estimate and the computation of the a posteriori covariance. The linearized measurements model function can be expressed as:

$$\mathbf{h}_t(\mathbf{x}_t) = \mathbf{\Theta}_t \times (\mathbf{1}_{3\times3}\mathbf{0}_{3\times3}) \times \mathbf{s}(\hat{\mathbf{x}}_t, t) \tag{2.19}$$

which is evaluated with the latest estimate $\hat{\mathbf{x}}_{t-1}$ of the parametre vector. Here $\mathbf{\Theta}_t = \mathbf{R}_z(\mathbf{GHA}(t))$ denotes the Earth rotation matrix that describes the transformation from the equator and equinox of date to the Earth-fixed Greenwich meridian system. Likewise, the partial derivatives $\mathbf{H}_{t-1} = \partial\mathbf{h}_t / \partial\hat{\mathbf{x}}_{t-1}$ of the computed measurements at time *t* are computed with respect to the estimated parametre vector $\hat{\mathbf{x}}_{t-1}$ as obtained from all previous measurements. This is a standard extended Kalman filter, and the resulting filter equations are given by Equation (2.9) ~ (2.11).

2.5.4 Discussion

Compared to classical Kalman filters using numerical orbit models, this method can cope with low measurement rates and data gaps of up to several days in size. Its built-in capability to adjust a free drag parametre as well as the analytical formulation of the orbit model facilitates mid-term forecasts and allows the implementation of onboard algorithms for the prediction of station contact or eclipse times. On the other hand, due to the limit of the SGP4 model itself, the short-term orbit solution accuracy is far less than the numerical method. It is around 1000 metres.

PoSAT-1 mission used such a SGP4 filter and generated an approximate 1.5km orbit accuracy using only one orbit data per day [*Montenbruck & Gill*, 1996]. Some simulation experiments also have been carried out using GPS/MET and MOMSNAV (MIR) mission data, and also around 1km positional accuracy was achieved. The detailed result of SGP4 filter from the BIRD mission haven't been published, but the same results also were achieved through their simulation studies.

2.6 Proposed Onboard Orbit Determination Methods

2.6.1 Motivations

The purpose of this research is to develop an orbit determination system providing metres to sub-metre level positional accuracy and mm/s velocity accuracy in near-real time to real time (normally means minutes to tens minutes after last GPS observation); while the computional burden is kept within the memory and computing capability limits for most LEO satellites. For the existing solutions and methods, we have the following observations:

- First of all, onboard point positioning solution can provide 10~20 metres positional accuracy, but the solution is vulnerable and it cannot provide continuous or predicted orbit information, thus the point positioning solution is not suitable for many missions.

- Secondly, a sequential Extended Kalman filter-based dynamical orbit determination process generates estimates of the instantaneous spacecraft state vector at discrete time steps that usually coincide with the arrival of new measurements. Such OD system is a quite simple filtering process, depending on the underlying dynamical model, and generates better results than the navigation solution. But the Kalman filter is really tricky one, with the stability being the most important issue. To achieve a satisfied result, process noise should be considered in the filter. The dedicated treatment of the process noise and the measurement weight scheme are the key issues for a stable Kalman filter, and this treatment is a challenge most of the time. Another problem with the Kalman filter is the convergence time, as it usually takes several hours to converge, which is not a problem for continuous operational GPS, but problems arises when the intermittent operation model is used. That means the Kalman filter will need initialization and re-convergence.

- The phase-connected kinematic method is suitable for onboard processing because it doesn't require any dynamic information. But it requires good pseudo-range measurement quality and good GPS satellite geometry, which is not always available.

- Furthermore, the SGP4 filter is not suitable for our purpose simply because of its limited accuracy. It could be useful as a long-term moderate accuracy orbit predictor, but not for a high accuracy real time onboard filter spacecraft.

Based on these considerations, research challenges to implement a near-real time onboard orbit determination system have been identified. These can be summarized as:

- how to increase the OD accuracy while maintaining the onboard computing burden to an acceptable level;
- how to increase the stability of the onboard filter; and
- how to satisfy the near-real time (even real time) requirements.

2.6.2 Summary of the Proposed Methods

To address these technical challenges a near-real time orbit determination method is proposed in this dissertation. The method has the following characteristics:

- Using the orbital model simplification techniques to be discussed in Chapter 3, and the Earth gravity approximation method to be tested in Chapter 4. These simplifications reduce the computational burden dramatically and retain the high accuracy of the complex models.
- Using a sequential carrier-phase smoothing method to improve the code measurement quality can greatly increase the orbit determination accuracy. Furthermore, a sliding-window processing method is proposed to reduce the onboard memory usage for the measurements as well.
- Using a stable weighted least squares filter with short-arc length, from 15 minutes to 2 hours, with a sliding-window method, the filter solution is available with 5~30 minutes latency

- Optionally the method has the ability to predict the orbit for 1 hour, and meet the requirements of many real time applications.

Table 2.3 gives a summary of proposed techniques and objectives. We discuss these techniques in the following chapters.

Table 2.3 Summary of research efforts toward a near-real time onboard orbit determination system.

	Techniques	**Objectives**
Orbit dynamical models	Simplifications: • Gravity model approximation • Lunar and solar ephemerides tables • Celestial parametres interpolation • Atmospheric models • Integral equations	Reduce the onboard computational burden and retain the full model accuracy.
Linear models: Observation and state transition equation	• Closed form state derivations • Closed form GPS single point positioning	Reduce the computational burden by simplifying the state transition matrix computing, and give an initial orbit estimation without initial input.
Observations improvement	• Effective outlier detection to control quality of code data • Phase smoothing for improved measurement accuracy • Stochastic models	Increase the GPS code measurement quality and reduce the onboard memory usage.
Orbit Estimation	• Short-arc orbit estimation • Sliding-window OD	Achieve metre level orbit determination accuracy with 20~40 minutes latency;
Software development	• A comprehensive library of data processing routines in the area of mathematics, astronomy, geodesy, GPS and estimation; • Independent software modules of orbit integration, GPS data editing, GPS ephemerides calculation, orbit filtering, smoothing, etc.	Establish an orbit determination platform to facilitate this research and FedSat OD projects.

Chapter 3
Simplifications of Dynamical Models for Low Earth Orbiters

In this chapter, a detailed description of the orbit dynamical models is given to provide a basis for the proposed method, based on precise dynamical models and precise orbit numerical integration approaches. Due to the limitation of power and computing capacity onboard a spacecraft, full accuracy dynamical models are not realistic, especially on small satellites, hence different schemes for orbit model simplifications are examined and new simplification methods are proposed.

3.1 Orbit Dynamic Models for LEO

Mathematical models employed to describe the motion of a LEO satellite can be divided into three categories:

- the gravitational forces acting on the spacecraft consist of the Earth's central body gravity, non-spherical geopotential, third-body perturbations; and
- the non-gravitational forces consist of drag, solar radiation pressure, Earth radiation pressure, and thermal radiation acceleration; and
- un-modelled or mis-modelled forces, such as solid earth tides, ocean tides, relativistic effects, Earth rotational deformation, etc.

Therefore, the equations of motion of a near-Earth satellite can be described in an inertial reference frame as:

$$\ddot{\mathbf{r}} = \mathbf{a}_g + \mathbf{a}_{ng} + \mathbf{a}_{emp} \tag{3.1}$$

where $\ddot{\mathbf{r}}$ is the position vector of the centre of mass of the satellite, $\mathbf{a}_g$ is the sum of the gravitational forces acting on the satellite, $\mathbf{a}_{ng}$ is the sum of the non-gravitational

forces acting on the surfaces of the satellite, and $\mathbf{a}_{emp}$ are the un-modelled forces which act on the satellite due to either a functionally incorrect or incomplete description of the various forces acting on the spacecraft, or inaccurate values for the constant parametres which appear in the force model.

In the following section the basic time and coordinate systems used in the orbit determination are first briefly described, followed by a detailed description of the force models.

3.1.1 Time and Coordinate Systems

Time System

An orbit integration problem involves several time systems. From the measurement systems, satellite laser ranging measurements are usually time-tagged in UTC (Coordinated Universal Time) and GPS measurements are time-tagged in GPS System Time (referred to here as GPST). Although the second length of both UTC and GPST are based on atomic time standards, UTC is loosely tied to the rotation of the Earth through the application of "leap seconds" to keep UT1 and UTC within a second. GPST is continuous to avoid complications associated with a discontinuous time scale [*Milliken & Zoller,* 1978]. Leap seconds are introduced on January 1 or July 1, as required. The relation between GPST and *UTC* is:

$$GPST = UTC + n \tag{3.2}$$

where n is the number of leap seconds since January 6, 1980. For example, the relation between UTC and GPS-ST in mid-July 1999 was $GPST = UTC + 13$ seconds. The independent variable of the near-Earth satellite equations of motion (Equation (3.1)) is typically TDT (Terrestrial Dynamical Time), which is an abstract, uniform time scale implicitly defined by the equations of motion. This time scale is related to the TAI (International Atomic Time) by the relation:

$$TDT = TAI + 32.184s \tag{3.3}$$

The planetary ephemerides are usually given in TDB (Barycentric Dynamical Time) scale, which is also an abstract, uniform time scale used as the independent variable for the ephemerides of the Moon, Sun, and planets. The transformation from TDB to TDT with sufficient accuracy for most applications has been given by *Moyer* [1981].

For a near-Earth missions like T/P, it is unnecessary to distinguish between TDT and TDB. New time systems are under discussion by the International Astronomical Union. This document will be updated with these time systems, as appropriate.

Coordinate System

The inertial reference system adopted for Equation (3.1) for the dynamic model is the ICRF geocentric inertial coordinate system, which is defined by the mean equator and vernal equinox at Julian epoch 2000.0. The Jet Propulsion Laboratory (JPL) DE-405 planetary ephemeris [*Standish,* 1998], which is based on the ICRF inertial coordinate system, has been adopted for the positions and velocities of the planets with the coordinate transformation from barycentric inertial to geocentric inertial.

Tracking station coordinates, atmospheric drag perturbations, and gravitational perturbations are usually expressed in the Earth-fixed, geocentric, rotating system, which can be transformed into the ICRF reference frame by considering the precession and nutation of the Earth, its polar motion, and the UT1 transformation, The 1976 International Astronomical Union (IAU) precession [*Lieske, et al.*, 1977, *Lieske,* 1979] and the 1980 IAU nutation formula [*Wahr*, 1981; *Seidelmann*, 1982] with the correction derived from VLBI analysis [*Herring, et al.*, 1991] will be used as the model of precession and nutation of the Earth. Polar motion and UT1-TAI variations were derived from Lageos (Laser Geodynamics Satellite) laser ranging analysis [*Tapley, et al.,* 1985; *Schutz, et al.,* 1988].

3.1.2 Gravitational Forces

The gravitational forces can be expressed as:

$$\mathbf{a}_g = \mathbf{a}_{geo} + \mathbf{a}_n \qquad (3.4)$$

where

$\mathbf{a}_{geo}$ = perturbations due to the geopotential of the Earth

$\mathbf{a}_n$ = perturbations due to the Sun, Moon and planets

Geopotential

The perturbing forces of the satellite due to the gravitational attraction of the Earth can be expressed as the gradient of the potential **U**, which satisfies the Laplace equation $\nabla^2 \mathbf{U} = 0$:

$$\nabla \mathbf{U} = \nabla(\mathbf{U_s}) = \mathbf{a_{geo}} \tag{3.5}$$

where $\mathbf{U}_s$ is the potential due to the solid-body mass distribution.

The perturbing potential function for the solid-body mass distribution of the Earth $\mathbf{U}_s$ is generally expressed in terms of a spherical harmonic expansion, referred as the geopotential, in a body-fixed reference frame [*Kaula*, 1966; *Heiskanen & Moritz*, 1967]:

$$\mathbf{U}_s(r,\lambda,\varphi)) = \frac{GM_e}{r} + \frac{GM_e}{r}\sum_{l=1}^{\infty}\sum_{m=0}^{l}\left(\frac{a_e}{r}\right)^l \overline{P}_{lm}(\sin\varphi)[\overline{C}_{lm}\cos m\lambda + \overline{S}_{lm}\sin m\lambda] \tag{3.6}$$

where

GM_e = the gravitational constant of the Earth

a_e = the mean equatorial radius of the Earth

$\overline{C}_{lm}, \overline{S}_{lm}$ = normalized spherical harmonic coefficients of degree *l* and order *m*

$\overline{P}_{lm}(\sin\phi)$ = the normalized associated Legendre function of degree *l* and order *m*

r, ϕ, λ = radial distance from the centre of mass of the Earth, the geocentric latitude and the longitude of the satellite

To ensure that the origin of spherical coordinates coincides with the centre of mass of the Earth, we define $\overline{C}_{10} = \overline{C}_{11} = \overline{S}_{11} = 0$.

N-Body Perturbation

The gravitational perturbations of the Sun, Moon and planets can be modelled with sufficient accuracy using point mass approximations. In the geocentric inertial coordinate system, the accelerations can be expressed as:

$$\mathbf{a}_n = \sum_i GM_i[\frac{\mathbf{r}_i}{r_i^3} - \frac{\mathbf{\Delta}_i}{\Delta_i^3}] \tag{3.7}$$

where

G = the universal gravitational constant

M_i = mass of the *i*-th perturbing body

$\mathbf{r}_i$ = position vector of the *i*-th perturbing body in geocentric inertial coordinates

$\mathbf{\Delta}_i$ = position vector of the *i*-th perturbing body with respect to the satellite

The values of $\mathbf{r}_i$ and M_i can be obtained from the Jet Propulsion Laboratory Development Ephemeris-405 (JPL DE-405) [*Standish*, 1998],

3.1.3 Non-gravitational Forces

The non-gravitational forces acting on the satellite can be expressed as:

$$\mathbf{a}_{\mathbf{ng}} = \mathbf{a}_{\mathbf{drag}} + \mathbf{a}_{\mathbf{solar}} \tag{3.8}$$

where

$\mathbf{a}_{\mathbf{drag}}$ = perturbations due to atmospheric drag

$\mathbf{a}_{\mathbf{solar}}$ = perturbations due to the solar radiation pressure

Since the surface forces depend on the shape and orientation of the satellite, the models are satellite-dependent. In this section, however, general models are described.

Atmospheric Drag

A near-Earth satellite of arbitrary shape moving with some velocity **V** in an atmosphere of density ρ will experience both lift and drag forces. The lift forces are small compared to the drag forces, which can be modelled as [*Schutz & Tapley*, 1980]:

$$\mathbf{a}_{\mathbf{drag}} = -\frac{1}{2}\rho(\frac{C_d A}{m})V_r \mathbf{V}_r \tag{3.9}$$

where

ρ = the atmospheric density

$\mathbf{V_r}$ = the satellite velocity relative to the atmosphere

V_r = the magnitude of $\mathbf{V_r}$

m = mass of the satellite

C_d = the drag coefficient for the satellite

A = the cross-sectional area of the main body perpendicular to satellite velocity $\dot{\mathbf{r}}$

The parametre $C_d A/m$ is sometimes referred to as the ballistic coefficient. When more detailed modelling is needed, the drag force on any specific spacecraft surface, for example, the solar panel, can be modelled as:

$$\mathbf{a}_{\mathbf{paneld}} = -\frac{1}{2}\rho\left(\frac{C_{dp}\left|A_p \cos\gamma\right|}{m}\right)V_r \mathbf{V}_r \qquad (3.10)$$

where

C_{dp} = the drag coefficient for the solar panel

A_p = the solar panel's area

γ = the angle between the solar panel surface normal unit vector, $\hat{\mathbf{n}}$ and satellite velocity vector, $\dot{\mathbf{r}}$

$\left|A_p \cos\gamma\right|$ = the effective solar panel cross-sectional area perpendicular to $\dot{\mathbf{r}}$

There are a number of empirical atmospheric density models used for computing the atmospheric density. These include the Jacchia 71 [*Jacchia*, 1971], Jacchia 77 [*Jacchia*, 1977], the Drag Temperature Model (DTM) [*Barlier, et al.*, 1977], DTM-2000 [*Bruinsma & Thvillier*, 2000], MSIS-90 and NRLMSISE-00 [*Hedin*, 1996]. The density computed by using any of these models could be in error anywhere from 10% to over 200% depending on solar activity [*Shum, et al.*, 1986]. To account for the deviations in the computed values of density from the true density, the computed values of density ρ can be modified during the orbit determination process.

Solar Radiation Pressure

The Sun emits a nearly constant amount of photons per unit of time. At a mean distance of 1 A.U. from the Sun this radiation pressure is characterized as a momentum flux having an average value of $4.56 \times 10^{-6} N/m^2$. The direct solar radiation pressure from the Sun on a satellite is modelled as [*Tapley & Ries*, 1987]

$$\mathbf{a}_{\mathbf{solar}} = -P(1+\eta)(\frac{A}{m})\nu\hat{\mathbf{u}} \tag{3.11}$$

where

P = the momentum flux due to the Sun

η = reflectivity coefficient of the satellite

A = the cross-sectional area of the satellite normal to the Sun

m = mass of the satellite

ν = the eclipse factor (ν = 0 if the satellite is in full shadow, $\nu = -1$ if the satellite is in full Sun, and $0 < \nu < 1$ if the satellites is in partial shadow)

$\hat{\mathbf{u}}$ = the unit vector pointing from the satellite to the Sun

Similarly, the solar radiation pressure perturbation on an individual satellite surface, such as the satellite's solar panel, can be modelled as

$$\mathbf{a}_{\mathbf{panels}} = -P(\frac{\left|A_p \cos\gamma\right|}{m})\nu(\hat{\mathbf{u}} + \eta_p\hat{\mathbf{n}}) \tag{3.12}$$

where

A_p = the solar panel area

η_p = the surface normal unit vector of the solar panel

γ = the angle between the solar panel surface normal unit vector $\hat{\mathbf{n}}$ and satellite-Sun unit vector, $\hat{\mathbf{u}}$

$\left|A_p \cos\gamma\right|$ = the effective solar panel cross sectional area perpendicular to $\hat{\mathbf{u}}$

The reflectivity coefficient η represents the averaged effect over the whole satellite rather than the actual surface reflectivity. Conical or cylindrical shadow models for the Earth and the lunar shadow are used to determine the eclipse factor ν. Since there

are discontinuities in the solar radiation perturbation across the shadow boundary, numerical integration errors occur for satellites which are in the shadowing region.

3.1.4 Other Perturbation Forces

Other non-gravitational perturbation forces, such as Earth solid tide, ocean tide, Earth rotation tide, relativistic effect, Earth radiation pressure, thermal radiation perturbations, yaw (steering) effect, etc., are too small to be considered here. Though these forces should be considered in precise orbit determination, they can be neglected in our research.

3.2 Simplification Schemes for Onboard Calculations

It is generally the case that more precise orbit state knowledge requires more complex dynamical models. It is especially true for the LEOs, which are heavily affected by the Earth's gravity field and atmospheric drag. On the other hand, the computing capacity onboard is always restricted for small to middle-sized spacecraft in these two respects [*Chiaradia*, 2002]:

- Heavy computing load always lead to greater power consumption, but limitations on power supply are always major problems for any satellite. The energy source comes from solar batteries, but they are limited by the solar panel size and battery.
- The cost of space-enabled hardware is very high for small satellites and the hardware requires strong resistance to radiation, temperature and concussion introduced by the violent space environment.

The onboard OD computing platform varies from mission to mission, but many aspects affect the computing performance. As far as the onboard OD computing burden is concerned there are two issues to address: CPU load and memory usage. The requirement of both will impact on the total computional burden and power consumption. CPU is the kernel part of the onboard computing facilities and it determines the processing speed. Its performance is influenced by the clock frequency, internal cache and memory bus bandwidth. For an onboard processing

unit, memory can be divided into Random Access Memory (RAM) and Read Only Memory (ROM). RAM operates at high speed and mainly provides the storage for the onboard operating system and OD programs, but it functions only while the system power is on, and thus cannot be used to store data. On the other hand, ROM keeps alive for a much longer time with little battery power support, and thus can be used to store static data. The performance of RAM and ROM can be evaluated by the capacity and read/write speed. We address the detailed computional burden in terms of CPU load (computing speed) and memory usage.

The onboard OD system comprises of several modules: data acquisition, GPS ephemerides calculation, orbit propagation and filtering processing.

3.2.1 Orbit Integration Computional Burden

Given the initial condition and a specific orbit dynamical model, the orbit propagation module calculates the satellite state vector and partials at a given time using a numerical stepwise integrator. From the software point of view, the computing load of orbit integration comes from two major computional tasks:

- Before the actual orbit integration start, some data must be made ready for use. This includes the Earth gravity harmonic coefficients, Earth rotation parametres, planetary ephemerides and geophysical data (such as F10.7 solar flux and geomagnetic index for atmospheric density calculation). All data are normally stored in onboard ROM and are fetched into RAM as soon as the OD program starts. Except for the I/O process, the program also does some initializations tasks on these data so that they can be used in subsequent orbit propagation processes.
- The second task is the orbit integration itself. With state vector and parametres known at t_0, it calculates the state vector and partials step-by-step from t_{i-1} to t_i, for $i = 1,\ldots,n$. There is a module to calculate the perturbation accelerations and partials, which is actually where the heavy computing takes place. It calculates the orbit perturbation accelerations and partials based on the input parametres and the given orbital dynamical model. The computing burden depends on how many times this module is called. Because we use *k*-

th order Runge-Kutta integrator, there are k steps for every t_{i-1} to t_i propagation process. So there are $n \times k$ calls to the derivation calculation function for the whole propagation.

We refer to the first part as the ***initialization module***, and the second part as the ***derivative computing module***. Figure 3.1a shows the detailed flow chart of orbit propagation. Figure 3.1b illustrates the derivation computing details.

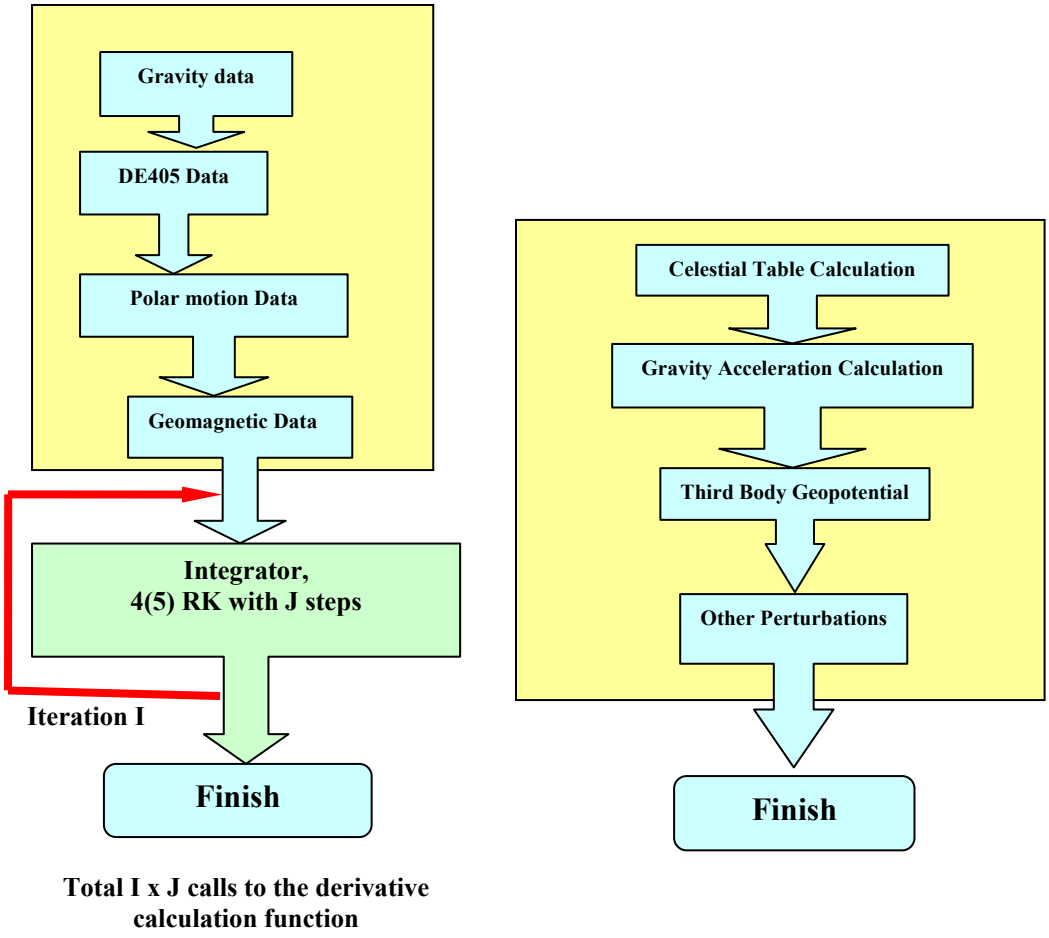

Figure 3.1a Computional flow chart of orbit integration; **Figure 3.1b** Calculation flow chart of derivatives computing module.

To understand the detailed computational burden, an orbit integration experiment was designed. Both the computing time and memory usage were determined by hundreds or thousands of repeated calls to these two modules; 200 calls and 20000 calls were used for the initialization module and derivation computing module, respectively. Though we cannot get 100 percent accurate figures from this test, we are more concerned with the relative computing burden distribution. The hardware

platform used was a PIII-1000Hz / 256M memory desktop computer, and the software is the QUT CRCSS FODT package. Table 3.1 gives the memory usage test results. This data was supposed to be uploaded to satellite once a month. Figure 3.2 and 3.3 gives the computing time distribution results for initialization and derivative computing modules, respectively.

Table 3.1 Storage requirement of orbit integration.

Data	**RAM**	**ROM**
Polar Motion	64 bytes per 5 days Usage: 10 days = 128 bytes	One month storage (text format) Usage = 456 bytes
Atmospheric Density Model	32 bytes per day Usage: 1 day = 32 bytes	One month storage (text format) Usage = 2,190 bytes
Planet Ephemerides	Usage: 16,352 bytes	One year storage (binary format) Usage = 97,894 bytes
Earth Gravity Model	Usage = 21,586 bytes	Usage = 88,935 bytes
Total:	Usage = 38,098 bytes = **37** Kbytes	Usage = 189,475 bytes = **185** Kbytes
	Data description	
Polar Motion	Using 5 days data from IERS bulletin B, which has 30 days prediction.	
Atmospheric Density Model	Using solar flux and the geomagnetic data, it is a daily complied data set. The atmospheric density model used is the MSIS86.	
Planet Ephemerides	Using DE405 data from JPL, data can be truncated to the desired period.	
Earth Gravity Model	Using 70 ×70 JGM-3 model, and up to 120 order and degree of Legendre polynominal coefficients.	

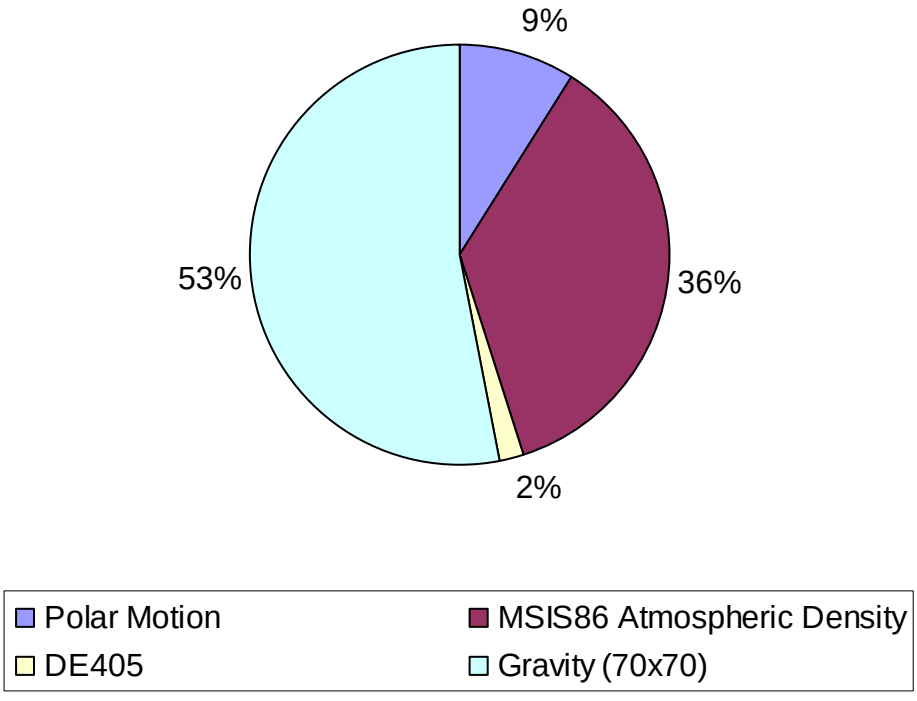

Figure 3.2 Computional time distribution of the initialization module.

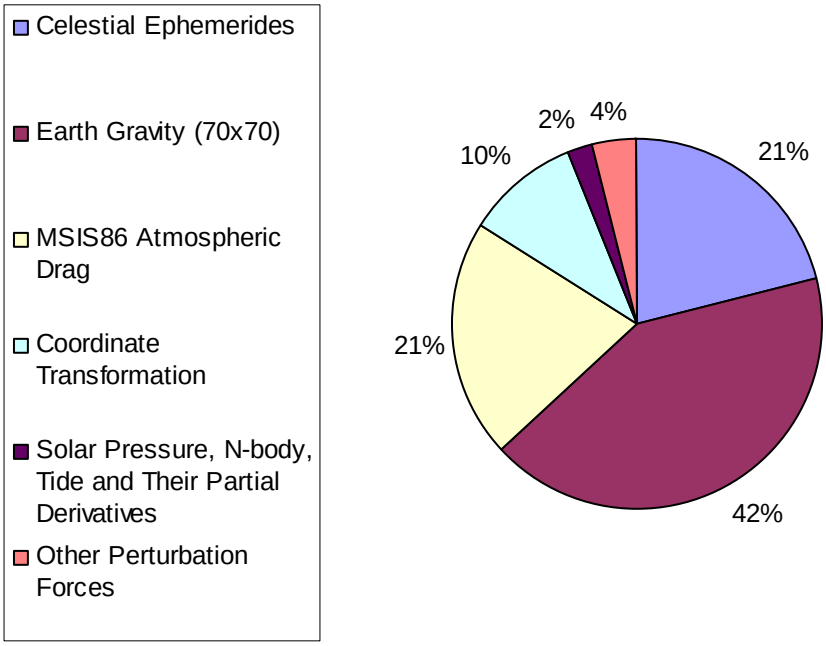

Figure 3.3 Computional time distribution for the partial derivatives computing modules.

From these figures it can be seem that the Earth gravity, atmosphere density and planetary ephemerides computing task take around 80% ~ 90% of computing time. Compared to the derivation computing module, the computing burden of the initialization module can be ignored. It is clear that 42% of the calculation burden comes from the Earth geopotential computations, because of the recursive nature of the spherical harmonic computation. The computing burden increases dramatically with the higher order & degree of spherical harmonic expression, so we can use a lower order gravity model, such as 10×10 ~ 30×30. Another method, which will be discussed in Chapter 4, changes the traditional recursive computing method, thus leading to a reduction in the computing burden. Furthermore, around 40% of computing burden comes from atmospheric density model and planet ephemerides computation, as can be seen in both initialization and propagation processes. For memory usage, around 200 Kbytes ROM is necessary for a one month mission, assuming a 70×70 Earth gravity model was used. The RAM usage varies within several Kbytes, depending on the software structure, memory allocation strategy and internal variable type.

3.2.2 Simplification Schemes

Based on the discussion in the previous sections, we have the following simplification schemes:

- Nearly 60% memory usage and 40% computing time in the orbit propagation are due to the Earth gravitational calculation. This includes the first and second-order partial calculation and the Legender polynominal coefficient propagation. These calculations are all recursive in nature. Different "order & degree" schemes can be tested against accuracy requirement. From previous experiment that $10 \times 10 \sim 20 \times 20$ is appropriate for onboard orbit determination, the computation burden decreases about 300% from the 70×70 model but only with 30% accuracy degradation [*Zhou & Feng*, 2002a].
- JPL DE405 ephemerides takes around 50% memory usage and about 20% computing time. Unlike the gravitation calculation, this part can be highly simplified because the accuracy of planetary ephemeris is much less important, as the order of magnitude of the acceleration is around $10^{-6} \sim 10^{-9} m/s^2$. Instead of using the DE405 interpolated ephemerides, an analytical sun & moon position algorithm will be tested.
- It is also found that the coordinate transformation process takes around 10% computing time because nutation, precession, polar motion, and planetary ephemerides are calculated for every integration step in real time. To minimize the calculation burden, we have used an interpolation method. In the initialization stage all of these ephemerides and parametres in a grid are calculated and stored, and then we can recover these parametres using different interpolation methods. In this way, around 10% computing burden can be relieved with only very small memory storage increase.
- Drag force takes 20% of the computing time. Although atmospheric drag is important for all LEO satellites, the calculation of a precise atmospheric density model is relatively heavy for an onboard platform. In addition to the calculation complexity, another problem is to get the real time Sun flux and geomagnetic data onboard. Instead of using an empirical density model, a

simplified upper atmospheric density model will be tested. This will greatly reduce the computing burden.

- The computing burden caused by the state transition matrix integration is very high if the full orbital model is considered. But the precise knowledge of the transition matrix is not required because the integration arc onboard is only several hours in length. A simplified method is used.
- Adaptive step size control in the orbit integrator may reduce some computing burden. In order to obtain a desired accuracy with minimum computational effort, the orbit integrator adjusts the time integration step size. The accuracy of the integration is compared to some desired accuracy and the step-size is increased or decreased, depending on whether the accuracy of integration is better or worse than the desired accuracy.

3.3 Simplified Solar and Lunar Coordinates

3.3.1 Introduction

For orbit determination the N-body gravitational perturbation from the Sun, Moon and all planets should be considered. The JPL provides a series of solar system ephemerides in the form of Chebyshev approximations. The Development Ephemerides are publicly available and have emerged as a standard source for high precision planetary and lunar coordinates. Currently the DE200 and DE405 ephemerides are most widely used for general applications.

All ephemerides are based on a rigorous numerical intergration of the respective equations of motion. In addition to the point-mass interactions among the Moon, the planets and the Sun, the perturbations from selected asteroids are considered, as well as relativistic post-Newtonian corrections to the equations of motion. Furthermore, the lunisolar torques on the figure of the Earth and the Earth and Sun's torques on the figure of the Moon are taken into account. The observational database for the development of DE405 comprised mainly optical transit measurements of the Sun and the planets since 1911, radar ranging to Mercury and Venus since 1964, tracking of deep space probes, planetary orbiters and landers since 1971, and lunar laser

ranging since 1970. Standard DE405 reading and interpolation methods are available from JPL. A small utility is also available to truncate the original data file to a shorter time span to minimize the file size.

Though DE405 is a right choice for orbit determination the computing requirement are too high for onboard processing. According to Newton's law of gravity the acceleration of a satellite by a point mass M is given by Equation (3.7). For a LEO satellite, $\mathbf{r}_i << (\mathbf{\Delta}, \mathbf{r}_j)$, the approximation can be made by $\Delta^3 = r_j^{\ 3}$:

$$\mathbf{a_n} = Gm_i \frac{r_\mathbf{i}}{\Delta^3}(\frac{\mathbf{r_i}}{r_\mathbf{i}}) \tag{3.13}$$

The order of magnitude of perturbation with respect to the Earth central body attraction can be expressed as:

$$\varepsilon = \frac{m_i}{M}(\frac{\mathbf{r_i}}{\Delta}) \tag{3.14}$$

For the Sun and Moon, and for the LEO satellite ($\mathbf{r}_i < 1.5$), we have:

$$\varepsilon = \begin{cases} 0.6\times10^{-7}\, m/s^2, & Sun \\ 1.2\times10^{-7}\, m/s^2, & Moon \end{cases} \tag{3.15}$$

For other planets, only acceleration from Jupiter is of the order of $10^{-13}\, m/s^2$. We only need to consider the acceleration from the Sun and the Moon for onboard orbit determination.

3.3.2 Methodology

Since the forces exerted by the Sun and the Moon are much smaller than the central attraction of the Earth, it is not necessary to know their coordinates to the highest precision when calculating the perturbing acceleration acting on a satellite. For many purposes it is even sufficient to use simple equations for the solar and lunar coordinates that are accurate to about 0.1% ~ 1% and follow from more advanced analytical theories for the motion of the Sun and the Moon [*Van Flandern & Pulkkinen*, 1979; *Montenbruck*, 1989, *Montenbruck & Pfleger,* 2000].

Geocentric solar coordinates can easily be obtained from the assumption of an unperturbed motion of the Earth around the Sun. Appropriate mean orbital elements,

which approximate the Sun's elliptic orbit with respect to the Earth and the ecliptic for some decades around the year 2000, are given by [*Montenbruck*, 1989]:

$$a = 149{,}600{,}000\text{km}, \quad e = 0.016709, \quad i = 0^\circ.000$$
$$\Omega + \omega = 282^\circ.9400; \quad M = 357^\circ.5256 + 35999^\circ.049T, \tag{3.16}$$

where

$$T = \left(JD - 2451545.0\right)/36525.0 \tag{3.17}$$

is the number of Julian centuries since 1.5 January 2000 (J2000), and JD is the Julian Date. The position coordinates may be found from these elements using the equations for Keplerian orbits that were derived in the previous chapter. Due to the small eccentricity and inclination, the use of some simple series expansions is, however, recommended to speed up the calculation without loss of accuracy. This results in the expressions:

$$\begin{aligned} \lambda_s &= \Omega + \omega + M + 6892'' \sin M + 72'' \sin 2M \\ r_s &= \left(149.619 - 2.499\cos M - 0.021\cos 2M\right) \times 10^6\, km \end{aligned} \tag{3.18}$$

for the Sun's ecliptic longitude λ_s and distance r_s, whereas the ecliptic latitude β_s vanishes within an accuracy of $1'$ [*Montenbruck*, 1989].

These values may be converted to Cartesian coordinates referring to the equator by applying an appropriate rotation:

$$\mathbf{r}_s = \mathbf{R}_x\left(-\varepsilon\right)\begin{pmatrix} r_s \cos\lambda_s \cos\beta_s \\ r_s \sin\lambda_s \cos\beta_s \\ r_s \sin\beta_s \end{pmatrix}, \quad \varepsilon = 23^\circ.4392911 \tag{3.19}$$

Since $\beta_s = 0$, the expression $\mathbf{r}_s$ may further be simplified to give:

$$\mathbf{r}_s = \begin{pmatrix} r_s \cos\lambda_s \\ r_s \sin\lambda_s \cos\varepsilon \\ r_s \sin\lambda_s \sin\varepsilon \end{pmatrix} \tag{3.20}$$

To be precise, the longitude λ_s, the latitude β_s, and the position vector $\mathbf{r}_s$ in Equation (3.19) refer to the mean equinox and ecliptic of J2000 (EME2000). Precession, which is a result of perturbing forces of the Sun, Moon and planets, gives rise to a slow motion of both the ecliptic and the equinox. While the ecliptic changes its orientation by less than $1'$ per century, the motion of the equinox is more pronounced, however, and amounts to $5030''$ per century. Referred to the mean

equinox of 1950, for example, the Sun's longitude is smaller than the above value by about 25150. In order to refer the coordinates to the equinox of some epoch T_{eqx} (measured in centuries since the epoch 2000), one has to add a correction of $1^{\circ}.3972T_{eqx}$ to the value of λ_s given above. The ecliptic latitude need not be changed since it varies by less than one arc-minute within a full century.

Series expansions similar to those for the Sun exist for the lunar coordinates as well. Due to the strong solar and terrestrial perturbations, a larger number of terms are, however, needed to describe the lunar motion in terms of the mean arguments of the lunar and solar orbit. The following relations allow the computation of lunar longitude and latitude with a typical accuracy of several arc-minutes and about 500km in the lunar distance. The calculation of the perturbations is based on five fundamental arguments: the mean longitude L_0 of the Moon, the Moon's mean anomaly *l*, the Sun's mean anomaly l', the mean angular distance of the Moon from the ascending node *F*, and the difference *D* between the mean longitudes of the Sun and the Moon. The longitude of the ascending node Ω is not explicitly employed. It is obtained from the difference $\Omega = L_0 - F$.

$$\begin{aligned}
L_0 &= 218^{\circ}.31617 + 481267^{\circ}.88088 \times T - 1^{\circ}.3972 \times T \\
l &= 134^{\circ}.96292 + 477198^{\circ}.86753 \times T \\
l' &= 357^{\circ}.52543 + 35999^{\circ}.04944 \times T \\
F &= 93^{\circ}.27283 + 483202^{\circ}.01873 \times T \\
D &= 297^{\circ}.85027 + 445267^{\circ}.1135 \times T
\end{aligned} \tag{3.21}$$

Using these values the Moon's longitude with respect to the equinox and ecliptic of the year 2000 may be expressed as:

$$\begin{aligned}
\lambda_m = L_0 &+ 22640'' \times \sin(l) + 769'' \times \sin(2l) \\
&- 4586'' \times \sin(l - 2D) + 2370'' \times \sin(2D) \\
&- 668'' \times \sin(l') - 412'' \times \sin(2F) \\
&- 212'' \times \sin(2l - 2D) - 206'' \times \sin(l + l' - 2D) \\
&+ 192'' \times \sin(l + 2D) - 165'' \times \sin(l' - 2D) \\
&- 110'' \times \sin(l + l') - 55'' \times \sin(2F - 2D).
\end{aligned} \tag{3.22}$$

Here, the first two terms describe the motion in an ellipse of eccentricity *e* = 0.055, whereas the remaining terms denote the various perturbations. The lunar latitude is given by:

$$
\begin{aligned}
\beta_m &= 18520'' \sin\left(F + \lambda - L_0 + 412'' \times \sin 2F + 541'' \times \sin l'\right) \\
&- 526'' \times \sin\left(F - 2D\right) + 44'' \times \sin\left(l + F - 2D\right) \\
&- 31'' \times \sin\left(-l + F - 2D\right) - 25'' \times \sin\left(-2l + F\right) \\
&- 23'' \times \sin\left(l' + F - 2D\right) + 21'' \times \sin\left(-l + F\right) \\
&+ 11'' \times \sin\left(-l' + F - 2D\right)
\end{aligned} \tag{3.23}
$$

where the leading term is due to the inclination of the Moon's orbit relative to the ecliptic, which amounts to approximately 5.1°. Finally the Moon's distance from the centre of the Earth is:

$$
\begin{aligned}
r_m &= 385{,}000 - 20{,}905 \times \cos\left(l\right) - 3{,}699 \times \cos\left(2D - l\right) \\
&- 2{,}956 \times \cos\left(2D\right) - 570 \times \cos\left(2l\right) + 246 \times \cos\left(2l - 2D\right) \\
&- 205 \times \cos\left(l' - 2D\right) - 171 \times \cos\left(l + 2D\right) \\
&- 152 \times \cos\left(l + l' - 2D\right)
\end{aligned} \tag{3.24}
$$

where terms smaller than 150km have been neglected. The spherical ecliptic coordinates may again be converted to equatorial Cartesian coordinates using the transformation:

$$
\mathbf{r}_m = \mathbf{R}_x\left(-\varepsilon\right) \begin{pmatrix} r_m \cos\lambda_m \cos\beta_m \\ r_m \sin\lambda_m \cos\beta_m \\ r_m \sin\beta_m \end{pmatrix} \tag{3.25}
$$

A change of the reference system from EME2000 to the equator and equinox of some epoch T_{eqx} is further accounted for in the same way as for the Sun's coordinates.

3.4. Interpolation of Planetary Ephemerides

As discussed before, full model calculation of the planetary ephemerides, nutation, precession and polar motion parametres introduce a high computing burden. An alternative method is to interpolate these values using a pre-calculated grid. Different parametres require a different grid density and different interpolation method. There are in total five types of parametres used in the orbit propagation: nutation, precession, polar motion, Sun and Moon ephemerides.

3.4.1 Nutation

The IAU 1980 nutation series with 106 terms was used. For calculations requiring values of the nutation angles with an accuracy of ± 1 mas, it is necessary to add some

correction terms due to the incomplete IAU 1980 theory. From VLBI and LLR observations, the IAU 1980 theory of nutation is known to be in error at the level of several milli-arcseconds and an improved nutation theory due to Herring et al (1991) is described in McCarthy et al. (1993). Nevertheless, the IAU 1980 series is retained as the official standard in the IERS convention and the existing deficiencies are compensated for by observed values of the celestial pole offsets $\delta\Delta\psi$ and $\delta\Delta\varepsilon$. Improved nutation angles are obtained by adding these corrections to the IAU 1980 values:

$$\begin{aligned} \Delta\psi &= \Delta\psi_{IAU1980} + \delta\Delta\psi \\ \Delta\varepsilon &= \Delta\varepsilon_{IAU1980} + \delta\Delta\varepsilon \end{aligned} \tag{3.26}$$

There are two methods to get these corrections. The planetary correction model and long-term tidal model are used in the first method. Herring et al (1991) published these two correction series based on analysis of the long-term VLBI observations. The second method is quite simple in that these two correction values are published in the Bulletin B of the IERS, and a simple triple interpolator is recommended by IERS. The second method is our choice for its simplicity.

Nutation calculations require three angle variables: $\Delta\psi$, $\Delta\varepsilon$ and ε. We need to inspect the daily variation of these values. Figure 3.4 illustrates a three day result. The result suggests a linear interpolator is adequate. The standard deviations of a linear interpolator for $\Delta\psi$, $\Delta\varepsilon$ and true obliquity ε are 10^{-2}, 10^{-2} and 10^{-1} mas, respectively, which is good enough for our onboard orbit determination application.

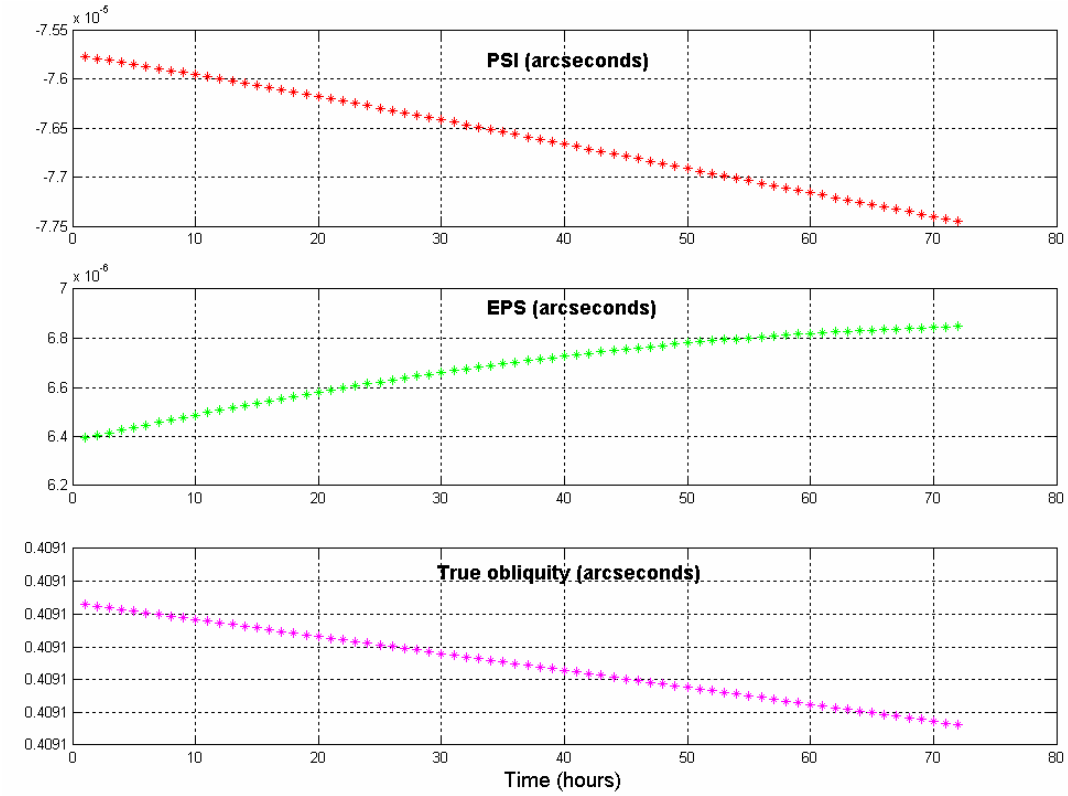

Figure 3.4 Nutation angle variations over three days (45th of 2002 ~ 47th 2002).

3.4.2 Precession

Compared to the nutation calculation, computation of precession is quite simple. The IAU 1976 theory of precession expression is used. The three precession angles ξ, ϑ and z are slowly-varying variables. Figure 3.5 shows a three-day variation of these values. The result also suggests a linear interpolator. The standard deviation of a linear interpolator for, ξ, ϑ and z are around the 0.01 mas level.

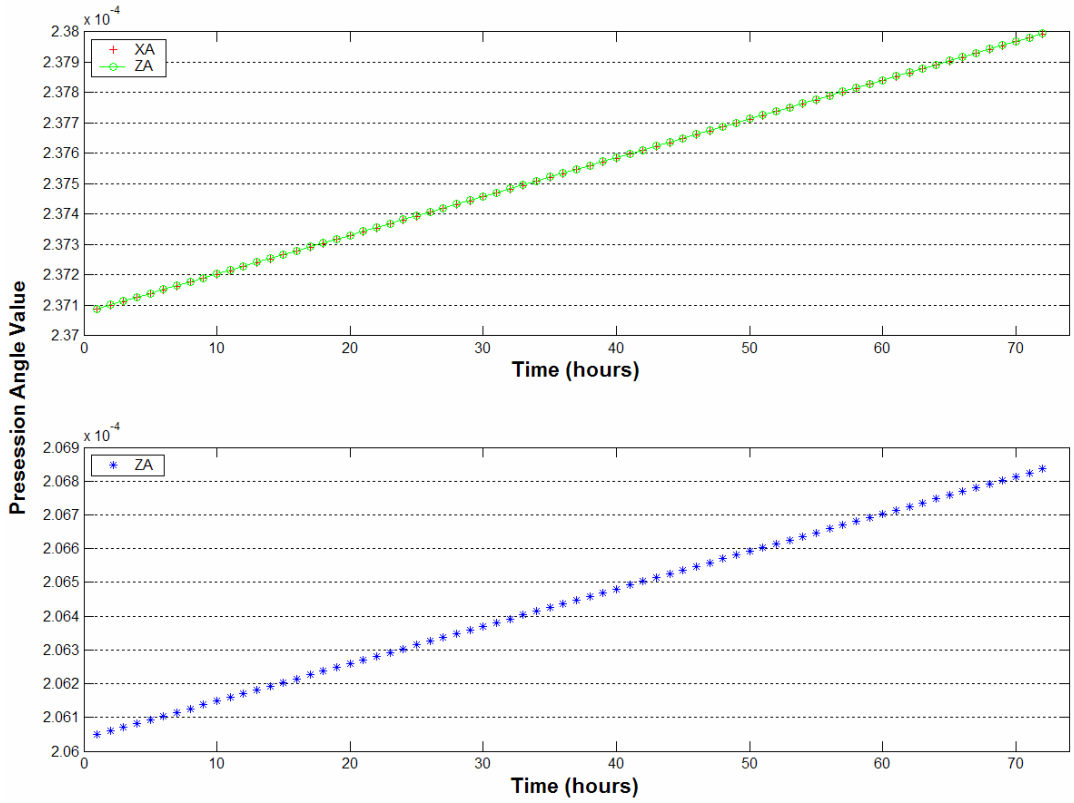

Figure 3.5 Precession angle variations over three days (45th of 2002 ~ 47th 2002).

3.4.3 Earth Rotation and Polar motion

The IAU precession and nutation theories yield the instantaneous orientation of the Earth's rotation axis, or, more precisely, the orientation of the Celestial Ephemeris Pole (CEP) with respect to the International Celestial Reference System. The rotation about the CEP axis itself is described by the Greenwich Mean Sidereal Time (GMST) that measures the angle between the mean vernal equinox and the Greenwich Meridian. Given the UT1-UTC and UT1-TAI time difference as monitored and published by the IERS, the Greenwich Sidereal Time at any instant can be computed. To obtain milli-arcsecond accuracy in the equation of the equinoxes, two additional terms $+0''.002649\sin\Omega - 0''.000013\cos\Omega$ with Ω denoting the longitude of the Moon's ascending node should be added to the right and side of the equation of the equinoxes. Two polar motion parametres x_p and y_p are used to define the Celestial Ephemeris Pole with respect to the IERS Reference Pole as a function of time. Variation of these parametres over 3 days is illustrated in Figure 3.6.

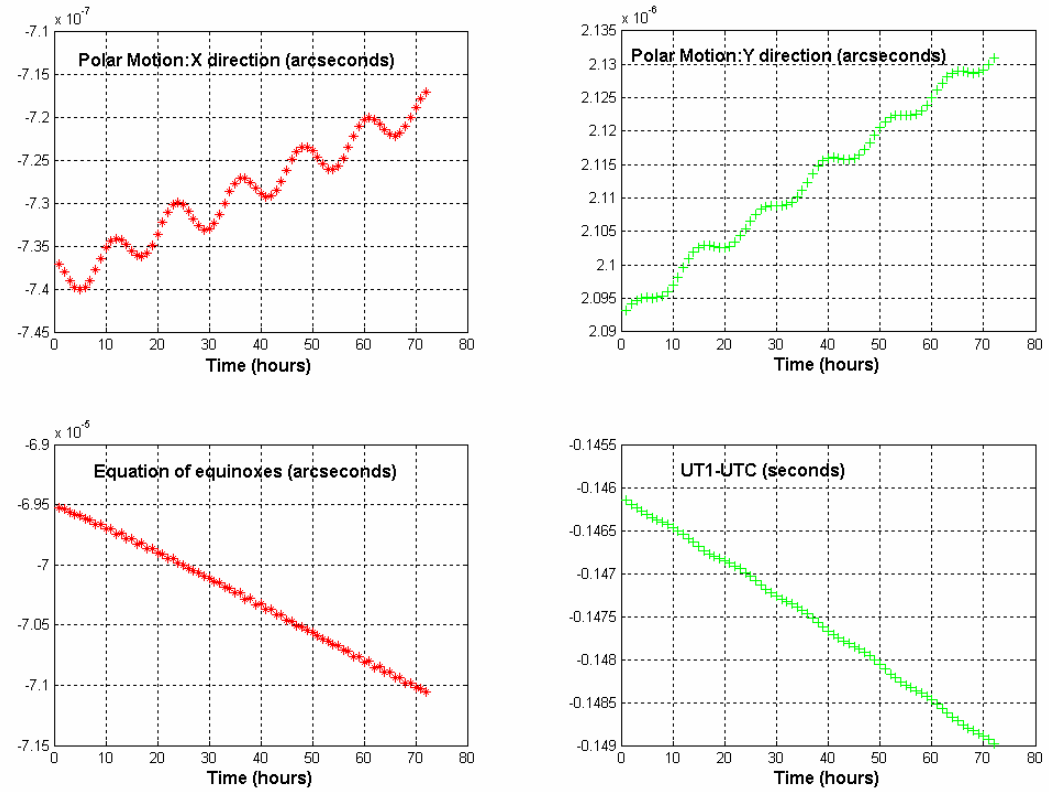

Figure 3.6 Polar motion parametre variations over three days (45th of 2002 ~ 47th 2002).

The interpolation of the polar motion parametres and UT1-UTC are more complicated than for nutation and precession. A revised 3rd order Legendre interpolation method is recommended by the IERS convention [*IERS convention*, 1996].

In our research context, the IERS B bulletin should be updated every month, which means it needs to be uploaded to the satellite each month. If the data is not updated on time, an extrapolater could be used, that is, the one month's prediction value must be obtained from the previous one month's data. For UT1-UTC, UT1-TAI, $\delta\Delta\psi$ and $\delta\Delta\varepsilon$, it is sufficient to use quadratic or even linear interpolation. For x_p and y_p, more care is needed. Even though polar motion cannot be readily predicted, extrapolation over a certain interval is nevertheless possible from previous data. For this purpose the motion of the pole may be modelled as a superposition of a linear motion (polar wander), and an oscillation with a period of 365.25 days (annual term), and an oscillation with a period of 435 days (Chandler term). Appropriate

coefficients that provide an extrapolation of tabulated polar motion data with an accuracy of about 0″.01 over one month are published twice per week in IERS Bulletin A issued jointly by the IERS and US National Earth Orientation Service (NEOS). Similar predictions are also provided by the US National Imagery and Mapping Agency (NIMA) as part of the GPS precise ephemeris generation process. [*NIMA*, 1999].

A more flexible model has been proposed by *Chao* [1985]. The two components of polar motion are represented by time dependent functions:

$$\begin{aligned} x_p &= a_x + b_x t + c_{ax}\cos(2\pi t / P_{ax} + \phi_{ax}) + c_{cx}\cos(2\pi t / P_{cx} + \phi_{cx}) \\ y_p &= a_y + b_y t + c_{ay}\cos(2\pi t / P_{ay} + \phi_{ay}) + c_{cy}\cos(2\pi t / P_{yx} + \phi_{cy}) \end{aligned} \qquad (3.27)$$

with a total of 16 free parametres $a_x, ..., \phi_{cy}$ that are obtained from a least squares fit to six years of past polar motion data. By allowing for different annual and Chandlerian periods P_a and P_c, as well as different phases ϕ_a and ϕ_c in the *x*- and *y*- component of polar motion, some additional degrees of freedom are introduced in this model which improves the prediction in times of notable period changes.

3.4.4 Solar & Lunar Coordinates

We use the simplified analytical method to calculate the Sun and Moon position in the inertial frame, as discussed in a previous section. Since the forces exerted by the Sun and Moon are much smaller than the central attraction of the Earth, it is not necessary to know their coordinates to the highest precision. Not only can we use the simplified method, but we also can use a linear or quadratic interpolator to get the coordinates from a pre-calculated Sun & Moon coordinate grid. We will discuss the impact of this in section 3.7.2.

3.4.5 Summary

Table 3.2 summarizes the interpolation method. The data grid is calculated at the initialization stage and the grid step varies depending on different data. To retain the interpolation accuracy, the grid step can be adjusted. For example, only 4 data points are needed in a two hour filtering process if a half hour grid step is used, this greatly

reduces the computational burden during the propagation stage, with only several k storage increase and small computing burden increase in the initialization stage.

Table 3.2 Celestial parametre interpolation schemes.

	Variables	Type	Grid step	Interpolation method
Nutation:	$\Delta\psi, \Delta\varepsilon, \varepsilon$	Calculated	30 minutes	Linear interpolator
Precession:	ξ, ϑ, z	Calculated	30 minutes	Linear interpolator
Sun & Moon:	$\vec{S}x, y, z$, $\vec{M}x, y, z$	Calculated	30 minutes	3rd Lengendre Polynominal
UT1:	UT1-UTC, UT1-TAI	IERS Bulletin	5 days	3rd Lengendre Polynominal
Polar motion:	x_p, y_p	IERS Bulletin	5 days	3rd Lengendre Polynominal

3.5 Symmetric-sphere Atmospheric Density Model

3.5.1 Introduction

From section 3.3.1 we can see that the MSIS86 atmospheric density model uses around 20% CPU time both in the initialization and in the partial computing modules. The modelling of air density at satellite altitude is quite a demanding task. The shape of the temperature profile in the thermosphere and algorithms for computing the exospheric temperature form the core of the current density model. Furthermore, the temperature profile is a function of solar activity, diurnal and annual effects and geomagnetic activity. Other important effects influencing density are seasonal latitudinal variation and semi-annual variation. Currently there are several upper atmospheric model in use, such as CIRA-72, CIRA-86; Jacchia-71, Jacchia-77; MSIS-86, MSIS-90 and DTM90. However, they are all very complicated numerical methods and depend heavily on the daily or monthly Sun flux and geomagnetic data which is not suitable for onboard processing. Another reason to use the simplified analytical density model is that although all the above models have not been modelled very well, they all have about a 5%~10% inherent uncertainty and 20%~30% total uncertainty.

3.5.2 Methodology

If only the balanced atmosphere is considered, according to hydrostatics the density distribution is approximately a form of exponentiation:

$$\rho = \rho_0 \exp\left[-(r - r_0)/H\right] \tag{3.28}$$

Here it is spheric atmosphere. ρ_0 is the atmospheric density of the reference spherical surface, where $r = r_0$, and H refers to the standard height of density. The expression is consistent with the law that density is decreasing with height increase. Meanwhile, according to the above mentioned atmosphere models, the change of density slows down along with height, therefore the indicated height of density increases slowly with height. A reasonable way of approximating this is to assume the linear relationship of H to h (200 ~ 600km) [*King-Hele*, 1964]. It can be expressed as:

$$H = H(r) = H_0 + \frac{\mu}{2}(r - r_0) \tag{3.29}$$

generally, $\mu \approx 0.1$, $\mu < 0.2$, the corresponding formula of density in Equation (3.28) is converted to:

$$\rho = \rho_0 \exp\left[-(r - r_0)/H(r)\right] = \rho_0\left[1 + \frac{\mu}{2}\left(\frac{r - r_0}{H_0}\right)^2\right]\exp\left[-(r - r_0)/H_0\right] \tag{3.30}$$

From the result of *King-Hele*, (1964), here referred to as Model CIRA-61, where h = 200km:

$$\rho_0 = 3.6 \times 10^{-10}\, kg/m^3, H_0 = 37.4km, \mu = 0.1 \tag{3.31}$$

Due to the Earth being an oblate spheriod, under the assumption of balanced gravity, the surface of atmosphere with equal density can be also viewed as an approximately oblate surface [*King-Hele*, 1964, 1976], then Equation (3.30) can be modified:

$$\rho = \rho_0 \exp\left[-(r - \sigma)/H(r)\right] = \rho_0\left[1 + \frac{\mu}{2}\left(\frac{r - \sigma}{H_0}\right)^2\right]\exp\left[-(r - \sigma)/H_0\right] \tag{3.32}$$

The above formula describes the oblate spherical atmosphere, where σ refers to the distance between the Earth centre and the ellipsoid surface that crosses the reference

point ($\rho = \rho_0, H = H_0$). Equation (3.32) basically reflects the atmosphere distribution in the space impacted by the gravity of the Earth. That distribution is relatively consistent with the distribution of mean density produced by those existing models for atmosphere. In the early researches as to the impact of atmosphere drag on satellite orbits, King-Hele (1964) and others adopted this expression of approximate density, where the corresponding reference point is at the perigee P_0 of the satellite orbit (the impact of atmosphere drag around perigee is the most significant), the density ρ_0 and the indicated height of density H_0 are ρ_{P0} and H_{P0}, respectively.

The impact of solar radiation on atmosphere density shows different periodic changes, and the diurnal effect due to the Earth's rotation is particularly distinct. The density in the daytime is much more than the one at night at the same height and latitude. Generally speaking, the density at local time 14h reaches the maximum and around this time the density changes rapidly, whereas the density is down to a minimum value at about 2 ~ 5 hours, when the density changes slowly. However, just as King-Hele (1964) pointed out, it is reasonable as the a order approximation to assume that the maximum and minimum of both the Earth's centre and diurnal effect are on the same line, about which the surfaces with equal density are symmetrical. Considering the changes of density with both height and time with this assumption in mind, we have:

$$\rho = \rho_0 (1 + F^* \cos\varphi) \exp\left[-(r - \sigma)\right] / H(r) \tag{3.33}$$

where φ is the angle between the satellite vector **r** and the vector $\mathbf{r}_m$ where the diurnal maximum density lies. With the assumption of the above described symmetrical diurnal effect, the relationship between the $\mathbf{r}_m$ and the Sun can be expressed as:

$$\alpha_m = \alpha + \lambda_m, \quad \delta_m = \delta \tag{3.34}$$

where α, δ are the Sun's equatorial latitude and longitude, respectively. λ_m is 30°. If F^* refers to the diurnal variation factor, its relation to the ratio f^* (daytime density night-time density ratio) can be described as:

$$f^* = \frac{\rho_{\max}}{\rho_{\min}} = \frac{1 + F^*}{1 - F^*}, \quad F^* = \frac{f^* - 1}{f^* + 1} \tag{3.35}$$

According to this definition, ρ_0 is the diurnal mean density on the reference ellipsoid surface where $r = \sigma$, i.e., $\varphi = 90^\circ$. ρ_0 can be calculated from the adopted atmosphere model and relevant parametres.

3.6 Integral Equation Method

3.6.1. Integral Equation

Integral Equation of Satellite Orbit

The integral equation method for satellite orbit integration was first proposed by Feng (2000). It begins with the differential equation of the two-body motion of a satellite, which comes from Newton's second law of motion and the universal gravitational law:

$$\ddot{\mathbf{r}} = -\frac{GM}{r^3}\mathbf{r} \tag{3.36}$$

where

$\ddot{\mathbf{r}}$ is the satellite acceleration vector

r is the satellite position vector

GM is the product of the gravitational constant G and Earth mass M

Including also the velocity vector $\dot{\mathbf{r}}$, Equation (3.36) can be rewritten as:

$$\dot{\mathbf{x}} = \mathbf{B}_t\mathbf{x} \tag{3.37}$$

where

$$\mathbf{x} = \begin{bmatrix}\mathbf{r}\\ \dot{\mathbf{r}}\end{bmatrix} = \begin{bmatrix}x & y & z & \dot{x} & \dot{y} & \dot{z}\end{bmatrix}^T$$

$$\mathbf{B} = \begin{bmatrix} 0 & 0 & 0 & 1 & 0 & 0 \\ 0 & 0 & 0 & 0 & 1 & 0 \\ 0 & 0 & 0 & 0 & 0 & 1 \\ -\frac{GM}{r^3} & 0 & 0 & 0 & 0 & 0 \\ 0 & -\frac{GM}{r^3} & 0 & 0 & 0 & 0 \\ 0 & 0 & -\frac{GM}{r^3} & 0 & 0 & 0 \end{bmatrix} \tag{3.38}$$

Given a set of position and velocity vectors at the initial time epoch $t = t_0$:

$$\mathbf{x}_0 = \begin{bmatrix} x_0 & y_0 & z_0 & \dot{x}_0 & \dot{y}_0 & \dot{z}_0 \end{bmatrix}^T$$

we can obtain an analytical solution of the two-body problem [*Goodyear*, 1965]:

$$\mathbf{x} = \mathbf{H}_t \mathbf{x}_0 \tag{3.39}$$

where

$$\mathbf{H} = \begin{bmatrix} h & 0 & 0 & g & 0 & 0 \\ 0 & h & 0 & 0 & g & 0 \\ 0 & 0 & h & 0 & 0 & g \\ \dot{h} & 0 & 0 & \dot{g} & 0 & 0 \\ 0 & \dot{h} & 0 & 0 & \dot{g} & 0 \\ 0 & 0 & \dot{h} & 0 & 0 & \dot{g} \end{bmatrix} \tag{3.40}$$

is the solution of the differential equation:

$$\dot{\mathbf{H}}_t = \mathbf{B}_t \mathbf{H}_t \tag{3.41a}$$

$$\mathbf{H}_{t_0} = \mathbf{I}_0 \tag{3.41b}$$

$\mathbf{I}_0$ is the 6-by-6 identity matrix. Refer to Appendix A for the computation of all the elements of the matrix H.

For the perturbed motion of a satellite, Equation (3.37) can be written as:

$$\dot{\mathbf{x}} = \mathbf{B}_t \mathbf{x} + f(t, \mathbf{x}_t) \tag{3.42}$$

where $f(t, \mathbf{x}_t)$ is the 6-dimensional vector, a function of the spacecraft state, which can be composed of all perturbing forces acting on the satellite, such as the non-spherical and inhomogeneous mass distribution within the Earth (central body), other celestial bodies (Sun, Moon etc); Earth and oceanic tides, atmospheric drag, Earth and solar radiation pressure and geomagnetic effects, etc.

To derive the solution of Equation (3.42), we redefine the $\mathbf{x}_0$ in Equation (3.39) as the function of time ξ_t:

$$\mathbf{x}_t = \mathbf{H}_t \boldsymbol{\xi}_t \tag{3.43}$$

which is regarded as the solution of Equation (3.42). To determine ξ_t we substitute Equation (3.41), together with its derivative:

$$\dot{\mathbf{x}}_t = \dot{\mathbf{H}}_t \xi_t + \mathbf{H}_t \dot{\xi}_t \tag{3.44}$$

into Equation (3.40) and using Equation (3.41a) obtain:

$$\dot{\xi}_t = \mathbf{H}_t^{-1} f(t, \mathbf{H}_t \xi_t) \tag{3.45}$$

The integration of Equation (3.45) gives:

$$\boldsymbol{\xi}_{\mathbf{t}} = \boldsymbol{\xi}_{\mathbf{t_0}} + \int_{t_0}^{t} \mathbf{H}_\tau^{-1} f(\tau, \mathbf{H}_\tau \boldsymbol{\xi}_\tau) d\tau \tag{3.46}$$

Substituting Equation (3.45) into Equation (3.43), and defining the state transition matrix:

$$\boldsymbol{\Phi}_{t,\tau} = \mathbf{H}_t \mathbf{H}_\tau^{-1} \tag{3.47}$$

We have the integral equation for motion of a satellite:

$$\mathbf{x}_t = \boldsymbol{\Phi}_{\mathbf{t},\mathbf{t_0}} \mathbf{x}_{\mathbf{t_0}} + \int_{t_0}^{t} \boldsymbol{\Phi}_{\mathbf{t},\tau} f(\tau, \mathbf{x}_\tau) d\tau \tag{3.48}$$

The solutions of Equation (3.40) with the initial value $\mathbf{x}_{t_0}$ and the integral Equation (3.48) should be equivalent. Comparing Equation (3.48) to (3.42) it can be seen that Equation (3.48) also consists of components due to the central body and perturbation forces. In particular, the first term gives the states of the satellite at time t from the states of the elliptic orbit at t_0, while the second term gives the state variations due to the perturbations during the interval (t_0, t). The matrices $\boldsymbol{\Phi}_{\mathbf{t},\mathbf{t_0}}$ and $\boldsymbol{\Phi}_{\mathbf{t},\tau}$ play roles of state transitions in both cases. As seen in a later section, it was these state transition matrices that make the numerical solution of the integral equation comparatively simple.

Equation (3.48) is called the "integral equation" due to the presence of the unknown function $\mathbf{x}_t$ under the integral symbol. Integral equations appear in the mathematical theory of many scientific and engineering branches, and are categorized into different types. Theoretical and numerical methods have been established for each type of integral equation. This integral equation belongs to the class of Hammerstein-Volterra integral equation of the second kind.

State Equations for Orbit Estimation

To be able to estimate the states of the orbit, we need to establish the state transition equation starting with the differential Equation (3.42). Considering some of unknown parametres in the perturbing forces, $\boldsymbol{\mu}$ absorbs variations on both sides of Equation (3.44):

$$\Delta\dot{\mathbf{x}}_{\mathbf{t}} = \frac{\partial\dot{\tilde{\mathbf{x}}}_{\mathbf{t}}}{\partial\tilde{\mathbf{x}}_{\mathbf{t_0}}}\Delta\mathbf{x}_{\mathbf{t}} + \frac{\partial\dot{\tilde{\mathbf{x}}}_{\mathbf{t}}}{\partial\boldsymbol{\mu}}\Delta\boldsymbol{\mu} \tag{3.49}$$

where $\Delta\dot{\mathbf{x}} = \dot{\mathbf{x}} - \dot{\tilde{\mathbf{x}}}$, $\Delta\mathbf{x} = \mathbf{x} - \tilde{\mathbf{x}}$, $\Delta\boldsymbol{\mu} = \boldsymbol{\mu} - \tilde{\boldsymbol{\mu}}$, and $\tilde{\mathbf{x}}$ is the nominal orbit solution as computed by Equation (3.48) with the initial state $\mathbf{x_0}$ and the parametres $\tilde{\boldsymbol{\mu}}$. The solution of the differential equation (3.51) is given by the following integral equation:

$$\Delta\mathbf{x}_t = \frac{\partial\tilde{\mathbf{x}}_{\mathbf{t}}}{\partial\tilde{\mathbf{x}}_{\mathbf{t_0}}}\Delta\mathbf{x}_{t_0} + [\int_{t_0}^{t}\frac{\partial\tilde{\mathbf{x}}_{\mathbf{t}}}{\partial\tilde{\mathbf{x}}_{\mathbf{t_0}}}(\frac{\partial\tilde{\mathbf{x}}_{\tau}}{\partial\tilde{\mathbf{x}}_{\mathbf{t_0}}})^{-1}\frac{\partial f(\tau,\mathbf{x}_\tau,\boldsymbol{\mu})}{\partial\boldsymbol{\mu}}d\tau]\Delta\boldsymbol{\mu} \tag{3.50}$$

where the partial derivation $\frac{\partial\tilde{\mathbf{x}}_t}{\partial\tilde{\mathbf{x}}_{t_0}}$ can be obtained from Equation (3.48)

$$\frac{\partial\mathbf{x}_{\mathbf{t}}}{\partial\mathbf{x}_{\mathbf{t_0}}} = \boldsymbol{\Phi}_{t,t_0} + \int_{t_0}^{t}[\boldsymbol{\Phi}_{t,\tau}\frac{\partial f(\tau,\mathbf{x}_\tau)}{\partial\mathbf{x}_\tau}]d\tau \tag{3.51}$$

Equation (3.51) is also an integral equation. Although the integral computation compartively simple, the computation of Equation (3.51) still involves relatively heavy computation because of the complexity of the partial derivatives. Ignoring the effects of perturbing forces on the partial derivatives, Equation (3.51) can be simplified as:

$$\frac{\partial\tilde{\mathbf{x}}_t}{\partial\tilde{\mathbf{x}}_{t_0}} \approx \boldsymbol{\Phi}_{t,t_0} \tag{3.52}$$

Thus, the difference equation (3.50) becomes:

$$\Delta\mathbf{x}_t = \boldsymbol{\Phi}_{\mathbf{t},\mathbf{t_0}}\Delta\mathbf{x}_{t_0} + [\int_t^t\boldsymbol{\Phi}_{\mathbf{t},\tau}\frac{\partial f(\tau,\mathbf{x}_\tau,\boldsymbol{\mu})}{\partial\boldsymbol{\mu}}d\tau]\Delta\boldsymbol{\mu} \tag{3.53}$$

Define $\boldsymbol{\Phi}^{\mu}_{t,t_0}$ as the state transition matrix relating $\Delta\mathbf{x}_t$ to $\Delta\mu$:

$$\boldsymbol{\Phi}_{\mu}(t,t_0) = [\int_{t_0}^{t}\boldsymbol{\Phi}(t,\tau)\frac{\partial f(\tau,\mathbf{X}(\tau),\boldsymbol{\mu})}{\partial\boldsymbol{\mu}}d\tau] \tag{3.54}$$

then the state equation can be written:

$$\Delta\mathbf{x}_{\mathbf{t}} = \boldsymbol{\Phi}_{\mathbf{t},\mathbf{t_0}}\Delta\mathbf{x}_{t_0} + \boldsymbol{\Phi}^{\mu}_{\mathbf{t},\mathbf{t_0}\,\mu}\Delta\boldsymbol{\mu} \tag{3.55}$$

In summary, using the integral equation (Equation (3.48)) to represent satellite orbits not only provides a simple and efficient numerical solution for satellite orbit prediction, but also gives the transition matrices for the force parametres at the same time. Compared to the numerical methods for orbit determination [*Webb &*

Zvmberge, 1995], this algorithm is significantly simplified, thus saving huge amount of computation (thanks to the simplicity of the matrix H in Equation (3.40) and the process in Equation (3.52)). However, this simplification introduces in some limitations to the application of the algorithm. The coefficients in H matrix remain valid only for two-body orbits. The computation of the state transition matrix $\mathbf{\Phi}_{t,t_0}$ is based on a two-body orbit instead of a perturbed nominal orbit. Using this matrix to transit the state biases over a long period will introduce some uncertainty. In general, the proposed algorithm is suitable for short-arc processing, as suggested for this study. But for long-arc batch filtering this simplification may cause some problems.

3.6.2 Step Control Algorithm

In order to obtain a desired accuracy with minimum computational effort, the orbit integrator adjusts the time integration step size Δt . The idea is quite simple. First, the accuracy of the integration is compared to some desired accuracy. Second, the step size is increased or decreased depending on whether the accuracy of integration is better or worse than the desired accuracy.

The accuracy of integration is determined by the so-called step-doubling procedure. In this procedure the position and velocity vectors of the satellite at the current time step *n*:

$$r_i^n, v_i^n; \quad i = x, y, z \tag{3.56}$$

are advanced by two time steps using the current step size Δt^n :

$$r_i^n \rightarrow^{\Delta t^n} r_i^{n+1} \rightarrow^{\Delta t^n} r_i^{n+2}, \; v_i^n \rightarrow^{\Delta t^n} v_i^{n+1} \rightarrow^{\Delta t^n} v_i^{n+2} \tag{3.57}$$

In addition, $r_i^{n^*}$ and $v_i^{n^*}$ are advanced using twice the current step size:

$$r_i^n \rightarrow^{2\Delta t^n} r_i^{n+1^*}, \; v_i^n \rightarrow^{2\Delta t^n} v_i^{n+1^*} \tag{3.58}$$

The accuracy is defined to be the difference between the two new aforementioned states, namely

$$\mathbf{\Delta}_i^n \equiv \mathbf{x}_i^{n+2} - \mathbf{x}_i^{n+1} \tag{3.59}$$

where the state vector $\mathbf{x}_i^n$ refer to both position and velocity vectors.

Next Δ_i^n is compared to a desired accuracy Δ_{i0}. To compute the new step size Δt^{n+1}, the following algorithm is used:

$$\Delta t^{n+1} = \begin{cases} S\Delta t^n \left|\dfrac{\Delta_0}{\Delta_n}\right|^{0.2} & \Delta_n \le \Delta_0 \\ S\Delta t^n \left|\dfrac{\Delta_n}{\Delta_0}\right|^{0.25} & \Delta_n > \Delta_0 \end{cases} \tag{3.60}$$

Where S is a safety factor (the recommended value of S is 0.9).

3.7 Experiment Studies

3.7.1 Description

The purposes of the experimental study are threefold:

1. To test the orbit dynamical model simplification algorithms discussed in previous sections.
2. To explore the efficiency and capacity of simplified methods to reduce the onboard computational burden.
3. To assess the accuracy of orbit integration using simplified methods compared with full models.

The experimental studies are based on the data from three LEO missions: T/P, SAC-C and CHAMP. Their altitudes are 1340km, 700km and 450km, respectively, and represent three typical LEO orbits. The reference ephemerides are post-processed results from JPL's GIPSY-OASIS II software. The position errors are at the centimetre level for T/P, and decimeter level for SAC-C and CHAMP. All the proposed methods are tested to validate the algorithm efficiency. Finally, we compare the orbit integration accuracy as well as computing time and memory usage of simplified method against the traditional full model strategies.

3.7.2 Truncated Earth Gravitational Model

The first step is to truncate the Earth gravity model. The order & degree of JGM-3 is up to 70×70. Higher order brings higher accuracy, but also brings much greater

computational burden. A proper balance between accuracy and computing burden is the objective of this investigation.

3.7.2.1 Order of Magnitude of Acceleration

The order of magnitude of acceleration is calculated from 2×2 (J_2) to 70×70 (highest accuracy). All the values are compared with the 70×70 model. Figure 3.7 illustrates the result. It is clearly shown that CHAMP requires a higher order of gravity model to achieve the same accuracy comparing with SAC-C and T/P. Satellites with lower altitude are more affected by Earth gravity field. To achieve a $10^{-6}\ m/s^2$ acceleration accuracy, T/P requires around 15×15 order & degree of gravity model, while SAC-C requires 30×30, and CHAMP requires 60×60.

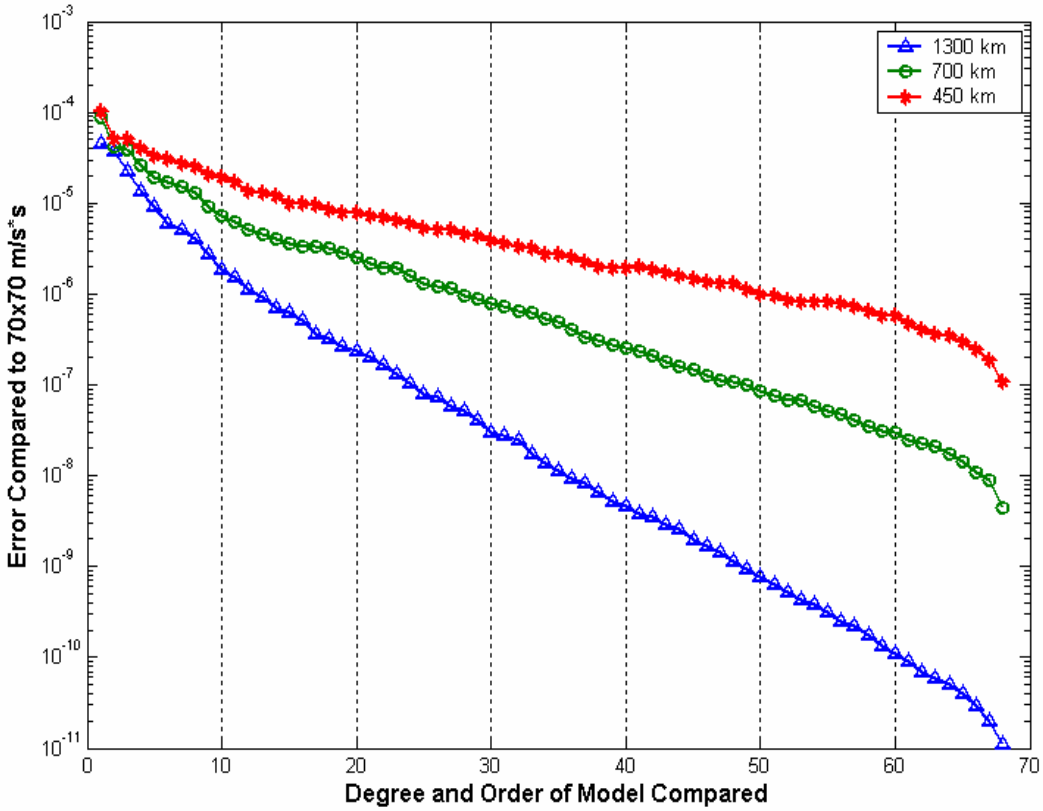

Figure 3.7 Comparison of gravity acceleration accuracy using different degree & order at different altitudes.

3.7.2.2 Computing Time versus Accuracy

Both computing time and orbit integration accuracy for different truncation schemes were studied. From the result of the previous experiment, we chose four typical JGM3 truncation schemes: 10×10, 20×20, 30×30 and 70×70.

One day's orbit integration was made for T/P, SAC-C and CHAMP. Except for the different truncated gravity models, the other dynamical models used in the integrator were kept the same:

- Third body gravity: Sun & Moon and all planets.
- Pole Motion: IERS Bulletin B.
- Celestial Frame: IAU 1980 nutation, IAU 1976 precession.
- Tidal potential model: 2^{nd} degree Legendre polynominal for the Sun & Moon.
- Solar pressure: direct effect with shadow consideration, the coefficients for T/P, SAC-C and CHAMP are: 0.003, 0.023 and 0.0, respectively.
- Atmospheric Drag: using MSIS86 density model, the ballistic coefficients are 0.001, 0.02 and 0.015 for the three missions.

It is very difficulty to obtain the precise values without an estimation process, thus the solar pressure and drag force parametres were roughly estimated by satellite physical parametres. Biased surface parametres cause big orbit integration error for LEO satellites, but this is not important in that we only want to know the relative accuracy and computing speed. Table 3.3 gives detailed results for the SAC-C test. We can see that the mathematical operations increase dramatically as the gravity model size increases.

Table 3.3 Computational burden and accuracy of SAC-C 24h orbit integration using different JGM-3 gravity model truncations.

Size	**Number of Coefficients**	**Number of Math Flops**	**Orbit Integration time (seconds)**	**Maximum Error Compared to** 70×70 (m)
10×10	126	1553	76.36	218.19
20×20	456	5103	91.14	80.41
30×30	986	10653	92.08	13.76
70×70	5160	52853	146.27	0.0

Figure 3.8 illustrates the orbit integration accuracy variation against computing time, the orbit integration errors being compared wit the use of a 70×70 model. We can see that the accuracy is unacceptable for all missions if only 10×10 model is used. 20×20 to 30×30 is a better choice, especially for T/P. The computing burden of the 30×30 truncated model is 60% less than that of the 70×70 model, but results in several metres accuracy loss.

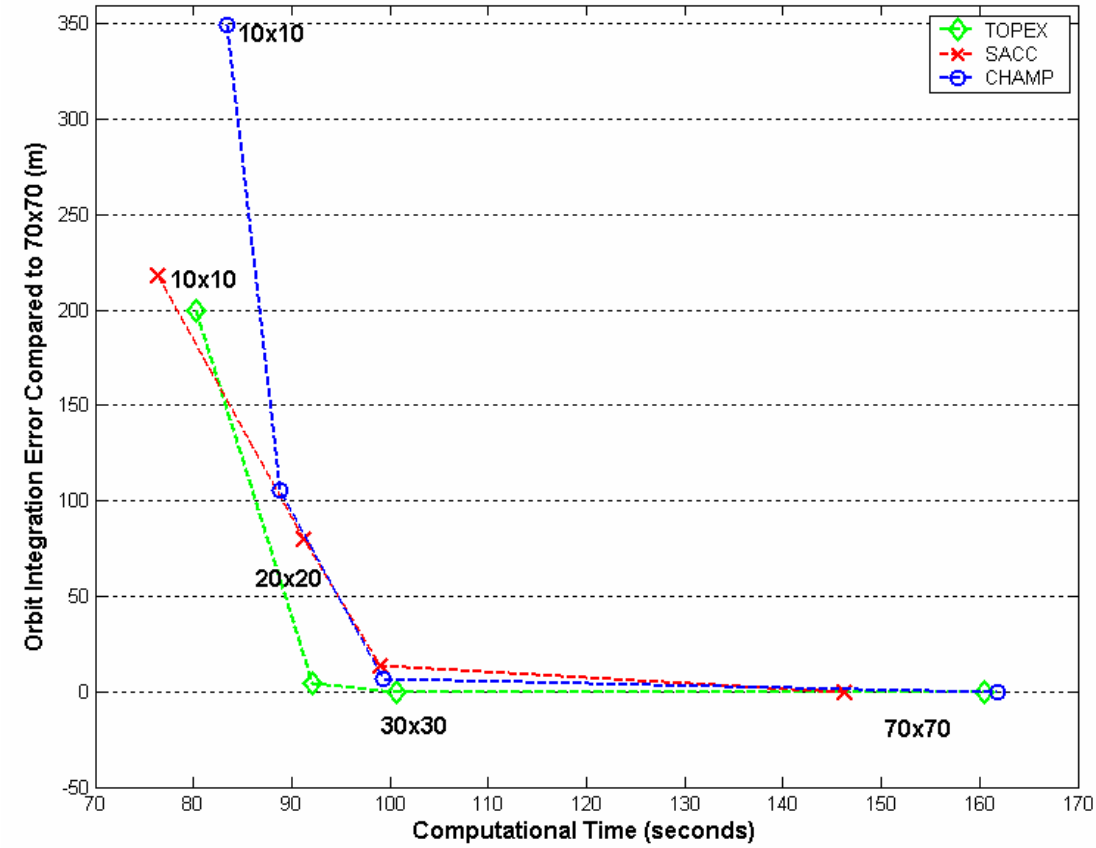

Figure 3.8 Orbit integration accuracy against computional time using various degree & order of JGM-3 model.

3.7.2.3 Short-arc Orbit Integration Performance

A short-arc refers to from tens of minutes to several orbit revolutions. For the proposed short-arc orbit determination method we only need to address the performance of the orbit integrator over a several hours arc. We chose 15 minutes, 1 hour and 2 hours for the short-arc orbit integration testing. The impact of the truncated gravity model was also considered. The results are shown in Figure 3.9. We can see that for the 15 minute arc, the orbit integration accuracy can be

controlled within several metres easily for all satellites, even with the 10×10 model. For 1 hour and 2 hour arcs, the same accuracy still can be achieved if higher than a 20×20 gravity model is used; but this is not the case for CHAMP. It is not possible to get below 10 metres orbit integration accuracy for CHAMP even using 70×70 model, this suggests more accurate atmosphere drag model should be considered, and that the drag coefficients also should be adjusted during the orbit estimation process.

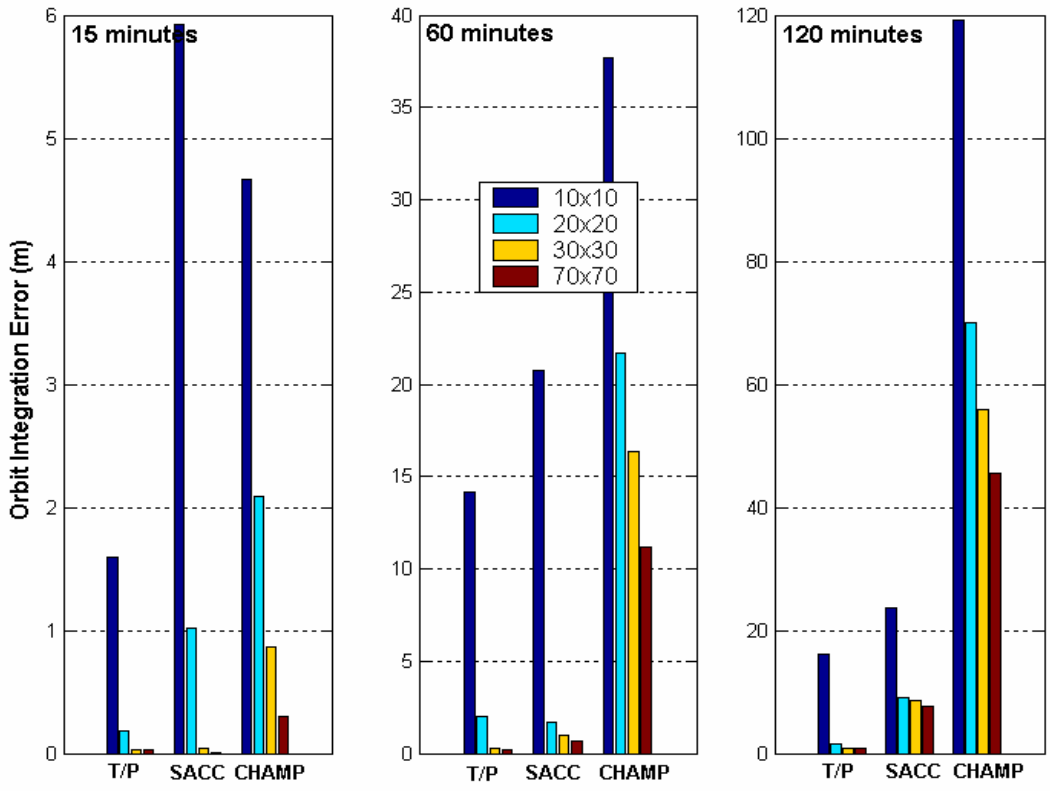

Figure 3.9 Short-arc orbit integration accuracy using various degree & order of JGM-3 model.

3.7.2.4 Simplified Solar & Lunar Ephemerides

This experiment is to validate the analytical, simplified solar & lunar coordinate calculation method described in section 3.3. Two aspects have been addressed: the positional error compared with the DE405 ephemerides; and the acceleration error introduced by this simplification.

Figure 3.10 illustrates the 3D coordinate error in the inertial system (ICRF) compared with the JPL DE405 data. It shows 0.001% and 0.01% error for the Sun and the Moon, respectively, which is good enough for the short-arc orbit integration. The lower part of Figure 3.10 shows the absolute 3D coordinate error.

Furthermore, Figure 3.11 shows the impact on the acceleration. The upper half shows the order of magnitude of the acceleration introduced by solar and lunar gravity; the lower part gives the difference between simplified method and using DE405 ephemerides. Three missions were included in this experiment. We can see that, unlike the Earth gravity effect, higher orbit are more likely affected by the solar and moon gravity. And the acceleration errors introduced by the simplification are around $10^{-11} m/s^2$ and $10^{-10} m/s^2$ for the Sun and Moon, respectively. From our discussion in section 3.2.1, an acceleration error smaller than $10^{-10} m/s^2$ is acceptable for our short-arc orbit determination method, hence this result is satisfactory.

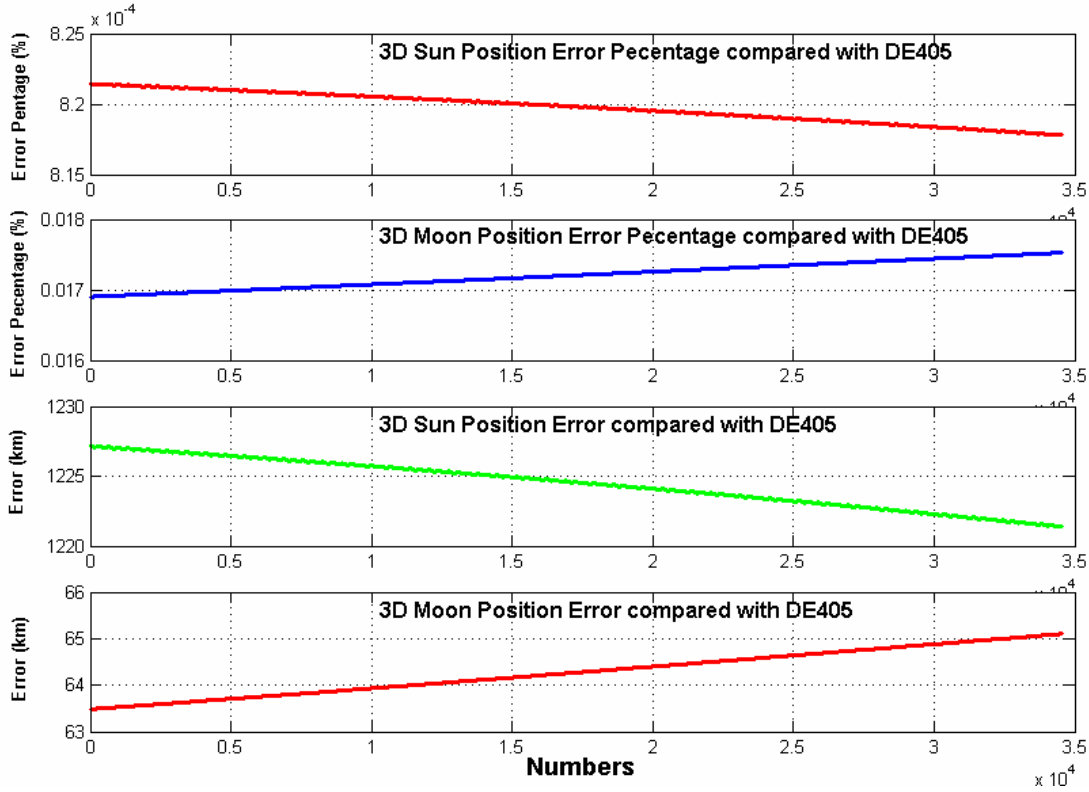

Figure 3.10 Simplified solar & lunar ephemerides error compared against JPL DE405.

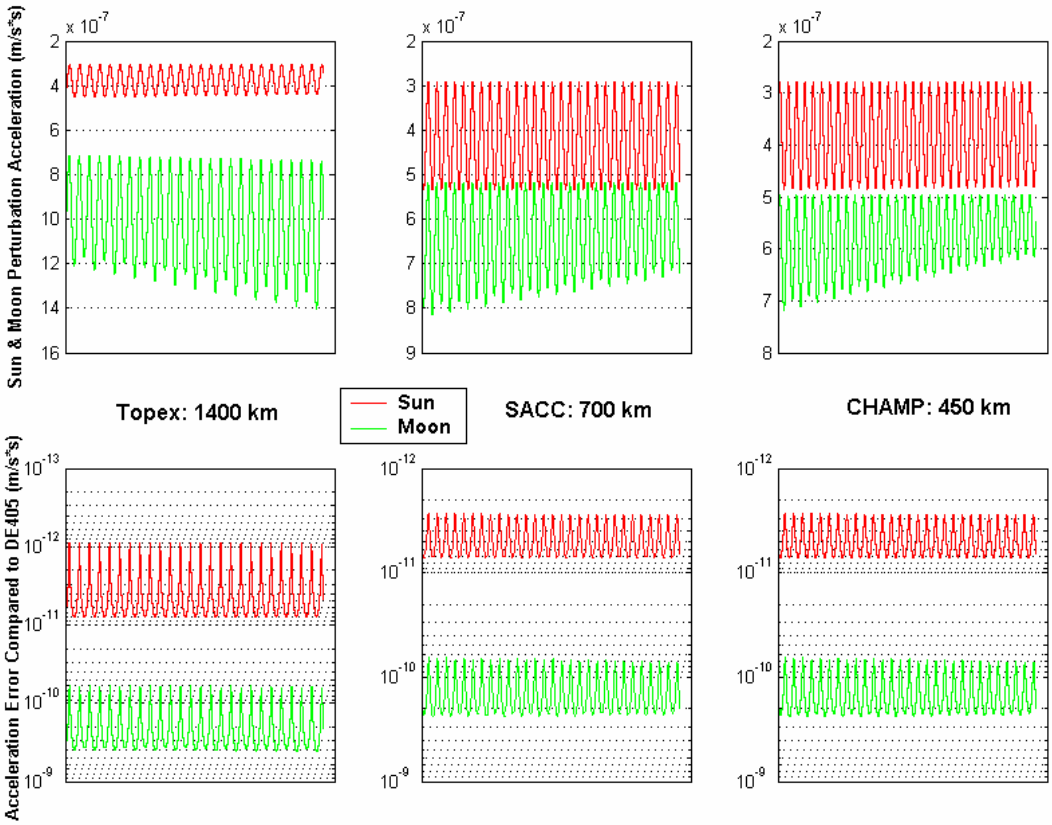

Figure 3.11 Solar & lunar perturbation order of magnitude using simplified model for different height missions.

3.7.3 Interpolation of Celestial Ephemerides

The objective of this experiment is to validate the methods developed in section 3.4. Instead of precisely calculating the nutation, precession, polar motion parametres, as well as the solar and lunar coordinates at every epoch, an interpolator was used. The best way to determine the accuracy of the interpolation is to check the coordinate transformation result between the terrestrial-fixed reference frame and celestial inertial reference frame. Coordinate transformation from ICRF to ITRF was tested on 14^{th}~16^{th}, February 2002. Both the reference ICRF and ITRF data are from JPL's precise SAC-C ephemerides. The interpolation method uses interpolated transformation parametres, and the transformed coordinates are compared against the standard non-interpolation ones. Figure 3.12 illustrates the coordinate error introduced by interpolated parametres and the RMS for the *x*, *y* and *z* components. It is noticed that only several centimetres error was introduced, which meets our requirement. It is also found that error in the *z*-axis is much bigger than for the other

components and this suggests large error from the polar motion parametres rather than from nutation and precession.

Furthermore, the interpolation accuracy of the simplified solar and lunar ephemerides was investigated. The 3D acceleration value was calculated using the interpolated method and then compared to using the DE405 precise ephemerides. Figure 3.13 shows the result. It is observed that the errors are at the same level as the result of Figure 3.11, suggesting that the interpolation error can be ignored.

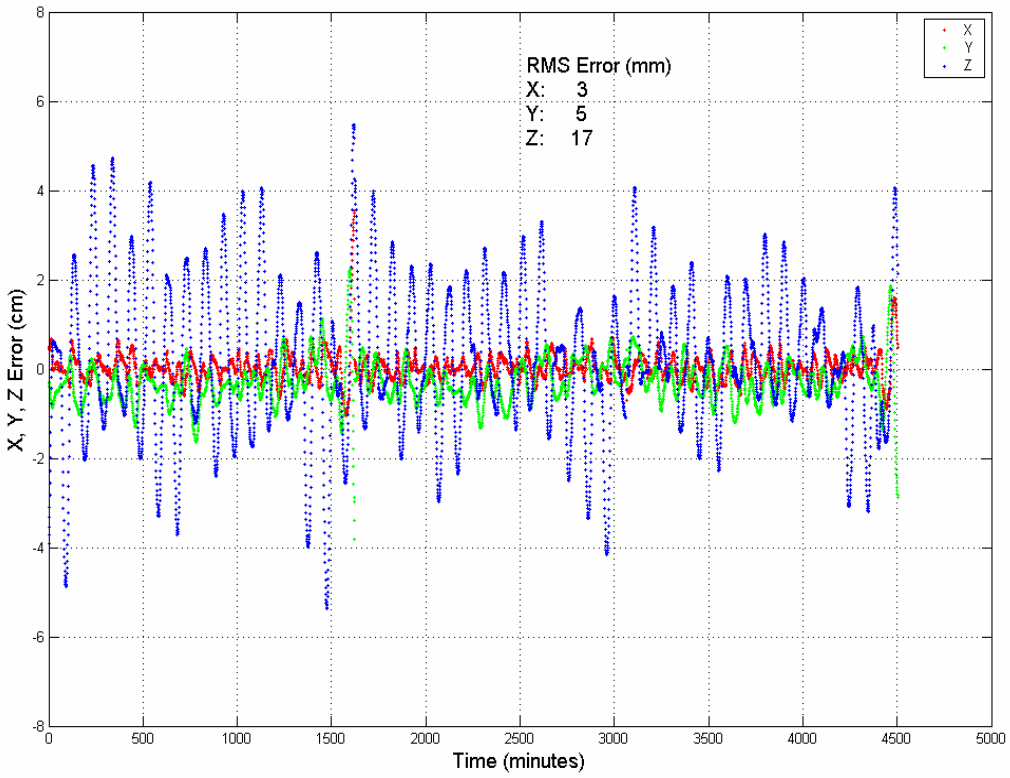

Figure 3.12 Coordinate transformation errors between ITRF and ICRF using interpolated parametres compared to the standard method.

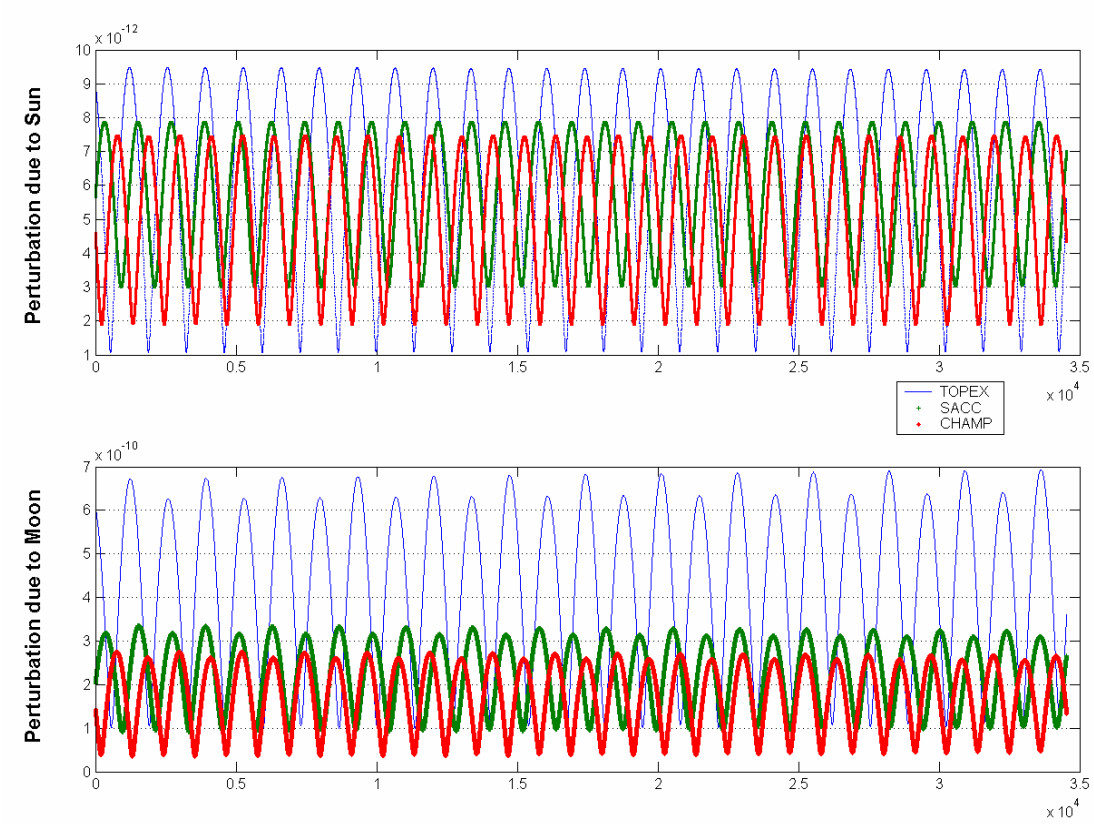

Figure 3.13 Solar & lunar perturbation error due to the interpolation.

3.7.4 Simplified Atmospheric Density Model

The simplified atmospheric model discussed in section 3.5 was tested. First, the performance of several well-known empirical atmospheric density models, including the MSIS 86, Jacchia 77 and DTM90, were compared. The CPU usage, mean density difference and maximum density difference were calculated based on values derived from the MSIS 86 model. Table 3.4 gives the result. We found big discrepancies even among these popular models due to the complexity of Earth's upper atmosphere. The proposed method is very simple compared with the traditional empirical methods. It is about 100 times faster in speed. On the other hand, it has a 30% mean density bias and 153% maximum density bias from MSIS86 model, and it is not clear to what extent this bias will affect the orbit integration accuracy. But we also can see that even a modern DTM90 model has a 19% mean density bias and 101% maximum density bias. Thus we can conclude that the proposed simplified atmosphere model has a performance roughly in accordance with current empirical models. To account for the uncertainty in atmosphere density

models we can tune the atmospheric drag coefficient during the orbit estimation process in order to compensate for the errors in the atmospheric density. We will discuss this later.

Table 3.4 Comparison of density models in terms of CPU time performance, mean, and maximum difference in density relative to MSIS86.

Model	**CPU**	$\Delta\rho_{mean}$ %	$\Delta\rho_{max}$ %
MSIS 86	100.00	-	-
Jacchia 77	3425.00	8.0	89
DTM90	9.30	19.0	101
Simplified Model	1.50	30.0	153

Figure 3.14 compares the atmospheric density calculated at T/P, SAC-C and CHAMP altitude using MSIS86 and the proposed method. Best agreement was found at the lowest altitude. This is due to the fact that the upper atmosphere is harder to model and thus needs more empirical data. We also found that density from MSIS86 indicates an hourly fluctuation, while the simplified method doesn't, except at CHMAP altitude. This suggests a deficiency in the upper atmosphere modelling.

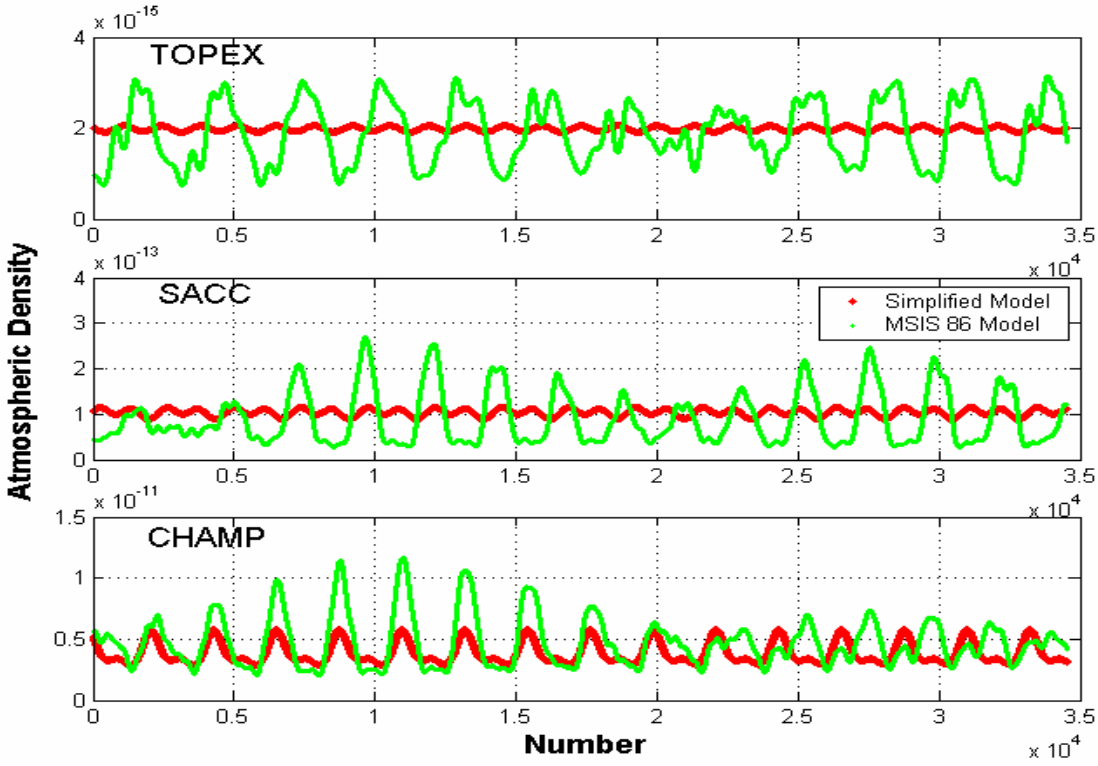

Figure 3.14 Atmospheric density difference between MSIS86 model and simplified model for different height missions.

3.7.5 Integral Equation Method and Step Size Control

From the description of the Integral Equation (IE) method in section 3.6.1, we can see that the accuracy of the IE method is of the same order as the RK4. What we like to test is the performance of the step size control with the IE method. The orbit integration setting is the same as in section 3.7.1 for three missions. The initial integration steps are 10s for all tests. Furthermore, the step changes are related to different truncation tolerances, we used 10^{-3} and 10^{-5} m. Table 3.5 lists the minimum, maximum and mean step sizes for three satellites with different error tolerance. It provides us with a guide as to how to determine the proper step size for the orbit integration.

Table 3.5 Step size change with different truncation tolerance.

	$t = 10^{-3}\ m$			$t = 10^{-5}\ m$		
	Min (s)	**Max (s)**	**Mean (s)**	**Min (s)**	**Max (s)**	**Mean (s)**
TOPEX	2.2	35.5	13.2	0.6	25.6	5.4
SACC	1.6	32.2	12.2	0.9	23.1	4.9
CHAMP	0.8	25.1	11.5	0.2	18.5	4.6

3.7.6 Orbit Integration with Full Simplified Consideration

Different algorithms have been validated in previous experiments. We are more concerned about the overall performance of the simplified method. In this experiment, orbit integration performance is compared between the full model and the simplified model. Table 3.6 lists the details of these two models. The results are derived from one day's orbit integration.

Figure 3.15 give the 3D position error from these two methods. The maximum 3D positional errors are 0.5m, 20m and 130m for T/P, SAC-C and CHAMP, respectively. This suggests a good orbit integration performance for T/P for a 24 hours arc length. Although not as good as T/P, the simplified method gives a satisfactory result for SAC-C with up to 4 hours' arc length; and up to 1 hour's arc for CHAMP.

Table 3.6 Comparison of simplified and full orbit model.

	Full Model	**Simplified Model**
Gravity	JGM3 70×70	JGM3 30×30
Planetary ephemerides	JPL DE405	Analytical method
Atmospheric density model	MSIS86	Simplified method
Upper wind model	HWV93	-
Solar pressure	Direct effect	Direct effect
Nutation, precession	IAU 1980 nutation / IAU 1976 precession, real time calculation	IAU 1980 nutation / IAU 1976 precession, interpolation method
Polar motion	IERS B bulletin	IERS B bulletin
Integrator	RK4(5) with 5 seconds step	Integration method with step control

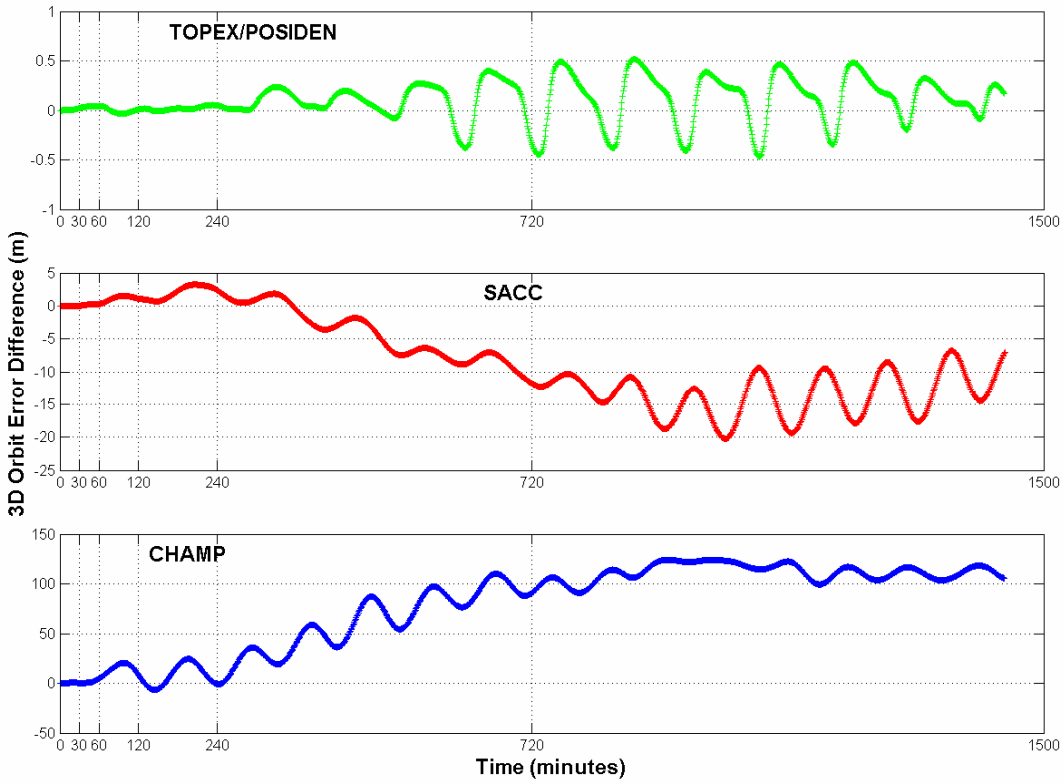

Figure 3.15 Comparison of 3D orbit integration error between simplified model and full model.

Figure 3.16 gives the radial, along-track and cross-track positional errors. This also suggests a similar conclusion to Figure 3.15. The computational burden is characterized by the computing speed. The experiment was carried out on a desktop PC, the configuration is PIII 1GHz, 256 Mbytes memory. The computing speed is measured by recording time tags at the beginning and end of the orbit integration program. Though we cannot get precise figures in this way, we are only interested in

the relative performance. Figure 3.17 gives the computing speed comparison between the simplified method and full model method. The simplified method is 3 ~ 4 times faster than the full model method. This result is quite encouraging.

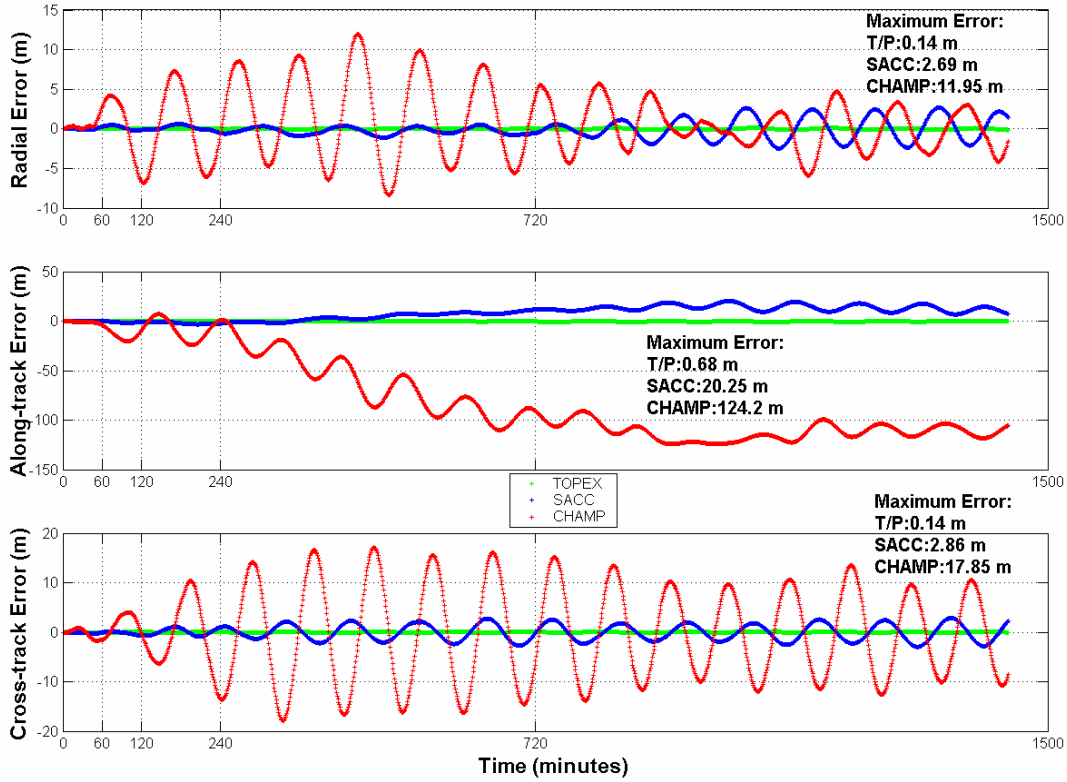

Figure 3.16 Comparison of radial, along-track and cross-track positional error between simplified model and full model.

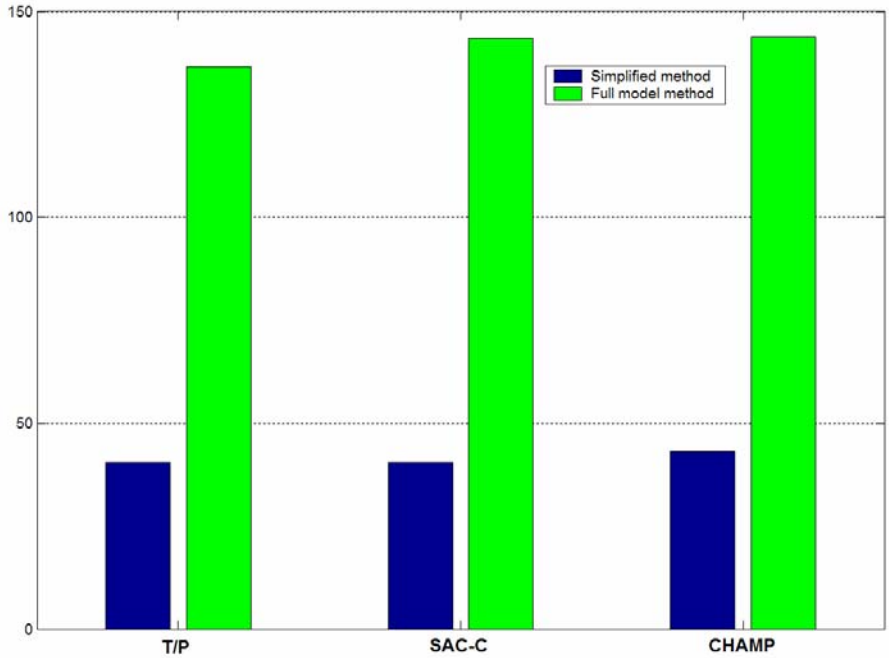

Figure 3.17 Computation speed comparison.

3.8 Conclusion

The research efforts on orbit dynamical model simplification have led to the establishment of a technical capability for onboard orbit determination in near-real time. The detailed computational burden of orbit integration was analyzed, and several model simplification schemes were identified, which can reduce the onboard computation resource requirement while retaining enough orbit integration accuracy. These simplification strategies can be summarized as follows:

- Reduce the degree & order of the Earth gravity model;
- Use an analytical method to obtain solar and lunar coordinates instead of the memory-consuming JPL DE405 interpolation method.
- Interpolate the nutation, precession and polar motion parametres from a given grid instead of calculating them precisely.
- Replace the traditional computation requiring an empirical atmospheric density model with a simplified analytical model.
- Use the Integral Equation method to propagate the orbit, as well as a step control algorithm.
- Simplify the orbital state transit matrix algorithm by only considering the J_2 term.

All the algorithms have been separately validated using real data from three LEO missions: T/P, SAC-C and CHAMP. Finally, the performance of orbit integration was evaluated and compared between the results from the full orbital models and the simplified models. Extensive testing has shown:

- For orbit integration using the full model, Earth gravity accounts for around 40% of the computing burden; atmospheric density model and planetary coordinates calculation account for around 20% of the computing burden each; and the nutation, precession, polar motion and time transformation tasks take another 10%.
- To obtain metres level accuracy, the 70×70 Earth gravity model can be simplified to 20 ~ 30 order & degree for satellites at altitudes of T/P and SAC-C. For a shorter arc, such as within 4 hours, this simplification is suitable for most LEO satellites.

- The computational burden of computing nutation, precession, polar motion, solar & lunar coordinates and the time transformation can be reduced by using an interpolation method and analytical solar & lunar ephemerides.
- The tested atmospheric density model reduced the computational dramatically, but the accuracy compared to MSIS86 was also degraded by around 30%. Considering the fact that even a precise DTM90 model has a 19% error compared to MSIS86, the proposed method is acceptable with nearly 60 times less computing time.
- The Integral Equation method with simplified orbital state transition matrix algorithm (algorithm in Appendix A) also reduces the computational effort, especially in the orbit estimation process.
- Compared to the full model method, the proposed simplified orbital model strategies using all algorithms can achieve metres level accuracy for a 4 hour short-arc for SAC-C and T/P. At the altitude of CHAMP, the same level accuracy can also be achieved with a 60 minute arc. The computational burden of the simplified method is 3 ~ 4 times less than that of the full model method.

The experimental study of the simplified orbit model has identified a means of developing an onboard orbit determination using limited computing resources onboard.

Chapter 4
Gravity Acceleration Approximation Method

Improving the speed of gravitational acceleration computations plays a critical role in reducing the overall computational burden of onboard real time or near-real time orbit determination processing. The most straightforward methods to improve the speed of computing gravitational accelerations include truncating the gravity model, pre-selecting a significant subset of coefficients, and tuning a truncated gravity field through estimation. Of these strategies the truncation method is most frequently used. From the test results presented in Chapter 3 truncation can reduce the computational burden by around 40% while retaining meter level orbit integration accuracy in most circumstances. If sub-metre accuracy for longer arcs is required, a higher order of Earth gravity model is still needed, especially for low altitude satellites. In this case, the truncating method is no longer suitable.

Based on research by *Hujsak* [1996], an alternative method was proposed to directly interpolate the gravitational acceleration from a grid of pre-computed values. The recursive gravitational computation is replaced by a much simpler interpolation method but requires several Mbytes more memory. The results show that the computational burden of the method is equivalent to that of a 5×5 gravity model. The following sections describe these methods in detail, and present extensive results to explore its possible application for onboard orbit determination.

4.1 JGM Earth Gravity Model Overview

4.1.1 Geopotential Spherical Harmonic Expression

Because the irregular distribution of the Earth mass is unknown, the geopotential coefficients have to be determined through the analysis of measurements. Three

principle types of observations are currently used to improve the Earth gravity models: satellite tracking, surface gravimetry and altimeter data. From around the 1960s, some gravity models have been developed using satellite data.

One of the most precise EGM96 currently available for orbit determination is the Joint Gravity Model (JGM). JGM was developed for the oceanographic mission T/P, which had challenging requirements for the radial orbit accuracy of 13cm. This mission led to cooperation between NASA's GSFC, the University of Texas Centre for Space Research (CSR) and the Centre National d'Etudes Spatiales (CNES) in the area of Earth gravity filed determination. As a result, the final pre-launch T/P gravity model JGM-1 of order and degree 70 was released in 1994 [*Nerem, et al.*, 1994]. It used the GEM-3 gravity model solution, but processing all of the data with improved models and constants. Its successor JGM-2 was a first post-launch T/P model, which included a six-month set of T/P SLR and DORIS data. A further improvement in accuracy was obtained with JGM-3 [*Tapley, et al.*, 1996], which comprised new T/P SLR, DORIS, as well as for the first time GPS tracking data of the T/P satellite. In addition, new SLR data from LAGEOS1, LAGEOS2 and Stella, as well as DORIS tracking of the SPOT2 satellite, were included.

Like other gravity models, the JGM3 geopotential model is usually represented by a spherical harmonic expression - the harmonic expression is given in Equation (3.6). In general, excluding the central two-body force, the non-spherical geopotential can be expressed in the Earth-fixed frame as:

$$\mathbf{U}_s(r,\phi,\lambda) = \frac{GM_e}{r}\sum_{l=2}^{\infty}\overline{C}_l\left(\frac{a_e}{r}\right)^l\overline{P}_l(\sin\phi) + \frac{GM_e}{r}\sum_{l=2}^{\infty}\sum_{m=1}^{l}\left(\frac{a_e}{r}\right)^l\overline{P}_{lm}(\sin\phi)[\overline{C}_{lm}\cos m\lambda + \overline{S}_{lm}\sin m\lambda] \tag{4.1}$$

The notation is the same as for Equation (3.6). The first term of the right-hand side of the equation is the sum of the zonal terms $\overline{C}_{l0}$, if one considers the more general case of mass distribution that is symmetric with respect to the axis of rotation. But the Earth is not an ideal rotational ellipsoid. The additional tesseral and sectorial geopotential coefficients are described by the second set of terms

Furthermore, according to *Koskela* [1967], acceleration components in the Up (**U**), East (**E**), and North (**N**) coordinate system in the Earth-fixed frame are:

$$a_U = -\frac{GM}{r^2}\left\{1+\sum_{n=2}^{\infty}(n+1)\left(\frac{a_e}{r}\right)^n \sum_{m=0}^{n} p_n^m(\sin\phi)\left[C_{nm}\cos m\lambda + S_{nm}\sin m\lambda\right]\right\}$$

$$a_E = -\frac{GM}{r^2\cos\phi}\left\{\sum_{n=2}^{\infty}\left(\frac{a_e}{r}\right)^n \sum_{m=0}^{n} m p_n^m(\sin\phi)\left[C_{nm}\sin m\lambda - S_{nm}\cos m\lambda\right]\right\}$$

$$a_N = \frac{GM}{r^2}\left\{\sum_{n=2}^{\infty}\left(\frac{a_e}{r}\right)^n \sum_{m=0}^{n} \cos\phi\, p_n^{m'}(\sin\phi)\left[C_{nm}\cos m\lambda + S_{nm}\sin m\lambda\right]\right\} \tag{4.2}$$

Where prime $(')$ indicates the derivative with respect to $(\sin\phi)$.

4.1.2 Gravity Acceleration and Partials

The acceleration $\ddot{\mathbf{r}}$ expressed in the inertial frame, which is equal to the gradient of $U_s(r,\phi,\lambda)$, may be expressed as:

$$\ddot{\mathbf{r}} = \frac{\partial U_s}{\partial \mathbf{r}} = \Theta_t\left[\frac{\partial U_s}{\partial r}\frac{\partial r}{\partial \mathbf{r}'(x,y,z)} + \frac{\partial U_s}{\partial \phi}\frac{\partial \phi}{\partial \mathbf{r}'(x,y,z)} + \frac{\partial U_s}{\partial \lambda}\frac{\partial \lambda}{\partial \mathbf{r}'(x,y,z)}\right] \tag{4.3}$$

where the Θ_t is a time-dependent matrix that describes the Earth's rotation, precession and nutation, and $\mathbf{r}'(x,y,z)$ is the satellite vector in the Earth-fixed frame. The second-order partial derivatives of the potential also can be expressed as:

$$\frac{\partial \ddot{\mathbf{r}}}{\partial \mathbf{r}} = \Theta_t^T\left[\frac{\partial}{\partial \mathbf{r}'(r,\lambda,\phi)}\left(\frac{\partial U_s}{\partial \mathbf{r}'(x,y,z)}\right)\right]\frac{\partial \mathbf{r}'(r,\lambda,\phi)}{\partial \mathbf{r}'(x,y,z)}\Theta_t \tag{4.4}$$

4.2 A Study of Gravity Acceleration Variation with JGM-3 Model

After the removal of the central body force, the order of magnitude of Earth gravity acceleration is around $10^{-2}\,m/s^2$. From Equation (4.1), we can see that the acceleration only depends on the coordinates (r,λ,φ) in the Earth-fixed frame. This suggests the idea to of a global gravity acceleration grid. But to get the necessary interpolation accuracy, the grid must be dense enough. On the other hand, a dense

grid requires much more memory space, thus an optimal grid size is important. In this section, the gravity acceleration variation with respect to (r, λ, φ) has been investigated.

4.2.1 JGM-3 Gravity Acceleration Variation with Respect to (r, λ, φ)

Given the latitude and longitude values (λ, φ), the acceleration was calculated at different altitudes. Three sets of (λ, φ) values were used in this test: (0, 0), (0, 60), (0, 80). For a circular or near-circular orbit, only a very thin orbit layer is needed. For example, the altitude range of SAC-C is from 7070km to 7090km. Figure 4.1 illustrates the variation.

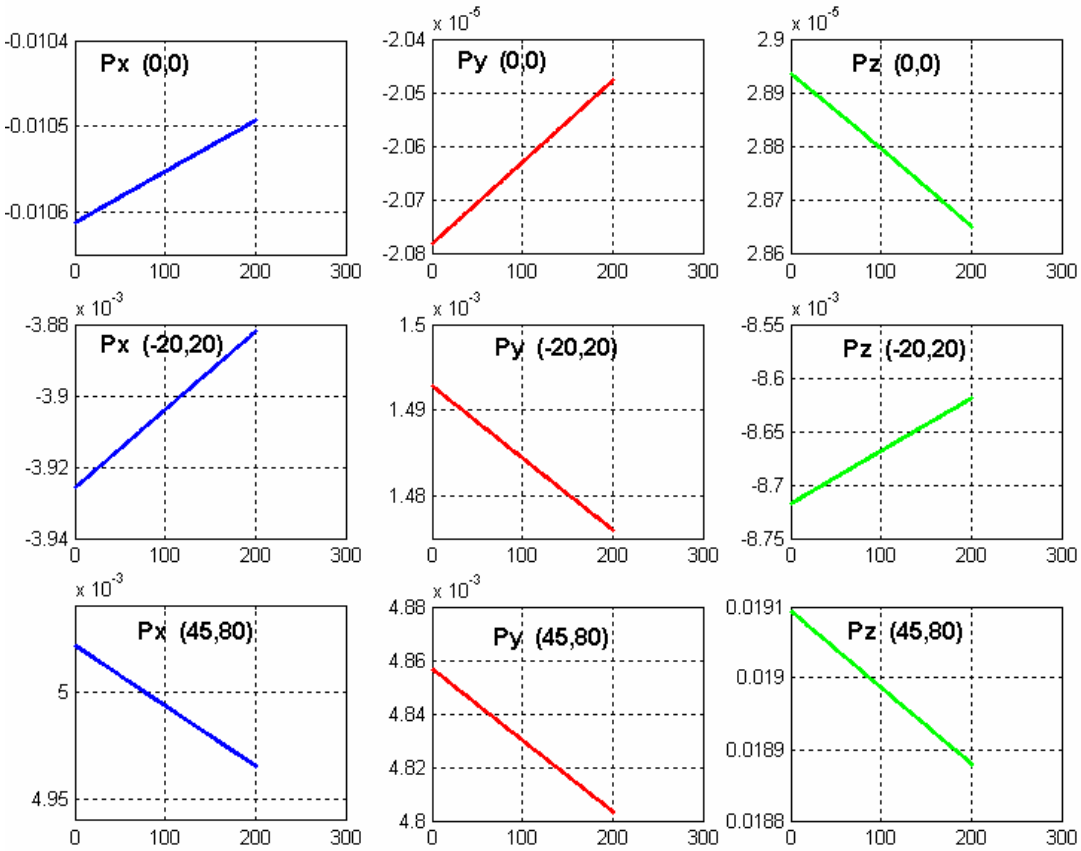

Figure 4.1 Gravity acceleration variations (m/s^2) with fixed longitude and latitude at altitude between 7070km to 7090km.

Obviously, it is quite reasonable to represent the acceleration using a low-order polynomial in the radian (r) direction.

Similarly, the test was carried out at a fixed (r, φ), allowing the geocentric longitude λ to change from 0 to 359 degree. Three sets of (r, φ) values were used in this test: (7080, 0), (7080, 60), (7080, 80). Figure 4.2 shows the result. The variation in longitude changes dramatically compared to variations in altitude.

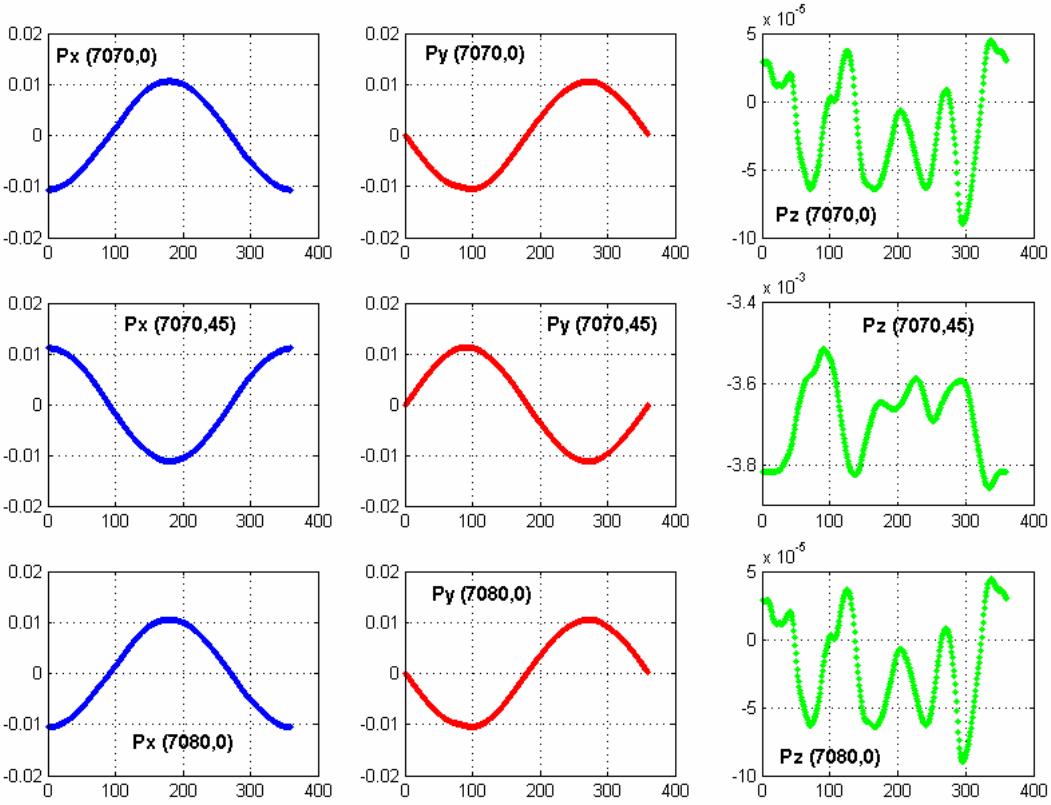

Figure 4.2 Gravity acceleration variations (m/s^2) with fixed height and latitude at longitude between 0 to 360 degrees.

Furthermore, given three sets of (r, λ): (7070, 0), (7080, 0) and (7090, 0), the variation with latitude is shown in Figure 4.3. This is similar behaviour to Figure 4.2. It is difficult to model this type of variation because the acceleration changes dramatically with different latitude.

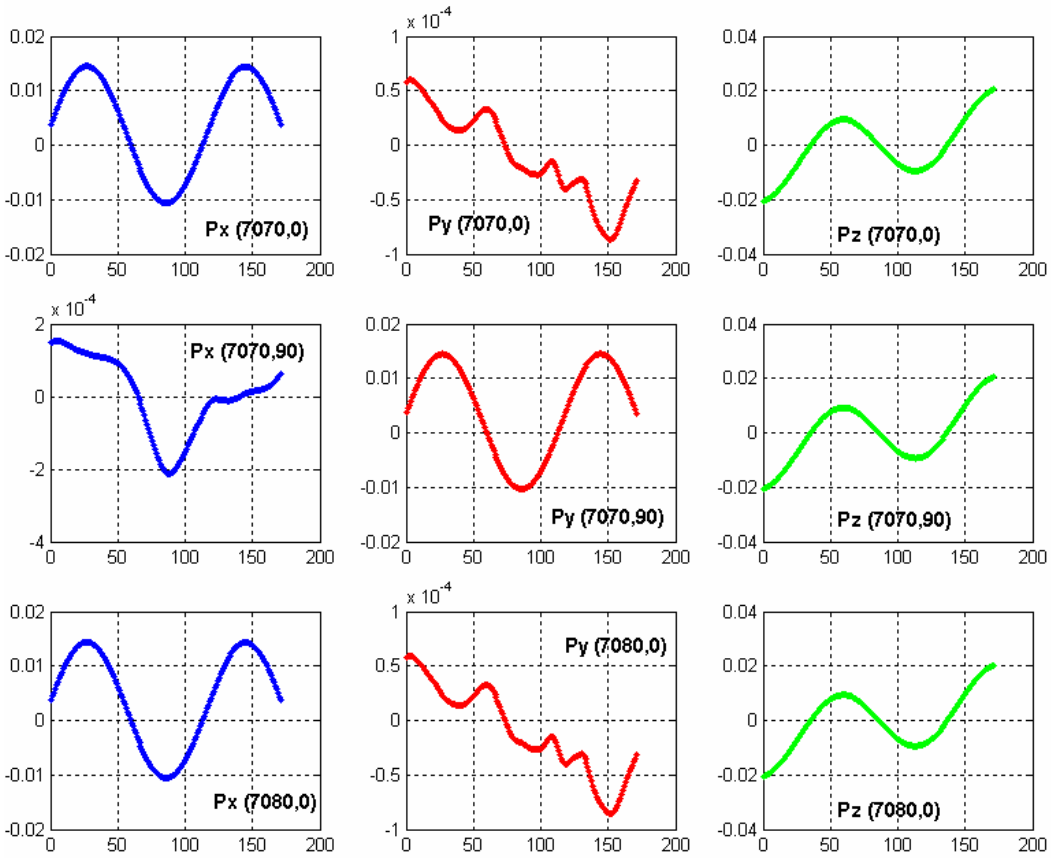

Figure 4.3 Gravity acceleration variations (m/s^2) with fixed height and longitude at latitude between -85 to 85 degrees.

4.2.2 Polynomial Approximation of Radial Gravity Acceleration Components

Based on the previous discussion, it is a quite straightforward to use a polynominal function to fit the gravity acceleration values in the height direction. In order to precisely fit the height acceleration variations, the accelerations at a certain number of sample points must be first calculated. The *m*-order *n*-point polynomial fitting can be expressed as:

$$P_{m-1}(x) = a_0 + a_1(x-\bar{x}) + a_2(x-\bar{x})^2 + \cdots + a_{m-1}(x-\bar{x})^{m-1}, \quad \bar{x} = \sum_{0}^{n-1} x_i / n \tag{4.5}$$

For a given (λ, φ) three gravitational acceleration components were calculated within the height range. Least squares methods are used to estimate the coefficient with the samples at n points The order from 3 to 10 was tested at three different points: $(0^\circ, 0^\circ)$, $(0^\circ, 45^\circ)$ and $(0^\circ, 80^\circ)$. To avoid loss of precision, the data points

were sampled for every 10 ~ 50 metres between the orbital radius 7070km to 7090km, resulting in 2,000 points. Table 4.1 illustrates the polynomial fitting result for different schemes. Figure 4.4 shows the RMS values of the radial gravity acceleration polynomial fitting as a function of different orders, while Figure 4.5 illustrates the maximum errors of the same fittings.

Table 4.1 Height direction gravity acceleration Legendre polynomial fitting results at $(0^{\circ},0^{\circ})$, $(0^{\circ},45^{\circ})$ and $(0^{\circ},80^{\circ})$, respectively.

Order	**X**			**Y**			**Z**		
	Square	**Abs**	**Max**	**Square**	**Abs**	**Max**	**Square**	**Abs**	**Max**
3	3.26e-18	3.11e-8	2.35e-10	3.39e-21	1.00e-9	7.64e-12	4.30e-20	3.57e-9	2.72e-11
4	6.34e-24	4.33e-11	3.69e-13	2.26e-25	8.18e-12	6.99e-14	2.28e-24	2.60e-11	2.22e-13
5	4.06e-29	1.11e-13	9.70e-16	8.18e-30	4.92e-14	4.59e-16	6.67e-29	1.41e-13	1.31e-15
6	1.21e-30	1.88e-14	1.02e-16	2.28e-34	2.57e-16	2.62e-18	1.21e-33	5.96e-16	6.02e-18
7	1.39e-30	1.91e-14	1.06e-16	5.48e-36	3.75e-17	2.20e-19	1.08e-35	5.36e-17	3.15e-19
8	2.77e-30	2.72e-14	2.36e-16	1.10e-35	5.45e-17	4.85e-19	2.13e-35	7.38e-17	6.81e-19
9	3.10e-30	2.88e-14	3.42e-16	1.22e-35	5.78e-17	6.95e-19	2.37e-35	7.63e-17	9.72e-19
10	3.85e-30	3.22e-14	2.20e-16	1.51e-35	6.37e-17	4.37e-19	2.95e-35	8.74e-17	6.37e-19
Order	**X**			**Y**			**Z**		
	Square	**Abs**	**Max**	**Square**	**Abs**	**Max**	**Square**	**Abs**	**Max**
3	4.33e-18	3.58e-8	2.71e-10	3.24e-20	3.10e-9	2.36e-11	4.58e-19	1.17e-8	8.83e-11
4	1.07e-23	5.63e-11	4.79e-13	1.46e-24	2.08e-11	1.78e-13	8.62e-25	1.60e-11	1.36e-13
5	3.92e-29	1.20e-13	9.30e-16	4.78e-29	1.19e-13	1.11e-15	1.65e-30	2.25e-14	1.83e-16
6	1.34e-30	1.99e-14	1.14e-16	1.17e-33	5.84e-16	5.91e-18	1.67e-31	6.97e-15	4.21e-17
7	1.51e-30	2.07e-14	1.16e-16	1.19e-35	5.70e-17	3.12e-19	1.90e-31	7.15e-15	4.81e-17
8	3.04e-30	2.81e-14	2.60e-16	2.45e-35	8.08e-17	7.39e-19	3.69e-31	9.99e-15	8.59e-17
9	3.40e-30	2.95e-14	3.75e-16	2.73e-35	8.50e-17	1.05e-18	4.14e-31	1.06e-14	1.25e-16
10	4.25e-30	3.35e-14	2.41e-16	3.40e-35	9.55e-17	6.51e-019	5.10e-31	1.18e-14	8.67e-17
Order	**X**			**Y**			**Z**		
	Square	**Abs**	**Max**	**Square**	**Abs**	**Max**	**Square**	**Abs**	**Max**
3	1.54e-18	2.13e-8	1.62e-10	2.61e-20	2.78e-9	2.12e-11	1.02e-17	5.51e-8	4.17e-10
4	3.02e-24	2.99e-11	2.54e-13	2.03e-24	2.45e-11	2.10e-13	1.80e-23	7.31e-11	6.21e-13
5	1.40e-29	6.55e-14	5.71e-16	8.99e-29	1.63e-13	1.52e-15	5.07e-29	1.25e-13	9.99e-16
6	6.05e-31	1.31e-14	8.15e-17	3.20e-33	9.68e-16	9.84e-18	4.33e-30	3.58e-14	1.98e-16
7	6.76e-31	1.34e-14	7.98e-17	3.94e-35	1.03e-16	8.47e-19	4.87e-30	3.61e-14	2.39e-16
8	1.29e-30	1.83e-14	1.47e-16	6.71e-35	1.36e-16	1.24e-18	9.42e-30	5.18e-14	4.61e-16
9	1.44e-30	1.91e-14	2.20e-16	7.37e-35	1.40e-16	1.57e-18	1.05e-29	5.50e-14	6.56e-16
10	1.78e-30	2.15e-14	1.59e-16	8.90e-35	1.55e-16	1.17e-18	1.29e-29	6.02e-14	3.89e-16

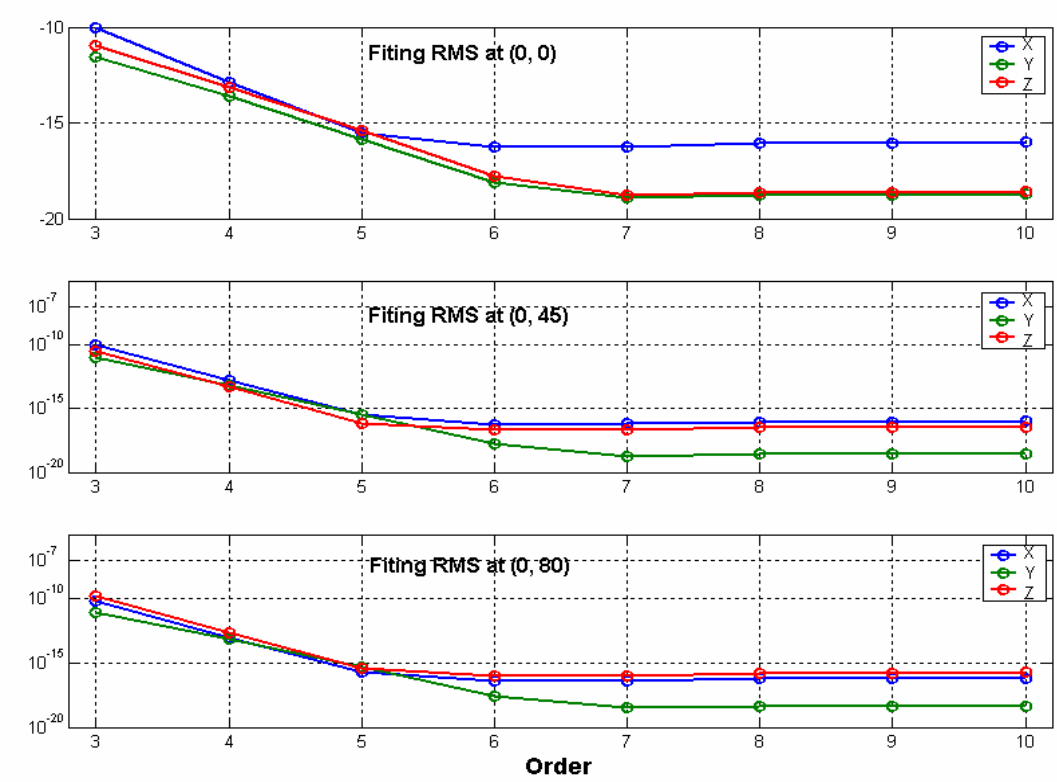

Figure 4.4 RMS error of the radial gravity acceleration (m/s^2) using polynominal fitting against the fitting orders.

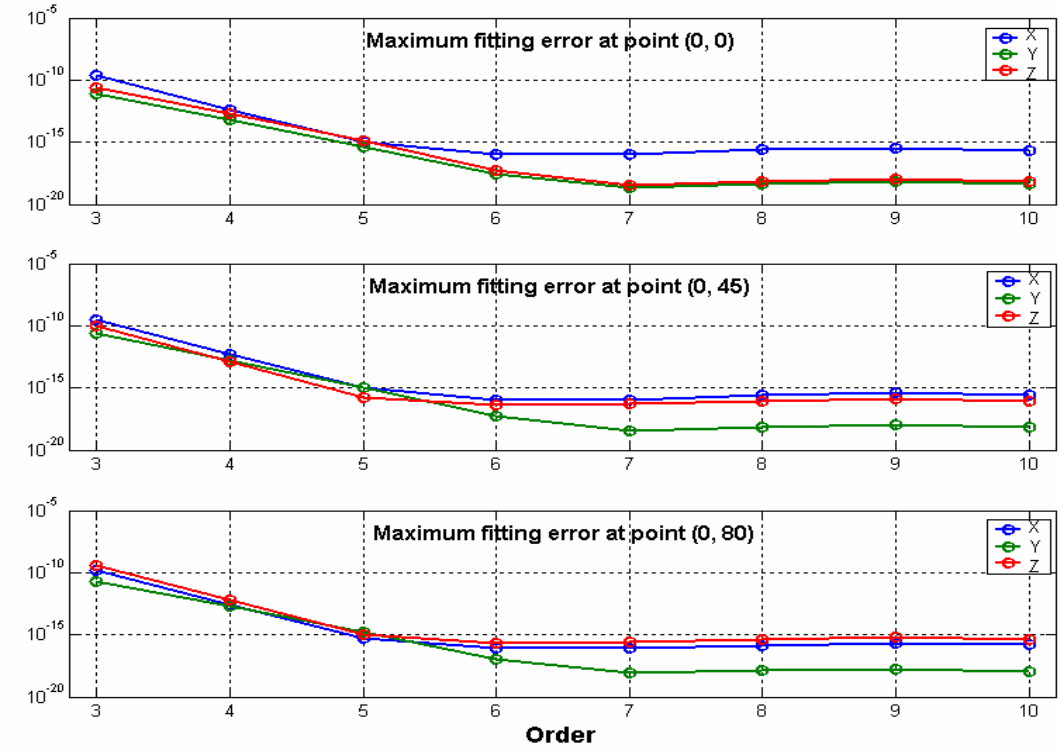

Figure 4.5 Maximum fitting error of the radial gravity acceleration (m/s^2) against different orders.

From these figures, it is clear that the polynomial function of 7 or higher is appropriate for the radial fitting, achieving a standard deviation of around$10^{-17} m/s^2$, which is quite a small perturbation source to a satellite. If further simplification is needed, a 3rd or 4th order polynomial fit can also achieve $10^{-10} m/s^2$ accuracy.

To test the fitting accuracy, 2000 points along the radius between 7070km to 7090km were randomly generated. The gravitational accelerations from the fitted polynomial are compared with the precisely computed ones, and the results are given in Table 4.2 and Figure 4.6.

Table 4.2 Statistics of height direction acceleration (m/s^2) recovery error at $(\lambda = 0^\circ, \varphi = 0^\circ)$.

Order	**X**		**Y**		**Z**	
	Max	**Std**	**Max**	**Std**	**Max**	**Std**
3	2.35e-10	4.54e-11	7.64e-12	1.46e-12	2.72e-11	5.22e-12
4	3.69e-13	6.29e-14	6.99e-14	1.19e-14	2.22e-13	3.78e-14
5	1.13e-15	1.81e-16	4.55e-16	7.09e-17	1.31e-15	2.03e-16
6	9.89e-17	2.43e-17	4.96e-18	9.43e-19	7.89e-18	1.21e-18
7	1.02e-16	2.76e-17	2.43e-18	7.20e-19	2.06e-18	6.03e-19
8	5.10e-16	1.14e-16	3.78e-18	1.03e-18	3.89e-18	1.03e-18
9	5.59e-16	1.20e-16	3.99e-18	1.04e-18	4.13e-18	1.04e-18
10	2.27e-16	5.67e-17	4.58e-18	1.32e-18	4.99e-18	1.44e-18

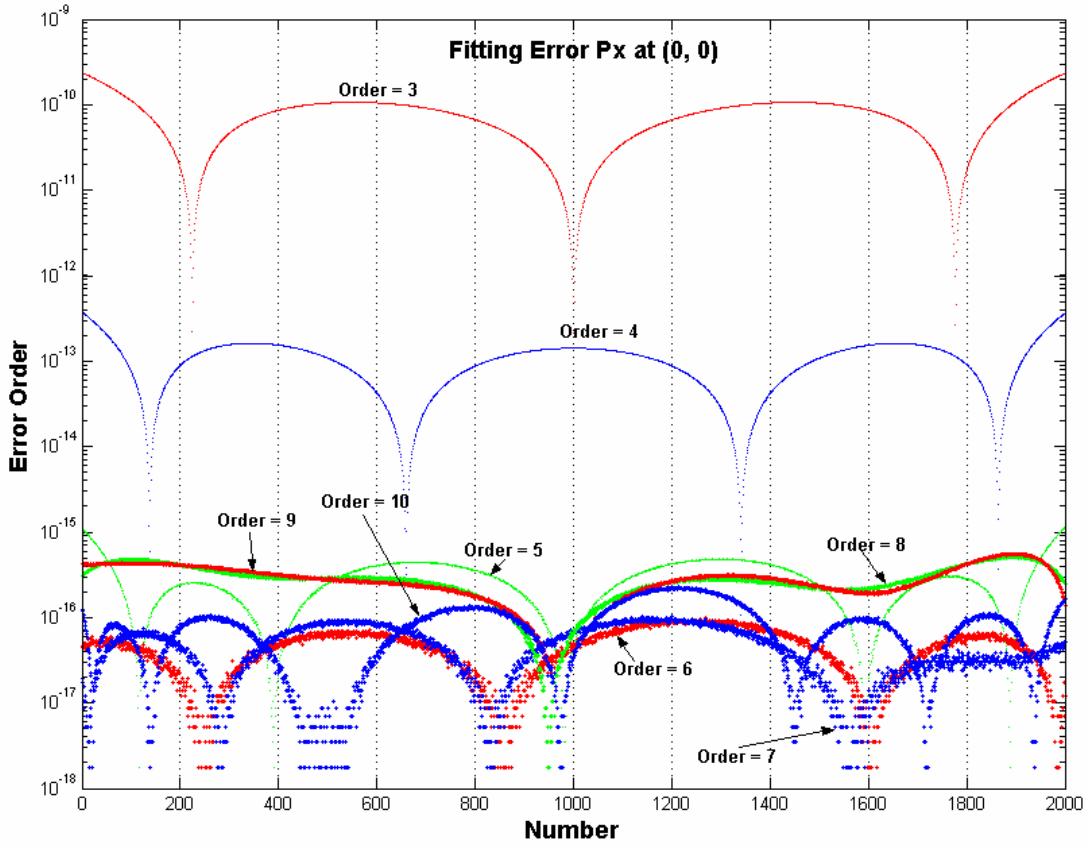

Figure 4.6 Radial gravity acceleration recovery errors at $(\lambda = 0^\circ, \varphi = 0^\circ)$, plotted against different orders of Legendre polynomial fitting.

The results also suggest using a 6th order fitting is adequate. However, if only considering $10^{-11} \sim 10^{-13} m/s^2$ accuracy, which is in the same order of the Jupiter gravitation, 4th order fitting is the optimum choice in terms of both accuracy and memory.

4.2.3 3D Gravity Acceleration Interpolation

The Earth gravity acceleration recovery result in altitude direction was satisfactory using a simple 6th order polynomial fitting, but the result is unknown if the recovery is carried out in the 3D space. In this section a 3D interpolator was implemented based on the modified quadratic Shepard method [*Robert*, 1988a, 1988b]. Through extensive testing, it was observed that only $10^{-7} m/s^2$ accuracy was achieved using a $1^\circ \times 1^\circ$ gravity grid, and $10^{-9} m/s^2$ accuracy was achieved using a $0.5^\circ \times 0.5^\circ$ grid. But the $0.5^\circ \times 0.5^\circ$ grid requires more than 20 Mbytes memory storage. Furthermore,

the 3D quadratic Shepard interpolation algorithm also has a large computational burden. Hence this 3D interpolation method is not applicable for onboard processing. Further research efforts are therefore required to solve this problem. The concept of "pseudo-centre" is proposed in the next section.

4.3 Method of Pseudo-centres

4.3.1 Introduction

Examining gravity acceleration approximation functions is motivated by the on-going debate between proponents of general perturbations, semi-analytic, and special perturbation methods of generating ephemerides for near-Earth satellites. While there is no doubt that the special perturbation methods provide the best accuracy for most applications, the computational burden for motivates research into alternative solution forms. The most complex acceleration model in special perturbations for near-Earth satellites .qw6is the gravity model. There have been several attempts to improve the computing speed for gravitational acceleration. Among these are model truncation, pre-selecting a significant subset of the geopotential coefficients, and developing an equivalent "mascon" representation. To date, the alternative solution of using stored gravity acceleration tables has been impossible to implement because of limited onboard computer memory.

The method to be examined below wrestles with the trade off between storage and computation. It was first developed by *Hujsak* [1996]. The size of the stored tables can be minimized by using more complex approximating and interpolating algorithms. On the other hand, the computational burden can be reduced by accepting a greater storage requirement. A different acceleration representation in terms of an earth's "pseudo-centre" [*Hujsak*, 1996] is defined, and used together with classical polynomial fitting and bi-variate interpolators to gain a computational advantage. The final algorithm:

- reads a large table of coefficients for a particular height,
- evaluates functions of height at points on a latitude-longitude interpolation grid,

- interpolates to find pseudo-centre coordinates at a position of interest, and
- and computes gravity accelerations and partials from the pseudo-centre coordinates.

The algorithm provides the full accuracy (if not precision) of the JGM-3 70×70 gravity model over altitudes from 400-1500km for a computational cost of a 5×5 models (from typical methods of evaluating the geopotential). The strategy presented here achieves that goal with a storage burden of 1.8 Mbytes or less.

4.3.2 Earth Pseudo-centres

Given the Earth-Centreed, Earth-Fixed (ECEF) gravitational acceleration on a spacecraft $\ddot{\mathbf{r}}$, and using the restricted two-body equation of motion, a pseudo-centre, $\mathbf{c}$ can be calculated. Figure 4.7 illustrates this concept.

$$\ddot{\mathbf{r}} = -\mu \frac{\boldsymbol{\rho}}{\rho^3} \tag{4.6}$$

In Equation (4.6), $\boldsymbol{\rho}$ is a pseudo-radius to the spacecraft from the pseudo-centre. In the above equation $\ddot{\mathbf{r}}$ is the non-spherical acceleration calculated using spherical harmonic coefficient expansion. Now the actual radius to the satellite is the pseudo-radius plus the pseudo-centre. A pseudo-centre is a vector from the centre of the Earth to where the centre of the Earth would need to be if the non-spherical acceleration acting on the satellite is equal to the restricted two-body acceleration acting on the satellite:

$$\mathbf{c} = \mathbf{r} - \boldsymbol{\rho} \tag{4.7}$$

By definition,

$$\rho = |\boldsymbol{\rho}|, \text{ and } \boldsymbol{\rho} = \rho \hat{\boldsymbol{\rho}} \tag{4.8}$$

Also, since the pseudo-radius vector is in the opposite direction of the acceleration:

$$\hat{\boldsymbol{\rho}} = -\frac{\ddot{\mathbf{r}}}{|\ddot{\mathbf{r}}|} \tag{4.9}$$

Therefore, substituting Equation (4.9) into Equation (4.7) yields:

$$\mathbf{c} = \mathbf{r} - \rho \hat{\boldsymbol{\rho}} \tag{4.10}$$

Now, dot product both sides of Equation (4.6) with $\hat{\boldsymbol{\rho}}$:

$$|\ddot{\mathbf{r}}| = -\mu \frac{1}{\rho^2} \tag{4.11}$$

Therefore:

$$\rho = \sqrt{\frac{\mu}{|\ddot{\mathbf{r}}|}} \tag{4.12}$$

Leading to the result:

$$\mathbf{c} = \mathbf{r} - \sqrt{\frac{\mu}{|\ddot{\mathbf{r}}|}}\hat{\boldsymbol{\rho}} \tag{4.13}$$

This pseudo-centre is simply the mechanization of the concept that the Earth appears as a point mass. Given the correct value for $\mathbf{c}$, Equation (4.6) is exact. This method for finding approximating functions and interpolated representations for $\mathbf{c}$ which are sufficiently accurate to be useful and simultaneously is computationally efficient. These approximations can be substituted into Equation (4.6) to recover the acceleration $\ddot{\mathbf{r}}$. If $\ddot{\mathbf{r}}$ is computed with all perturbations and the two-body acceleration, then analysis shows that $|\mathbf{c}| < 15km$ for $h \geq 100km$ and $|\mathbf{c}| \to 0km$ as $h \to \infty$. If the $C_{2,0}$ term is omitted from Equation (4.6) then $|\mathbf{c}| < 250m$. This distinction will become important later.

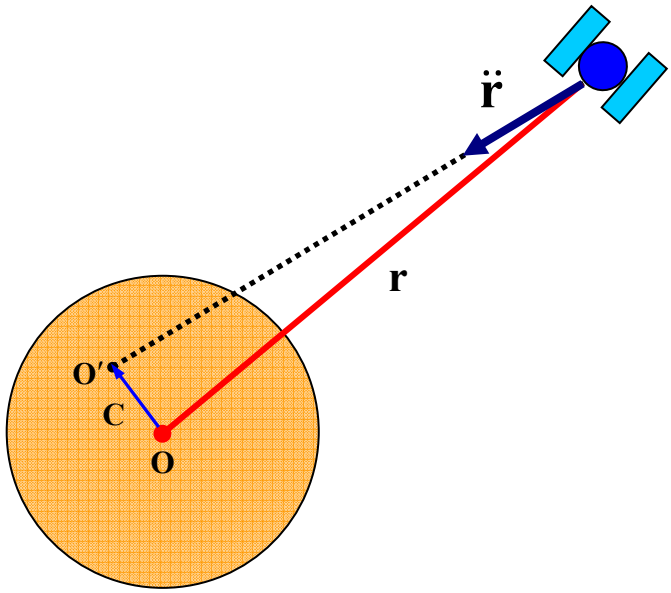

Figure 4.7 Concept of Earth pseudo-centres.

4.3.3 Acceleration Formulation for Pseudo-centres Independent of $C_{2,0}$

Having noted the storage benefit of omitting $C_{2,0}$ accelerations from the pseudo-centre definition, we introduce a new definition for the pseudo-centre. We simply add the $C_{2,0}$ acceleration to the right-hand side of Equation (4.6), and since the $C_{2,0}$ acceleration appears on both sides of the expression, then $\mathbf{c}$ is independent of $C_{2,0}$:

$$\ddot{\mathbf{r}} = -\mu \frac{\boldsymbol{\rho}_0}{\rho_0^{\,3}} + \ddot{\mathbf{r}}_{2,0} \tag{4.14}$$

where $\ddot{\mathbf{r}}_{2,0}$ is the acceleration due to $C_{2,0}$. Let:

$$\ddot{\mathbf{r}}_0 = \ddot{\mathbf{r}} - \ddot{\mathbf{r}}_{2,0} = -\mu \frac{\boldsymbol{\rho}_0}{\rho_0^{\,3}} \tag{4.15}$$

where

$$\hat{\boldsymbol{\rho}} = -\frac{\ddot{\mathbf{r}}_0}{|\ddot{\mathbf{r}}_0|},\ \mathbf{c} = \mathbf{r} + \boldsymbol{\rho} = \mathbf{r} + \rho\hat{\boldsymbol{\rho}} = \mathbf{r} + \sqrt{\frac{\mu}{|\ddot{\mathbf{r}}_0|}}\hat{\boldsymbol{\rho}} \tag{4.16}$$

We have the acceleration due to the $C_{2,0}$ as:

$$\ddot{\mathbf{r}}_{2,0} = \begin{bmatrix} -C_{2,0}\dfrac{3}{2}\dfrac{\mu r_1}{r^3}\left(\dfrac{R_E}{r}\right)^2\left(5\left(\dfrac{r_3}{r}\right)^2 - 1\right) \\ -C_{2,0}\dfrac{3}{2}\dfrac{\mu r_2}{r^3}\left(\dfrac{R_E}{r}\right)^2\left(5\left(\dfrac{r_3}{r}\right)^2 - 1\right) \\ -C_{2,0}\dfrac{3}{2}\dfrac{\mu r_3}{r^3}\left(\dfrac{R_E}{r}\right)^2\left(5\left(\dfrac{r_3}{r}\right)^2 - 3\right) \end{bmatrix} \tag{4.17}$$

and $C_{2,0} = -J_2 = -1.082626925638815 \times 10^{-3}$ (JGM-3), The computational burden for Equation (4.17), depending on code efficiency, is 33 multiplication operations, 11 addition operations, and one square root. Allowing 5 multiplications and 4 additions for the square root, the totals are 38 multiplications and 15 additions.

4.4 Radial Pseudo-centres Polynominal Fit

As discussed in Section 4.2, for a given (λ, φ) the pseudo-centres within the height range are fitted to give a set of coefficients for recovery. Different order and height increment are tested to give the best fitting scheme. The standard spherical harmonic

calculation for gravitational acceleration can be expressed as in Figure 4.7. Remember we set the $C_{2,0}$ = 0, as discussed above.

To maximize simplification for onboard computing, all the procedures in the dashed rectangle in Figure 4.8 are included in the acceleration approximation. Thus the output from the interpolation can be directly added to the perturbation acceleration.

Again, polynomial order from 3rd to 10th was tested, and the height increment was from 50m to 4km in the 20km altitude range of SAC-C, that is 7070km to 7090km. The interpolator can be expressed as:

$$x = \frac{h - h_{\min}}{h_{\max} - h_{\min}} \tag{4.18}$$

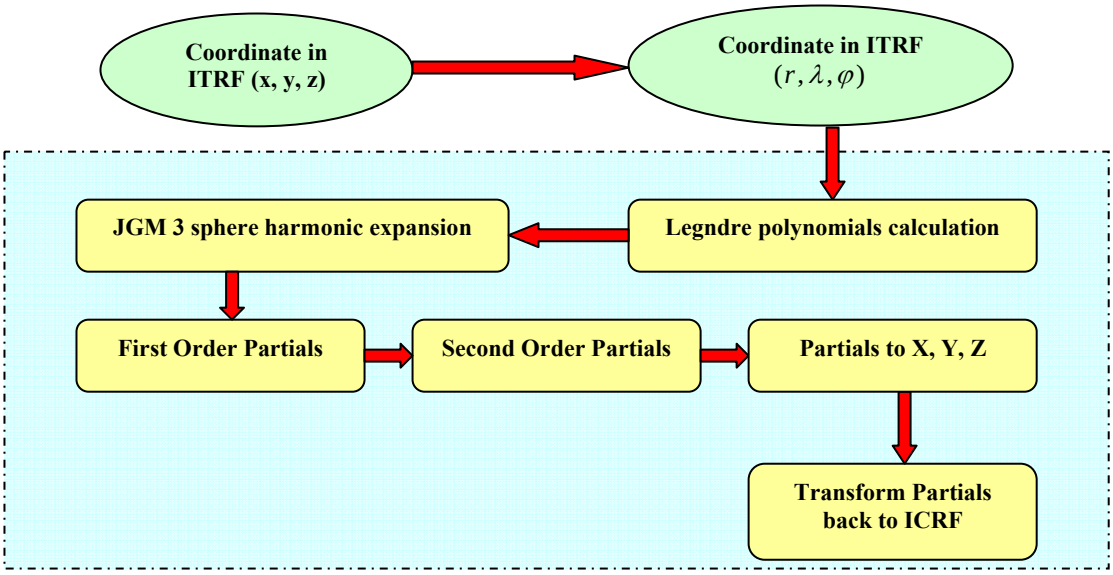

Figure 4.8 Gravitational spherical harmonic calculation flow chart.

4.5 Bi-variate Pseudo-centres Interpolation on a Sphere

4.5.1 Pseudo-centre Interpolation on a Sphere at a Common Height

The Earth's surface is naturally subdivided into "rectangles" in latitude and longitude, with constant increments in latitude ($\Delta\phi$) and variable increments in longitude ($\Delta\lambda$). Polynomial coefficients for the height function are stored for each

vertex of the “rectangle”. This subdivision makes indexing into the array of stored points an easy (and computationally efficient) exercise.

There are a variety of two-dimensional interpolation methods. The criteria for selecting an interpolation algorithm prioritizes computational speed and accuracy (versus σ_c), with storage requirements being treated as a secondary issue. These criteria practically eliminate all higher-order interpolators where first and second partial derivatives are used [*Press, et al.*, 1992] to describe the variations in the dependent function $\mathbf{c}(\varphi, \lambda, h)$ over the domain φ and λ.

Ultimately the choice reduces to three bi-variate interpolation techniques, the three-point, four-point, and six-point methods listed in *Abramowitz* and *Stegun* [1992], from which the six-point bi-variate interpolation formula was selected:

$$\begin{aligned}\hat{\mathbf{c}}(\phi_p, \lambda_q, h) &= \mathbf{c}(\phi_0 + p\Delta\phi, \lambda_0 + q\Delta\lambda, h) \\ &= .5q(q-1)\mathbf{c}(\phi_0, \lambda_0 - \Delta\lambda, h) \\ &\quad + .5p(p-1)\mathbf{c}(\phi_0 - \Delta\phi, \lambda_0, h) \\ &\quad + (1 + pq - p^2 - q^2)\mathbf{c}(\phi_0, \lambda_0, h) \\ &\quad + .5p(p-2q+1)\mathbf{c}(\phi_0 + \Delta\phi, \lambda_0, h) \\ &\quad + .5q(q-2p+1)\mathbf{c}(\phi_0, \lambda_0 + \Delta\lambda, h) \\ &\quad + pq\mathbf{c}(\phi_0 + \Delta\phi, \lambda_0 + \Delta\lambda, h)\end{aligned} \tag{4.19}$$

where

$$p = \frac{\lambda_p}{\lambda_p - \lambda_0} \text{ and } q = \frac{\phi_p}{\phi_p - \phi_0} \tag{4.20}$$

We have $0 \le p < 1$ and $0 \le q < 1$, and $\Delta\phi$ and $\Delta\lambda$ and a convenient grid in latitude and longitude. Figure 4.9 illustrates this concept.

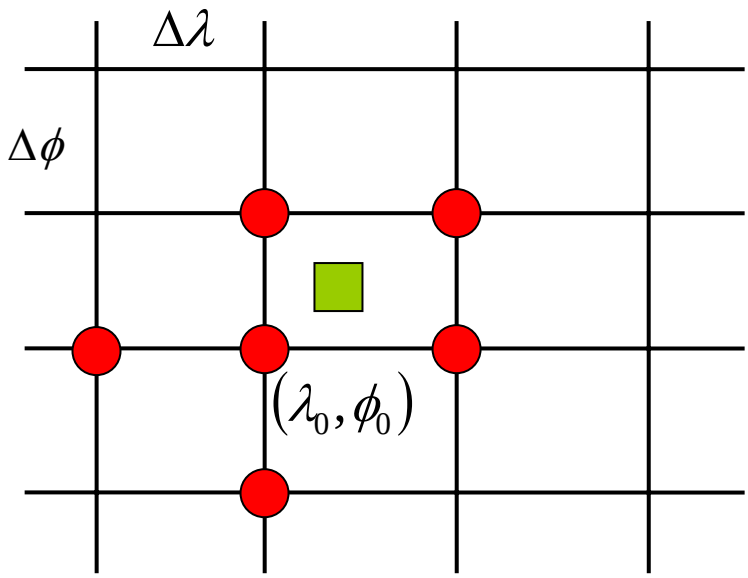

Figure 4.9 Six-point bi-variate interpolation at a common height.

Equation (4.24) requires 20 multiplication operations and 14 addition operations for each component **c**, or 60 multiplications and 42 additions for all three components. Computing p and q adds one additional multiplication and two additional operations each, for a total of 62 multiplication and 46 addition operations.

A parametric study was performed where the size of the longitude grid was varied to determine the trade-off between accuracy and the interpolation grid size ($\Delta\phi$ and $\Delta\lambda$). Values of $\Delta\phi$ studied included $0.4^\circ \le \Delta\phi \le 1.5^\circ$ and the respective longitude increments $\Delta\phi = \Delta\lambda / |\cos\phi|$, with $\Delta\lambda$ constrained to be less than 5° near the poles. A representative, but not exhaustive, search over the surface of the Earth and over heights between 100km and 1500km was performed. At each position (ϕ_0, λ_0, h) a set of six interpolation points were identified:

$$\begin{Bmatrix} (\phi_0, \lambda_0, h), & (\phi_0 - \Delta\phi, \lambda_0, h), & (\phi_0 + \Delta\phi, \lambda_0, h), \\ (\phi_0, \lambda_0 - \Delta\lambda, h), & (\phi_0, \lambda_0 + \Delta\lambda, h), & (\phi_0 + \Delta\phi, \lambda_0 + \Delta\lambda, h) \end{Bmatrix}$$

The full acceleration due to JGM-3 was computed for each interpolation point using Equation (4.1), the corresponding pseudo-centres were computed, and the pseudo-centre components were substituted into Equation (4.24). Accuracy assessment was made for p = 0.5, q = 0.5.

In general, the latitude grid $\Delta\phi$ depends on height. At h=100km smaller increments ($\Delta\phi = 0.5^{\circ}$) are required for $E(c_i < .2)$. However, at $h \geq$ 400km larger increments ($\Delta\phi = 1.0^{\circ}$) suffice.

4.5.2 Gravity Grid

The grid size is decided by the satellite trajectory that is projected on the Earth-fixed frame. Of course, this grid must cover the entire possible trajectory that the satellite would go through.

Table 4.3 Spacecraft trajectory ranges expressed in the ECEF frame.

	Radius Range (km)	**Latitude Range (degree)**	**Longitude Range (degree)**
T/P	7714 ~ 7718	-66 ~ 66	0 ~ 360
FEDSAT	7175 ~ 7186	-85 ~ 85	0 ~ 360
SACC	7075 ~ 7088	-82 ~ 82	0 ~ 360
CHAMP	6771 ~ 6808	-87 ~ 87	0 ~ 360

To achieve a satisfied interpolation result, a dense grid is needed. From the results of Section 4.2 and the last section, we can see that the acceleration depends more on the latitude than the longitude because the solid Earth is approximately symmetrical around the rotational axis. Thus we can use a larger grid in the longitude direction and a smaller one in the latitude direction. Furthermore, larger increments of longitude as latitude increases can reduce storage requirements. Instead of using a single grid size, we divided the whole Earth's surface into several bands with different grid sizes. In order to simplify indexing into the arrays holding the pseudo-centre coefficients, there is an overlap between sets of pseudo-centres coefficients. Only single precision (4 bytes) floating point values were used. The number of storage bytes needed for each latitude and longitude is calculated by:

Polynomial order × 3 pseudo-centre components × 4 bytes

Table 4.4 SAC-C gravitational acceleration approximation $1^\circ \times 1^\circ$ grid with order = 4.

	latitudes	$\Delta\lambda$	# lons	# lats	# bytes each	total bytes
1	$-85^\circ \sim -73^\circ$	3.0	122	13	48	76,128
2	$-75^\circ \sim -59^\circ$	2.0	182	17	48	148,512
3	$-61^\circ \sim -47^\circ$	1.5	242	15	48	174,240
4	$-49^\circ \sim 49^\circ$	1.0	362	99	48	1,720,224
5	$47^\circ \sim 61^\circ$	1.5	242	15	48	174,240
6	$59^\circ \sim 75^\circ$	2.0	182	17	48	148,512
7	$73^\circ \sim 85^\circ$	3.0	122	13	48	76,128
						2,517,984

4.5.3 Experiment Result

Previous experiments suggest a $10^{-9} \sim 10^{-10}$ m interpolation accuracy for the pseudo-centre position in the altitude direction. Then a $10^{-7} \sim 10^{-9}$ m pseudo-centre accuracy can be achieved after the final sphere interpolation. The acceleration then can be recovered through Equations (4.13) and (4.22). In this section, the acceleration was recovered using this method at three small $0.5^\circ \times 0.5^\circ$ zones:

I: $\lambda = 0^\circ \sim 20^\circ;\quad \varphi = 0^\circ \sim 10^\circ;\quad h = 7070 \sim 7080 km,\ \Delta h = 1 km$

II: $\lambda = 0^\circ \sim 20^\circ;\quad \varphi = 50^\circ \sim 60^\circ;\quad h = 7070 \sim 7080 km,\ \Delta h = 1 km$

III: $\lambda = 0^\circ \sim 20^\circ;\quad \varphi = 74^\circ \sim 84^\circ;\quad h = 7070 \sim 7080 km,\ \Delta h = 1 km$

The results were compared to the original calculated value.

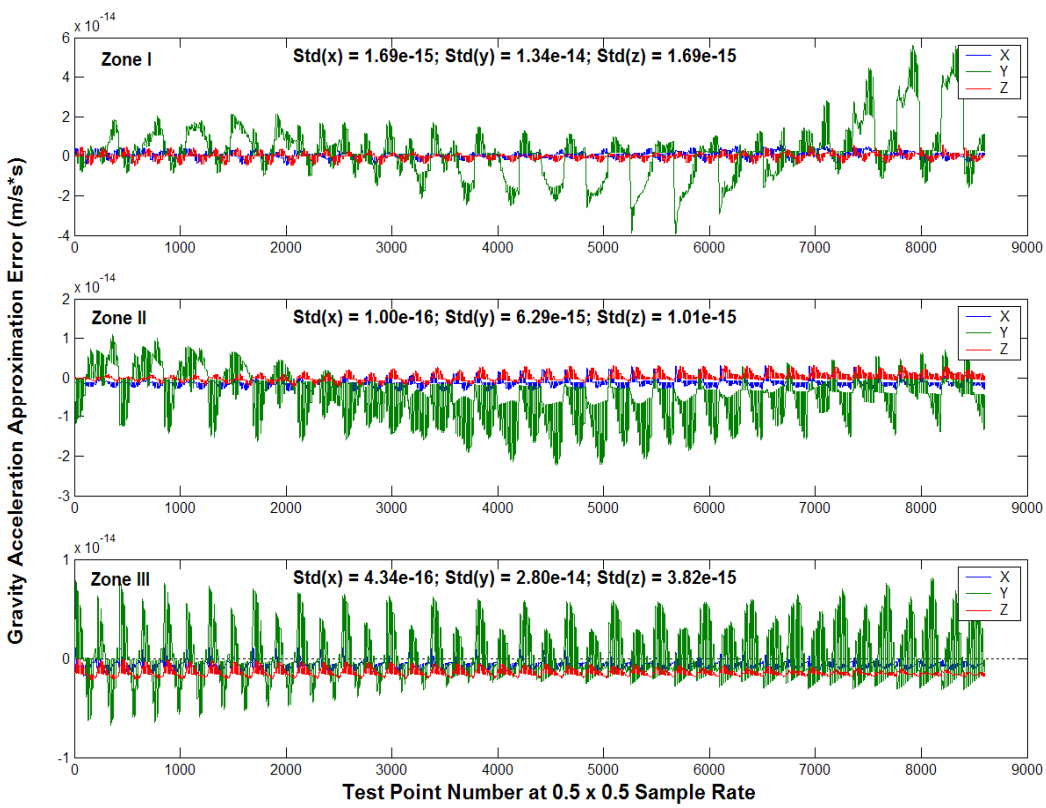

Figure 4.10 Gravity acceleration interpolation accuracy compared with the rigorously calculated value.

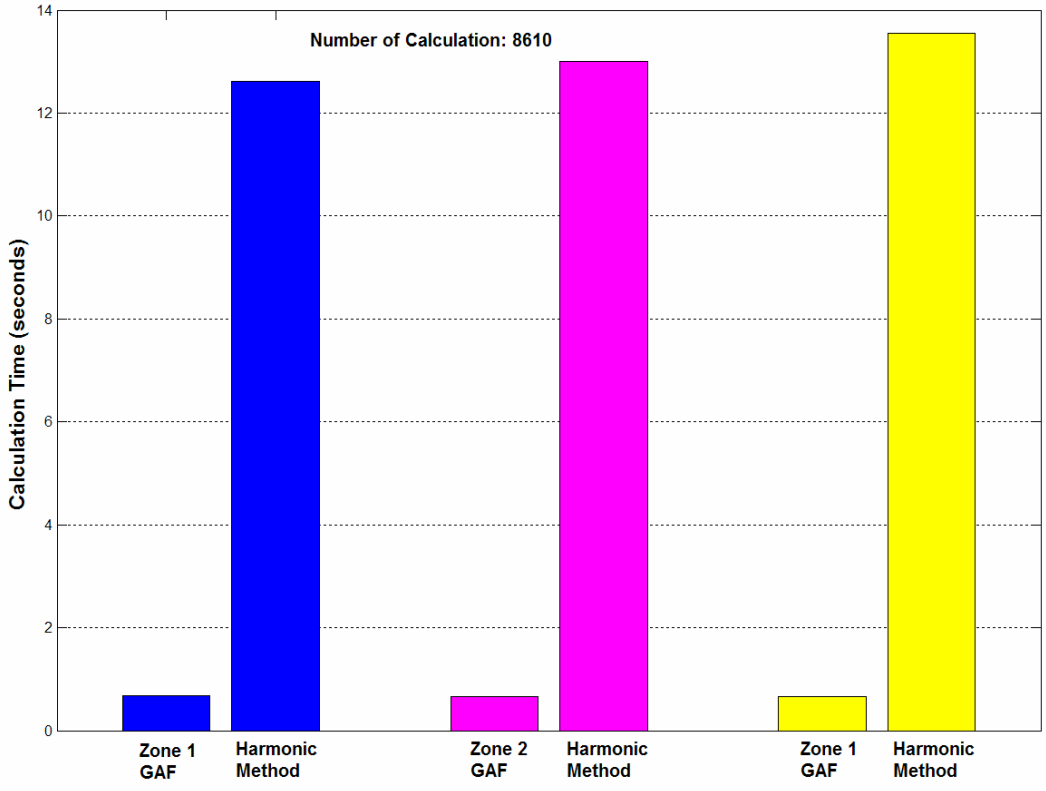

Figure 4.11 Computing time compared with the spherical harmonic method.

The gravity acceleration recovery error is around $10^{-14} \sim 10^{-16} m/s^2$, of the order of the gravity attraction from the planet Neptune. On the other hand, the computational burden is much less than the traditional method using a 70×70 Earth gravity model.

4.6 Accuracy Analysis for Complete Algorithms

There are two ways to assess the end-to-end accuracy of the algorithm. One way is to implement it in ephemeris integration and to compare ephemeris accuracies. The second method is a systematic search over the Earth, evaluating the acceleration accuracy at a great number of latitudes, longitudes, and heights, and comparing the approximation to that from the complete model. Having tested the latter in the previous section, this section will present the results from the first type of test.

4.6.1 Accuracy Analysis

A test was implemented to step through all longitudes and latitudes, on a representative grid, and at each selected longitude (λ_0) and latitude (ϕ_0) to define a local grid of six points, as described earlier. This analysis was performed once for an interpolation domain of $\Delta\phi = 0.5^\circ$, $\Delta\lambda = \Delta\phi / \cos\phi$ (constrained to $|\Delta\lambda| < 5^\circ$ and again for $\Delta\phi = 1.0^\circ$. The search grid over the northern hemisphere of latitude $\phi_0 \in \{-85^\circ, 85^\circ\}$ and longitude $\lambda_0 \in \{0^\circ, ..., 359.5^\circ\}$. Not all points on the Earth were evaluated. The evaluation grid was 5° in latitude and 10° in longitude.

In general the worst-case error statistic (Equation (4.18)) at any test point (ϕ_0, λ_0) was found at a height of 7090km, where JGM-3 errors are smallest, and therefore more difficult to satisfy. Worst-case error statistics for $E(c_i)$ were generally less the 0.2 over the entire northern hemisphere. In a few cases where $E(c_i) \approx 0.5$, it appears that the least squares solution for a_j and b_j in Equation (4.22) converges to a relative minimum instead of the absolute minimum. If the accuracy criterion is $E(c_i) < .1$, then $\Delta\phi = 0.5^\circ$ is required. However, relaxing the criterion to $E(c_i) < .2$, allows $\Delta\phi = 1.0^\circ$, which greatly reduces storage requirements.

4.6.2 Orbit Integration Using the Gravity Acceleration Approximation Method

From Section 4.5.3 we can see that the recovered gravitational acceleration is at the $10^{-14} \sim 10^{-16} m/s^2$ level. This error is a high-order perturbation and can be neglected for most applications. However, the method must be validated through a real orbit integration test. This is critical because the cumulative effect of random errors introduced by these approximations is not known.

As discussed in Chapter 3, the simplified method achieves metres level accuracy for short-arcs, compared to using a full model. In this test we replace the truncated 30×30 gravity model with the proposed gravity acceleration method. A 6^{th} order polynomial generated $1^\circ \times 1^\circ$ gravitational acceleration grid for SACC was used. Figure 4.12 illustrates the accuracy of 1 day's orbit integration using a 30×30 gravity model and the gravity approximation method, with the results compared to the 70×70 full model. We can see great improvement in orbit integration.

In addition, we compared the computational burden of orbit integration with 70×70 gravity model, with 30×30 gravity model and the gravity approximation method. Figure 4.13 illustrates the result.

We found that the Gravity Acceleration Approximation Method reduced computing time by around 800% compared to the 70×70 gravity model, with a small memory usage increase.

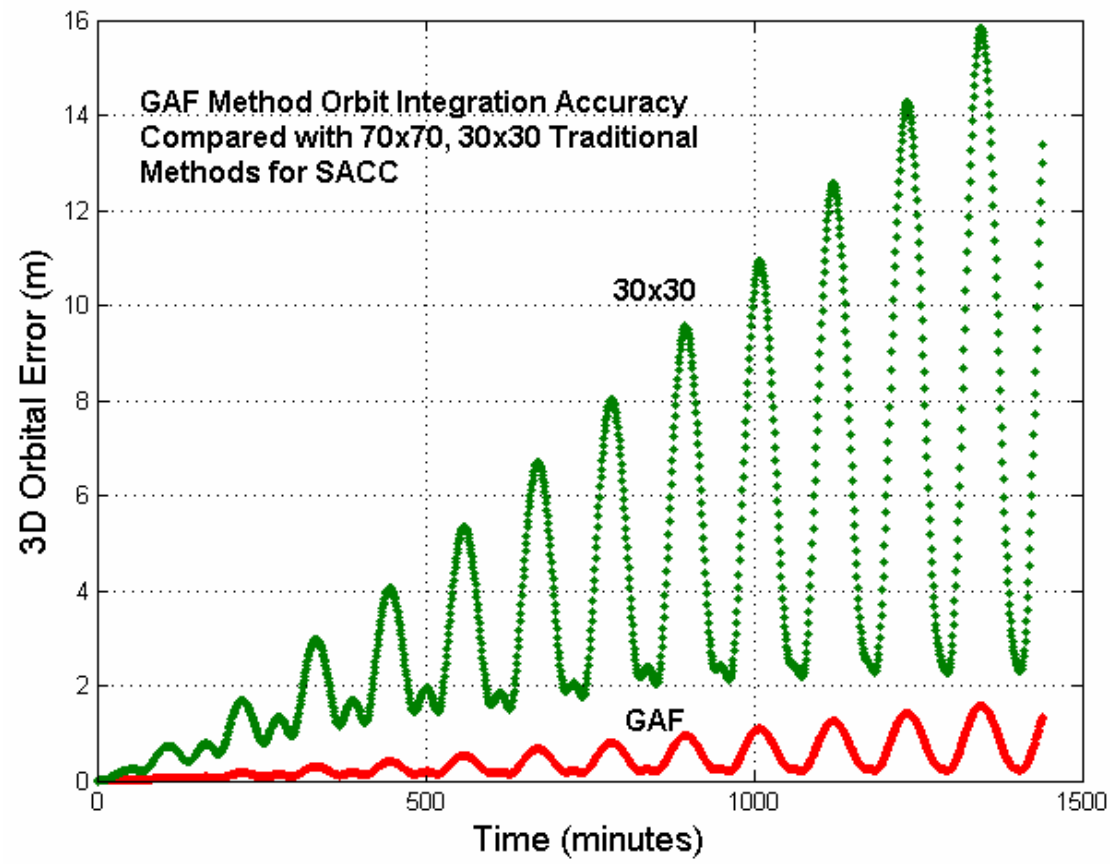

Figure 4.12 Comparison of orbit integration accuracy between Gravity Approximation Method (GAF) with the traditional method.

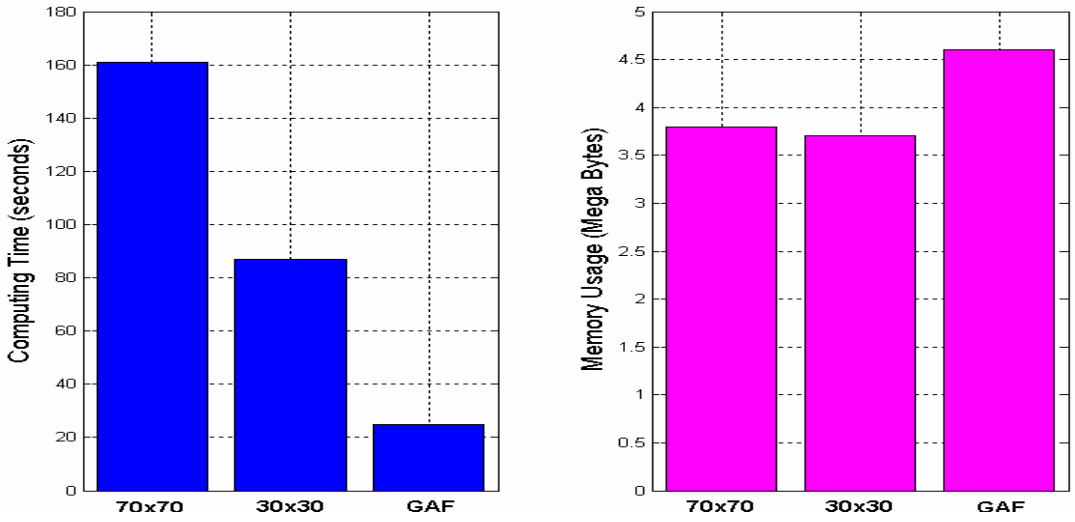

Figure 4.13 Comparison of computational burden between Gravity Approximation Method (GAF) with the traditional method.

4.7 Computional and Storage Requirements

4.7.1 Computional Burden

The computational burden for each step in calculating gravity acceleration discussed in each section above is now summarized in Table 4.5

Table 4.5 GAF method calculation burden summary.

Calculation	Multiplications	Additions
C20 recovery (Equation 4.18)	38	15
Six-point interpolation (Equation 4.19)	62	46
4^{th} order polynomial (Equation 4.16)	127	110
Total	**227**	**171**

This computational burden is comparable to the computational overhead of a 5×5 acceleration model, with a margin for computing indices into the tables, loop indexing, and decision functions. The following were calculated from one programmer's implementation of Equation (4.1) and the associated support calculations (including recursive generation of Legendre polynomial evaluations):

Table 4.6 Calculation burden summary for spherical harmonic calculation.

Degree and Order	Multiplications	Additions
4×4	184	134
5×5	236	198
6×6	356	286
8×8	576	438
12×12	1160	902
30×30	6164	4970

These calculations assume that $r,\phi,\lambda,\cos\phi,\sin\phi,\cos\lambda,\sin\lambda$ are available as common input to both methods and that conversion of the output accelerations between the ECI and ECEF frame is external to both methods.

4.7.2 Storage Requirements for Complete Algorithm

The storage strategy has a direct bearing on the storage penalty for the Gravitational Acceleration Approximation Method implementation. It also has a direct bearing on the RAM requirements for exploiting this algorithm. The following seeks to take

advantage of a larger bin size in longitude $(\Delta\lambda)$ at higher latitudes, while holding the latitude bins fixed at 0.5° or 1.0°, as studied above.

The storage strategy identifies broad latitude bands within which the longitude bin size $(\Delta\lambda)$ is constant. These bands necessarily overlap because the interpolator uses three latitude values $(\phi_0 - \Delta\phi, \phi_0, \phi_0 + \Delta\phi)$. Furthermore, to reduce the complexity of computing an index into the table, the longitude grid extends from $-\Delta\lambda$ to (or beyond) 360°. When the longitude increment $\Delta\lambda$ exactly divides 360°, then the longitude grid terminates at 360°, otherwise the longitude grid extends one point beyond 360°.

There is only one point at either pole, and the equator is duplicated in adjacent northern hemisphere and southern hemisphere tables. This is because the increment to latitude $(\Delta\phi)$ is negative in the southern hemisphere. Again it was decided to duplicate the equator (and one latitude increment) in these tables to reduce complexity in indexing the table.

The polynomial coefficients a_j and b_j in Equation (4.22) are stored as "single precision" floating point variables (unformatted). The storage penalty for each (ϕ_0, λ_0) in the table is:

3 components of pseudo-centre × **4** coefficients × 4 bytes = **48** bytes

This storage scheme is not optimized for latitude band selection and some additional saving are possible.

4.8 Summary

An alternative method to calculating the Earth gravity acceleration has been validated in this chapter. Instead of calculating the harmonic coefficient using the recursive algorithm, an Earth pseudo-centre grid was generated on the ground and a simple two-step interpolator was used to recover the gravity acceleration on-the-fly. Extensive testing was shown that:

- The Earth gravity acceleration changes smoothly in the altitude direction and can be easily recovered from a grid using 3~6 order polynomial interpolation; with the acceleration accuracy being around $10^{-16} \sim 10^{-18} m/s^2$.
- The Earth pseudo-centre can be recovered at the $10^{-9} \sim 10^{-10} m$ level in the altitude direction using a similar 3 ~ 6 order polynomial interpolation; while a final $10^{-7} \sim 10^{-9}$ m accuracy can be achieved after the spherical interpolation;
- The Earth gravity acceleration can be recovered at the $10^{-14} \sim 10^{-16} m/s^2$ accuracy level using a $1^\circ \times 1^\circ$ pseudo-centre grid. The computational burden is much less than for the conventional method.
- Using the Gravity Acceleration Approximation Method, the computational burden of orbit integration is equivalent to that of a 5×5 gravity model, but with the accuracy of a 70×70 model.

This method shows a great promise for onboard orbit determination. Though the results are very encouraging, more improvements can be made:

- There are alternatives in force model formulation which can be used to make special perturbations more computationally competitive, with semi-analytic and analytic techniques. This development is but one example. Elementary techniques have been used to generate a hundred-fold improvement in gravity acceleration computational efficiency, achieving 70×70 accuracy for the computational burden of a 5×5 model, with a storage penalty of 2.5 Mbytes. With some additional work there should be additional savings in both computational efficiency and in storage requirements.
- The storage penalty of 2.5 Mbytes is still not optimal. There are savings in simply using more latitude bands (e.g. smaller incremental changes in $\Delta\lambda$). An investigation of other functional forms is planned, including continued fractions, in an effort to reduce the number of coefficients to be stored.
- The computational burden is not optimal. The possibility of other function as forms in place of quotients of polynomials hints at other efficiencies.

Chapter 5
Quality Control and Improvement of Onboard GPS Measurement Processing

The quality of onboard GPS measurements and navigation solutions is normally worse than those obtained on the ground due to the harsh observation conditions in space. As a consequence, great care has to be taken to minimize the degradation of the measurement quality. This mostly concerns the process of outlier detection. In addition, if we take the GPS measurements at every sample epoch of 1 ~ 10 seconds directly to form the observation equations, the nominal orbit and partial derivations need to be generated at these epochs, which in turn results in a heavy computational load. To improve this situation, a sliding-window carrier-phase smoothing filer has been designed to generate a smoothed observable every several minutes. With no Selective Availability (SA) and an improvement of the broadcast ephemerides, this technique is reasonable and feasible. This chapter will focus on outlier detection and phase smoothing procedures to facilitate clean and compacted GPS data for efficient onboard orbit estimation.

5.1 GPS Code Measurement Models

GPS measurements include code-based pseudo-ranges, which are computed from measured transit time, and carrier phase-based ranges. Since these ranges are biased by satellite and receiver clock errors and other errors, they are called “pseudo-ranges”. In this context, onboard orbit determination is based on pseudo-range data, regardless of smoothing with carrier-phase or not. In the following subsections, we examine the error sources of the GPS code measurements.

5.1.1 Basic Zero-difference Code Observation Equations

The code measurement P_i^k from a spaceborne receiver to a GPS satellite can be modelled as:

$$P_i^k = \rho^k - C\delta t^k + C\delta t + \Delta\rho_{rel}^{k,i} + \Delta\rho_{ion}^{k,i} + \Delta\rho_{gps\_ant}^{k} + \Delta\rho_{ant} + \varepsilon_i^k \qquad (5.1)$$

where

i = subscript identifying the L_1 or L_2 frequency

k = subscript identifying different GPS satellite

ρ^k = geometic range between the GPS satellite k and the receiver

C = speed of light

δt^k = GPS satellite's clock error

δt = receiver's clock error

$\Delta\rho_{rel}^{k,i}$ = relativistic effect

$\Delta\rho_{ion}^{k,i}$ = ionospheric delay

$\Delta\rho_{gps\_ant}^{k}$ = GPS satellite antenna phase centre offset

$\Delta\rho_{ant}$ = Spacecraft GPS antenna phase centre offset

ε_i^k = random measurement noise of range

5.1.2 Ionospheric Delay

The ionosphere is a region of the Earth's upper atmosphere, approximately 100km to 20,000km above the surface, where electrons and ions are present in quantities sufficient to affect the propagation of radio waves. The path delay will be proportional to the number of electrons along the slant path between the satellite and the receiver, and the electron density distribution varies with altitude, time of day, time of year, solar and geomagnetic activity, and the time within the 11 year solar sunspot cycle. The magnitude of the ionospheric path delay depends on the frequency of the radio signal. The ionospheric bending on L_1 GPS measurements will vary from about 0.15m to 50m [*Clynch & Coco*, 1986]. However, more accurate corrections can be made by using the dual frequency ionosphere-free combination:

$$P_{IF} = \frac{f_1^2}{f_1^2 - f_2^2} P_1 - \frac{f_2^2}{f_1^2 - f_2^2} P_2 \tag{5.2}$$

where f_1 and f_2 are the frequency for the L_1 and L_2 carrier waves, respectively.

5.1.3 Relativistic Effect

The relativistic effects on GPS measurements can be summarized as follows. Due to the difference in the gravitational potential, the satellite clock tends to run faster than the ground station's [*Spilker*, 1978; *Gibson*, 1983]. These effects can be divided into two parts: a constant drift and a periodic effect. The constant drift can be removed by offsetting the GPS clock frequency a little lower before launch to account for that constant drift. The periodic relativistic effects can be modelled for a high-low measurement as:

$$\Delta\rho_{srel} = \frac{2}{C}(\mathbf{r}_s \cdot \mathbf{v}_s - \mathbf{r}_g \cdot \mathbf{v}_g) \tag{5.3}$$

where

$\Delta\rho_{srel}$ = correction for special relativity

C = speed of light

$\mathbf{r}_s, \mathbf{v}_s$ = the position and velocity of the LEO satellite or tracking stations

$\mathbf{r}_g, \mathbf{v}_g$ = the position and velocity of the GPS satellite

The coordinate speed of light is reduced when light passes near a massive body causing a time delay, which can be modelled as [*Holdridge*, 1967]

$$\Delta\rho_{grel} = (1+\gamma)\frac{GM_e}{C^2}\ln(\frac{r_{tr} + r_{rec} + \rho}{r_{tr} + r_{rec} - \rho}) \tag{5.4}$$

where

$\Delta\rho_{grel}$ = correction for general relativity

γ = the parametreized post-Newtonian (PPN) parametre (γ =1 for general relativity)

GM_e = gravitational constant for the Earth

ρ = the relativistically uncorrected range between the transmitter and the receiver

r_{tr} = the geocentric radial distance of the transmitter

r_{rec} = the geocentric radial distance of the receiver

The total relativity correction is:

$$\Delta\rho_{rel} = \Delta\rho_{srel} + \Delta\rho_{grel} \tag{5.5}$$

5.1.4 GPS Satellite Antenna Phase Centre Offset

Satellite antenna phase centre offsets must be dealt with appropriately. These offsets are given in the same satellite-fixed coordinate system that is also used to express solar radiation pressure. Starting on 1998-Nov-29 (GPS Week 986, day 0) the IGS products incorporated the antenna phase centre offsets given in Table 2.1. The origin of the coordinate system is at the satellite's centre of mass, the *k*-axis points toward the Earth centre, the *j*-axis points along the solar panel axis, the *i*-axis completes the right-handed coordinate system and lies in the Sun-satellite-Earth plane.

Table 5.1 GPS satellite antenna phase centre offset values adopted by IGS.

Block II/IIA:	(0.279m, 0.000m, 1.023m)
Block IIR:	(0.000m, 0.000m, 0.000m)

The offset then can be described in Earth-Centred and Earth-Fixed (ECEF) frame as:

$$\Delta\boldsymbol{\rho}_{gps\_ant} = (\hat{\mathbf{i}}, \hat{\mathbf{j}}, \hat{\mathbf{k}})^{-1}\mathbf{O}^{\mathbf{T}} \tag{5.6}$$

where $(\hat{\mathbf{i}}, \hat{\mathbf{j}}, \hat{\mathbf{k}})$ is the unit vector of the coordinate system. **O** is the antenna phase centre offset given in Table 5.1.

5.1.5 LEO GPS Receiver Antenna Phase Centre Offset

For the GPS receiver onboard a satellite, the antenna offset also must be dealt with. The orbit integration equations are solved for using the inertial, Cartesian J2000 system. That means the satellite trajectory is represented by the movement of the mass centre of the satellite. To account for the GPS antenna offset, the offset must be transferred from different spacecraft coordinate systems to the inertial system. The spacecraft coordinate system includes Height-Crosstrack-Alongtrack (HCL) system, Earth-Probe-Sun (EPS) system, UVW system, etc. This depends on different missions.

Table 5.2 Spacecraft GPS receiver antenna phase centre offset values.

Mission	Coordinate System	Antenna offset (mm)
Topex / Poseidon	Body-fixed HCL system	(4700.0, 1947.0, 41.0)
SACC	Body-fixed HCL system	(810.8, -345.0, -29.4)
CHAMP	Body-fixed HCL system	(-1488.0, 0.0, -392.0)
FedSat	Body-fixed HCL system	(38.0, 24.0, 16.0)

5.1.6 Single-difference Code Observation Equation

The receiver's clock error δt is the biggest error source in Equation (5.1). The clock in a receiver is not as accurate as the one in the GPS satellite. A bias of 0.001 seconds equals approximately 300 kilometres error in length units. However, this error can be removed if we take a single-difference between different GPS satellites at the same epoch. In this way, the receiver clock is removed from the observable.

$$\Delta P_i^{k,j} = P_i^k - P_i^j = \Delta\rho^{k,j} + C(\delta t^k - \delta t^j) + \Delta E^{k,j} + \varepsilon_i^k - \varepsilon_i^j \qquad (5.7)$$

where:

$\Delta P_i^{k,j}$ = difference between two measurements from satellites k and j

$\Delta\rho_i^{k,j}$ = difference between two geometric distances

$\delta t^k, \delta t^j$ = clock error for satellite k and j

$\Delta E^{k,j}$ = residual system error

$\varepsilon_i^k - \varepsilon_i^j$ = measurement noise

On the other hand, the measurement noise $\varepsilon_i^k - \varepsilon_i^j$ will be $\sqrt{2}$ times larger than the zero-differenced data.

5.2 Outlier Detection

The proposed outlier detection method is a recursive filter that processes the un-differenced GPS measurements. The main problem when processing un-differenced GPS data is to reliably and automatically detect outliers in code observations. The data cleaning of differenced GPS data is much easier because many common error sources may be removed by forming the differences, in particular receiver and satellite clock errors. However, several algorithms have been developed which seem to be reasonably successful in "cleaning" zero-differenced GPS data. Similar to the TruboEdit program of GIPSY, the developed algorithm is suitable for the onboard short-arc filter.

The algorithm requires the use of dual-frequency code and phase observations. The major problem with this approach resides is that it depends heavily on the quality of the code observations. In particular, the noise of the code observations is assumed to be below 0.5 the wide-lane cycles, i.e., 43cm. This requirement is easily fulfilled if anti-spoofing (AS) is not active. For most state-of-the-art geodetic receivers the noise of the code observations under those conditions is at the 20cm level.

Each satellite is processed one-by-one in the following steps:

(1) Basic screening to delete the large outliers and delete short phase connect arcs.
(2) Screening of wide-lane linear combination for outliers and cycle slips.
(3) Screening of the difference between the code and phase ionosphere-free linear combinations. This screening is performed to remove bad observations, which were accepted in the wide-lane screening.

5.2.1 GPS Observation Linear Combinations

To process the un-differenced GPS data, the most useful method is to form different linear combinations using basic carrier phase and / or code measurements. The code and phase linear combination can be expressed as:

$$L_{m,n} = m * L_1 + n * L_2 \,,\; P_{m,n} = m * P_1 + n * P_2 \qquad (5.8)$$

Theoretically we can form an infinite number of these "artificial" observables with different *n* and *m*, but only very few of them are actually useful for the purpose of outlier detection, ambiguity fixing and reducing the ionospheric effect. Three properties of linear combination signals are the key points: the wavelength, ionospheric effect and the noise level.

The linear combinations of L_1 and L_2 GPS signals are usually performed to assist the cycle slip detection and cycle ambiguity resolution processes, and certain combinations can also be used to eliminate the first-order ionospheric effect. The linear combination of the phase's signal, which preserves the integer nature of the cycle ambiguity, can be formulated as follows (in cycle units):

$$\phi_{m,n} = m * \phi_1 + n * \phi_2 \qquad (5.9)$$

And the linear combination in length unit can be formulated as:

$$L_{m,n} = \lambda_{m,n} * f_{m,n} = \frac{m * f_1 * L_1 + n * f_2 * L_2}{m * f_1 + n * f_2} \tag{5.10}$$

The basic properties of the linear combination signal can be expressed as:

$$\begin{aligned} &\text{Frequency:} && f_{m,n} = m * f_1 + n * f_2 \\ &\text{Wavelength:} && 1/\lambda_{m,n} = m/\lambda_1 + n/\lambda_2 \\ &\text{Cycle Ambiguity:} && N_{m,n} = m * N_1 + n * N_2 \end{aligned} \tag{5.11}$$

The linear combination will not change the magnitude of the frequency-independent errors and biases, such as ephemeris error and tropospheric bias, but it will change the magnitude of the frequency-dependent errors and biases, such as ionospheric bias, noise, and multipath. The magnitude of the ionospheric effect on the linear combination is:

$$dion_{m,n} = \frac{m * f_1 * dion_1 + n * f_2 * dion_2}{m * f_1 + n * f_2} \tag{5.12}$$

where $dion_1$ and $dion_2$ are the magnitude of ionospheric effects on the L_1 and L_2 signals, respectively. The first-order ionospheric effects in length unit can be expressed as:

$$dion_1 = C / f_1^2,\ dion_2 = C / f_2^2 \tag{5.13}$$

where the C is a constant whose value is dependent on Slant Total Electron Content. Thus the Equation (5.11) can be written as:

$$dion_{m,n} = \frac{C}{f_1 * f_2} * \frac{m * f_2 + n * f_1}{m * f_1 + n * f_2} \tag{5.14}$$

The magnitude of the ionospheric effect on the linear combination can be written as function of the magnitude of the ionospheric effect on L_1 signal as:

$$dion_{m,n} = isf * dion_1, \quad isf = \frac{f_1}{f_2} * \frac{m * f_2 + n * f_1}{m * f_1 + n * f_2} \tag{5.15}$$

where the *isf* is the Ionospheric Scale Factor.

Furthermore, the linear combination process will also alter the noise level of the observations. If the noise in the L_1 and L_2 phases are characterized by the same

standard deviation in cycle units σ_ϕ, then the standard deviation of the linear combination phase in length units $\sigma(L_{n,m})$ can be written as:

$$\sigma(L_{m,n}) = \lambda_{m,n} * (m^2 + n^2)^{1/2} * \sigma_\phi \tag{5.16}$$

Based on the above equation, the noise level of the linear combination phase can be written as a function of the noise level of L_1 phase in length units:

$$\sigma(L_{m,n}) = nsf * \sigma(L_1), \quad nsf = \frac{\lambda_2 * (m^2 + n^2)^{1/2}}{m * \lambda_2 + n * \lambda_1} \tag{5.17}$$

where the *nsf* is the Noise Scale Factor.

Based on the above analysis, Figures 5.1 and 5.2 illustrate the wavelength, ionospheric scale factor and noise scale factor for different linear combinations. Table 5.3 lists some commonly used linear combinations.

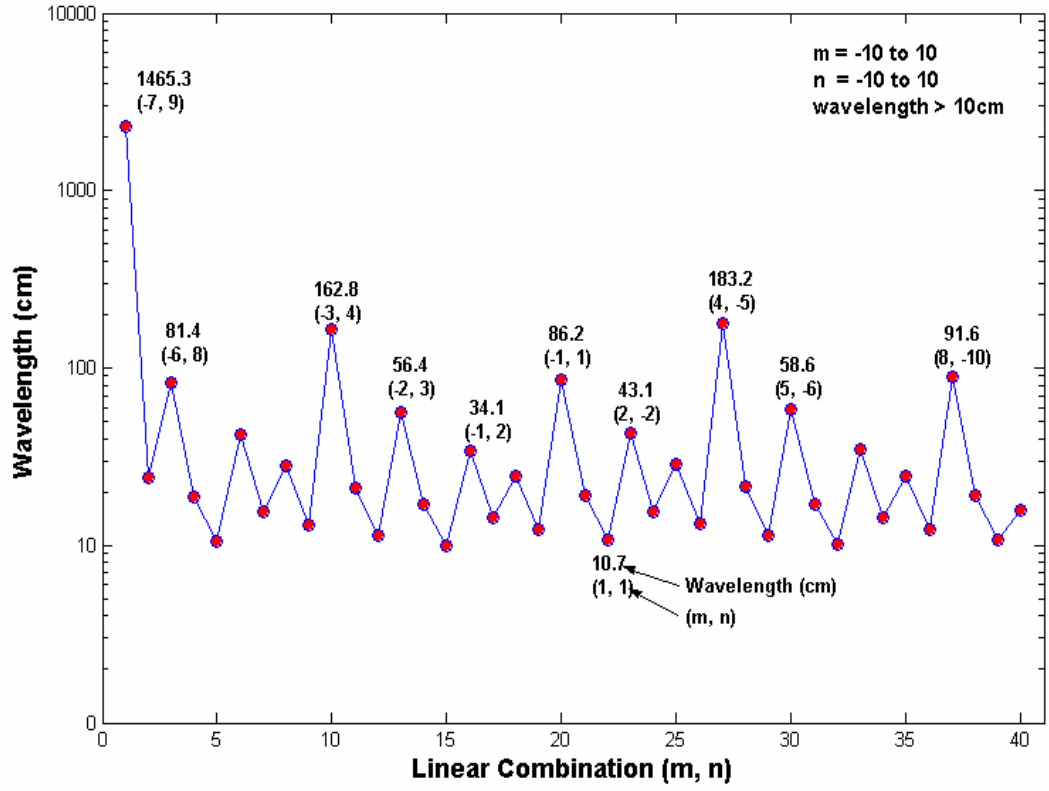

Figure 5.1 GPS observation linear combination property: wavelength.

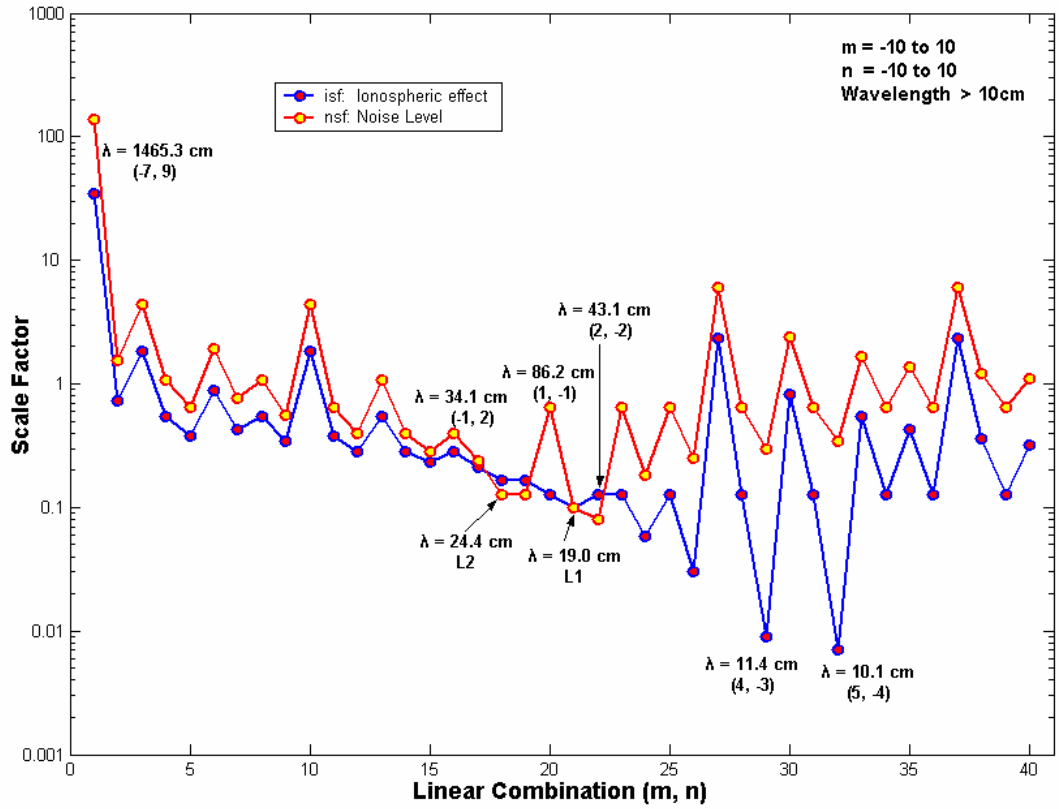

Figure 5.2 GPS observation linear combination property: Ionospheric & Noise Scale Factors.

Table 5.3 Some linear combinations of the GPS phase observables.

m	n	Wavelength (cm)	isf	nsf	description
-7	9	1465.3	350.4	877.9	
-3	4	162.8	18.2	42.8	Double wide-lane
-2	3	56.4	5.5	10.7	
-1	2	34.1	2.8	4.0	Semi wide-lane
0	1	24.4	1.6	1.3	L2 signal
1	-1	86.2	-1.3	6.4	Wide-lane
1	0	19.0	1.0	1.0	L1 signal
1	1	10.7	1.3	0.8	Narrow-lane
2	-2	43.1	-1.3	6.4	Half wide-lane
4	-3	11.4	0.09	3.0	Narrow-lane
5	-4	10.1	-0.07	3.4	Narrow-lane

5.2.2 Basic Screening

At this stage, unreasonable range and phase errors, such as negative range measurement and very big range values, are deleted. Normally these errors are caused by receiver malfunction. A set of criteria is established for different missions.

The most useful ones are $P_{\max}$ and $P_{\min}$, based on the geometry between spacecraft and GPS satellite:

$$P_{\max} = \alpha_1 \times (\sqrt{(H_{\max}^{S} + r_{earth})^2 - r_{earth}^{\ 2}} + \sqrt{(H_{\max}^{GPS} + r_{earth})^2 - r_{earth}^{\ 2}}) + P_{clock}$$
$$P_{\min} = \alpha_2 \times (H_{\min}^{GPS} - H_{\max}^{S}) - P_{clock} \tag{5.19}$$

Using an amplifier factor of 1.2 and 0.8 for $P_{\max}$ and $P_{\min}$, respectively. With a max of 300km clock error, we can derive the information in Table 5.4.

Table 5.4 Screening criterion for the P-code measurements.

	$P_{\max}$ (m)	$P_{\min}$ (m)
TOPEX	36,500,000	14,800,000
SACC	35,000,000	15,300,000
CHAMP	34,300,000	15,900,000
FEDSAT	35,200,000	15,200,000

The ionospheric delay can be expressed as the difference of the two P-codes:

$$\Delta\rho_{ion} = P_2 - P_1 \tag{5.20}$$

If the magnitude of any ionosphere combination is larger than a given value, both P_1 and P_2 will be deleted. The big value in this combination will either suggest a large ionospheric delay or simply an outlier. We can delete them in both cases. Typically a 15m value is used in our experiments.

Furthermore, another strict screening criterion is to delete any data within short phase-connect arc which is shorter than a given value. Experimentally we have found that an arc less than 1 ~ 2 minutes will lead to lots of outliers. A very short phase-connect arc is also not very useful in the phase smoothing process. But more attention should be paid when the measurement sample rate and the onboard GPS operational mode is unusual.

5.2.3 Data Screening Based On Wide-lane Combination

The wide-lane combination, which was called the Melbourne-Wübbena combination in early GPS literature, is a linear combination of both carrier-phase (L_1 and L_2) and P-code (P_1 and P_2) observables [*Wübbena*, 1985; *Melbourne*, 1985]. This

combination eliminates the effects of the ionosphere, geometry, clocks and the troposphere. It comes from the wide-lane combination of both code and phase measurement. The phase of the wide-lane combination is defined by the phase difference $\Phi_1 - \Phi_2$ (in cycles). Hence the wide-lane phase delay can be expressed as:

$$L_w \equiv -\Phi_w \lambda_w = \frac{f_1 L_1 - f_2 L_2}{f_1 - f_2} = \rho + d_{ion} f_1 f_2 / \left(f_1^2 - f_2^2\right) + \lambda_w b_w \qquad (5.21)$$

where the wide-lane wavelength is $\lambda_w \equiv c/\left(f_1 - f_2\right) \approx 86.2cm$, and the wide-lane bias is $b_w \equiv b_1 - b_2$, which is an integer number because both b_1 and b_2 are integers. Then the code wide-lane combination

$$P_w \equiv \frac{f_1 P_1 + f_2 P_2}{f_1 + f_2} = \rho + d_{ion} f_1 f_2 / \left(f_1^2 - f_2^2\right) \qquad (5.22)$$

That is, by subtracting Equation (5.20) from (5.19), the Melbourne-Wübbena combination can be expressed as:

$$L_w = \frac{1}{f_1 - f_2}(f_1 L_1 - f_2 L_2) - \frac{1}{f_1 + f_2}(f_1 P_1 + f_2 P_2) \qquad (5.23)$$

and we obtain the wide-lane bias

$$b_w = \frac{1}{\lambda_w}\left(L_w - P_w\right) \qquad (5.24)$$

Apart from the wide-lane ambiguity the remaining signal should be pure noise, with an RMS error of approximately 0.7 times the RMS of the code observations on the L_1 frequency. If the noise of the Melbourne-Wübbena combination has an RMS error below 0.5 wide-lane cycles (43cm) it is almost a trivial task to detect all cycle slips and outliers. Only very few epochs are needed to estimate the wide-lane ambiguity, and hence jumps and outliers can easily be detected. Of course, only the difference between the cycle slips on the two frequencies is detected $\left(n_w = n_1 - n_2\right)$. Note that in the very unlikely case where the integer number of cycle slips on the two frequencies is identical (i.e., $n_1 = n_2$) no cycle slip will be detected $\left(n_w = 0\right)$.

The best way to improve the reliability of screening data is to generate arcs as long as possible. An arc is defined by specifying a minimum number of continuous observations and a maximum time for data gaps. Typical values are a minimum of

10 data points per arc and a maximum of 3 minutes without observations before starting a new arc.

An onboard filter calculates time-averages of b_w both before and after a cycle slip or outlier, and the difference is required to be close to an integer. That is, an a priori RMS scatter σ of 0.5 wide-lane cycles is assumed, and the algorithm sequentially updates the averaged wide-lane biases and the RMS scatter, using the following recursive formulae:

$$\hat{b}_{w_i} = \hat{b}_{w_{i-1}} + \frac{1}{i}\left(b_{w_i} - \hat{b}_{w_{i-1}}\right) \tag{5.25a}$$

$$\sigma_i^2 = \sigma_{i-1}^2 + \frac{1}{i}\left[\left(b_{w_i} - \hat{b}_{w_{i-1}}\right)^2 - \sigma_{i-1}^2\right] \tag{5.25b}$$

where $\hat{b}_{w_i}$ is the mean wide-lane bias, and i is the current number of data points in the data arc. Subsequent epoch estimates $\hat{b}_{w_{i+1}}$ are required to lie within $4\sigma_i$ of the running mean $\hat{b}_{w_i}$. The filter deletes isolated outliers, and any two consecutive outliers within one cycle may indicate a cycle slip. Then, beginning with these two points, it starts a new average and continues time averaging until a new potential cycle-slip is discovered, and so on.

The critical data length required for a successful wide-lane phase connection is dependent on the pseudo-range precision and multipath. For currently available space GPS receivers it is as little as one minute before and after each cycle slip and outlier.

5.2.4 Data Screening Based On Ionosphere-Free Combination

We found that sometimes the data was not cleaned successfully due to systematic errors in the Melbourne-Wübbena combination. These systematic errors are most likely caused by the filtering and smoothing procedures employed in the receivers. Therefore, an additional data-screening step was added to the program. In this step we build the difference between ionosphere-free linear combinations for the phase and code observations:

$$L_I = \frac{1}{f_1^2 - f_2^2}(f_1^2 L_1 - f_2^2 L_2) - \frac{1}{f_1^2 - f_2^2}(f_1^2 P_1 - f_2^2 P_2) \qquad (5.26)$$

As in the case of the Melbourne-Wübbena combination this linear combination should consist of noise only. The disadvantage is the amplified noise (about 3 times the noise of the P_1 observations). The noise is thus about 4 times larger than the noise of the Melbourne-Wübbena combination. Nevertheless, the check is useful for removing errors caused by systematic effects. The check consists of an outlier rejection scheme, which is very similar to the one used for screening the Melbourne-Wübbena combination. The starting value for the maximum RMS is larger (typically 1.6 ~ 1.8 metres), to account for the higher noise of these observations.

5.3 Phase Smoothing Filter

5.3.1 Methodology

The application of the above procedures ensures the code and phase observations have been quality cleaned out. This enables us to now smooth the code observations, using carrier phase observations, for the continuous data arcs. For code smoothing it was decided to actually replace the code observations in a clean observation arc by the phase observations shifted by the mean difference code-phase in the arc. Of course, we have to account for the opposite sign of the ionospheric effect for the code and phase observations.

Briefly, carrier-phase-aided smoothing simply averages the point-by-point difference between the continuous phase measurements (which are extremely precise but have an arbitrary bias) and the simultaneously acquired pseudo-range measurements (which are far noisier but unbiased), thereby smoothing down pseudo-range noise over the averaging period to produce a precise estimate of the phase bias. With just a few minutes of averaging a 1-sec pseudo-range noise of 1m can be reduced to 10 ~ 20cm. (In general the noise reduction will not go as the square-root of the number of samples because of the low-frequency multipath error in the pseudo-range data.) The averaged phase-pseudo-range bias can then be added back to any phase point (or all

of them) to produce absolute pseudo-range measurements more precise than the original data.

For real time applications this smoothing can be carried out recursively to maintain a running current estimate of precise pseudo-range, an estimate that will improve with time as more points are averaged. If we let P_n denote the pseudo-range measurement acquired at time *n* and d_n the delta-range measurement between times *n-1* and *n* obtained from continuous carrier-phase, then the smoothed pseudo-range P_{n+1} at time *n+1* is given by:

$$P_{n+1} = \frac{n}{n+1}(P_n + d_{n+1}) + \frac{1}{n+1}P_{n+1} \qquad (5.27)$$

Intuitively we see that this simply averages the current pseudo-range value P_{n+1} in with the previously averaged value P_n that has been propagated forward with the current delta-range measurement d_{n+1} So long as phase is continuously tracked; there is no error growth from continuously propagating the current averaged pseudorange forward with delta range. This smoothing can therefore be carried out indefinitely while continuous phase lock is maintained. (If phase continuity is broken, the smoothing process may have to be restarted.) Note that since SA dither is identical on the carrier and pseudo-range, this technique does not smooth SA dither error, only measurement error. But since SA dither does not therefore interfere, this is the most effective way of smoothing and compressing pseudo-range over long periods and is used extensively in many GPS applications. The noise of the smoothed pseudo-range is decreased:

$$\delta^2(\overline{P}) = \frac{1}{n}\delta^2(P) \qquad (5.28)$$

5.3.2 Sliding-window Phase Smoothing

There are several ways to employ this kind of smoothing in real time operations. For the slow update process described here we can simply replace all 1 or 10 seconds pseudo-ranges acquired over the update interval (say, 300 measurements over 5 minutes) with the single smoothed pseudo-range produced at the end of the interval, and then restart the smoothing operation for the next interval (in order to maintain

independence of successive smoothed points). This greatly reduces the data rate (and the required processing time in direct proportion), frequency content in the long-term corrections) and leads to no loss of precision (since all acquired pseudo-range measurements go into the smoothed result). Where precise high rate data are required, such as for the fast corrections, one can simply carry out Equation (5.25) continuously and use the resulting smoothed pseudo-ranges at each 1-second time step. This will result in highly correlated absolute errors between successive smoothed points, while the relative point-to-point precision will approach that of pure carrier-phase. For our onboard short-arc method we used the first approach, which generates the smoothed pseudo-range data every 1 ~ 5 minutes.

For the slow updates the nominal update interval will be 5 minutes, but could be set to any value. This smoothing filter is a recursive estimator which processed the measurements sequentially, as they come in, and each full 5 minute measurement update requires just a small amount of additional computation.

5.4 Close-form Single Point Position Algorithm

5.4.1 Introduction

Traditionally because the observation equation related to a standard GPS point positioning is non-linear, a recursive least squares method is required to solve for the user position and receiver clock bias. An initial position estimate is always needed for this recursive method. Basically an estimate within 300km of the correct value is enough for a convergent solution. But for a high-speed space application, sometimes it is hard to obtain such a good initial coordinate value. Furthermore the short-arc processing also requires frequent re-initialization if the data is not available for a long arc. To solve this initialization problem a closed-form non-recursive single point position algorithm was proposed.

The quest for an analytical and non-iterative solution to the GPS absolute positioning problem has received much attention [*Abel* & *Chaffe*, 1991; *Bancroft*, 1985; *Chaffe* & *Abel*, 1994; *Grafarend* & *Shan*, 1997a, 1997b]. Many close-form formulas have

been proposed for a direct solution based on four GPS pseudo-range observations. The solution is exact as it uses only four measurements to solve for the four unknowns – the receiver's 3D position components and the clock bias of the GPS receiver.

5.4.2 Methodology

The observation equation for the pseudo-range measured between the receiver with unknown position $\mathbf{r} = (x, y, z)$, and the satellite i with known position $\mathbf{r}^i = (x^i, y^i, z^i)$, is given by [*Yang*, 1995; *Goad & Tang*, 1997]:

$$P^i = \sqrt{\left(x^i - x\right)^2 + \left(y^i - y\right)^2 + \left(z^i - z\right)^2} + c \cdot \delta T - c\delta T^i + e^i \qquad (5.29)$$

Equation (5.27) is a non-linear equation with multiple unknowns. The first term on the right-hand side is the geometric distance between the receiver and the satellite. The receiver clock error expressed in units of length is denoted as $c \cdot \delta t$, with c the speed of light in a vacuum. The satellite clock error is $c\delta t^i$ which, together with the satellite's position $\left(x^i, y^i, z^i\right)$, is available from the broadcast navigation message. The measurement noise is characterized by the error term ε^i .

In order to solve for the receiver's position (x, y, z) and clock error $c \cdot \delta t$, Equation (5.29) must undergo simplification. Since the satellite's clock error is known from the navigation message, it can be removed from the observation equation. It is also common practice to discard the ionospheric and tropospheric effects and the measurement noise. Thus, we obtain

$$P^i = \sqrt{\left(x^i - x\right)^2 + \left(y^i - y\right)^2 + \left(z^i - z\right)^2} + c \cdot \delta t \qquad (5.30)$$

There are four unknowns in Equation (5.29), so four pseudo-range measurements are needed to obtain a unique answer. Substituting b for $c \cdot \delta T$ and rewriting Equation (5.29) as:

$$P^i - b = \sqrt{\left(x^i - x\right)^2 + \left(y^i - y\right)^2 + \left(z^i - z\right)^2} \qquad (5.31)$$

leads to

$$\begin{aligned} P^{i\,2} - 2P^i b + b^2 &= \left(x^i - x\right)^2 + \left(y^i - y\right)^2 + \left(z^i - z\right)^2 \\ &= x^{i\,2} - 2x^i x + x^2 + y^{i\,2} - 2y^i y + y^2 + z^{i\,2} - 2z^i z + z^2 \end{aligned} \qquad (5.32)$$

or alternatively,

$$\begin{aligned}&\left(x^{i2}+y^{i2}+z^{i2}-P^{i2}\right)-2\left(x^{i}x+y^{i}y+z^{i}z-P^{i}b\right)\\&=-\left(x^{2}+y^{2}+z^{2}-b^{2}\right)\end{aligned} \tag{5.33}$$

Define the Lorentz inner product for 4-space as [*Bancroft*, 1985]:

$$\left\langle \mathbf{g},\mathbf{h}\right\rangle \equiv \mathbf{g}^{T}\mathbf{M}\mathbf{h} \tag{5.34}$$

with $\mathbf{g},\mathbf{h}\in R^{4}$ and a 4×4 matrix

$$\mathbf{M}_{4\times 4}=\begin{bmatrix}\mathbf{I}_{3\times 3} & 0\\ 0 & -1\end{bmatrix},\ \mathbf{M}^{-1}=\mathbf{M}=\mathbf{M}^{T} \tag{5.35}$$

It can be observed that

$$\left\langle \mathbf{M}\mathbf{g},\mathbf{M}\mathbf{h}\right\rangle \equiv \left\langle \mathbf{g},\mathbf{h}\right\rangle \tag{5.36}$$

Substituting Equation (5.34) into Equation (5.33), we obtain the following relationship:

$$\frac{1}{2}\left\langle \begin{bmatrix}\mathbf{r}^{i}\\ P^{i}\end{bmatrix},\begin{bmatrix}\mathbf{r}^{i}\\ P^{i}\end{bmatrix}\right\rangle -\left\langle \begin{bmatrix}\mathbf{r}^{i}\\ P^{i}\end{bmatrix},\begin{bmatrix}\mathbf{r}\\ b\end{bmatrix}\right\rangle +\frac{1}{2}\left\langle \begin{bmatrix}\mathbf{r}\\ b\end{bmatrix},\begin{bmatrix}\mathbf{r}\\ b\end{bmatrix}\right\rangle =0 \tag{5.37}$$

for each pseudorange measured to satellite *i*. Since four pseudo-range observations are required to solve for four unknowns, we can define the matrix **B** as:

$$\mathbf{B}=\begin{vmatrix}x^{1} & y^{1} & z^{1} & P^{1}\\ x^{2} & y^{2} & x^{2} & P^{2}\\ x^{3} & y^{3} & z^{3} & P^{3}\\ x^{4} & y^{4} & z^{4} & P^{4}\end{vmatrix} \tag{5.38}$$

Where (x^{i},y^{i},z^{i}) are the coordinates of the *i*-th satellite and P^{i} is the measured pseudo-range to satellite *i* (*i* = 1, 2, 3, 4). Then the four pseudo-range equations can be expressed as:

$$\boldsymbol{\alpha}-\mathbf{B}\mathbf{M}\begin{bmatrix}\mathbf{r}\\ b\end{bmatrix}+\Lambda\boldsymbol{\tau}=0 \tag{5.39}$$

where

$$\Lambda=\frac{1}{2}\left\langle \begin{bmatrix}\mathbf{r}\\ b\end{bmatrix},\begin{bmatrix}\mathbf{r}\\ b\end{bmatrix}\right\rangle,\ \text{and}\ \boldsymbol{\tau}=\begin{bmatrix}1\\ 1\\ 1\\ 1\end{bmatrix} \tag{5.40}$$

And $\boldsymbol{\alpha}$ is a 4×1 vector with

$$\alpha_i = \frac{1}{2}\left\langle \begin{bmatrix} \mathbf{r}^i \\ P^i \end{bmatrix}, \begin{bmatrix} \mathbf{r}^i \\ P^i \end{bmatrix} \right\rangle \tag{5.41}$$

Solving Equation (5.39) results in:

$$\begin{bmatrix} \mathbf{r} \\ b \end{bmatrix} = \mathbf{M}\mathbf{B}^{-1}\left(\Lambda\boldsymbol{\tau} + \boldsymbol{\alpha}\right) \tag{5.42}$$

Substituting Equations (5.36), (5.40) and (5.41) into (5.39) finally gives the following quadratic equation [*Bancroft*, 1985]:

$$\left\langle \mathbf{B}^{-1}\boldsymbol{\tau}, \mathbf{B}^{-1}\boldsymbol{\tau} \right\rangle \Lambda^2 + 2\left[\left\langle \mathbf{B}^{-1}\boldsymbol{\tau}, \mathbf{B}^{-1}\boldsymbol{\alpha} \right\rangle - 1\right]\Lambda + \left\langle \mathbf{B}^{-1}\boldsymbol{\alpha}, \mathbf{B}^{-1}\boldsymbol{\alpha} \right\rangle = 0 \tag{5.43}$$

Equation (5.41) is a quadratic system, so its solution produces two roots that correspond to two potential locations in space, only one of which is correct. Determining which location is the correct answer, however, requires additional information from other sources; for instance from the approximate position of the receiver, or preferably, from extra GPS satellites. The latter method will be discussed in the next section. We present here a simple method to check the valid solution.

5.4.3 Method using All Visible GPS Satellites

The quadratic system in Equation (5.41) yields two potential locations in space when only four pseudo-range measurements are used. If five or more satellites are available, then the resulting redundancy can be exploited to identify the correct location. With extra satellites, several sets of four measurements can be formed. Since each set will include the correct location in one of its two roots, we are able to single out the correct location in each four-measurement set by comparing the different location pairs. The final result is then obtained by averaging all suitable positions.

Unfortunately, the above procedure is somewhat clumsy and inconvenient. To expand Equation (5.39) so as to directly include more than four pseudo-range measurements we need to increase the dimension of the matrix **B** and the vectors $\boldsymbol{\alpha}$ and $\boldsymbol{\tau}$, with additional rows associated with the extra satellites. For the analytical solution to work, however, the dimension of the system must be reduced to four, and this can be achieved by multiplying the system by the matrix **B** as follows:

$$\mathbf{B}^T\boldsymbol{\alpha} - \mathbf{B}^T\mathbf{B}\mathbf{M}\begin{bmatrix}\mathbf{r}\\ b\end{bmatrix} + \mathbf{B}^T\Lambda\boldsymbol{\tau} = 0 \tag{5.44}$$

After similar derivation steps, the solution to Equation (5.44) takes the following form [*Goad, et al.*, 1996]:

$$\left\langle \left(\mathbf{B}^T\mathbf{B}\right)^{-1}\mathbf{B}^T\boldsymbol{\tau}, \left(\mathbf{B}^T\mathbf{B}\right)^{-1}\mathbf{B}^T\boldsymbol{\tau} \right\rangle \Lambda^2 + 2\left[\left\langle \left(\mathbf{B}^T\mathbf{B}\right)^{-1}\mathbf{B}^T\boldsymbol{\tau}, \left(\mathbf{B}^T\mathbf{B}\right)^{-1}\mathbf{B}^T\boldsymbol{\alpha} \right\rangle - 1 \right]\Lambda + \left\langle \left(\mathbf{B}^T\mathbf{B}\right)^{-1}\mathbf{B}^T\boldsymbol{\alpha}, \left(\mathbf{B}^T\mathbf{B}\right)^{-1}\mathbf{B}^T\boldsymbol{\alpha} \right\rangle = 0 \tag{5.45}$$

It is noticed that the solution to Equation (5.43) incorporates all available pseudorange measurements in a least squares sense, as the coefficients of the quadratic equation are now minimum two-norm values, i.e., the sum of squares of the coefficients is minimum. However, the solution is different from the usual least squares solution given by the traditional iterative procedure which on the other hand, generates minimum two-norm pseudo-range residuals.

5.5 Experiment Studies

5.5.1 Experiment Description

The purposes of the experimental study are threefold:

- to explore the spaceborne GPS measurement quality and test the outlier detection algorithm;
- to validate the proposed closed-form SPP algorithm;
- to assess the accuracy of phase smoothing and validate the sliding-window method.

In all the following experiments, three day GPS data from SAC-C (14 to16 February, 2002) was used. All the data are SA-free dual-frequency measurements. Table 5.5 gives the GPS data overview. All the results are compared to the JPL ephemrides, which has centimetre level accuray.

Table 5.5 SAC-C GPS data overview of day 045, 046 and 047 of 2002.

	Sample rate (s)	Measurement type	Epochs	Observations	SVs < 4	Average SVs
SACC (04502~04702)	10	$P_1 / P_2 / L_1 / L_2$	25,860	200,138	45 (131) = 0.1%	7.7

5.5.2 Observation Linear Combination and Outlier Detection

Several important linear combinations describe in Section 5.2.1 were studied to detect outliers and cycle slips.

5.5.2.1 P-code Geometry Combination for Ionospheric Delay

Theoretically, the ionospheric delay can be expressed by $\Delta\rho_{ion} = P_2 - P_1$. If the ionospheric delay derived from this expression is very large, it suggests the presence of an outlier. Table 5.6 lists the ionospheric delay for all satellites in view. We found most delays (98.4%) are below 5 metres, which is quite reasonable. We also find that 0.8% data has a RMS of 209840m. Without deleting these large outliers, the overall RMS is 25057m. After deleting these 6644 measurements, we obtained an overall RMS of 2.73m. The result suggests we should delete any measurements with larger than 15m ionospheric delay.

Table 5.6 Statistics of ionospheric delay for all the satellites.

	Percentage (number)	RMS (m)
$\leq$ **2** *m*	9.6% (79,335)	1.37
$\leq$ **5** *m*	98.4% (813,879)	2.48
$\leq$ **15** *m*	99.2% (820,876)	2.73
> 15m	0.8% (6,644)	209840
All	827,520	25057

Figure 5.3 shows the ionospheric delay for SV5 and SV28. Big outliers were seen for both satellites. These unreasonable measurements should be deleted.

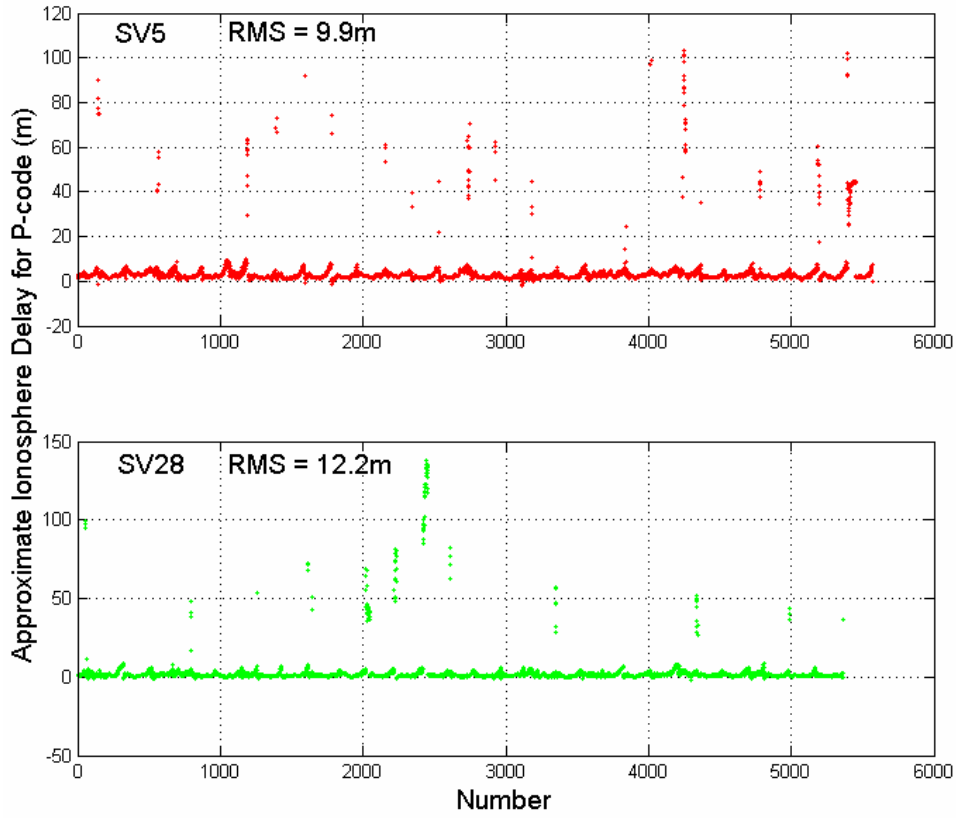

Figure 5.3 Ionospheric delay for SV5 and SV28.

5.5.2.2 Melbourne-Wübbena Combination

As discussed in Section 5.2.3, this combination eliminates the effects of the ionosphere, geometry, clocks and the troposphere. It comes from the wide-lane combination of both the code and phase measurements. If a discrepancy was found during the recursive checking described in Equation (5.23) it was labelled either an outlier or cycle slip. Figure 5.4 shows the Melbourne-Wübbena combination for SV5. Among all of these points with larger error we can see that there are some scattered points which indicate outliers, while the continuous outliers indicate a cycle slip. This is a quite straightforward detection method that is good for onboard processing. In Figure 5.4 we labelled three cycle slips and label all the other points beyond $4\sigma_i$ values as outliers. Then the outliers were removed from the raw measurements. The cycle slips can simply be fixed by the RMS difference and a low weight will be attached to these fixed measurements in the following processing. If the most stable situation is required just remove the cycle slip affected data as well.

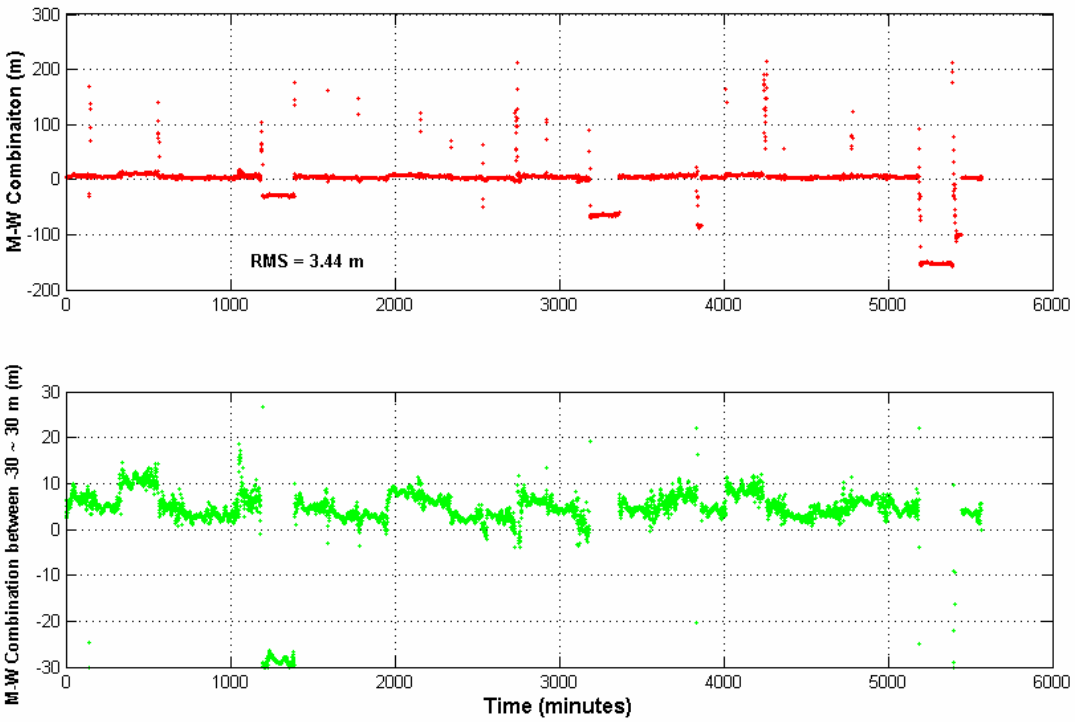

Figure 5.4 Melbourne-Wübbena combination residual of SV5.

5.5.2.3 Ionosphere-Free Linear Combination

This linear combination should consist of noise only. Though the noise is about four times larger than that of the Melbourne-Wübbena combination, it is useful to detect some system error neglected by other detection steps. Figure 5.5 shows the result from SV5, we only found one outlier in segment IV, where the far right point has a value that exceeds $4\sigma_i = 5.3\,\text{m}$.

5.5.2.4 Summary

During this experiment, several outlier detection methods were tested; Table 5.7 gives the detected outlier statistics from different methods. We found 11% measurements have been removed, which is a high percentage for some. But we can adjust three detection-control values: phase-link arc length, ionospheric delay threshold, and P-code noise, to allow more measurement, to pass the detection process.

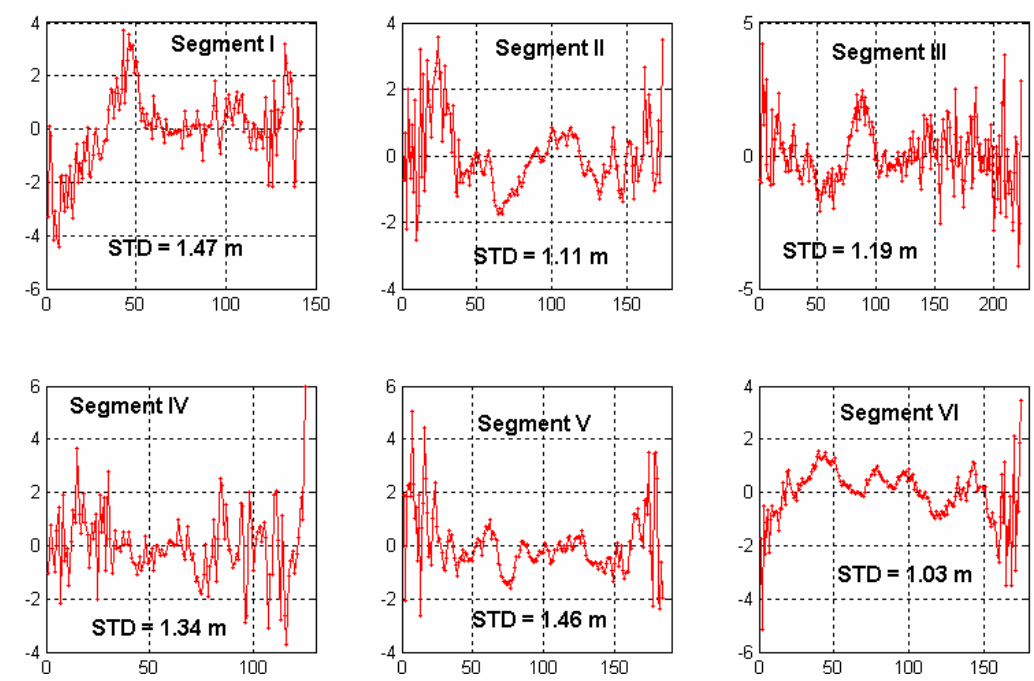

Figure 5.5 Ionosphere-free linear combination for SV5.

Table 5.7 Outlier detection summary.

	Number of outliers	Percentage
Errors	2	0.0%
Short phase-link arc	2458	1.2%
Ionosphere delay	13648	6.8%
Melbourne-Wübbena Combination	1565	0.8%
Ionosphere-free combination	57	0.0%
P-code noise check	4473	2.2%
Overall	22203 (200140)	11.1%

5.5.3 Code Measurement Quality and Residual Analysis

After the outlier detection process in previous experiments, a “clean” GPS data set was obtained. In this section the quality of the code measurement was inspected by means of the single point positioning results and the residuals.

5.5.3.1. Single Point Positioning Result

Both the broadcast ephemerides and IGS ephemerides were used to produce SPP solutions using SACC flight data. Figure 5.6 illustrates the 3D position RMS error of 6.8m and 4.9m for the broadcast ephemerides and IGS solutions, respectively. These

results are reasonable. Figure 5.7 gives the GDOP and satellite visibility. Figure 5.8 shows the receiver GPS clock bias derived from the SPP solution.

5.5.3.2 P-code Noise

After the system errors have been removed from the GPS measurements, the positional accuracy is determined by the measurement noise and geometry only. The measurement noise includes the signal noise, hardware noise and multipath effect. In this chapter, the noise of both P_1 and P_2 were inspected using the following expression [*Zhou, et al.*, 2003]:

$$PM_{1t} = \left(P_{1t+1} - P_{1t}\right) - \lambda_1\left(L_{1t+1} - L_{1t}\right),$$
$$PM_{2t} = \left(P_{2t+1} - P_{2t}\right) - \lambda_2\left(L_{2t+1} - L_{2t}\right) \qquad t = 0, 1, 2\ldots \qquad (5.46)$$

Here λ_1 = 0.1903 metres for the frequency of f_1 (1575.42 *MHz*), and λ_2 = 0.2442 metres for the frequency of f_1 (1227.60 *MHz*). PM_{1t} and PM_{2t} mainly contain receiver noise and multipath errors. The standard deviations of the observations P_1 and P_2 are given as:

$$\sigma_{P1} = \sqrt{\frac{\sigma^2_{PM_1}}{2}}, \qquad \sigma_{P2} = \sqrt{\frac{\sigma^2_{PM_2}}{2}} \qquad (5.47)$$

There are 28 satellites in view over these three days. Table 5.8 gives the statistics of PM_1 and PM_2 from a set of 24h SAC-C data on day 045~047, 2002. Figure 5.9 shows that the RMS is 39.5cm and 32.8cm for P_1 and P_2, respectively. Figure 5.10 illustrates the relationship between measurement noise and elevation angle. We found larger noise when the elevation angle was lower than 25 degree. The overall RMS value is 23.5cm when measurements were only collected from elevations higher than 25 degree, which is 16cm less than that of all data considered.

Table 5.8 Overall P-code noise statistics for all satellites.

	<=0.2m	**<=0.5m**	**<=1.0m**	**<=2.0m**	**<=5.0m**	**>5.0m**
PM_1	64.1% 9.7cm	86.9% 18.7cm	96.3% 28.2cm	99.7% 37.1cm	100% 39.5cm	0
PM_2	64.9% 9.9cm	90.1% 19.1cm	98.2% 26.9cm	99.9% 31.4cm	100% 32.8cm	0

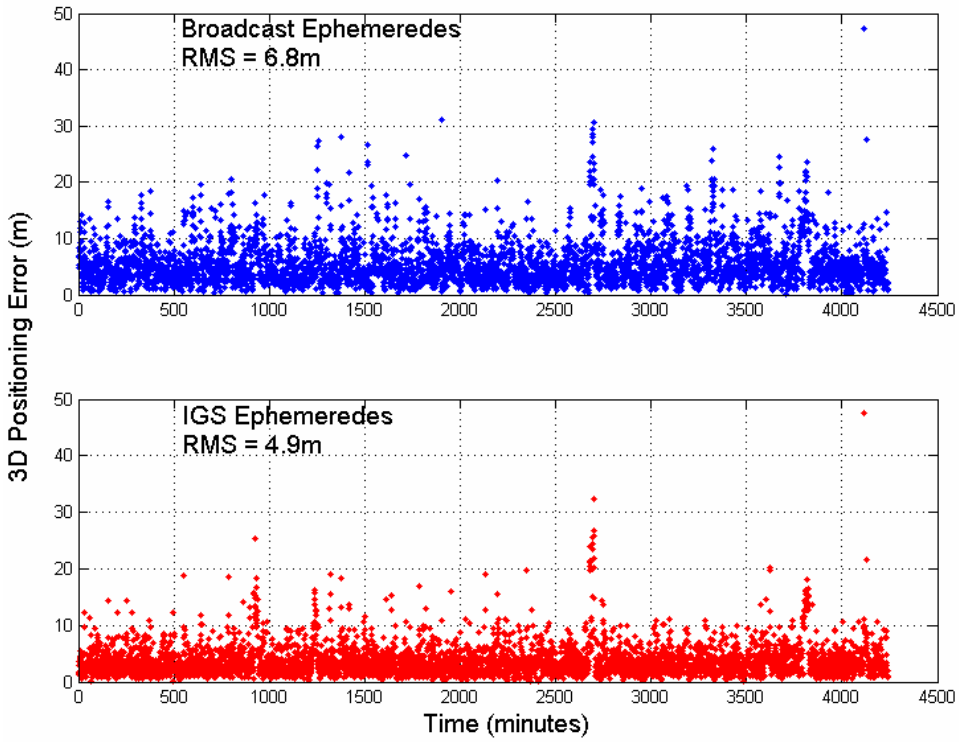

Figure 5.6 Single Point Positioning (SPP) results from SAC-C data of three days (04502 ~ 04702).

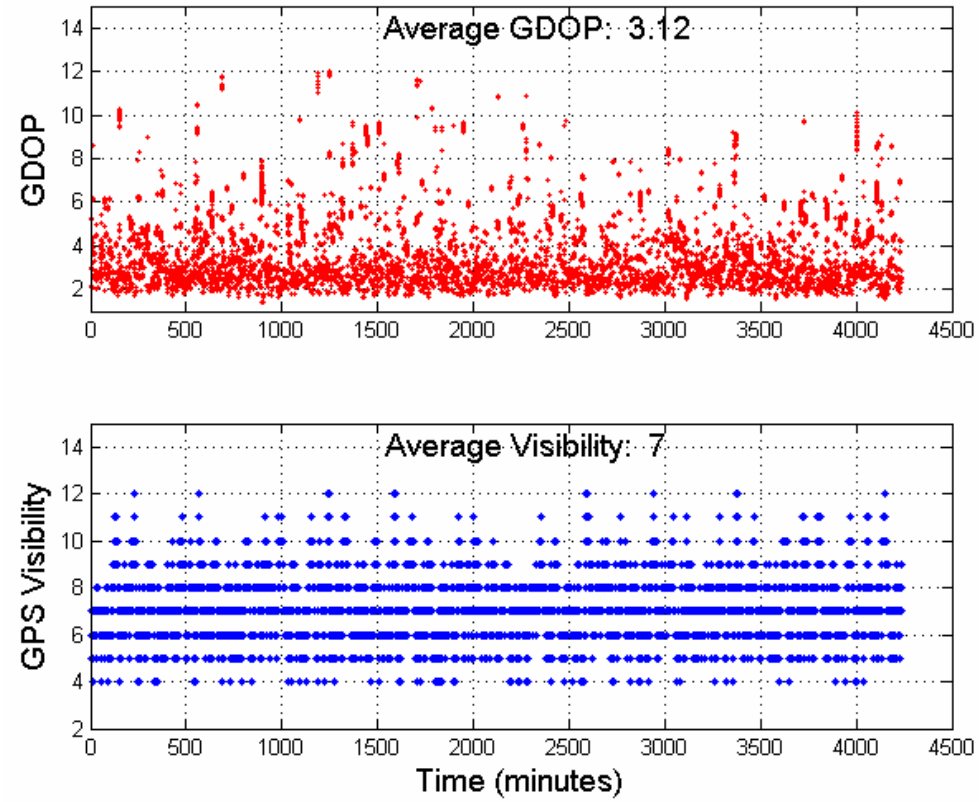

Figure 5.7 GDOP (with a cut-off value of 12) and GPS satellite visibility.

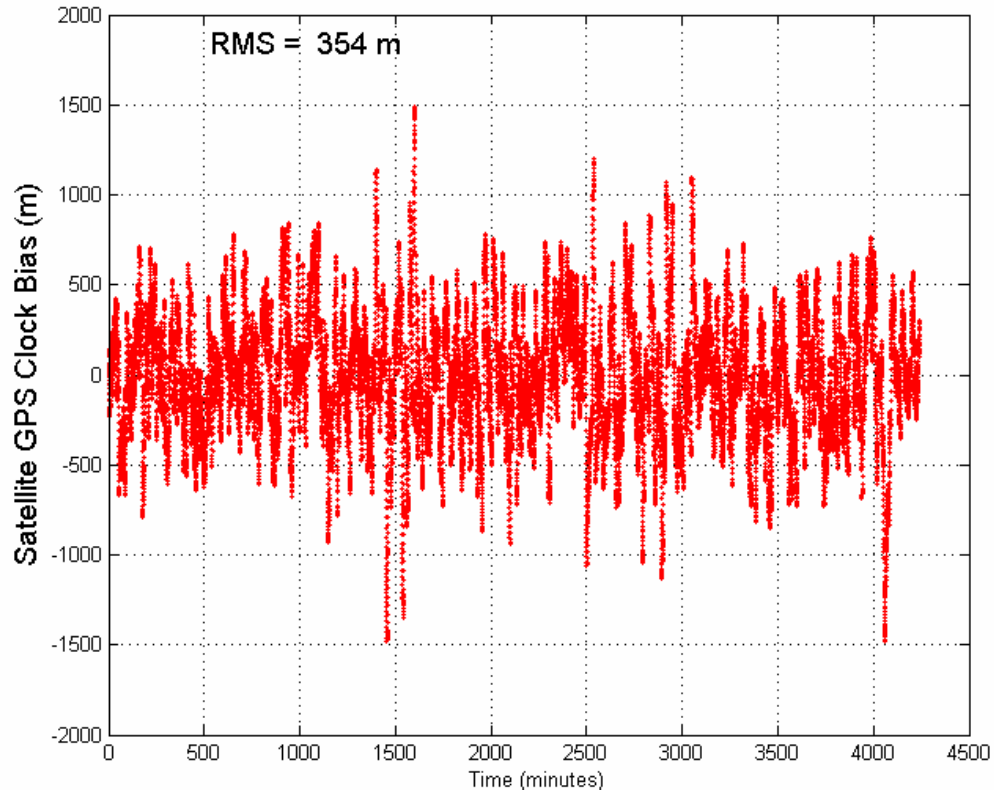

Figure 5.8 SACC-C GPS clock drift over three days (04502 ~04702).

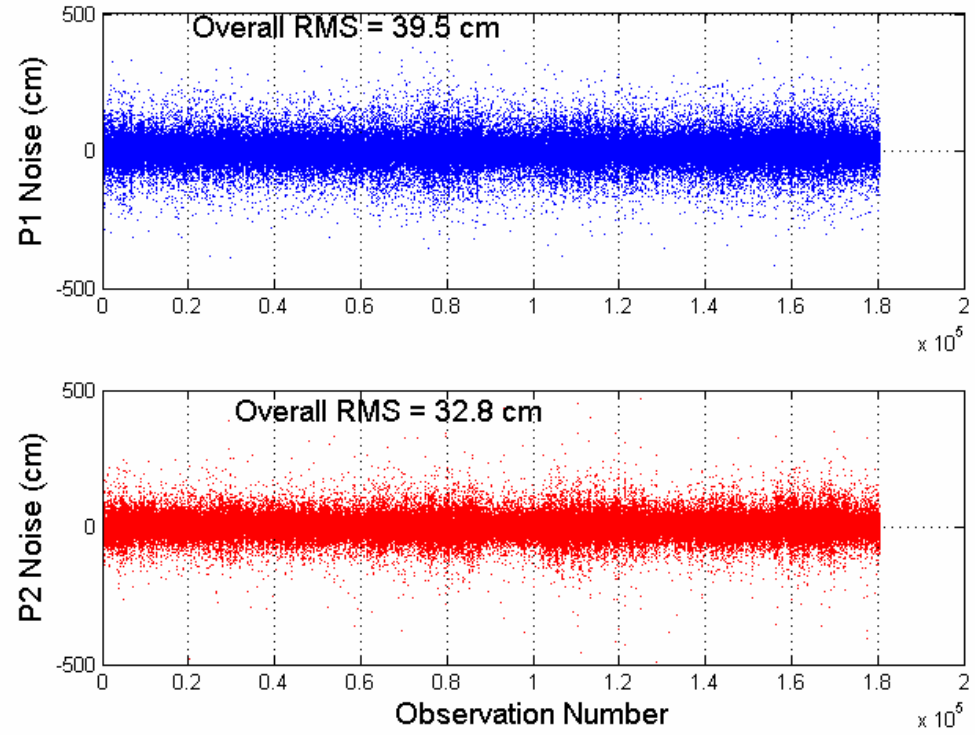

Figure 5.9 Overall P-code noise for three days (04502 ~04702).

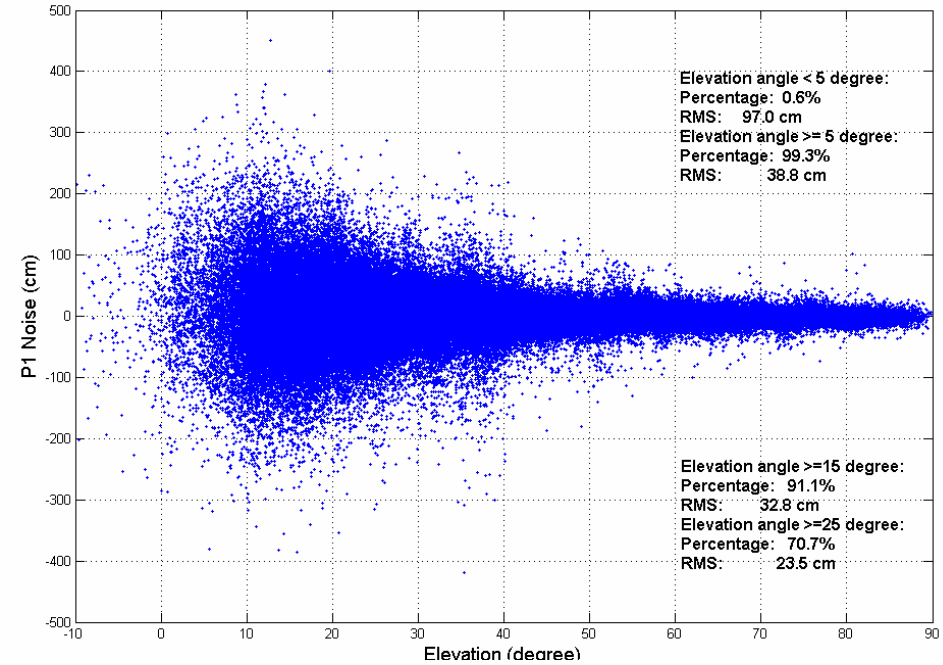

Figure 5.10 Overall P_1 noise with respect to the elevation angle.

5.5.3.3 Residuals

The measurement residuals were calculated using the precise SACC orbits, which has centimetre level accuracy. If the GPS ephemerides are known at the centimetre level as well the residuals should represent the GPS measurement residual and some small system errors (coordinate transformation, relativistic effects, etc). Figure 5.11 shows the measurement residuals using the broadcast ephemerides and IGS ephemerides, respectively. We found the RMS using IGS result to be 2.67m, and for broadcast ephemerides solution it is 3.66m. Even with the IGS solution the value of 2.67m is still high considering that the RMS of P-code noise is around 30cm (derived in the previous section). After we account for the ionosphere-free differential noise and some un-modelled system errors, around a 1 ~ 1.5 metre discrepancy can be attributed to the GPS clock bias. Although the IGS final solution has < 0.1 *ns* [*IGS*, 2004] clock accuracy, the 5 minute interval can still introduce an interpolation error. For the broadcast ephemerides the standard deviation currently is 2m for GPS orbits and 7 *ns* for GPS clock [*IGS*, 2004]. So a 3.66m RMS error seems reasonable. Furthermore, the relativistic effect and antenna offset in GPS measurements have been inspected. Figure 5.12 and Figure 5.13 give the results.

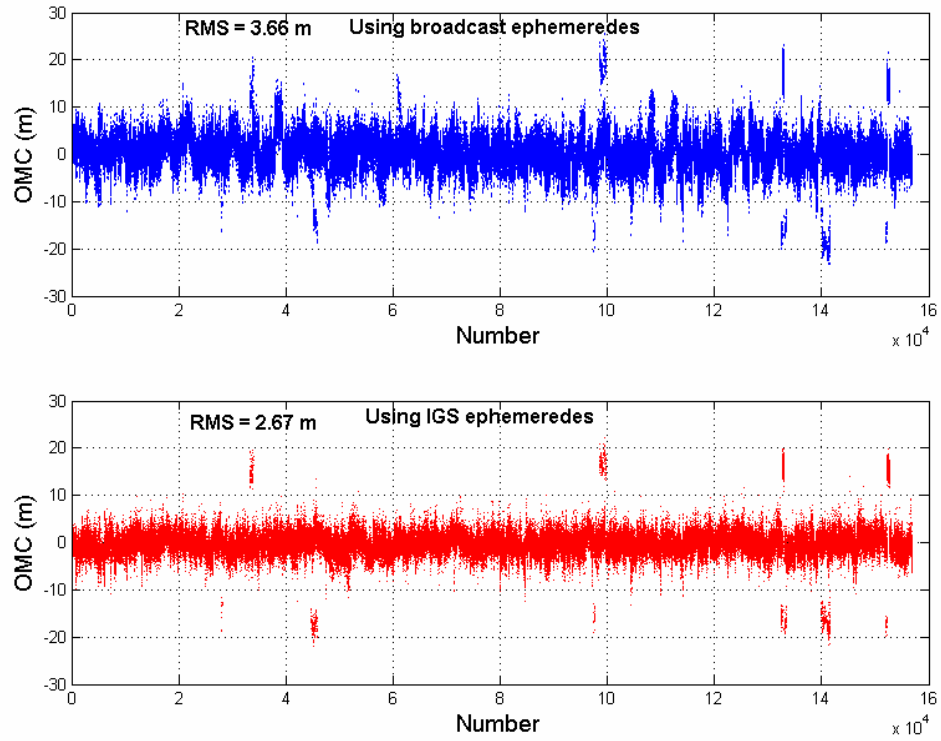

Figure 5.11 Code (ionosphere-free combination) residual using precise SACC ephemerides.

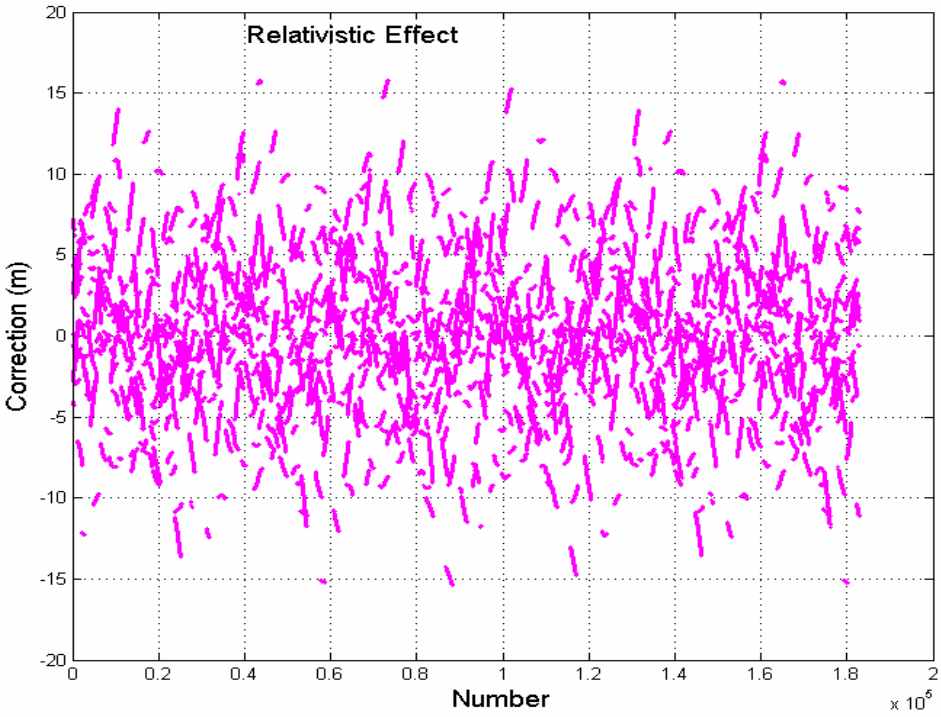

Figure 5.12 Relativistic effect for the P_1 / P_2 ionosphere combination.

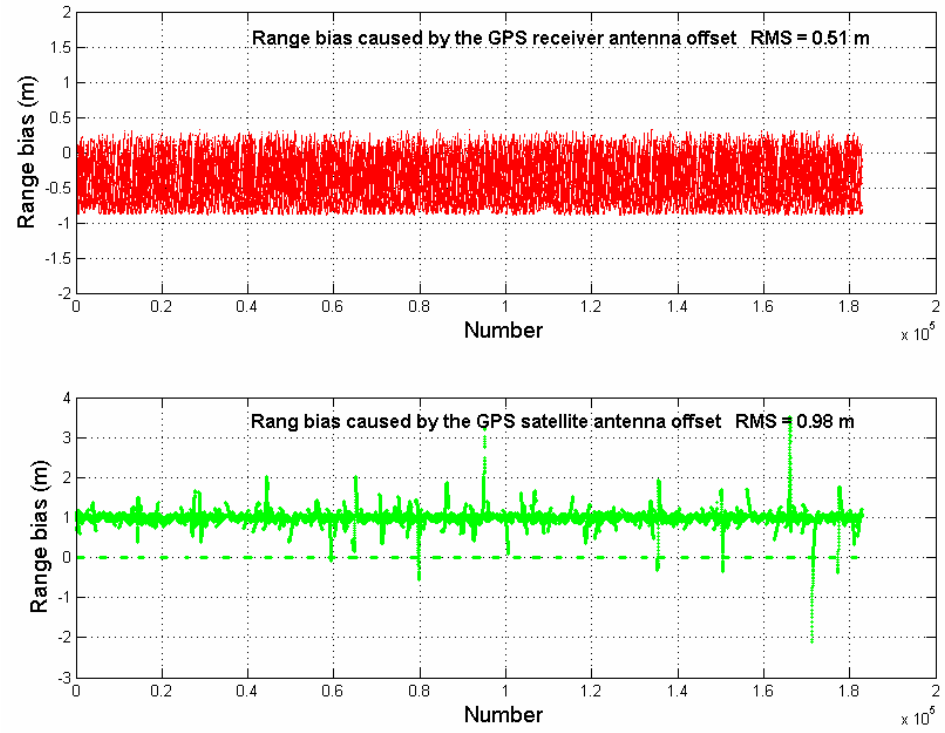

Figure 5.13 Antenna phase centre offset for both GPS satellite and spacecraft.

5.5.4 SPP Result Using Closed-form Formulation

The closed-form single point positioning algorithm was also tested. The measurements were treated in the normal manner. Figure 5.14 shows the detailed results. It is found that a 3D positional error of better than 100 m can be achieved over 83.1 % of the measurement epochs. The RMS value is around 37m, which is quite reasonable. In only 0.7 % of the cases did the 3D positional error exceed 10 kilometres error. Of course another condition of this method is there must be at least four satellites visible. The results suggest that the closed-form algorithm is a fast and reliable one for initialization purposes.

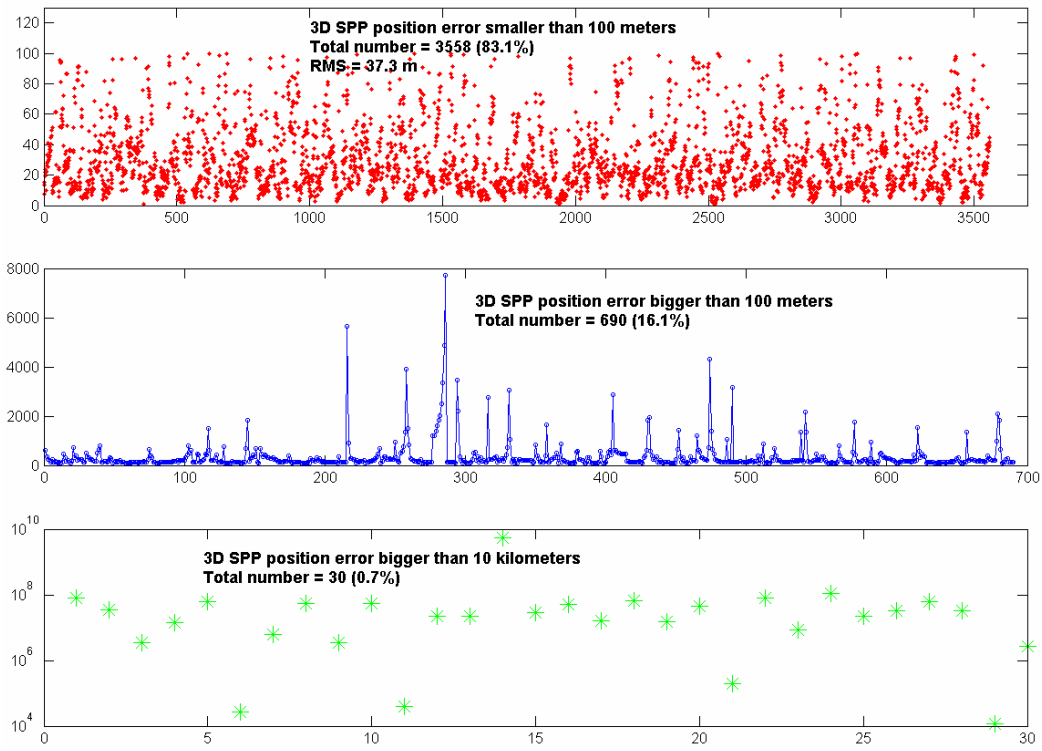

Figure 5.14 Closed-form SPP result for three days (04502 ~ 04702).

5.5.5 Sliding-window Phase Smoothing

5.5.5.1 Phase Connection Arc Length

As described in Section 5.3 carrier-phase smoothing requires continuous code and phase measurements. The smoothing quality depends on the phase-connected arc length; a better result can be obtained with a longer phase connection arc. As an outlier detection step, we normally delete the whole arc data where the arc length is less than 2 minutes and the number of data points is less than 10. After this outlier deletion process, the phase-connected arc length was calculated for all satellites in view. The result is presented in Figure 5.15. It is observed that 85 % of arcs are longer than 20 minutes; and some 8% are shorter than 5 minutes.

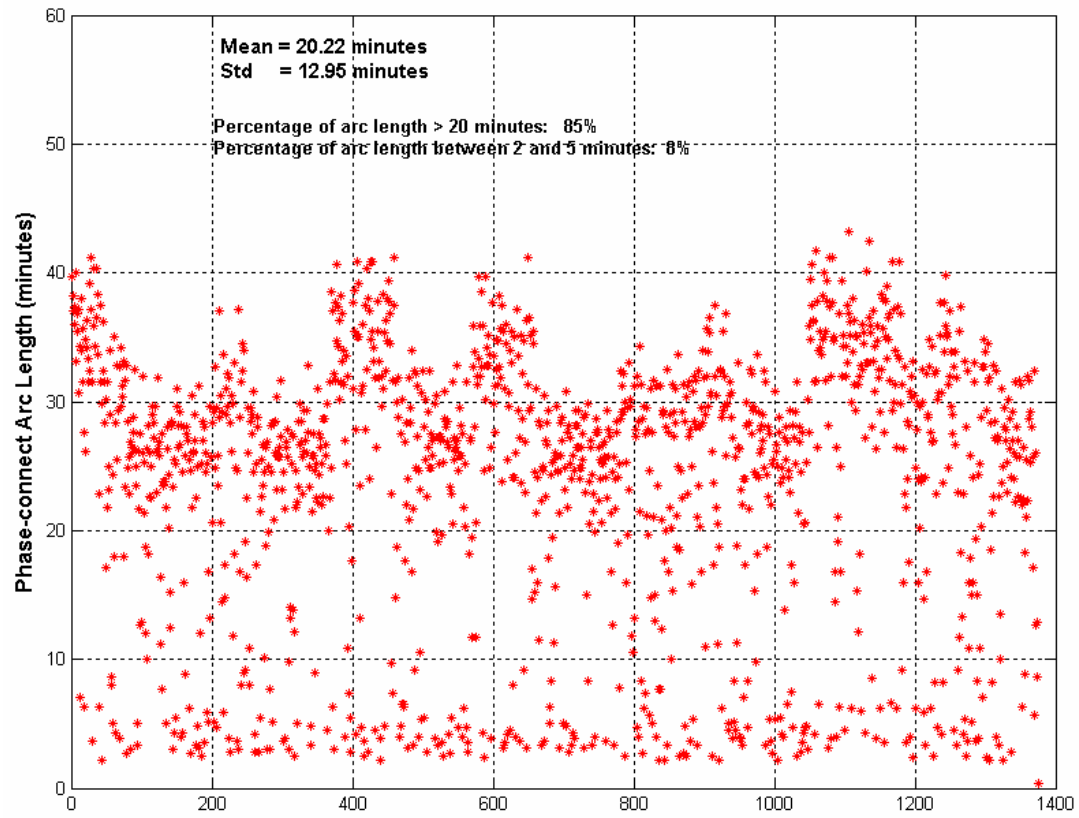

Figure 5.15 Phase connection arc length for all satellites in view.

5.5.5.2 Phase-smoothing with Different Arc Lengths

Carrier-phase smoothing results using different arc lengths are presented here. The arcs are: 5 minutes, 10 minutes, 15 minutes and 20 minutes, respectively. We only used the broadcast ephemerides and the results were compared with the non-smoothed SPP solution. Figure 15.16 gives the 3D SPP positioning error with a RMS value. Table 5.9 gives the P-code noise comparison between the smoothing value and raw value.

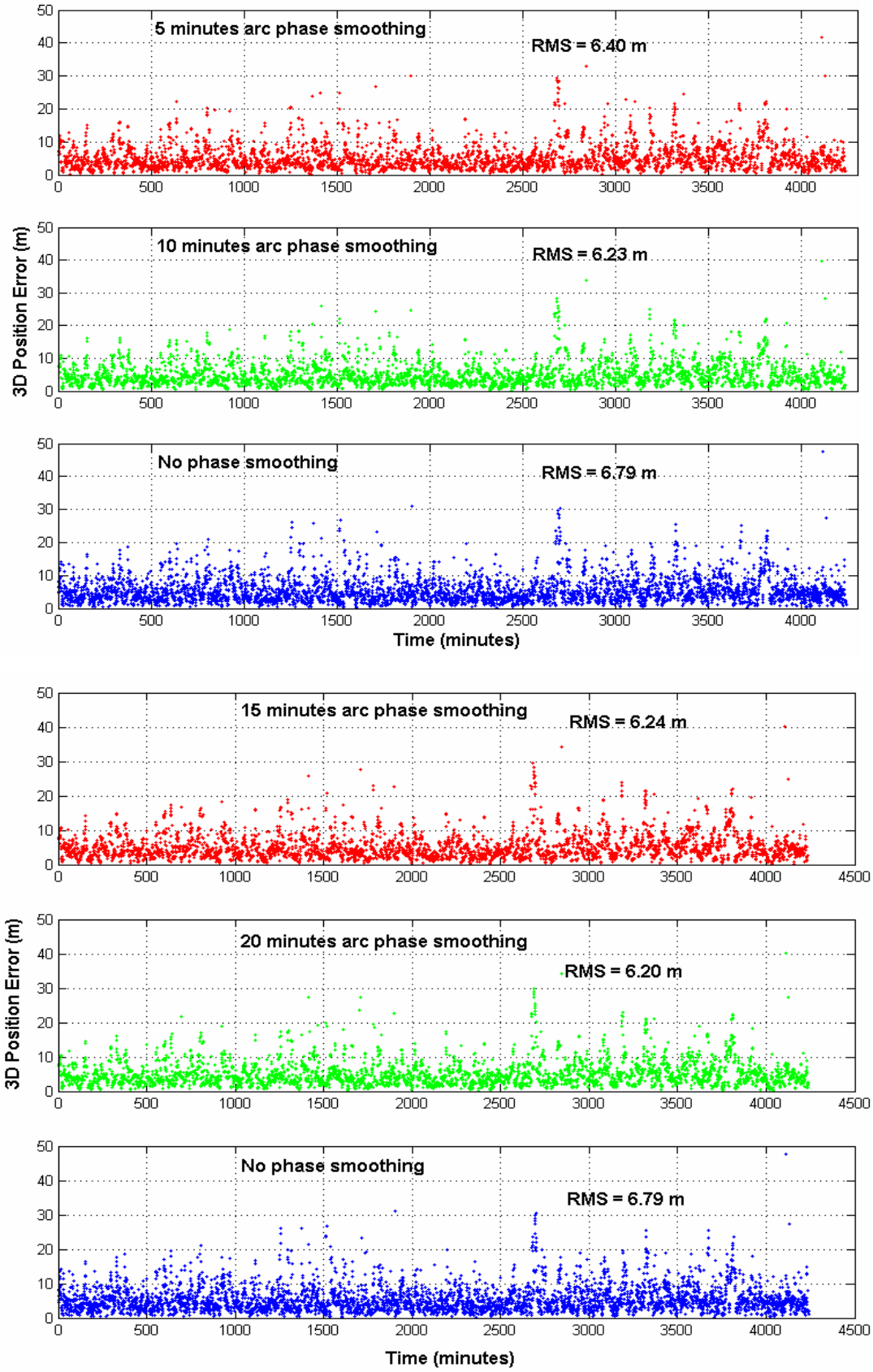

Figure 5.16 SPP results with phase smoothing (5 minutes, 10 minutes, 15 minutes, 20 minutes) compared with non-smoothing.

Table 5.9 Overall P_1/P_2 noise statistics after phase smoothing.

Scheme		<=0.2m	<=0.5m	<=1.0m	<=2.0m	<=5.0m	>5.0m
Raw	P_1	64.1% 9.7cm	86.9% 18.7cm	96.3% 28.2cm	99.7% 37.1cm	100% 39.5cm	0
	P_2	64.9% 9.9cm	90.1% 19.1cm	98.2% 26.9cm	99.9% 31.4cm	100% 32.8cm	0
5min	P_1	97.7% 0.7cm	98.2% 2.7cm	98.9% 6.5cm	99.6% 14.3cm	100% 21.3cm	0
	P_2	95.8% 1.1cm	97.0% 4.1cm	98.1% 8.9cm	99.1% 16.9cm	100% 35.3cm	0
10min	P_1	99.0% 0.4cm	99.2% 1.4cm	99.4% 3.8cm	99.7% 9.9cm	100% 16.5cm	0
	P2	97.6% 0.9cm	98.4% 3.2cm	99.0% 6.7cm	99.4% 11.4cm	100% 28.1cm	0
15min	P_1	99.4% 0.2cm	99.5% 1.0cm	99.6% 2.6cm	99.8% 7.4cm	100% 12.8cm	0
	P2	98.29% 0.8cm	98.8% 2.9cm	99.3% 6.0cm	99.7% 10.0cm	100% 22.1cm	0
20min	P_1	99.6% 0.2cm	99.7% 0.8cm	99.7% 2.3cm	99.9% 6.1cm	100% 10.6cm	0
	P2	99.6% 0.1cm	99.6% 0.6cm	99.7% 1.8cm	99.8% 5.1cm	100% 17.1cm	0

We found the 20 minutes smoothing only improved the SPP accuracy about 60 centimetres, which is quite small compared to the improvement in the measurement noise level. There are two possible reasons for this. First, the least squares process with an average of 7 visible GPS satellites absorbs much of the measurement noise. Second, the ionosphere-free combination and the between satellites difference introduce additional process noise which reduces the advantage of smoothing. We plot the P_1/P_2 code noise with respect to elevation angle in Figure 5.17 dramatic improvement can be seen after the 20 minutes smoothing.

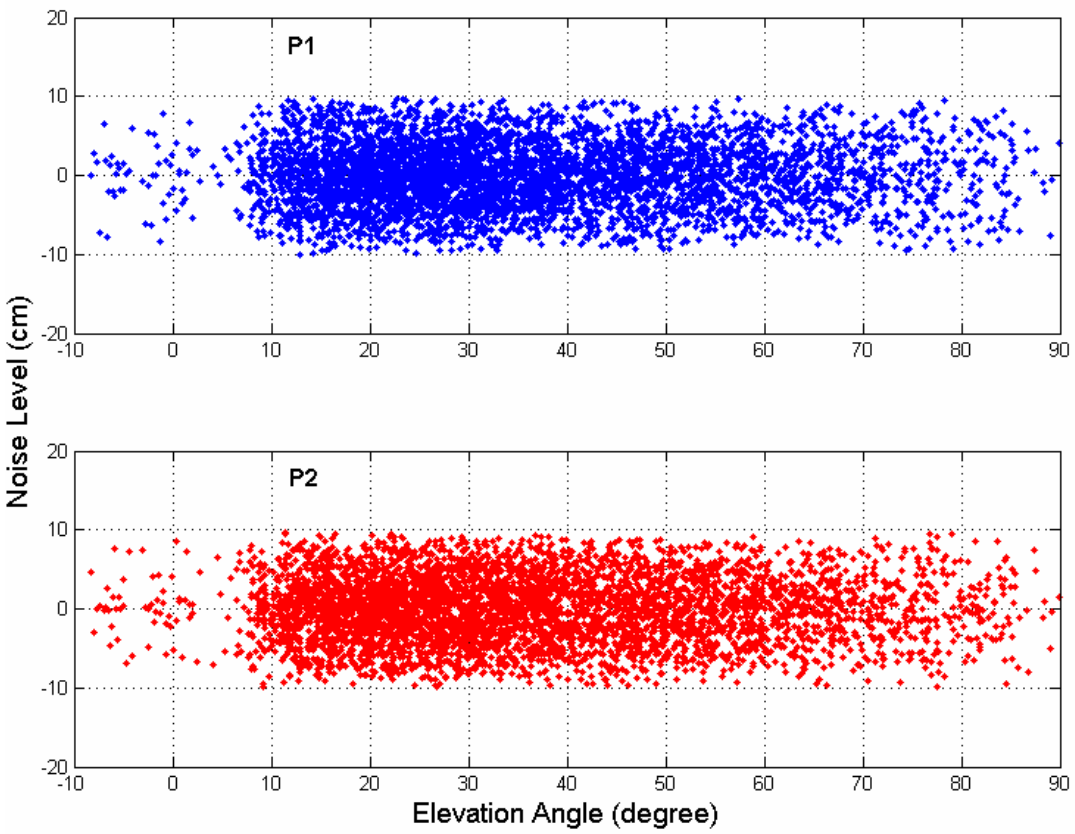

Figure 5.17 P_1/P_2 code noise with respect to elevation angle after 20 minutes phase smoothing for SV5.

5.5.5.3 Sliding-window Smoothing

Sliding-window smoothing sequentially processes 10 to 15 minutes data, and generates a smoothed measurement every 5 minutes. From previous experiment results we found that the best smoothing arc length is 10 to 20 minutes. Table 5.10 gives the different window sizes and the storage requirement. For example, if the short-arc is 2 hours, and we choose a window size of 5 minutes, we can get 24 epoch measurements, and the measurement storage is around 192 bytes. The sliding-window method can reduce the computing time and storage requirement while retaining measurement accuracy.

The following test evaluated the sliding-window smoothing performance by comparing the SPP solution accuracy. Figure 5.18 illustrates the SPP 3D RMS error and computing time. Nine configurations were used; the $m \times n$ means the smoothing arc

is *m* minutes and window size is *n* minutes. It was observed that the computing time was reduced a little bit compared to processing all the available data and the quality of the measurements remained at the same level.

Table 5.10 Measurements and storage requirements for short-arc orbit determination using sliding-window phase smoothing.

Measurement number and Storage (bytes)	30 minutes	1 hour	2 hours
Every 1 minute	30 / 240	60 / 480	120 / 960
Every 2 minutes	15 / 120	30 / 240	60 / 480
Every 5 minutes	6 / 48	12 / 96	24 / 192

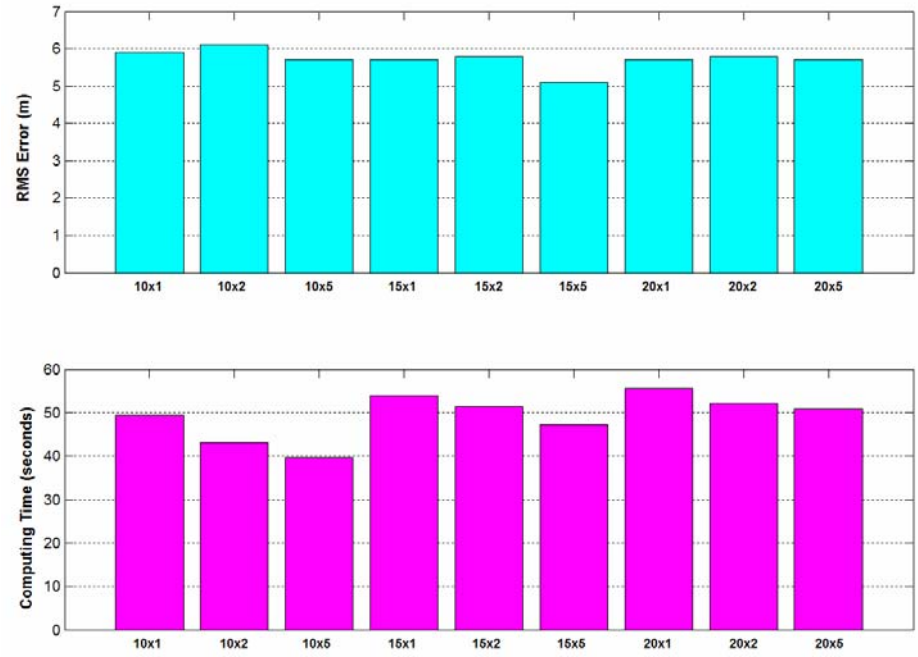

Figure 5.18 Comparison of SPP results and computational burden with different sliding-window smoothing strategies.

5.6 Summary

In this chapter, GPS code measurements and their error source have been described, and different outlier detection methods have been discussed. A sliding-window carrier phase smoothing algorithm has been validated through extensive experiments. This method can reduce the measurement storage and retain the carrier-phase smoothing precision. Furthermore, a closed-form single point position algorithm was also validated. It can be used to provide initial position with tens of metres accuracy

without any a priori information. Together, these techniques facilitate high accuracy onboard GPS processing. In summary, we have reached the following conclusions:

- An outlier detection scheme was developed, consisting of separate modules, each requireing little computing resource. It can also detect cycle slip and fix them using a simple method and lower weight is given to these required measurements to prevent performance degrading.
- The closed-form SPP algorithm generates positioning solution with tens of metres error. This accuracy can be achieved for 83% of measurements. Furthermore, the error is smaller than 10km for 99% of measurements, which is still a good initial estimate for the subsequent orbit filtering process.
- The carrier-phase smoothing reduces the code noise from 39.5cm and 32.8cm down to 17.1cm and 10.6cm, for P_1 and P_2 respectively.
- We found that best SPP result was achieved with 10 ~ 20 minutes smoothing. For the sliding-window smoothing the results are basically the same with different window sizes. The 5 minute window size with 10 ~ 20 minutes smoothing is a good choice for onboard processing.

Chapter 6
Short-arc Orbit Determination

This chapter deals with orbit estimation from the measurements. For stability and accuracy consideration, and based on previous efforts toward the simplified orbital model and GPS measurement model, a short-arc filter is proposed in this chapter. To address both the accuracy and computational burden challenge, the filter has the following characteristics:

- It is a weighted least squares batch filter. A parametre regularization technique is also used to minimize the singularity effect arising from poor satellite geometry and measurement distribution.
- Using the orbit model simplification strategy proposed in Chapter 3, but with the gravity approximation method proposed in Chapter 4 instead. These simplifications are especially suitable for onboard data processing or real time orbit computation.
- Using the sliding-window carrier-phase smoothing filter to refine GPS code measurements, and reduce the number of data points.
- Achieving improved orbit solutions when the uncertainty of GPS observations is higher than the modelling errors, and correction for dynamic model biases when the GPS observations are more accurate.

6.1 Weighted Least Squares Filter

6.1.1 Least Squares Problem

The basic idea of least squares estimation as applied to orbit determination is to find the trajectory and the model parametres for which the square of the difference between the modelled observations and the actual measurements becomes as small as possible or, in other words, a trajectory which best fits the observations in a least squares of the residuals sense (Figure 6.1). In reality, since different measurements

have different units and reliability, a weighting factor is applied to each residual and it is the square of the weighted residuals that is minimized. In order to arrive at a mathematical formulation of this principle let:

$$\mathbf{x}_t = \left(\mathbf{r}_t, \mathbf{v}_t, \mathbf{p}, \mathbf{q}\right)^T \tag{6.1}$$

denote a time-dependent, *m*-dimensional vector comprising the satellite's position $\mathbf{r}_t$ and velocity $\mathbf{v}_t$ as well as the free parametres $\mathbf{p}$ and $\mathbf{q}$ that affect the force and measurement model. The time evolution of $\mathbf{x}_t$ may be described by an ordinary differential equation of the form

$$\dot{\mathbf{x}} = f\left(t, \mathbf{x}\right) \qquad \text{with an initial value at epoch } t_0 \text{: } \vec{x}_0 = \vec{\mathbf{x}}_{t_0} \tag{6.2}$$

Furthermore, let:

$$Z = (\mathbf{z}_1, \cdots, \mathbf{z}_n) \tag{6.3}$$

denote an *n*-dimensional vector of measurements taken at times $t_1,...,t_n$. The observations are described by:

$$\mathbf{z}_{i,t_i} = \mathbf{g}_i\left(t_i, \mathbf{x}_{t_i}\right) + \boldsymbol{\varepsilon}_i = \mathbf{h}_i\left(t_i, \mathbf{x}_0\right) + \boldsymbol{\varepsilon}_i \tag{6.4}$$

or:

$$\mathbf{z} = \mathbf{h}\left(\mathbf{x}_0\right) + \boldsymbol{\varepsilon}_i \tag{6.5}$$

Here $\mathbf{g}_i$ denotes the model value of the ith observation as a function of time t_i and the instantaneous state $\mathbf{x}_{t_i}$ whereas $\mathbf{h}_i$ denotes the same value as a function of the state $\mathbf{x}_0$ at the reference epoch t_0 . The quantities $\boldsymbol{\varepsilon}_i$ account for the differences between actual and model observations due to measurement errors, which are usually assumed to be randomly distributed with zero mean value.

The least squares orbit determination problem may now be defined as finding the state $\hat{\mathbf{x}}_0$ which minimize the loss function:

$$J\left(\mathbf{x}_0\right) = \boldsymbol{\rho}^T \boldsymbol{\rho} = \left(\mathbf{z} - \mathbf{h}\left(\mathbf{x}_0\right)\right)^T \left(\mathbf{z} - \mathbf{h}\left(\mathbf{x}_0\right)\right) \tag{6.6}$$

(i.e. the squared sum of the residuals $\boldsymbol{\rho}_i$) for a given set of measurements $\mathbf{z}$. It is noted that the given formulation of the loss function requires all measurements to be of equal type and quality. This assumption simplifies the subsequent presentation but will later be dropped to arrive at a completely general formulation. In order to avoid

a non-unique determination of $\mathbf{x}_0$, it is further assumed that the number of observations *n* is at least equal to the number of unknown *m*.

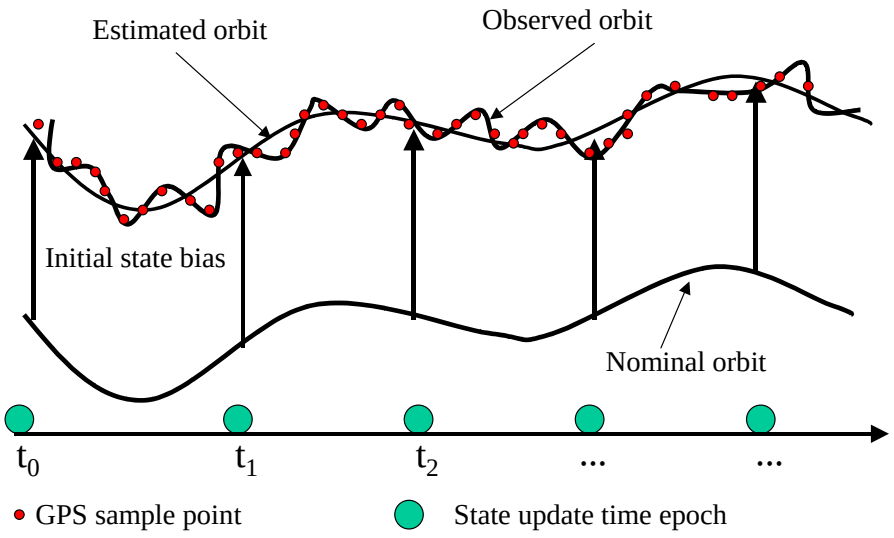

Figure 6.1 Concept of least squares orbit estimation.

6.1.2 Linearization and Normal Equation

The practical solution of the least squares orbit determination problem is complicated due to the fact that $\mathbf{h}(\mathbf{x}_0)$ is a highly non-linear function of the unknown vector $\mathbf{x}_0$, which makes it difficult or impossible to locate the minimum of the loss function without additional information. As mentioned above, an approximate value $\tilde{\mathbf{x}}_0$ of the actual epoch state is, however, often known, which may be used to simplify the least squares problem considerably.

Linearizing all quantities around a reference state $\tilde{\mathbf{x}}_0$, which is initially given by $\tilde{\mathbf{x}}_0$, the residual vector is approximately given by:

$$\boldsymbol{\rho} = \mathbf{z} - \mathbf{h}(\mathbf{x}_0) \approx \mathbf{z} - \mathbf{h}(\tilde{\mathbf{x}}_0) - \frac{\partial \mathbf{h}}{\partial \mathbf{x}_0}(\mathbf{x}_0 - \tilde{\mathbf{x}}_0) = \Delta\mathbf{z} - \mathbf{H}\Delta\mathbf{x}_0 \qquad (6.7)$$

Here $\Delta\mathbf{x}_0 = \mathbf{x}_0 - \tilde{\mathbf{x}}_0$ and $\Delta\mathbf{z} = z - \mathbf{h}(\tilde{\mathbf{x}}_0)$ denote the difference between the actual observations and the observations predicted from the reference trajectory. Furthermore, the partial derivatives:

$$\mathbf{H} = \left.\frac{\partial \mathbf{h}(\mathbf{x}_0)}{\partial \mathbf{x}_0}\right|_{\mathbf{x}_0 = \tilde{\mathbf{x}}_0} \qquad (6.8)$$

gives the relationship of the modelled observations with respect to the state vector at the reference epoch t_0. Equation (6.7) provides a prediction of the measurement residual after applying a correction $\Delta\mathbf{x}_0$ to the reference state and re-computing the models observation $\mathbf{h}$.

The orbit determination problem is now reduced to the linear least squares problem of finding $\Delta\mathbf{x}_0$ such that:

$$J(\Delta\mathbf{x}_0) = (\Delta\mathbf{z} - \mathbf{H}\Delta\mathbf{x}_0)^T (\Delta\mathbf{z} - \mathbf{H}\Delta\mathbf{x}_0) \tag{6.9}$$

i.e., the predicted loss function after applying a correction $\Delta\mathbf{x}_0$ becomes a minimum. If the Jacobian has full rank *m*, i.e., if the columns of **H** are linearly independent, this minimum is uniquely determined by the condition that the partial derivatives of **J** with respect to $\Delta\mathbf{x}_0$ vanish:

$$\left.\frac{\partial(\Delta\mathbf{z} - \mathbf{H}\Delta\mathbf{x}_0)^T (\Delta\mathbf{z} - \mathbf{H}\Delta\mathbf{x}_0)}{\partial\Delta\mathbf{x}_0}\right|_{\Delta\mathbf{x}_0 = \Delta\tilde{\mathbf{x}}_0} = 0 \tag{6.10}$$

Using the relation

$$\frac{\partial\mathbf{a}^{\mathrm{T}}\mathbf{b}}{\partial\mathbf{c}} = \mathbf{a}^{\mathrm{T}}\frac{\partial\mathbf{b}}{\partial\mathbf{c}} + \mathbf{b}^{\mathrm{T}}\frac{\partial\mathbf{a}}{\partial\mathbf{c}} \tag{6.11}$$

to compute the derivatives of $\boldsymbol{\rho}^T\boldsymbol{\rho}$, the general solution of the linear least squares problem may be written as

$$\Delta\hat{\mathbf{x}}_0 = (\mathbf{H}^T\mathbf{H})^{-1}(\mathbf{H}^T\Delta\mathbf{z}) \tag{6.12}$$

after a proper rearrangement. The matrix $\mathbf{H}^T\mathbf{H}$ is an *m*-dimensional symmetric square matrix, which is also known as the normal equations matrix. Since ***H*** was assumed to have full rank, the inverse of $\mathbf{H}^T\mathbf{H}$ exists, even though it need not actually be computed. Instead $\Delta\hat{\mathbf{x}}_0$ may be obtained by solving the *m*-dimensional normal equations:

$$(\mathbf{H}^T\mathbf{H})\Delta\hat{\mathbf{x}}_0 = (\mathbf{H}^T\Delta\mathbf{z}) \tag{6.13}$$

using standard techniques for positive definite linear systems of equations (e.g. Cholesky's algorithm).

Due to the non-linearity of **H** the simplified loss function differs slightly from the rigorous one and the value of $\mathbf{x}_0 = \tilde{\mathbf{x}}_0 + \Delta\hat{\mathbf{x}}_0$ determined so far is not yet the exact

solution of the orbit determination problem. It may, however, be further improved by substituting it for the reference value $\tilde{\mathbf{x}}_0$ and repeating the same procedure. Based on this idea the non-linear problem can be solved by iteration:

$$\mathbf{x}_0^{j+1} = \mathbf{x}_0^j + \left(\mathbf{H}^{jT}\mathbf{H}^j\right)^{-1}\mathbf{H}^{jT}\left(\mathbf{z} - \mathbf{h}\left(\mathbf{x}_0^j\right)\right) \tag{6.14}$$

which is started from $\mathbf{x}_0^0 = \tilde{\mathbf{x}}_0$ and continued until the relative change of the loss function is smaller than a prescribed tolerance for successive approximations. The Jacobian:

$$\mathbf{H}^j = \left.\frac{\partial \mathbf{h}(\mathbf{x}_0)}{\partial \mathbf{x}_0}\right|_{\mathbf{x}_0 = \mathbf{x}_0^j} \tag{6.15}$$

should be updated in each iteration to ensure an optimum convergence, but may also be replaced by the constant value $\mathbf{H}^0$. Even though the number of iterations increases in this case, the total computational effort can often be reduced, due to the large amount of work that is otherwise required for the integration of the state transition matrix.

6.1.3 Observation Weight

The algorithm implies that that all observations are treated equally, even though the observation vector **z** is generally composed of different measurement types. The accuracy of each measurement type may, however, easily be accounted for by weighting all observations with the inverse of the mean measurement error σ_i, i.e. by replacing the residuals $\boldsymbol{\rho}_i$ with the normalized residuals:

$$\hat{\boldsymbol{\rho}}_i = \frac{1}{\sigma_i}\boldsymbol{\rho}_i = \frac{1}{\sigma_i}\left(\mathbf{z}_i - \mathbf{h}_i\left(\mathbf{x}_0\right)\right) \tag{6.16}$$

Here σ_i should consider the total expected error in the measurement due to both random noise and systematic errors (e.g. refraction). As a result the basic least-squares Equation (6.12) remains essentially unchanged except that **H** and $\Delta\mathbf{z}$ are replaced by the modified values:

$$\hat{\mathbf{H}} = \mathbf{S}\mathbf{H} \text{ and } \Delta\hat{\mathbf{z}} = \mathbf{S}\Delta\mathbf{z} \tag{6.17}$$

Here **S** is a square diagonal matrix:

$$\mathbf{S} = diag\left(\sigma_1^{-1},...,\sigma_n^{-1}\right) = \begin{pmatrix} \sigma_1^{-1} & & 0 \\ & \ddots & \\ 0 & & \sigma_n^{-1} \end{pmatrix} \tag{6.18}$$

which divides the *i* th row of a matrix or vector by σ_i upon multiplication from the left. Alternatively the solution of the weighted least squares problem may be written as

$$\Delta\hat{\mathbf{x}}_0 = \left(\mathbf{H}^T\mathbf{W}\mathbf{H}\right)^{-1}\left(\mathbf{H}^T\mathbf{W}\Delta\mathbf{z}\right) \tag{6.19}$$

using the weight matrix:

$$\mathbf{W} = \mathbf{S}^2 = diag\left(\sigma_1^{-2},...,\sigma_n^{-2}\right) \tag{6.20}$$

Both representations are equally well suited to handling uncorrelated measurement errors, which are fully described by the corresponding values σ_i. The weight matrix may, however, also be used for correlated measurement errors, in which case **W** becomes a non-diagonal matrix.

As alternatives to constant weighting normally used in GPS analysis, there are some other possible methods that may be used [*Vermeer*, 1997; *Teunissen, et al*., 1999; *Collins* & *Langley*, 1999; *Hartinger* & *Brunner*, 1999]:

- Weighting as a cosecant function of the satellite elevation angle [*Vermeer*, 1997; *Collins* & *Langly*, 1999]. This is because the amount of signal noise increases towards the horizon, similar to the tropospheric error, which has a cosecant shape, according to various models of the tropospheric mapping function, such as Marini, Chao, Davis and Herring mapping functions.
- Weighting as square of a cosecant function of the satellite elevation angle [*Vermeer*, 1997; *Hartinger* & *Brunner*, 1999]. This is from the fact that GPS residuals reveal a more swiftly increasing noise level for low elevation angles.
- Exponential weighting schemes that weight corresponding observations observed from near the horizon very much lower [*Euler*, 1991].
- Weighting that reflects receiver generated signal-to-noise ratio (SNR) values [*Collins* & *Langley*, 1999; *Hartinger* & *Brunner*, 1999]. Normally, SNR represents the carrier-to-noise-power-density ratio (C/N_0), which varies with the elevation of the arriving signal. *Langley* [1997] derived phase variance (m) using C/N_0 (dB-Hz) values as follows:

$$\sigma_{L_i} = B(\frac{\lambda_i}{2\pi})^2 10^{-0.1C/N_0}, \; i = 1,2 \qquad (6.21)$$

where B is the carrier tracking loop bandwidth (Hz). It should be noted that some receiver manufacturers do not provide either SNR or C/N_0.

Hartinger and *Brunner* [1999] used the SIGMA-ε model where the phase variances are computed using C/N_0 values and thus observation weight directly echoes signal quality. Their experimental results show that baseline RMS of the SIGMA-ε model is much less than that in the case of equal weighting, especially at low elevation cutoff angle.

Collins and *Langley* [1999] reported that, in the presence of multipath, the cosecant and SNR weighting schemes yield a significant improvement over the equal-weighting scheme. Moreover, according to the scaling effect of the a posteriori variance factor, the cosecant and SNR schemes are almost numerically equivalent.

The amount of observation noise increases and can indicate the presence of multipath, which mostly occurs in signals from low satellite elevation angles. It should be more appropriate to apply a step function using a combination of uniform weight for high elevation angle observation and lower weight at low elevation angle. Deweighting observations at high elevation angles will lose valuable information. The step function variance may be given as:

$$\sigma^2(ele) = \begin{cases} \sigma^2 & ele > \alpha \\ \sigma^2 \cos^2(ele) & ele < \alpha \end{cases} \qquad (6.22)$$

or

$$\sigma^2(ele) = \begin{cases} \sigma^2 \cos(ele) & ele > \alpha \\ \sigma^2 \cos^2(ele) & ele < \alpha \end{cases} \qquad (6.23)$$

where α is the elevation threshold angle.

6.1.4 Numerical Problems

As is evident from the mathematical formulation of the least squares problem, the number of observations must at least be equal to the number of unknowns, but

should be considerably larger to reduce the influence of individual measurement errors. A large number of observations may still, however, be insufficient if the tracking geometry and distribution do not provide enough information on all estimation parametres. The direct solution of the normal equations:

$$\left(\mathbf{H}^{\mathbf{T}}\mathbf{H}\right)\Delta\hat{\mathbf{x}}_0 = \mathbf{H}^{\mathbf{T}}\Delta\mathbf{z} \qquad (6.24)$$

will then give rise to numerical difficulties, even if the normal equation matrix is not exactly singular.

To avoid this stability problem many numerical methods have been formulated, such as QR factorization, UDU factorization and singular value decomposition (SVD). They are all effective for stabilizing the least square filter, but the computational cost to introduce such methods for onboard implementation is also high.

We propose a so-called regularization parametreization method combined with the LU decomposition method. To be able to solve the ill-conditioned system, we minimize the function:

$$J_\alpha\left(\Delta\hat{\mathbf{x}}_0\right) = \left(\Delta\mathbf{z} - \mathbf{H}\Delta\hat{\mathbf{x}}_0\right)^T\left(\Delta\mathbf{z} - \mathbf{H}\Delta\hat{\mathbf{x}}_0\right) + \alpha(\mathbf{L}\Delta\hat{\mathbf{x}}_0)^T(\mathbf{L}\Delta\hat{\mathbf{x}}_0) \qquad (6.25)$$

over all $\Delta\hat{\mathbf{x}}_0$ in a compact set satisfying

$$\left\|\Delta\mathbf{z} - \mathbf{H}\Delta\hat{\mathbf{x}}_0\right\| < \varepsilon \qquad (6.26)$$

Here, the α is some fixed positive number, the so-called regularization parametre, and $\mathbf{L}$ is some linear operator (e.g. $\mathbf{L}\Delta\hat{\mathbf{x}}_0 = \Delta\hat{\mathbf{x}}_0$ or $\mathbf{L}\Delta\hat{\mathbf{x}}_0 = \Delta'\hat{\mathbf{x}}_0$). Under certain mild conditions, the problem Equation (6.23) has a unique solution, denoted by $\Delta_\alpha\hat{\mathbf{x}}_0$. Moreover, $\Delta_\alpha\hat{\mathbf{x}}_0$ will converge to the solution of Equation (6.22) as $\alpha \to 0$, provided that $\varepsilon^2 \to 0$ no less rapidly than α. The linear operator $\mathbf{L}$ is often chosen in such a way that it will help to suppress wild oscillations in functions Δx_0 which satisfy Equation (6.24). However, this effect should not be too strong so that all oscillations in Δx_0 are damped out. Using a variational argument, the solution of Equation (6.23) can be shown to be the solution of:

$$(\mathbf{H}'\mathbf{H} + \alpha\mathbf{L}'\mathbf{L})\Delta\hat{\mathbf{x}}_0 = \mathbf{H}'\Delta\mathbf{z} \qquad (6.27)$$

where $\mathbf{H}'$ and $\mathbf{L}'$ are the operators that are conjugate to $\mathbf{H}$ and $\mathbf{L}$ respectively. Equation (6.27) is a $n \times n$ linear system. It can be well solved using a LU decomposition method.

6.1.5 Comparison of Least Square Batch Filter and Sequential Filter

As has been pointed out in the introduction, the estimation techniques commonly employed for orbit determination purposes are closely related to each other and a smooth transition is possible from the batch least squares method to the various forms of Kalman filter. Each type of estimator has inherent advantages and disadvantages and a trade-off is usually required to select the most suitable estimation method for a particular application:

- ***Measurement processing and state correction***: The classic batch least squares method computes the epoch state estimate after processing the full set of observations. If improved epoch state estimates are required after each measurement, a formulation involving Givens rotations or the recursive least squares method may be used. The Kalman filter in contrast processes a single scalar or vector measurement at a time and yields sequential state estimates at the measurement times.
- ***Treatment of non-linearities***: Due to the non-linear relation between the epoch state vector and the modelled measurements, multiple iterations are required in the least squares method to compute a state estimate that actually minimizes the loss function. Using the extended Kalman filter these iterations may in general be avoided, since the reference solution is changed with each observation. Problems may more arise. However, in the case of large deviations between the a priori state and the actual state as well as poor management of the covariance;
- ***Computer implementation***: When using a Kalman filter for orbit determination there is no need to store measurements from previous time steps. Storage requirements are therefore smaller than for the least squares method, in which various data have to be stored for subsequent iterations.
- ***Numerical stability***: Both filters and least squares estimators may be subject to numerical problems in the case of bad observability as indicated by an ill-

conditioned normal equation matrix or covariance matrix. However, numerically stable algorithms employing different types of matrix factorizations are available; The increase in computing effort and storage requirement is generally negligible and the stabilized algorithms can therefore be recommended for most applications.

- ***Divergence***: A divergence of the least squares solution from one iteration to the next may occur in rare instances of bad observability, a bad initial state estimate or high level of non-linearities. All of these could also cause a Kalman filter to diverge. In addition, divergence of the state estimate from the true solution is likely to occur in a Kalman filter when the covariance becomes small and the filter becomes insensitive to new observations. Process noise may be incorporated into the filter to avoid divergence, but heuristic assumptions and simulations are often required to determine the appropriate noise model for a particular situation, unless a physical description of the process noise density matrix is available.
- ***Process noise***: A unique feature of the Kalman filter as compared to the least squares method is the incorporation of process noise into the estimation process. Aside from being required to avoid filter divergence problems, it may be employed to generate more realistic covariance predictions in the presence of unmodelled accelerations. Furthermore, it may be used to reduce the influence of past observations on the state estimate as compared to more recent observations.
- ***Influence of bad data points***: The batch estimator and the recursive least squares method process all data points using a common reference trajectory. This facilitates the handling of bad data points, which may be recognized by residuals that are considerably larger than the average value. In general the least squares technique is therefore more robust and easier to handle than the Kalman filter. The latter requires a careful balance between a priori covariance, measurement weighting and process noise to allow a rejection of bad data points.

Traditional applications in which Kalman filters are preferred to batch least-squares techniques include the onboard navigation of manned or unmanned spacecraft

requiring a real time state estimate [*Battin & Levine*, 1970]. Filtering techniques are, furthermore, used in the field of interplanetary orbit determination and navigation. By incorporating appropriate process noise, unmodelled statistical accelerations due to attitude thruster activities or radiation pressure modelling simplifications may be accounted for, which provides more realistic estimates of the injection error near the target planet [*Campbell, et al.,* 1983]. The batch least squares method on the other hand is commonly employed for off-line orbit determination of Earth-bound satellites [*Long, et al.*, 1989; *Soop*, 1983] and for the estimation of geodetic parametres from satellite orbits [*McCarthy, et al.*, 1993]. A comparison indicating a good agreement of orbit determination results from precision batch least squares and sequential estimation programs (GTDS, RTOD/E) for satellites tracked by the Tracking Data and Relay Satellite System (TDRSS) has recently been established by a study conducted on behalf of the Goddard Space Flight Centre [*Oza, et al.,* 1992]. Similar conclusions have been obtained by Halain et al. (1998) for single and multi-station tracking of geostationary satellites.

6.2 Covariance Analysis for a Batch Filter

6.2.1 Dynamical Orbit Error for a LEO

The typical accuracy of instantaneous point positioning is 5 ~ 15 metres without the SA effect; the major error contributors are GPS orbit and clock error and pseudo-range measurement noise (including multipath). A typical dynamical filter, such as a least squares filter, reduces the position error by smoothing measurement error against an orbit model over the fitting arc. Metre-level random errors may readily be reduced to decimetres or below. At the same time, key systematic errors such as GPS orbits, satellite clocks and multipath may be largely uncorrelated with the low orbiter dynamics and, therefore, attenuated in the solution.

But the improvement from the dynamical filtering is reduced when the altitude is low, for instance, below 800km. As the filter smooth measurement error, it introduces dynamic model error and process error. For a LEO satellite the orbit modelling is much more complicated due to the following effects: high order

harmonic items of Earth gravity; Earth solid tide; and surface forces from atmospheric drag. Model adjustments made during the dynamic filtering process may offer only partial improvement. Any remaining model errors will appear directly in the orbit solution. Gravity and drag model errors are often dominant, and both increase rapidly as the satellite altitude decreased. Thus, accurate dynamic orbit estimation becomes problematical at low altitudes. For example, the motion of Lageos, a dense inert sphere at about 6000km altitude, can be modelled to within a few centimetrees over periods of weeks; the motion of T/P, a larger vehicle at 1336km attitude, to about 10cm over 10 days; the motion of SAC-C, at 800km attitude, to one or two metres over one day; and the motion of the CHAMP, at 300~400km, to roughly 10m over an orbit revolution. Under such circumstances, kinematic information is important to correct the orbital model error. Table 6.1 compares the orbit integration error for different arcs for different missions: T/P, SAC-C and CHAMP. The models used are the same for these missions except different drag parametres.

Table 6.1 Un-modelled dynamical error for different arc against different missions.

	15 minutes	**1 hour**	**2 hours**	**6 hours**	**12 hours**	**1 day**
T/P	3cm	19cm	63cm	1m	2m	13m
SAC-C	13cm	74cm	8m	59m	248m	946m
CHAMP	30cm	12m	46m	517m	2067m	8102m

Dynamic model errors often reveal themselves in the post-fit residuals. That is, they create systematic discrepancies between the actual measurements and theoretical measurements derived from the modelled trajectory. Imagine a case in which a force varies randomly from one time step to the next and is, therefore, unpredictable, but can be observed in the post-fit residuals. A number of forces (drag, gravity anomalies) can appear to behave in this way.

In a typical Kalman filter, to observe un-modelled motion, the filter models the time-varying satellite force as the sum of a deterministic component (the standard dynamic model) and a stochastic component, which is the process noise model. This is a way of telling the filter that the state transition information in $\mathbf{\Phi}$ is incomplete—that there is another component that the filter cannot predict, but that it can try to observe in the data and estimate at each time step. This means that at each time step,

in addition to applying the standard dynamic updates, the filter will examine the discrepancy between the dynamic state estimate and the apparent state as indicated geometrically by the measurements. From that discrepancy it will estimate a local correction to the dynamical model, valid only over the current update. When added to the dynamic model, that correction will reduce the disagreement between the observations and the solution trajectory at this epoch. As it proceeds through the data the filter will generate a sequence of local force model corrections, one at each update time, bringing the solution trajectory into better agreement with observations. But that may be undesirable when bad measurements are present, after only one bad measurement is enough with conventional (sparse) tracking data, as the data acquired at any one time are often weak and insufficient by themselves to determine position. A relaxed constraint on process noise estimate may result in a large and erroneous adjustment to the state, or may cause the solution to fail. This is one reason why a Kalman filter is not as stable as a least-squares filter.

Starting from another point of view, the model error problem can be avoided to some extent if only short-arc data are processed in a least squares filter, because the model error propagation is not very serious within a 1 ~ 2 hour arc.

6.2.2 Covariance Analysis of the Batch Filter Result for LEO

There are two parts to the GPS observation equation: random measurement noise and system un-modelled error. Both affect the performance of the batch filter.

Normally the measurement noise vector $\vec{\mathbf{v}}$ is assumed to be white noise with zero mean value, with the standard normal distribution. Thus the error covariance related to the estimation $\vec{x}$ depends on the number of observation number. The more data in a batch filter, the better the noise is reduced. Of course, things are not that simple in real situations due to data correlation, the data quality distribution and system model error, all of which affect the final filtering result. If a carrier-phase smoothing filter is carried out for the P-code data, the original P-code noise can change from metres level to decimetre level. This will ease the demand for large number of observation.

On the other hand, the dynamic model error increases with longer filtering arc. These errors come from both the dynamic model error and the integrator truncation accumulation error. The behaviour of these system errors cannot be modelled as stochastic ones, thus they will not be alleviated using more measurements; they only depend on the accuracy of the measurements. One can model the system in a high-parametreized procedure, as in GPISY, where more than 40 parametres are used in the dynamic model. In this manner, a longer arc is preferred because the full strength of dynamic filtering can be gained. Obviously, this strategy is not suitable for onboard processes.

Another type of system error comes from the GPS measurement modelling. Typically, GPS ephemerides and clock error, ionospheric delay and receiver clock bias are the dominant error sources. Nowadays, the broadcast ephemerides and clock accuracy are much better than before. By comparing the broadcast ephemerides with the IGS result we can see that there is normally about a 1~2m discrepancy between them. One study [*Bertiger & Yunk*, 1990] showed that errors in the GPS orbits were attenuated by roughly a factor of two in the dynamic solution. That is, 1 ~ 2 metres GPS orbit error resulted in errors of 0.5 ~ 1 metre in the solution orbit. For other types of error sources, by forming the ionosphere-free combination and single-difference between different satellites, the residual should be at the decimetre level. In all, the measurement modelling error residual typically will be around 1 metre.

6.2.3 Parametreization

Parametreization is an important issue when only small set of measurements is used in the filter. In orbit determination, in addition to the six state vector variables, a set of orbital or measurement model parametres are estimated during the filtering process. However, in comparison with the state vector, the orbital parametre is much more sensitive to bad measurements. If not handled well the solution will depart from the true trajectory. The least squares filter always tries to minimize the sum of the squares of the residuals. If the measurements are corrupted or poorly distributed, more weight will be put on the parametre part in the filtering process because the parametres are more sensitive, thus making this parametre take more responsibility than it should. Usually this results in a solution that is far beyond the dynamical

boundary; of course sometimes the solution is still accurate, but the revised dynamic model is only valid for the current batch of data and is definitely not suitable for the next batch or for orbit prediction.

Another problem is the correlation between parametres if more than one orbital parametre is estimated. In the filter an assumption is made that all the parametres inependent, thus resulting in a diagonal state transition matrix. However, in reality some parametres are correlated, such as the drag and solar pressure coefficients. It is very hard to give apriori covariance information to these parametres. Some biases will be introduced by the parametre estimation.

From this consideration, and based on LEO dynamic model characteristics, a set of parametreization schemes was carefully selected, as indicated in Table 6.2. The table only lists some suggestions based on our experiment and data set selection. Actually this setting should be mission specific, for example, only solar pressure parametre is enough for T/P. For FedSat, though it is on a 780km altitude, the drag coefficient is not necessary because of the small and regular shape of the satellite.

Table 6.2 Parametreization schemes for LEO short-arc filter.

Scheme	Parametres	Characteristics
I	6 state vector only	Most stable, suitable for extreme short-arc, like 10~15 minutes.
II	**I** + drag coefficient	Sensitive to errors and high correlation to the velocity estimation, but this scheme is suitable for a typical LEO mission.
III	**I** + drag + solar pressure correction	Account for all the along track model error, high accuracy but unstable.

Depending on different situations, two short-arc strategies are considered in this research: discrete short-arc filter and sliding-window short-arc. The details are described below.

6.3 Short-arc Least Square Filter

6.3.1 Introduction

From previous analyses, if precise measurements are available a short-arc filtering is preferred for onboard orbit determination. As its name implies, the short-arc filter is a least squares estimator using a small set of GPS measurements, and it processes the data batch by batch in a forward direction. The arc length depends on different requirements: it can be from 15 minutes to 2 hours, or longer. The basic concept of the short-arc filter is illustrated in Figure 6.2.

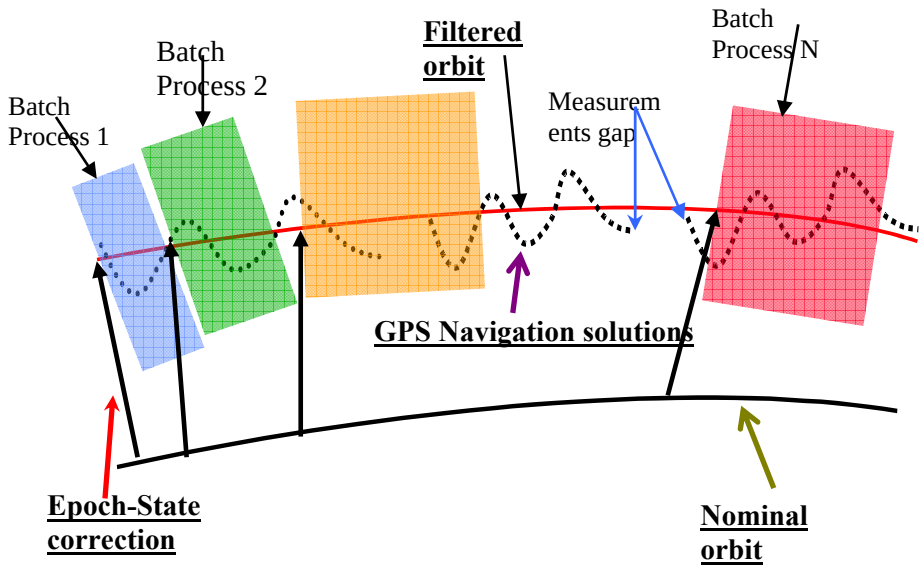

Figure 6.2 Concept of short-arc orbit determination.

6.3.2 Discrete Short-arc Techniques

The basic short-arc filter processes every single batch separately, the measurements are discarded after the process, and no relation exists between the adjacent batches. That is, the orbit solution is available only after all the measurements in this batch are collected. This results in a time latency from 15 minutes to 2 hours. Obviously it is not an optimal strategy for onboard usage. However, sometimes this is the only feasible choice because no continuous GPS measurements are available. For many micro-satellites, due to the power or computer capacity limit, the GPS can only operate a short time for every one or two orbits. With FedSat, for example, only 15

minute GPS data is available for every orbit revolution of about 100 minutes in length. Using the discrete filter a satisfied solution can still be obtained for these missions.

6.3.3 Sliding-window Short-arc Techniques

If continuous (for at least several hours) GPS measurements are available onboard, a more effective short-arc filter can be used. Instead of collecting the data batch-by-batch, the sliding-window filter only updates several minutes of the measurements, and processes the new data together with the old data. In this way, the processing will step forward every several minutes but still process the whole set of data. Figure 6.3 illustrates this concept. The update depends on the short-arc length, which typically can be from 5 minutes to 30 minutes. In this way the orbit solution will be available in several minutes, which is suitable for onboard real time or near-real time applications.

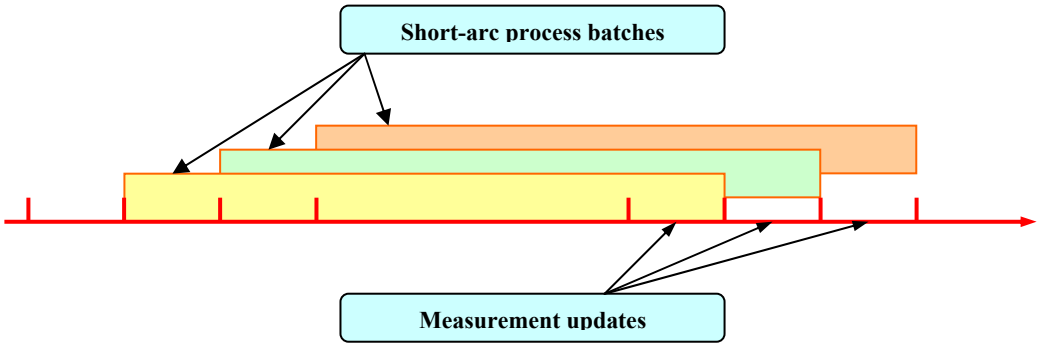

Figure 6.3 Concept of sliding-window short-arc filter.

Another advantage of this method is that it can decrease the onboard CPU time and memory usage for the following three reasons:

- Measurements from the last batch are used in the new batch, and some calculation results can be stored for current usage, such as carrier-phase smoothing results, GPS broadcast ephemerides transformed to the ECI coordinate system, and GPS measurement model corrections. These results can be used for the next few batches, and this will greatly relieve computional burden because only new measurements need to be processed in every batch.

- The state vector solution in the ECI coordinate frame from the last batch can be also stored for following batch usage. It is used as the nominal orbit input to the new batch, and only the nominal orbit for the updated arc is calculated. Generally, the update arc is only about several minutes in length and the computional burden is minimized. However, this is only valid for the first iteration of the least squares filter because the initial state vector and parametres have been corrected after the first iteration, and a new nominal orbit must be generated based on this new information. That means the full arc orbit integration is needed from second iteration. On the other hand, because the filtering result of the last batch greatly benefits the current one by providing the precise nominal orbit and corrected parametres information, this results in fewer iterations and a more stable solution.

- The state transition matrix can be treated the same way as the nominal orbit, that is, the first calculation of the state transition information is omitted. We know this will relieve the calculation burden because the solving of second-order variational equations is a time-consuming job. However, unlike the nominal orbit, the previous state transition matrix needs to be mapped to the current initial epoch before it can be applied to the current calculation (See Figure 6.4). The last batch begins from t_0 to t_k, all the partials are calculated with respect to epoch t_0. New updates begin from t_k to t_n, and the new partials are related to epoch t_k. Because of the sliding-window the data from t_0 to t_i is discarded, and the partials from t_i to t_k need to be mapped to t_k instead of t_0. In this way a new estimation will made at t_k. The state equation for the last batch can be written regarding transition matrix $\mathbf{\Phi}_{0,k}$ as:

$$\begin{aligned}
&\vec{\mathbf{X}}_0 = \mathbf{\Phi}_{0,0}\vec{\mathbf{X}}_0 \\
&\vec{\mathbf{X}}_i = \mathbf{\Phi}_{i,0}\vec{\mathbf{X}}_0 \quad \Rightarrow \quad \mathbf{\Phi}^{-1}{}_{k,0}\vec{\mathbf{X}}_k = \vec{\mathbf{X}}_0 \quad \Rightarrow \\
&\cdots\cdots \\
&\vec{\mathbf{X}}_k = \mathbf{\Phi}_{k,0}\vec{\mathbf{X}}_0
\end{aligned}$$

$$\Phi_{0,0}\vec{X}_0 = \Phi^{-1}{}_{k,0}\vec{X}_k \qquad \vec{X}_0 = \Phi^{-1}{}_{0,0}\Phi^{-1}{}_{k,0}\vec{X}_k$$

$$\Phi_{i,0}\vec{X}_i = \Phi^{-1}{}_{k,0}\vec{X}_k \quad => \quad \vec{X}_i = \Phi^{-1}{}_{i,0}\Phi^{-1}{}_{k,0}\vec{X}_k \quad =>$$

$$\cdots\cdots \qquad \cdots\cdots$$

$$\Phi_{k,0}\vec{X}_k = \Phi^{-1}{}_{k,0}\vec{X}_k \qquad \vec{X}_k = \Phi^{-1}{}_{0,0}\Phi^{-1}{}_{k,0}\vec{X}_k$$

$$\Phi'_{i,k} = \begin{bmatrix} \Phi^{-1}{}_{i,0}\Phi^{-1}{}_{k,0} \\ \cdots\cdots \\ \Phi^{-1}{}_{k,0}\Phi^{-1}{}_{k,0} \end{bmatrix}$$

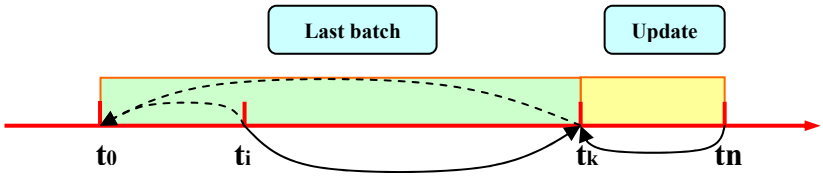

Figure 6.4 State transition matrix mapping in sliding-window short-arc filter.

The new state transition matrix is stored with other data at every batch. We can see that the first iteration in the filter is really fast due to most calculation having already been done in the previous batch. Only data from new updates are calculated. In most cases, after the first iteration with precise filtering information from previous data, the convergence speed is fast, a normally one or two more iterations is enough. Based on the previous discussion, a sliding-window filter is an optimum choice for onboard processing (more experimental results will be presented in the next section).

Furthermore, we observed distinct edge effects from previous short-arc results, especially for the shorter arcs. This is because the whole integration arc is considered equally in the least squares filter, but the orbital model error grows with time, and best result is around the middle of the arc. To circumvent this effect we use a different method in this test to get remove the solution either side of the arc. Obviously we have to use overlapping data to generate a continuous solution.

6.4 Experiment Results

6.4.1 Long-arc OD

For comparison, best filtering results are presented here using one day SACC GPS data. A full orbital model and IGS solution was used. To compare the result with the following short-arc ones we did not use high parametreization schemes, only two orbital parametres were estimated. Table 6.3 summarizes the OD data processing strategies. Figure 6.6 shows the position and velocity error compared to JPL precise solution. It can be seen that a 3D positional accuracy of 80 *cm* was achieved, while the 3D velocity error is 2 *mm/s*. The result is quite reasonable because only code measurements were used. All the results below were compared against JPL ephemerides, which have centimetre level accuracy.

Table 6.3 Long-arc OD data processing strategies.

Orbit force modelling	
Earth Gravity Model	JGM 3, 70x70
Third body gravity	Sun & moon, all planets except Pluto
Planet ephemerides	JPL DE405
Solar pressure	Direct effect
Atmospheric density model	MSIS 86
Pression / Nutation	IAU1976 / IAU 1980 (with corrections)
Polar motion	IERS bulletin B
GPS Data Processing modelling	
P code noise threshold	5m
GPS ephemerides	IGS final solution
Carrier phase smoothing	Every 15 minutes
GPS Data processing mode	Ionosphere free P code with single difference
Estimation Strategy	
Filtering arc	1 day batch
Parametre estimation	8 (6 state vector, drag and solar pressure coefficients)

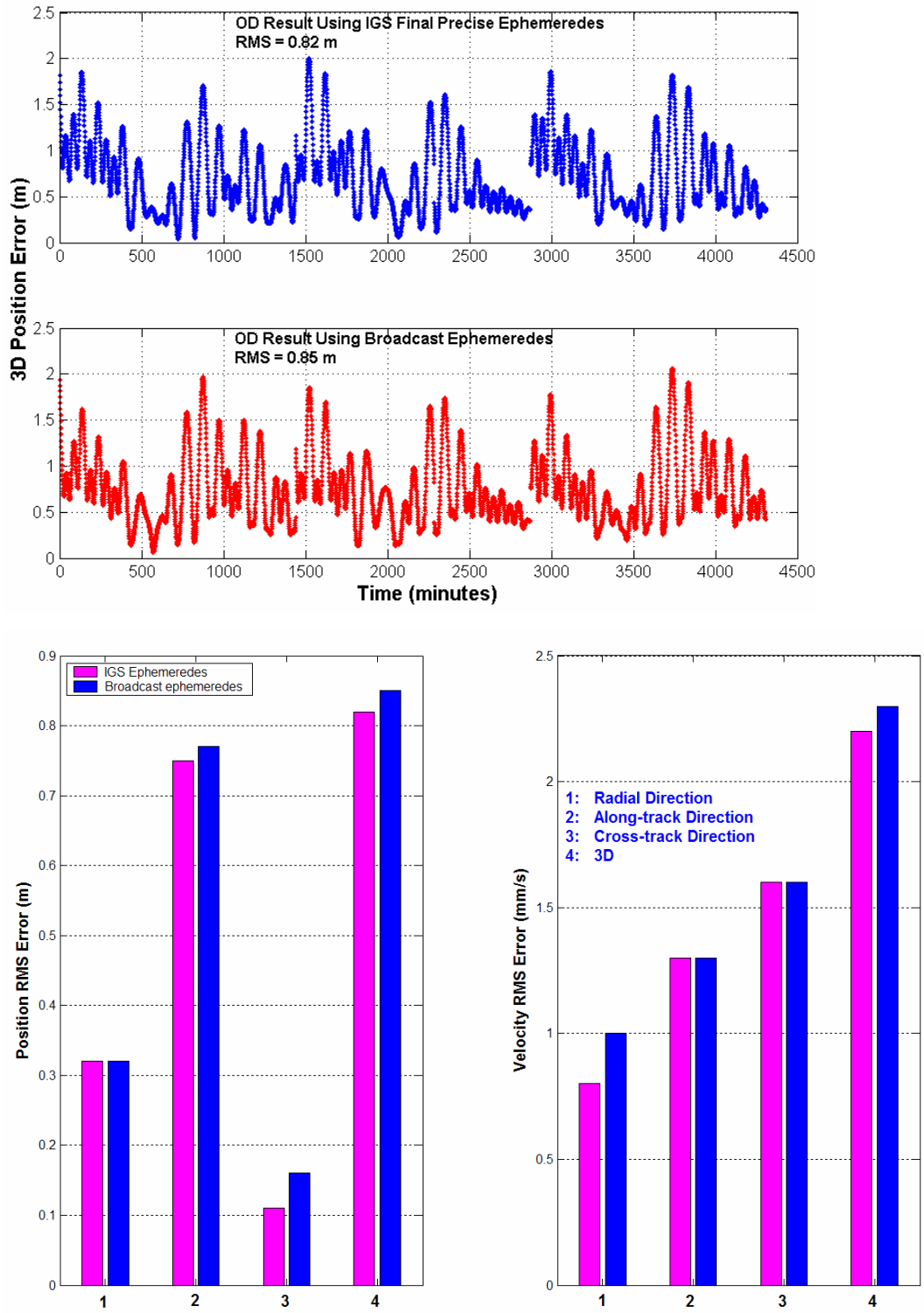

Figure 6.5 24 hours OD result for SACC using broadcast and IGS ephemerides.

6.4.2 Discrete Short-arc Results

As described in Section 6.3.3 discrete short-arc means batch-to-batch and that there is no correlation between each batch. Three days' SAC-C GPS data has been

processed using different arc lengths: 15 minutes, 30 minutes, 1 hour, 2 hours, 3 hours and 4 hours. The main purpose of this test is to estimate the achievable orbit determination accuracy with short arcs. The full orbital model mentioned in the previous section was used and orbital parametres were estimated. The 3D RMS orbit errors for every option are illustrated in Figure 6.7. It is observed that the best result was achieved by a 2 hour arc. Longer arc filtering generated even worse results, which suggests orbit system error exceeds the measurement noise level as the arc becomes longer than 2 hours. Figure 6.8 shows the RMS error in the along-track, cross-track and radial components. Figure 6.9 shows the velocity error.

6.4.3 Sliding-window Short-arc and Parametreization

The performance of sliding-window short-arc filtering was also tested. Table 6.4 lists the window sizes and update rates for the different schemes. The window size is around 3 times the update rates, so we can use 66% of the data as solutions from every batch. The results are presented and discussed in the next section.

Table 6.4 Sliding-window short-arc data selection overview.

	update rates (minutes)	overlap length (minutes)	pre-overlap (minutes) Discarded measurements
15 minutes	3.0	6.0	3.0
30 minutes	5.0	10.0	5.0
1 hour	10.0	20.0	10.0
2 hours	20.0	40.0	20.0
3 hours	60.0	60.0	30.0
4 hours	80.0	80.0	40.0

Furthermore, orbit parametre estimation was introduced. We used two schemes:

- I: atmosphere drag coefficient
- II: atmosphere drag coefficient and solar pressure coefficient

When scheme II was considered only longer arcs (1~4 hours) were tested because the estimation process is unstable with very short arcs. All the results are presented in the next section.

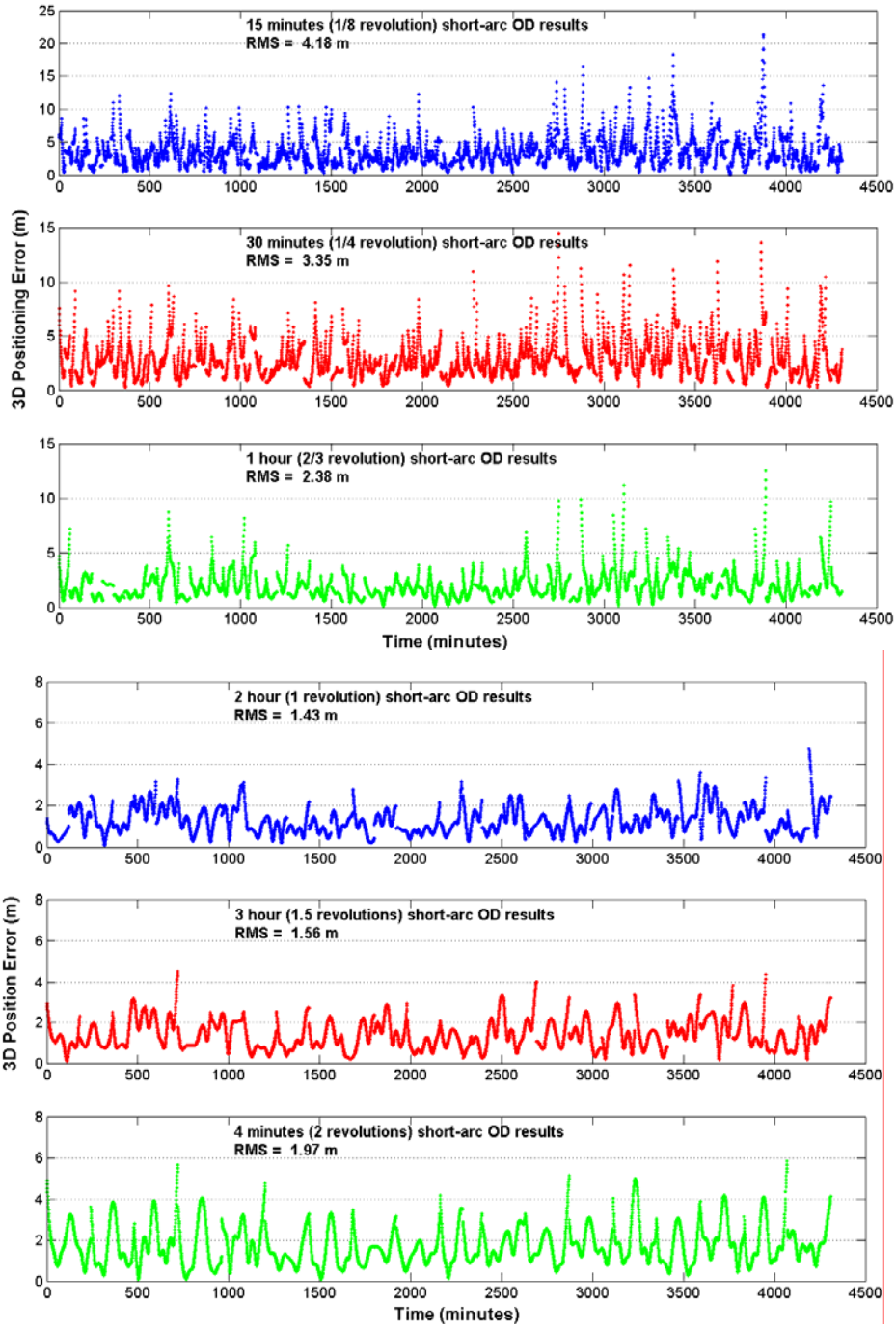

Figure 6.6 Illustration of discrete short-arc estimation results using different arc lengths.

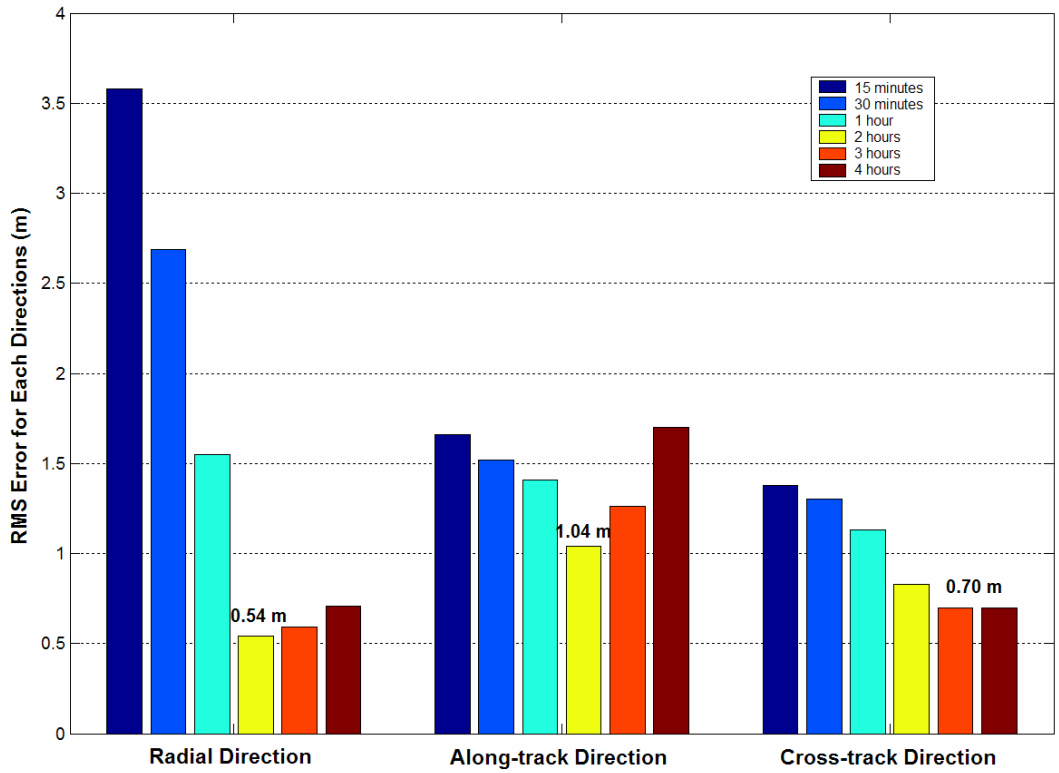

Figure 6.7 Comparison of the along-track, cross-track and radial orbital error for all the discrete short-arc schemes.

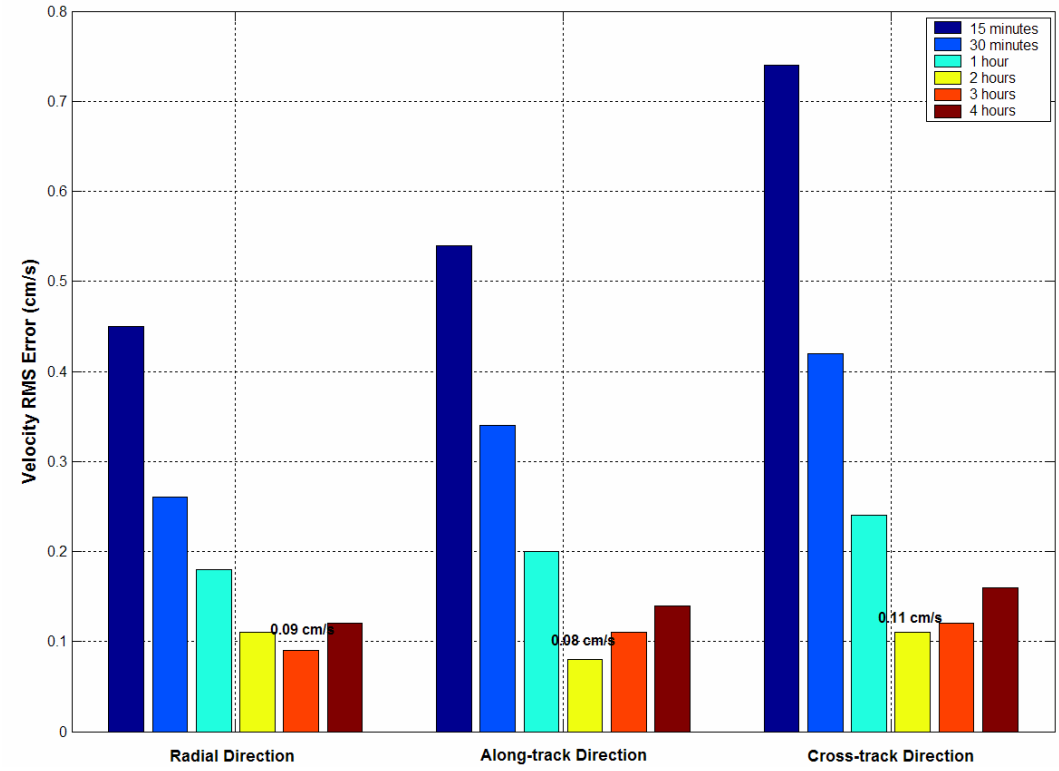

Figure 6.8 Comparison of the velocity errors for all the discrete short-arc schemes.

6.4.4 Error Analysis

Based on the filtering results of the previous sections, experiments were carried out to study the filtering residuals with different arc lengths for LEO Orbits. The following aspects were inspected:

- Pre-fitting and post-fitting residuals were analyzed. We want to distinguish the errors caused by different sources, such as orbital model error, measurement model and measurement noise. The use of the JPL precise ephemerides results this split to be made.
- Orbital model errors caused by different arc length, and the parametre estimation results in a short-arc filter.
- The effect of different weighting schemes on the residuals.
- The batch filter convergence speed, as this greatly affects the computional efficiency.

Figure 6.9 compares all short-arc filtering schemes. We found that filtering with sliding-windows of 2-to-4 hours and 7 or 8 parametres (6 states+1 for drag coefficient +1 for SRP), usually gives good results, achieving 3D RMS of 1.3 m. Figure 6.16 compares the pre-fit residuals of the OD filter for all the short-arc filtering schemes, showing the residual growth with the data arc.

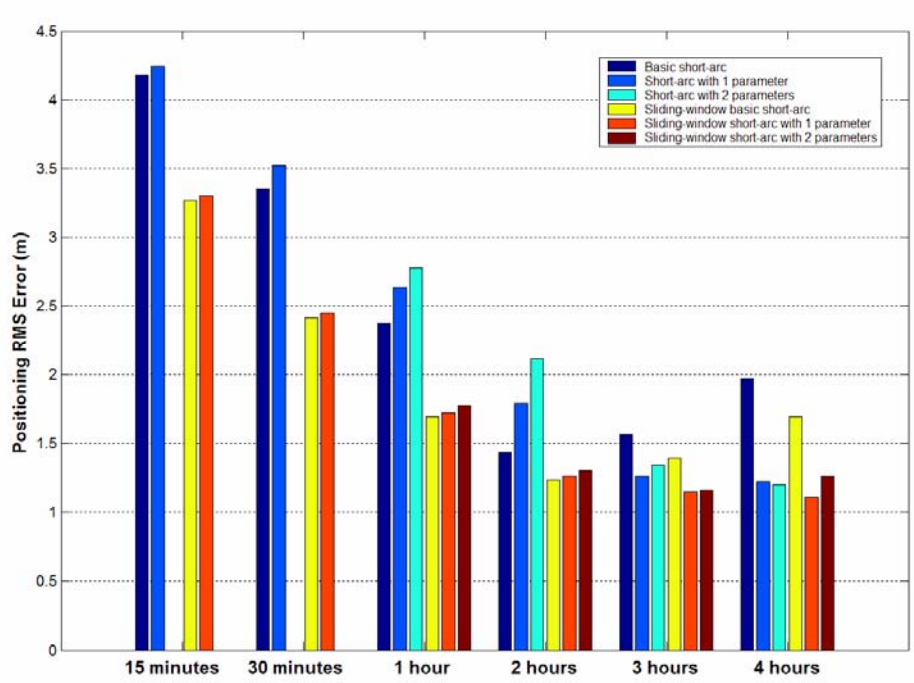

Figure 6.9 Comparison of 3D RMS for all the short-arc filtering schemes.

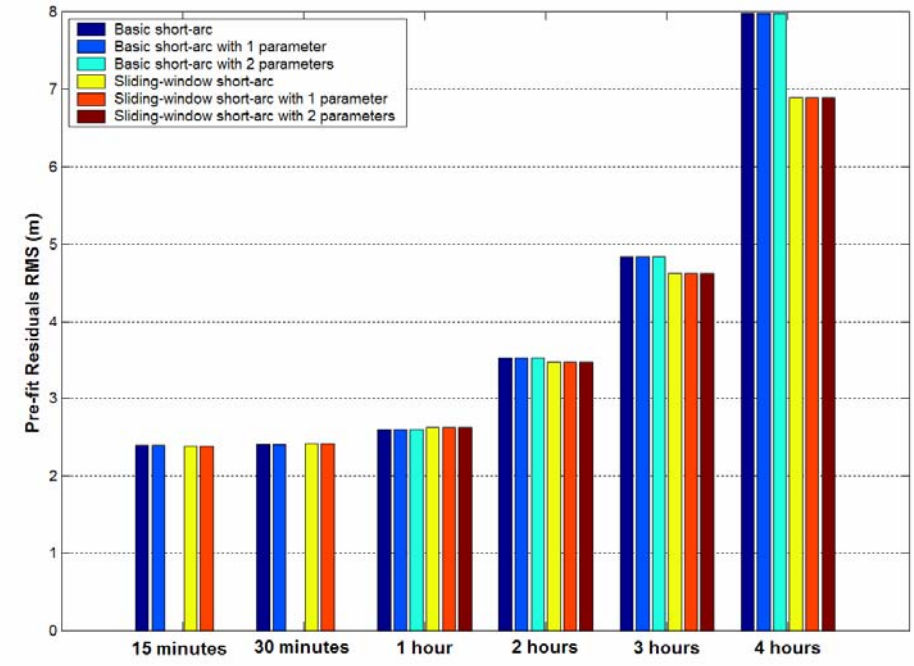

Figure 6.10 Comparison of pre-fit residuals of OD filter for all the short-arc filtering schemes.

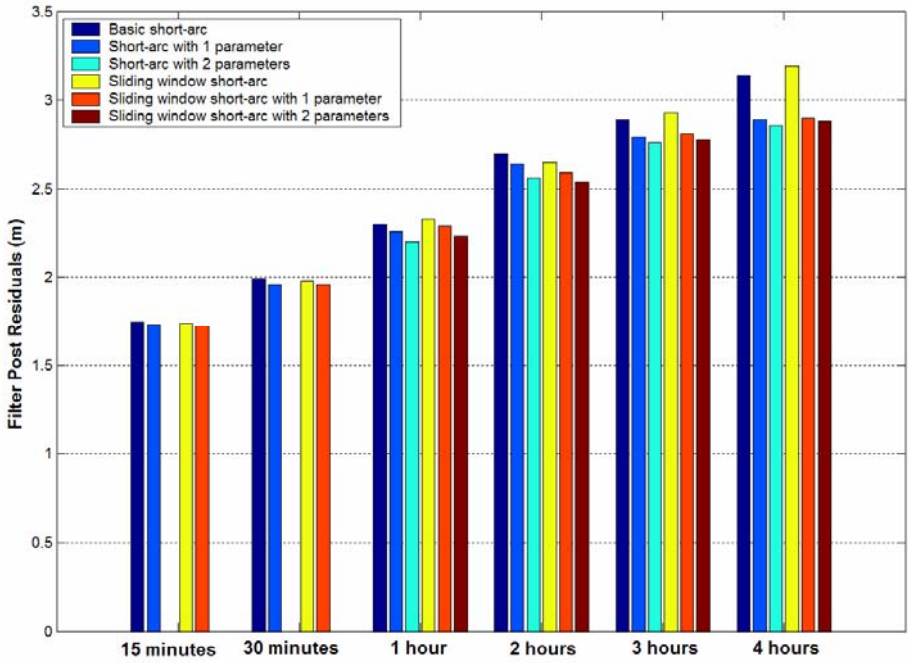

Figure 6.11 Post residuals of OD filter for all the short-arc filtering schemes.

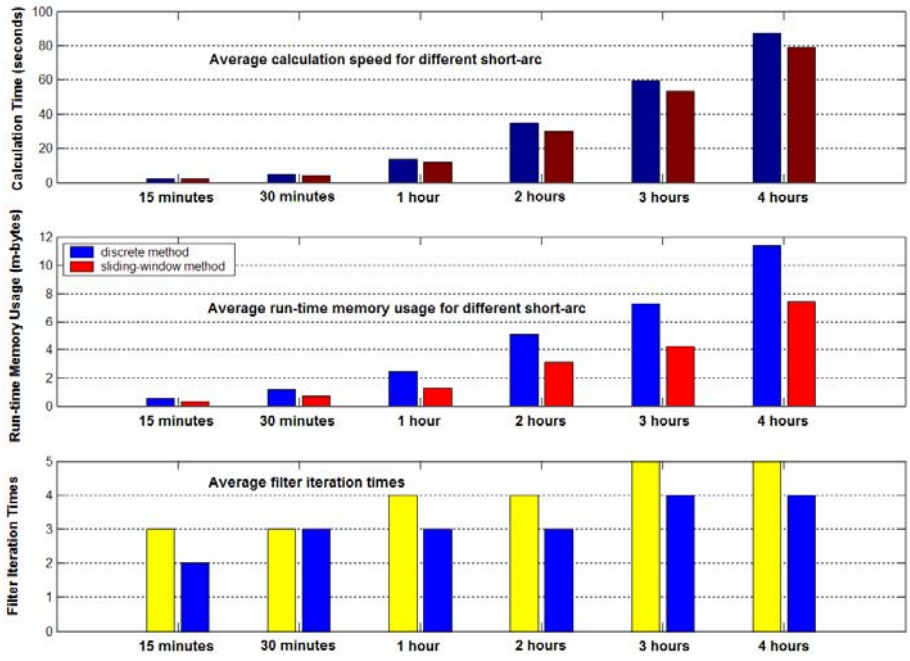

Figure 6.12 Comparison of computational burden for all the short-arc filtering schemes.

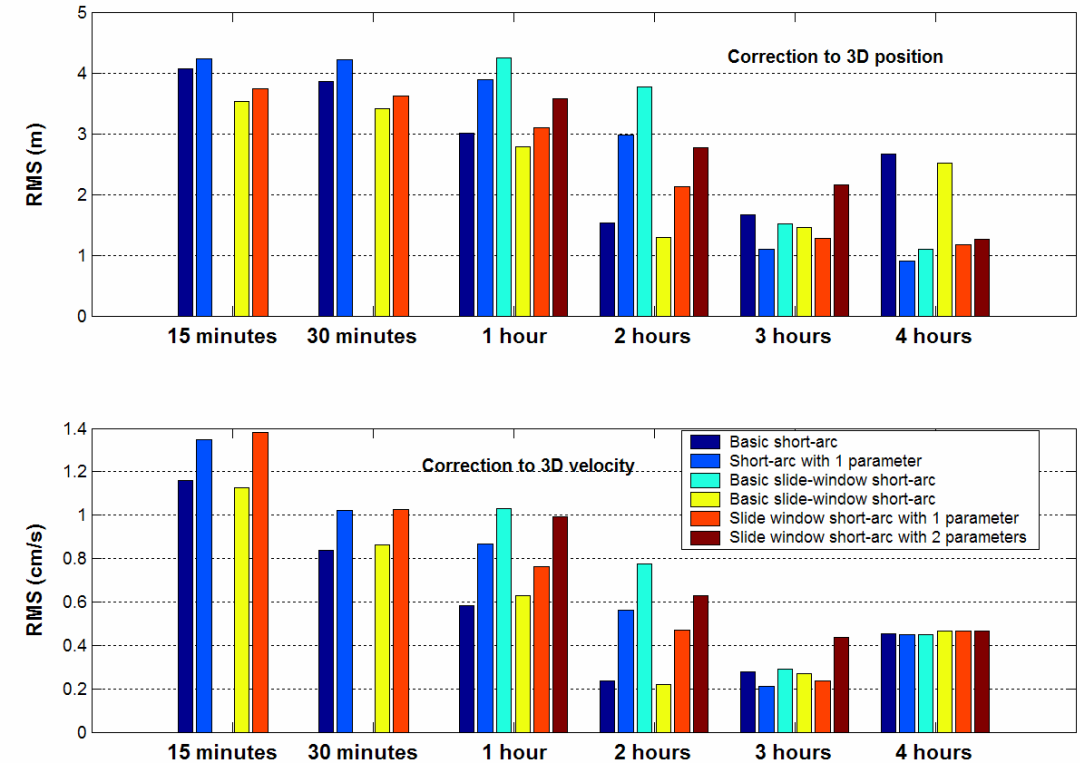

Figure 6.13 Comparison of state vector corrections RMS for all the short-arc filtering schemes.

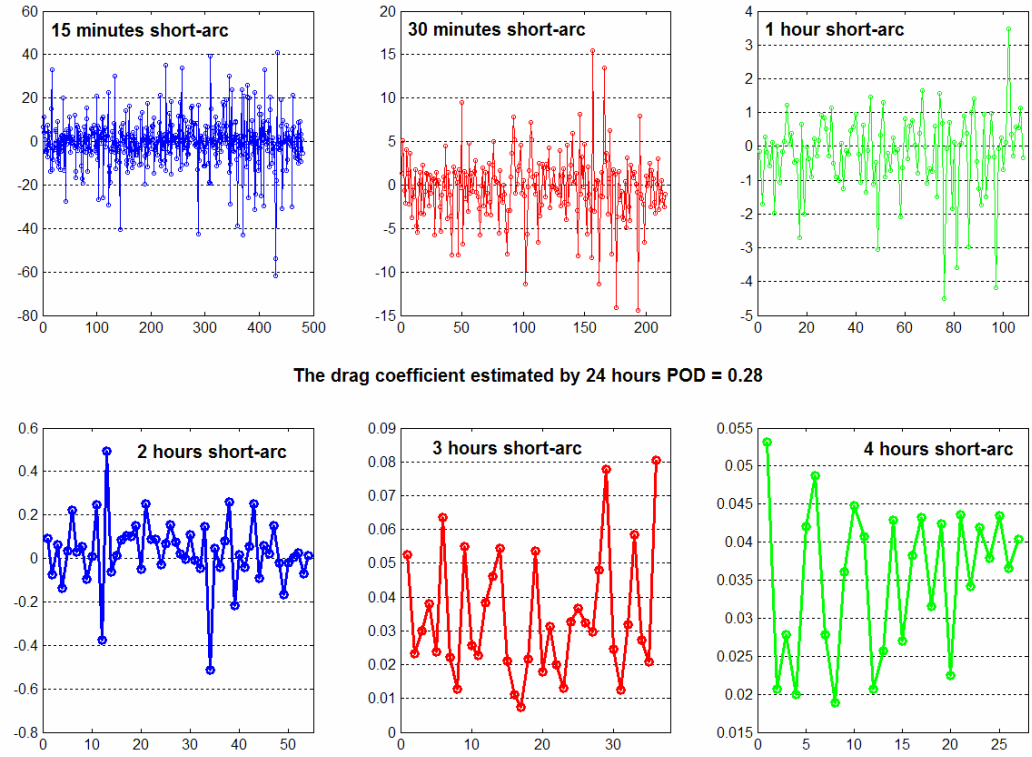

Figure 6.14 Estimated drag coefficient from the sliding-window short-arc filtering with 1 parametre configuration.

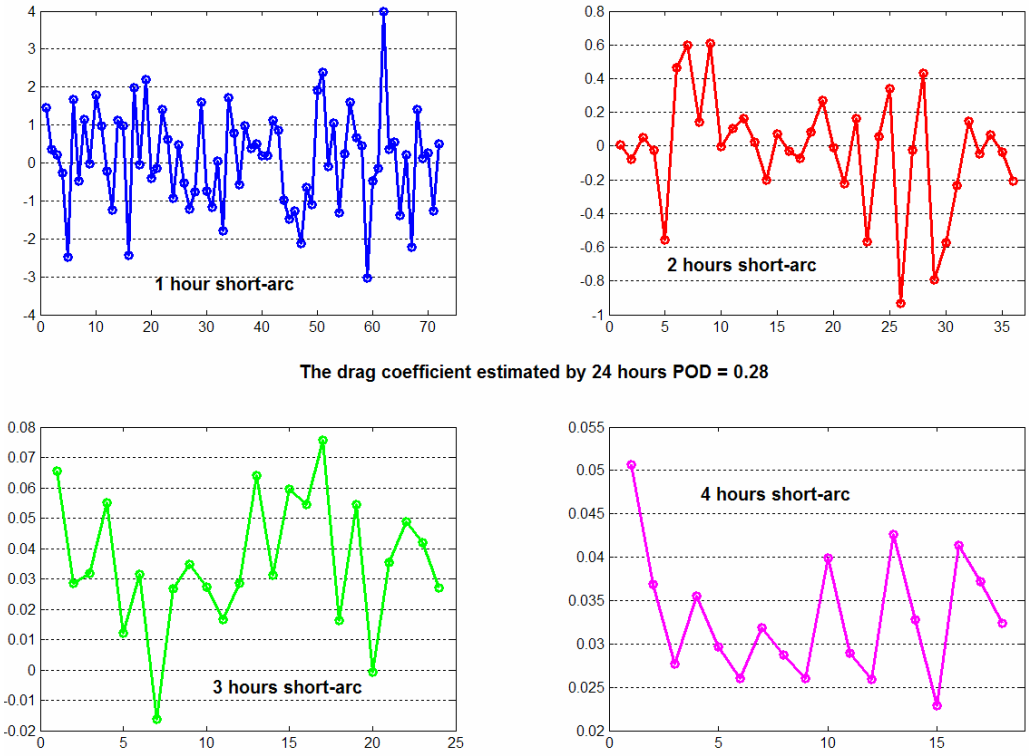

Figure 6.15 Estimated drag coefficient from the sliding-window short-arc filtering with 2 parametres configuration.

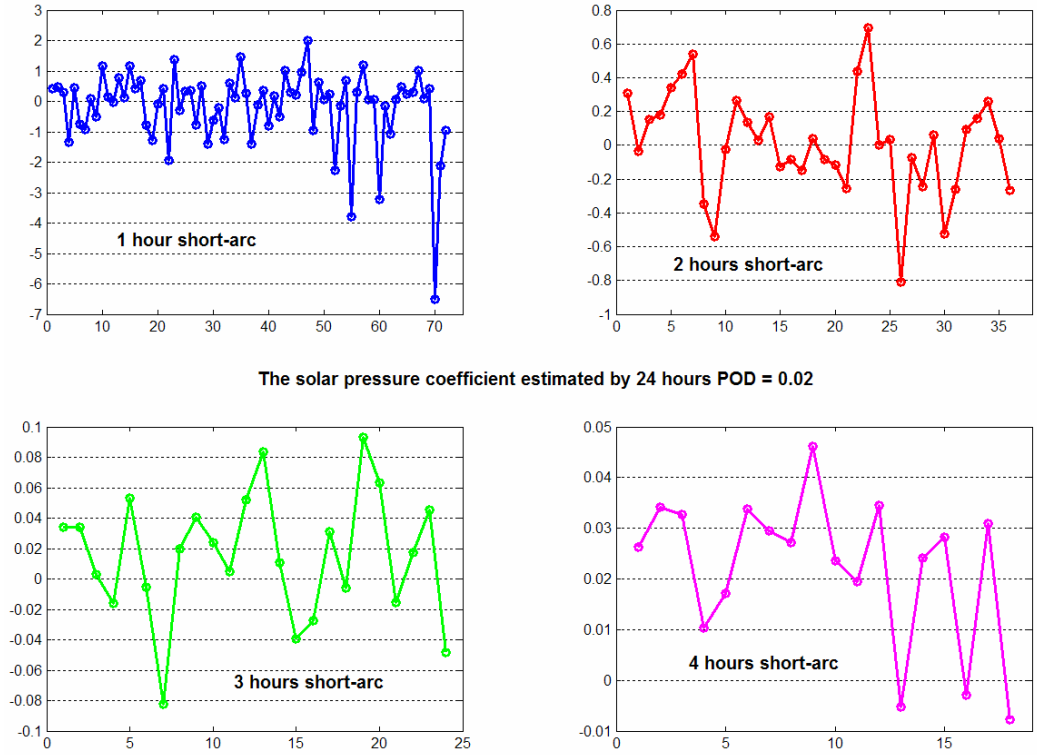

Figure 6.16 Estimated solar pressure coefficient from the sliding-window short-arc filtering with 2 parametres configuration.

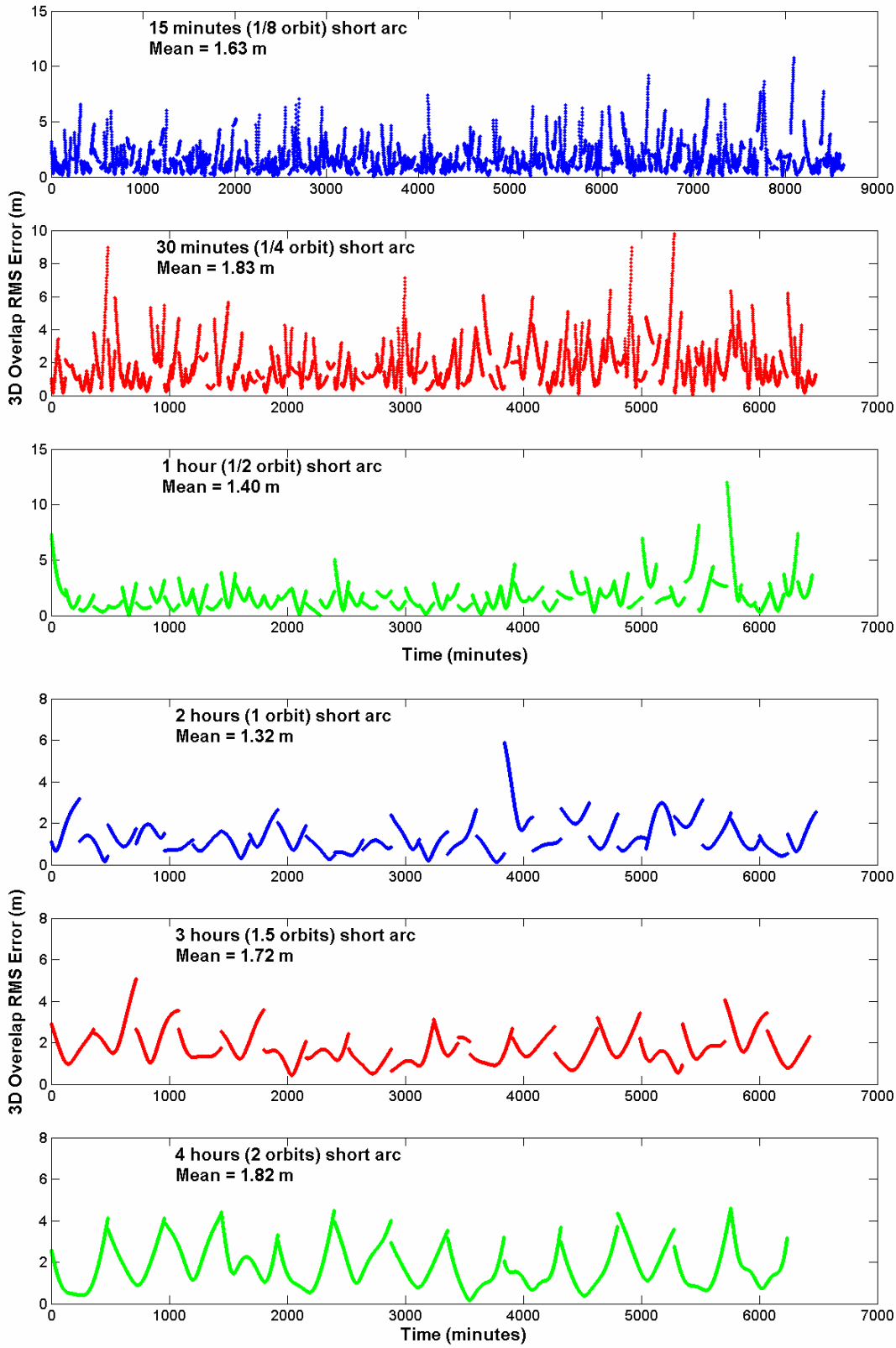

Figure 6.17 Overlap positional errors from non-parametreization sliding-window short-arc results.

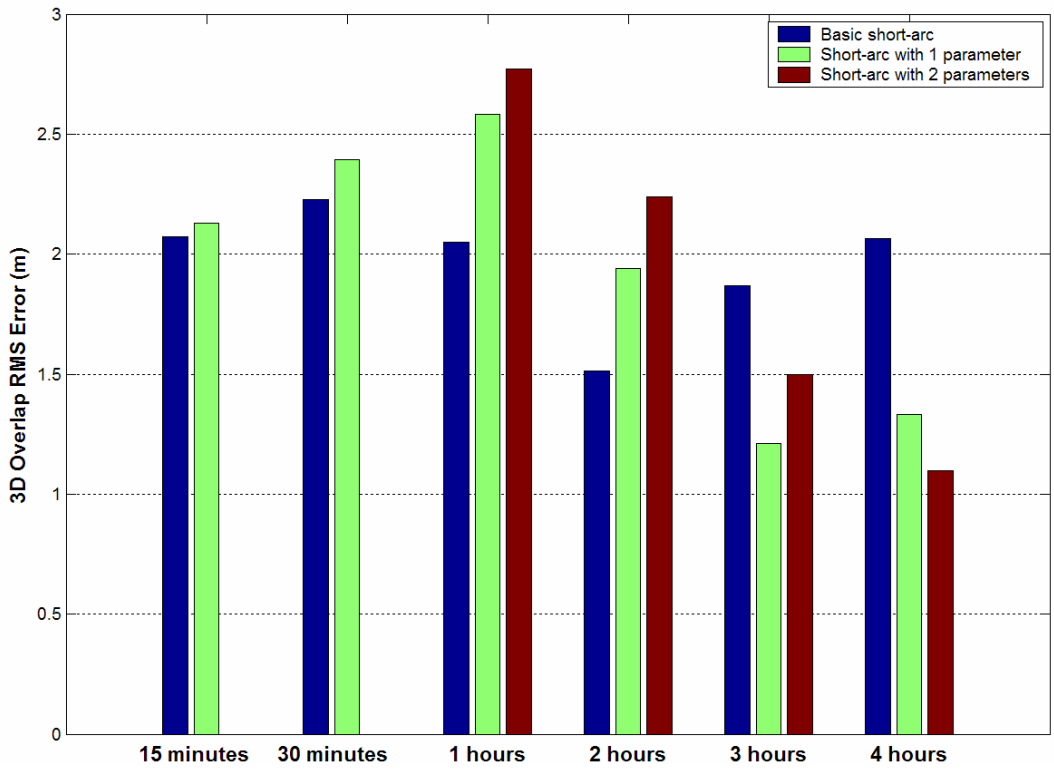

Figure 6.18 Comparison of overlap positional 3D RMS error from sliding-window short-arc results.

6.4.5 Accuracy vs. Computional Burden

After the proposed techniques discussed in Chapters 3, 4, 5 and 6 have been combined into the short-arc filter, the overall orbit determination performance was tested. We used the simplified orbit dynamical model introduced in Chapter 3, but with the Earth gravity acceleration approximation method. In addition we used the sliding-window carrier-phase smoothing method combined with the simple outlier detection algorithm discussed in Chapter 5. We used the sliding-window method because it generally outperforms its discrete counterpart. The position and velocity accuracies were compared with both the long-arc orbit determination and the onboard navigation solution. We also investigated the computional burden. Table 6.5 lists the candidate test schemes. Figure 6.19 shows the orbit error in the along-track, cross-track, radial directions and 3D for all the short-arc filtering schemes, from SPP to long-arc OD results. Figure 6.20 illustrates the corresponding velocity errors. All results are with reference to JPL's GIPSY-OSISS POD solutions accurate at centimetre level. In comparison with the long-arc orbital accuracy of 3D RMS of

0.8m, an accuracy of 1.2m was achieved with a 2-hour short-arc. For velocity, better accuracy is achieved with 2-hour short-arc data.

Figure 6.21 compares the computional burden. The computing time compared long-arc OD, SPP and sliding-window short-arc methods. It was observed that the computation time for 2-hour short-arc methods could be shortened from about 1000 second to 30 seconds. This improvement is very significant for onboard orbit determination.

Table 6.5 Short-arc filtering comparison test schemes.

Schemes	Method	Orbital model	Arc length	Updates
I	SPP (IGS)	-	-	-
II	24 hours discrete arc	Full	24 hours	-
III	Sliding-window short-arc	Simplified	30 minutes	10 minutes
IV	Sliding-window short-arc	Simplified	1 hour	20 minutes
V	Sliding-window short-arc	Simplified	2 hours	40 minutes

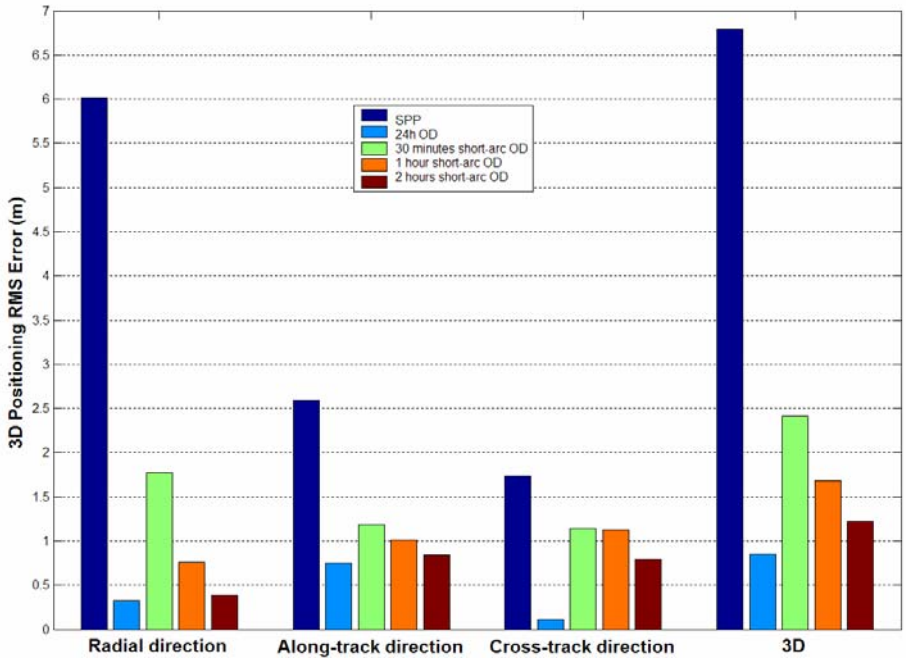

Figure 6.19 Comparison of the along-track, cross-track, radial and 3D orbital error for all the short-arc filtering schemes with SPP and long-arc OD results.

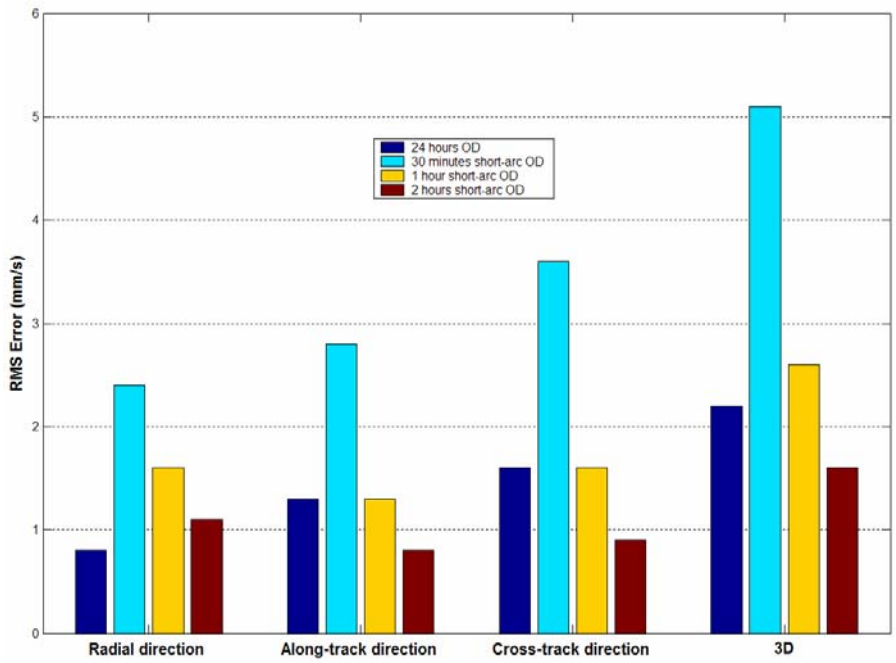

Figure 6.20 Comparison of the along-track, cross-track, radial and 3D velocity error for all the short-arc filtering schemes with the long-arc OD result.

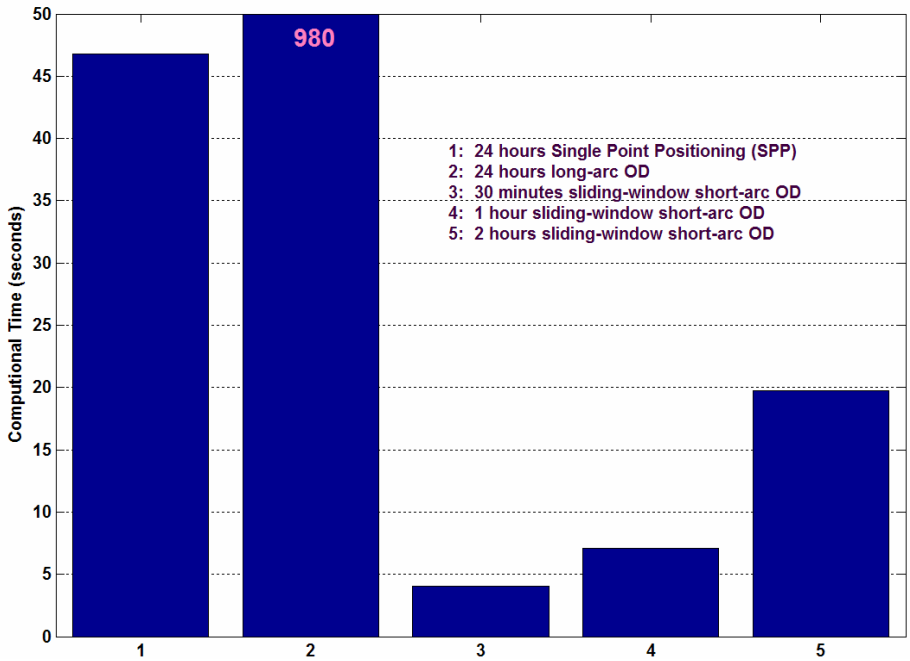

Figure 6.21 Comparison of computing time for all the short-arc filtering.

6.5 Summary

A dynamic approach is necessary for onboard orbit determination at different altitudes in order to achieve metre-level orbit accuracy and provide continuous orbit

solutions in circumstances where there are few GPS observations. A simple but robust dynamic method has been proposed based on short-arc batch estimation, in order to address both orbit accuracy and computional burden issues critical for onboard orbit determination with GPS code measurements.

Furthermore, the sliding-window short-arc method can fulfill the requirement for near-real time onboard orbit determination onboard. It updates the processing arc every 5 ~ 40 minutes, and generates the orbit solution with 5 ~ 40 minute delays, with high accuracy, after the last observation. The computation time for the process takes several seconds to 20 seconds to complete using a PIII processor.

The experimental results from three day data sets of the SAC-C mission have demonstrated that use of the shorter data arcs allows for simplifications of both the physical and observational models. We can make the following conclusions for SAC-C:

- With a data arc as short as 30 minutes, a 3D position RMS error of 2.5 *m* and 3D velocity RMS error of 5 *mm/s* can be achieved with 5 minutes latency. The solution is more stable than that of a traditional Kalman filter, and it doesn't require any initialization process (which is around 4~6 hours for a typical Kalman filter). Furthermore, the computional burden is comparable to Kalman filter processing.

- With a data arc of 1~2 hours, a 3D position RMS error of 1 *m* and 3D velocity RMS error of 2 *mm/s* can be achieved with 10 ~ 20 minutes latency. The radial component position accuracy was 40 *cm*, which can satisfy many scientific applications. The accuracy is nearly reaching that of a ground-based long-arc OD using the same data sets (smoothed code, standalone) with much less computing burden.

In summary, the result achieved with the proposed short-arc strategies is quite encouraging and promising, suggesting a new method for onboard orbit determination.

Chapter 7
Orbit Determination for FedSat

The above chapters focus on models and estimations issues, including simplification of orbital models, improvement of measurements and development of short-arc estimation strategies. In this chapter, we present the results from FedSat orbit determination mission and tracking. This section, on the one hand, will further verify the theory and concepts proposed models and methods, and on the other hand, demonstrate the effects of the proposed strategies in a ground-based near-real time precise orbit determination system for FedSat, which has supported the FedSat scientific missions, such as Ka-band tracking and GPS atmosphere studies, within the CRCSS community, since its successful launch in December 2002.

7.1 Overview of FedSat

Although Australia was the third nation in the world to be able to launch a satellite in the 1960s, it is some thirty years since WRESAT, a small amateur satellite was launched. This situation changed in 1997 with the establishment of the Cooperative Research Centre for Satellite Systems (CRCSS) under the Australian Government's CRC Program. The first and primary project of the CRCSS is to launch a low Earth orbiting microsatellite, FedSat, into an 800 kilometre circular polar orbit with an inclination of 98.7°. FedSat was successfully launched into the orbit at the Tanegashima Space Centre in Japan on 14th December 2002, and has been operating for the following three years.

FedSat is not a mission dedicated to a single scientific or engineering goal. Instead, it carries a range of experimental research payloads, which are based on the engineering and scientific activities of the participants in the CRCSS, in order to gain experimental information. These CRCSS activities are focused under four

programs, the Space Science Program (University of Newcastle, NSW; La Trobe University, Melbourne), the Communications Program (University of South Australia, Adelaide; University of Technology, Sydney) and the Satellite Systems Program including navigation and high performance computing (Queensland University of Technology, Brisbane). The payloads include a fluxgate magnetometre, Ka-band satellite communication system, a GPS receiver and a high performance computing platform.

The GPS payload of FedSat, the BlackJack Receiver, is a joint project between CRCSS and NASA, USA. It is a space enabled specific receiver, costing about US$500,000. It can provide real time orbit and time information for the onboard and ground scientific usage. Figure 7.1 shows the FedSat mission launch phases. Figure 7.2 shows the FedSat in the assembly laboratory and deployment in space.

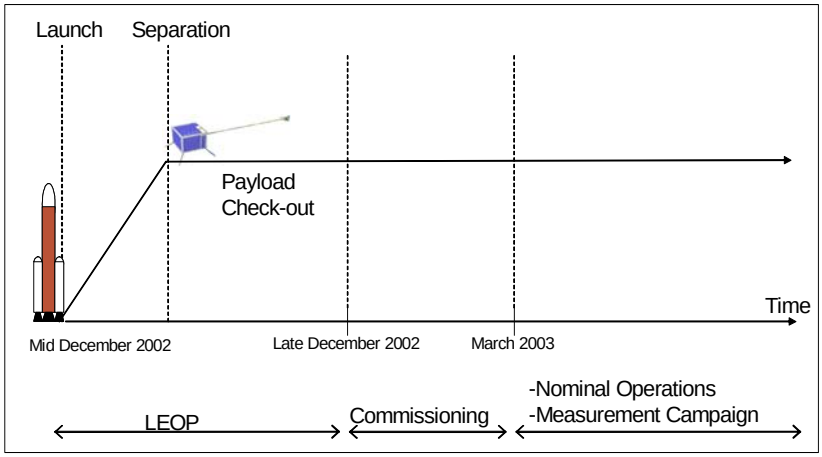

Figure 7.1 FedSat payload mission phase.

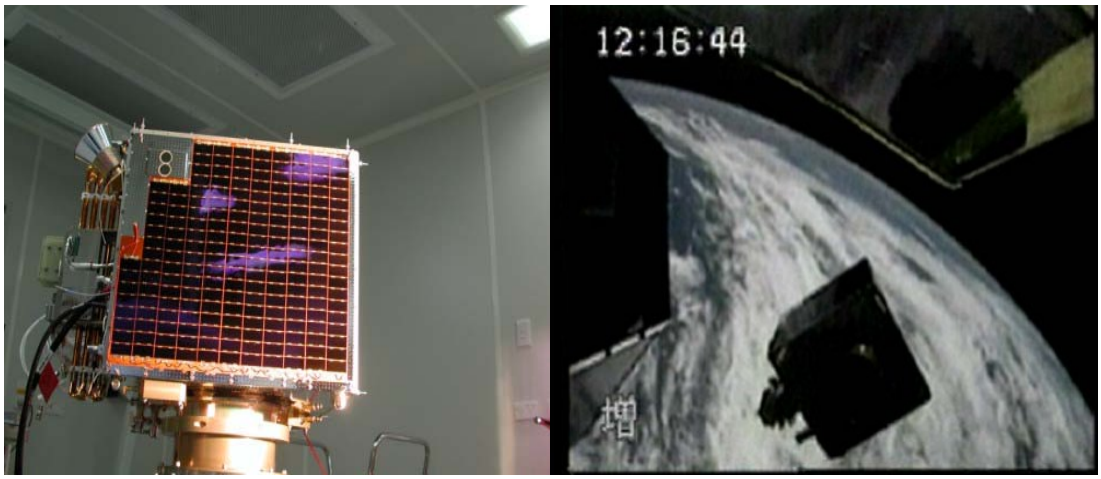

Figure 7.2 FedSat in the assembly laboratory (left) and deployment in space (right).

7.2 Orbit Determination of FedSat

7.2.1 Introduction

A low Earth orbiting (LEO) satellite collecting GPS data with an onboard GPS receiver can compute its state (position & velocity) in diverse ways, the choice depending on, in part, the type of orbit and mission requirements. FedSat, like many other LEO satellites, uses GPS for engineering and scientific missions. The requirements for orbit knowledge include:

- Real-time state knowledge for routine tracking operations and onboard engineering needs. A 3D RMS accuracy of hundreds of metres is needed.
- Near real-time orbit state knowledge for space-based Wide Area Differential GPS positioning studies and FedSat Doppler positioning testing, requiring an accuracy of metre-level or better.
- After-the-fact precise orbit determination for scientific analysis, such as GPS atmospheric sounding, to achieve orbit accuracy of a few decimetres or better.

A large number of the existing GPS flight experiments have demonstrated that GPS can meet the stringent needs for the most dynamically unpredictable flight vehicles with continuous tracking of GPS satellites. The principal difference between FedSat and other GPS-based LEO satellites is that FedSat onboard GPS data collection will not be continuously carried out due to the limitation of power supply. More specifically, only a total of 20 minute time per orbit period, which is about 100 minutes, will be allocated to GPS continuous operation. This tracking scenario changes almost everything: from achievable orbit accuracy of different levels, to techniques for improved real time positioning and orbit determination.

7.2.2 Problems with FedSat Orbit Determination Using GPS

7.2.2.1 Duty Cycle GPS Operation Mode

Unlike many other GPS-based LEO satellites, the FedSat flight GPS receiver only operates in duty-cycle mode, or 20 minutes per orbit (100.9 minutes) due to the strict

limitation of power supply onboard the satellite, although it may occasionally turn to continuous operation for precise orbit experiments. Pre-launch testing revealed that it took 4 to 5 minutes for the GPS receiver to start normal operation after power supply is available. This means there will be observations of 1-by-15 minutes per orbit effective for orbit determination.

Knowing the achievable orbit accuracy under specific operation conditions and processing modes was of primary concern to the operators. Our pre-launch covariance analysis was given towards the 1-by-15 operations [*Feng*, 1999, 2000]. It is now necessary to study the orbit accuracy in the cases of 1-by-15 minutes operations. Because a filtering processing is unlikely to proceed onboard the FedSat, we must use the flight GPS data downloaded each day to compute and typically predict the orbit into future 24 to 48 hours for real time operation use on the ground.

Results show that under the assumption of expected GPS standalone positioning performance where the 3D positional RMS accuracy about 10m to 15m, the effective data set of 1-by-15 minute per orbit for 24 hours can still result in quality predicted orbit for 48 hours. The predominated errors in the predicted orbit are the uncertainty of atmospheric force, which alone would reach 80 metres within 72 hours of prediction. The second largest modelling errors, solar radiation pressure, will lead the orbit errors of less than 10 metres. Considering all the effects including the atmospheric drag, the accuracy requirements of 100 metres in each component can be satisfied within two days of prediction. Figure 7.3 shows the GPS observation arc for FedSat.

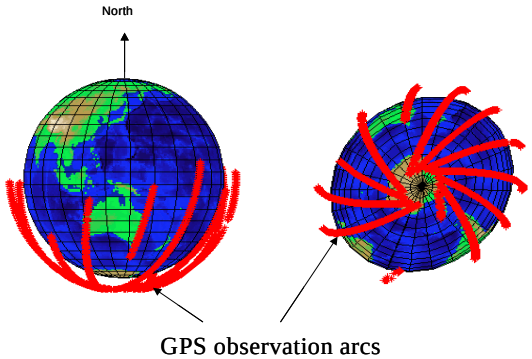

Figure 7.3 FedSat GPS duty cycle operation.

7.2.2.2 Aft-looking GPS Antenna

Normally in a LEO satellite mission, an upward-looking antenna is used for onboard navigation, timing and precise orbit determination purposes, and the antenna mounted towards other directions are used for different scientific missions. FedSat collects GPS data with its only aft-looking antenna, for both orbit determination and other scientific applications such as atmosphere occultation. As a result, only two-thirds of the hemisphere can be observed, and about half the measurements are collected at negative elevations. Figure 7.4 illustrates the image of the FedSat and the GPS antenna looking towards the anti-velocity direction. According to the altitude of the FedSat and the radius of the Earth, the negative elevation will reach –27.5 degrees. Therefore, the field of view of the aft-looking antenna is nearly two-thirds of the hemisphere. The mask angles for orbit determination or positioning are 90 and –25 degrees respectively. The satellites with the elevations between –25 and –27.5 degrees maybe occulted, and their measurements can be used for atmospheric occultation studies [*Yunck*, 2002].

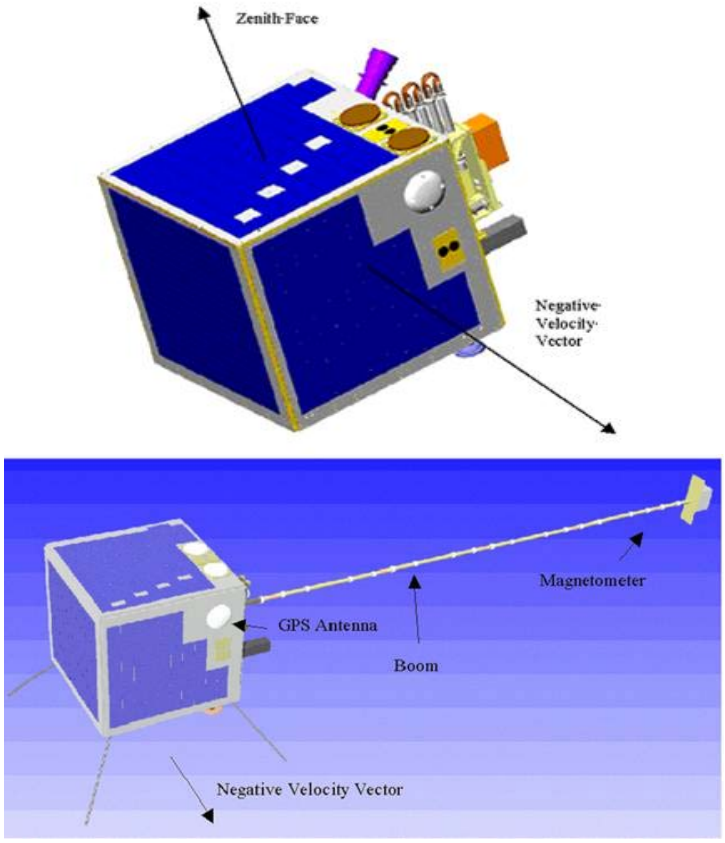

Figure 7.4 FedSat aft-look GPS antenna location.

Figure 7.5 shows how the FedSat aft-looking antenna views the GPS satellites in two-thirds of the sky, that is, the scope of elevation from –27 to 90 degrees. To avoid the effect of the atmosphere under 100km on the measurements, we can set the mask angle of –25 degrees in the process. The signals with elevation angles between –25 and –27 degrees are subject to the tropospheric delays, which, can be used for atmospheric occultation studies. In fact, due to the effect of occultation, the signals with elevation between –27 to –28.5 degrees are often received in the FedSat orbit. Our experiment result illustrates the distribution of the measurements against the elevation angles. We have observed that the majority of the measurements are collected with the elevations of under 20 degrees. The result is presented in the following sections.

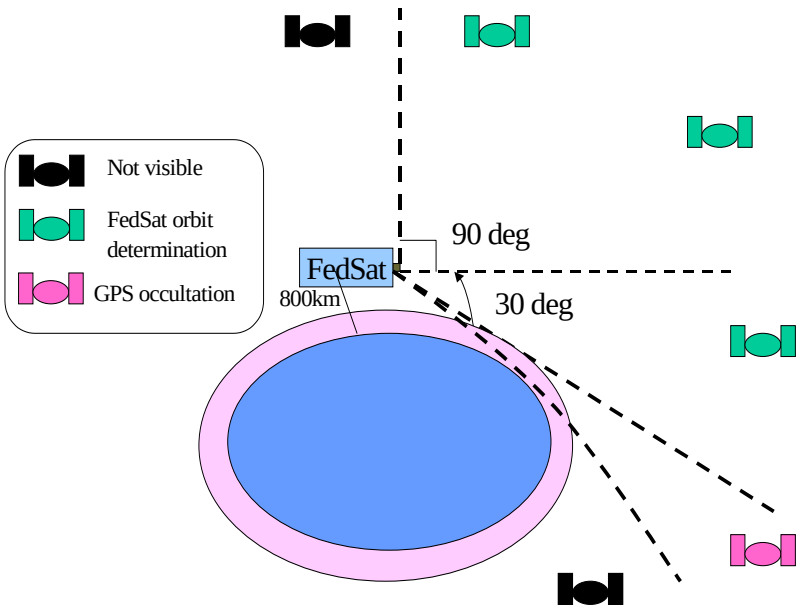

Figure 7.5 GPS measurement scenario in FedSat.

7.3 FODT Software Package

7.3.1 Introduction

To facilitate the research work and engineering application, a comprehensive GPS orbit determination software package, FedSat Orbit Determination and Tracking Software (FODT) has been developed during this research. Based on previous work

done in CRCSS, FODT has been developed by the author to perform the orbit determination using GPS for FedSat. It can fulfill the following tasks:

- Dynamic model analysis; it contains a full set of precise orbit dynamic model implementation. The first and second order partial derivatives of the state vector and parametres with respect to the initial parametres also have been fully implemented using precise models.
- High accuracy orbit integrator for short or middle term. Several numerical methods are implemented in the software, including 4^{th} Runge-Kutta, $7/8^{th}$ Runge-Kutta, $6/4^{th}$ Runge-Kutta-Nystrom and 4^{th} order Integra Equation Method.
- Precise Point Positioning (PPP) for spacecraft with or without the IGS precise ephemerides products.
- Near real time orbit determination (OD) using GPS measurements for LEO orbiters.
- Comprehensive GPS code/phase measurements analysis tools, which can give a detailed report of GPS measurement quality. This can be done in a pre or post process sense.
- Furthermore, FODT also provides a powerful real-time software development scheme for onboard orbit determination algorithm validation.

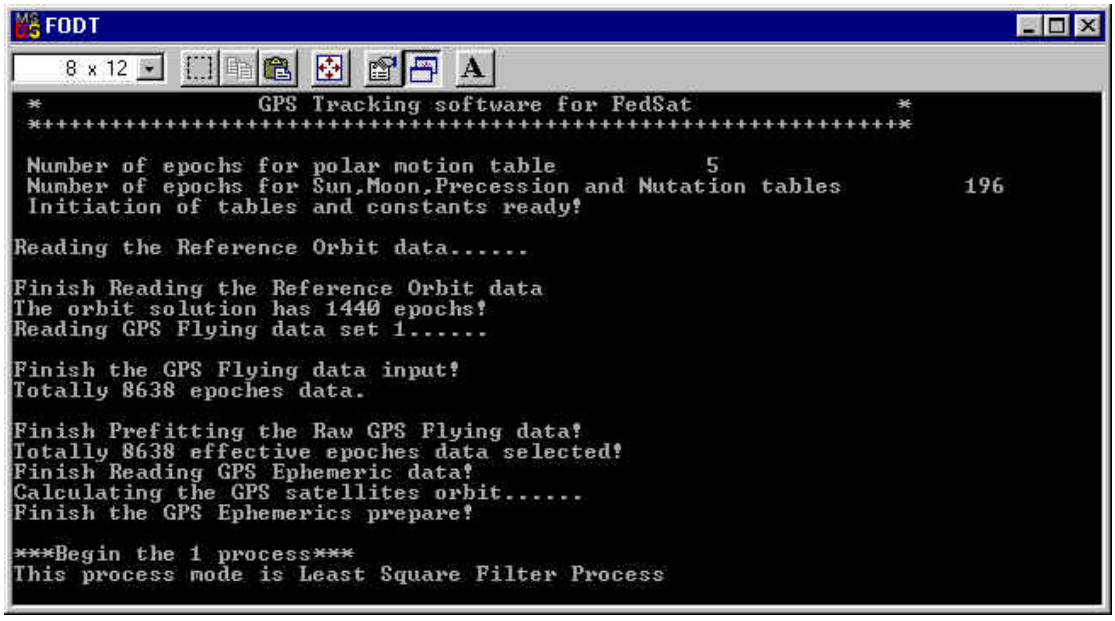

Figure 7.6 FODT software interface in DOS environment.

From the very beginning, FODT was designed as a modulated software package. It is in a third-tier logical structure. It contains a basic library, which provides more than 600 common functions to the upper level modules; each level two module can fulfill a single logical operation, such as data edit, GPS ephemerides calculation, single point positioning, etc; In level three, some scripts are used to configure and link level two modules to accomplish a complicated job. Figure 7.7 illustrates this concept.

From the programming point of view, FODT has been coded using ANSI C and FORTRAN; it contains 15 modules, more than 300 source files and around 70,000 lines of source code in total.

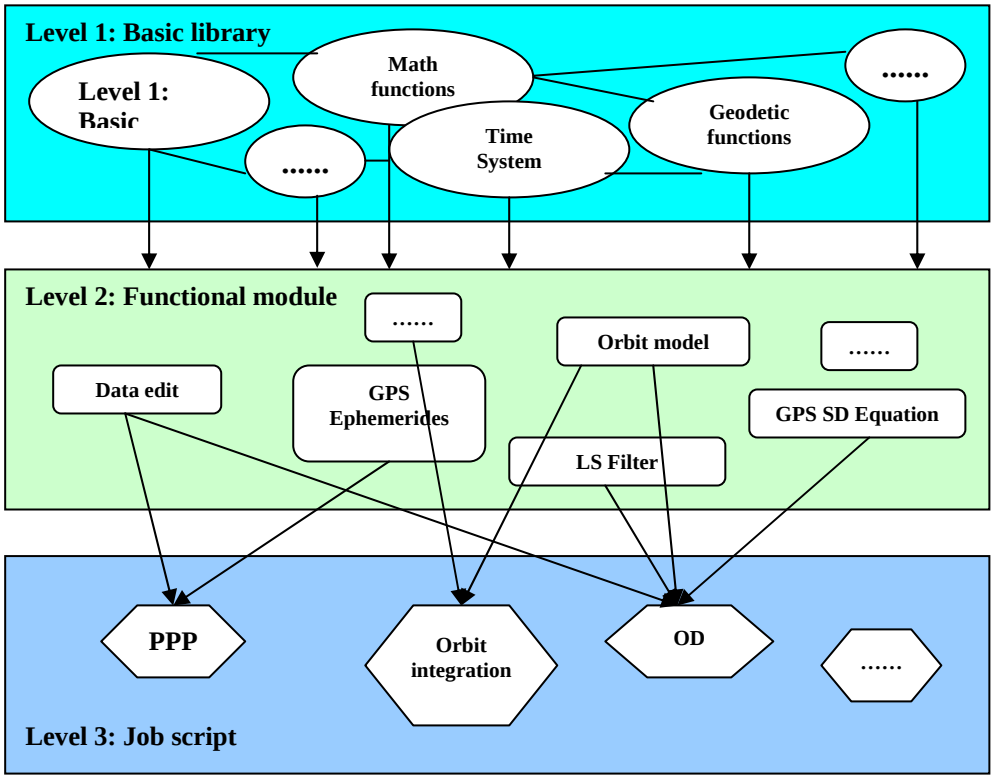

Figure 7.7 FODT software module structure.

7.3.2 Orbit Determination Module

Among all the modules in FODT, the most important one is the precise orbit determination module. It is used to support the FedSat Ground Autonomous Ka-Band communication system tracking. As showed in Figure 7.8 it contains four parts:

data acquisition and fitting, orbit modelling, measurement modelling, orbit filtering and orbit prediction.

The Data Edit (DE) module reads flight RINEX file, detects and excludes the outliers in code measurements, based on statistics of linear combination of code and phase observables. This process depends on flight measurements only, and is independent from Selective Availability, satellite orbit and geometry. The criteria for acceptance or rejection of a measurement vary from mission to mission in each procedure, achieving a balance between information quality and quantity for overall orbit accuracy. This module outputs a file of clean and standardized RINEX file for follow-up processing.

Orbit Modeling (OM) module, operated as a stand-alone program and subroutine, computes spacecraft orbits using numerical integration. OM starts from specified initial orbits, uses several forces models to integrate the differential equation to produce a nominal orbit, which is a set of time-tagged state vectors, together with the partial derivatives that relates the current states to the epoch-state, which is at the beginning or the end of the data arc. Two numerical integration methods have been built into OM to create an orbit trajectory and partial derivatives simultaneously: an adaptive-size fourth-order Runge-Kutta Method based on differential equation and a fixed-size Integration Equation (IE) method as described in *Feng* [2001].

Measurement Modeling (MM) module calculates the GPS orbit and clock bias from either broadcast or IGS ephemerides, then establishes the linear relationships between GPS measurements and the epoch state of the orbit. First, it computes the theoretical distances between using the nominal orbit of the spacecraft and GPS orbits, and then forms the pre-fit residuals with the range observations. Next it computes the design matrix of the partial derivatives of the ranging measurements with respect to the state elements, which include at a minimum, the adjustments to the six state parametres, and may include the adjustments to physical parametres: solar radiation pressure (SRP) as well as atmospheric drag coefficients. A detailed discussion of construction of the observation equation may be seen in *Liu* [2000], *Feng* [2001] and *Yunck* [1996].

Orbit Filtering (OF) module is a batch least squares estimator, which estimates the set of six state parametres along with some physical parametres, such as atmospheric coefficients and solar radiation pressure coefficient, using the data over a period of hours to days.

Orbit Prediction (OP) module consists of orbit integration and orbit representation processes. Orbit integration uses the improved epoch-state and estimates of physical parametres instead, propagating 2 to 3 days forward for real time FedSat tracking use. These orbit solutions are presented in a given format and time steps, such as SP3 at 60 seconds, in both Earth centred and Earth Initial (ECI) and Earth-Centred and Earth-Fixed (ECF) coordinate systems. Orbit Representation uses a polynomial function, such as Chebyshev polynomial, to represent the orbit as a continuous function of time segment by segment. This process must not lead to loss of orbit accuracy.

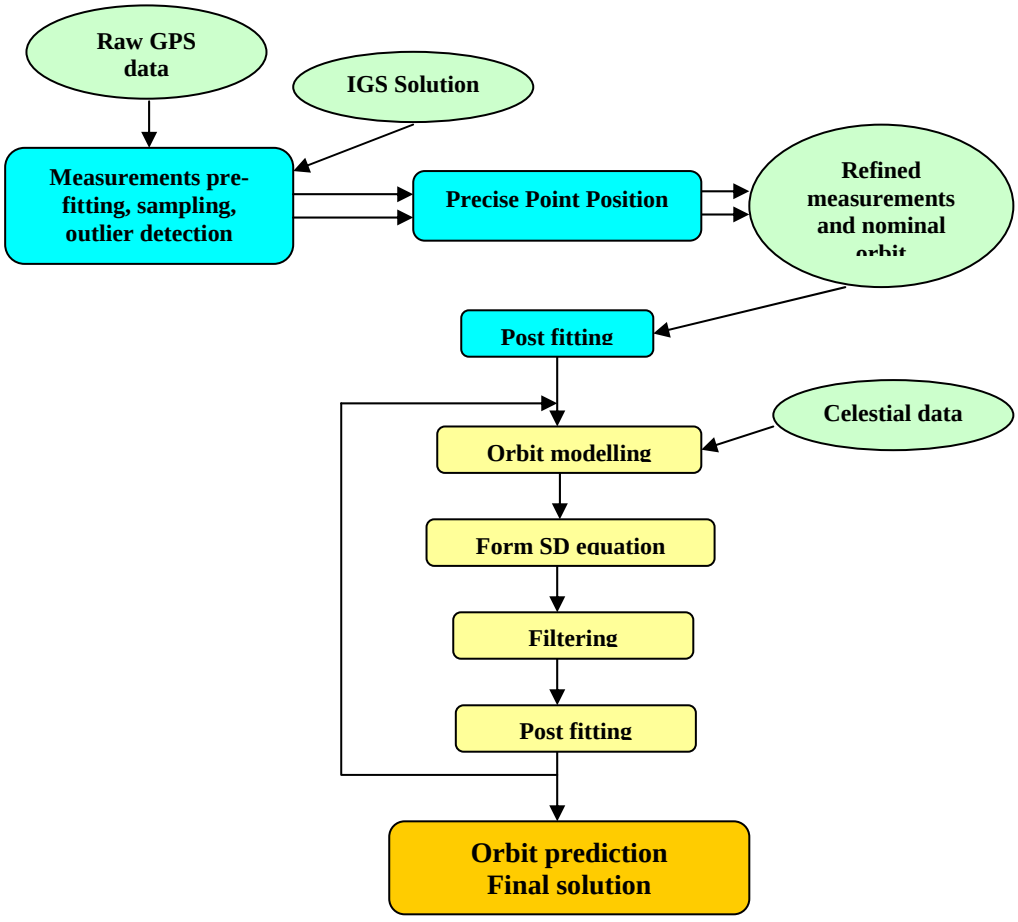

Figure 7.8 Orbit determination module.

7.4 FedSat GPS Data Quality Analysis

After the initial testing process, GPS flight data has been collected. Table 7.1 and 7.2 summarizes the data set collected for our experiments. The following sections will discuss the results in detail.

Table 7.1 Experimental dataset overview.

	30/31	**01**	**02**	**03**	**08/09**	**014**
# of data arcs	13	7	2	2	7	1
Arc length (min)	5 to 15 minutes					
Onboard navigation Solutions	Given at rate of 10 seconds					
Raw GPS data	Recorded at 1-second					

Table 7.2 GPS raw data overview for days 364, 365 2002.

File	**Epochs**	**Observations**	**SVs < 4**	**SVs >= 4**	**average SVs**
fed36402.obs	9734	56005	1339 (3694)	8395 (52311)	5.75
fed36502.obs	714	3654	2 (4)	712 (3650)	5.12

Continue

File	**Arcs**	**Min Arc length**	**Max Arc length**	**Average arc length**
fed36402.obs	14	380s	974s	698s
fed36502.obs	1	777s	777s	777s

7.4.1 GPS Measurement Quality Analysis

Firstly, the GPS measurement quality is of concern, because FedSat only has one aft-looking GPS antenna onboard. The GPS satellite visibility is poorer than other satellites with up-looking antenna. Figure 7.5 shows how the FedSat aft-looking antenna views the satellites in the two-thirds of the sky, that is, the scope of elevation from –27 to 90 degrees. To avoid the effect of the atmosphere under 100km on the measurements, we can set the mask angle of –25 degrees in the process. The signals with elevation angles between –25 and –27 degrees are subject to the tropospheric delays, which, can be used for atmospheric occultation studies. In fact, due to the effect of occultation, the signals with elevation between -27 to –28.5 degrees are often received in the FedSat orbit. Figure 7.9 illustrates the distribution of the measurements against the elevation angles. We have observed that the majority of the measurements are collected with the elevations of under 20 degrees.

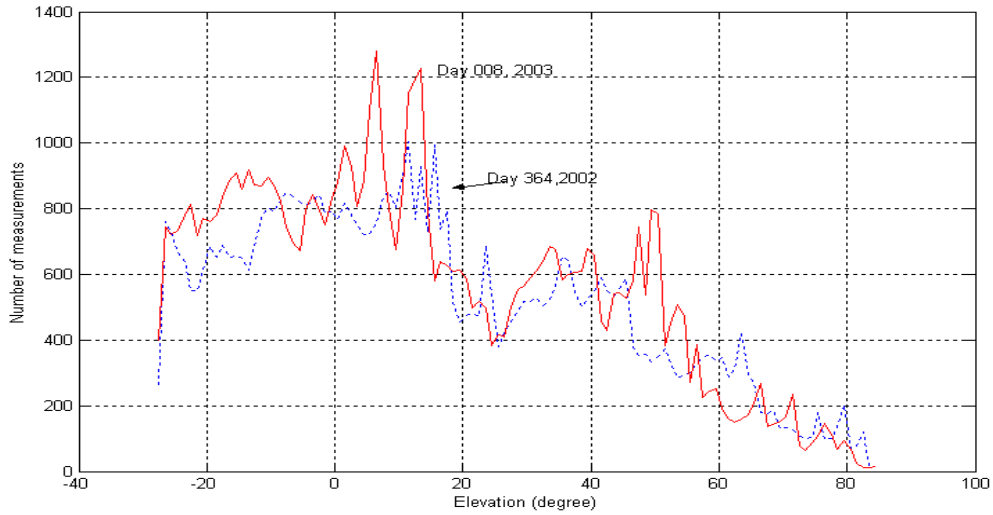

Figure 7.9 Number of measurements with respect to elevation angles of FedSat GPS data on day 364 and 365 of 2002.

During the initial operational period, the GPS receiver onboard the spacecraft turns on for 20 minutes for every orbit of about 100 minutes. After each cold start, it takes normally 1 to 5 minutes for the receiver to reacquire the signals from GPS satellites, and to capture four satellites for navigation solutions. Figure 7.10 illustrates the GPS operation times in these data sets.

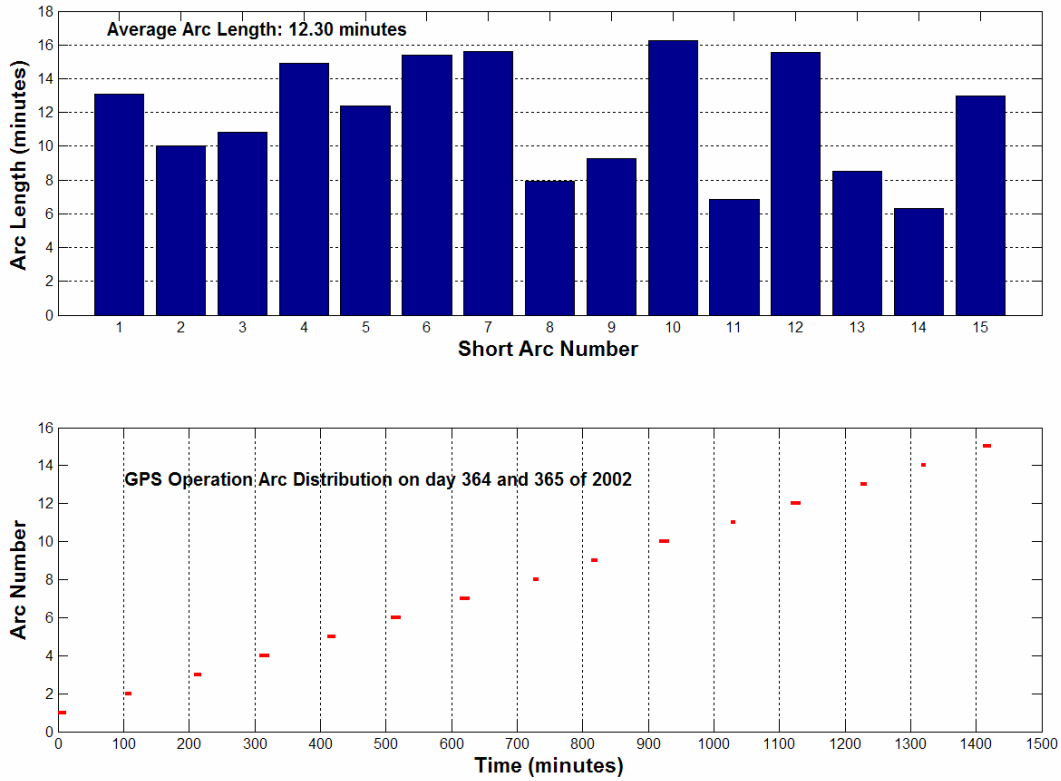

Figure 7.10 FedSat GPS operation arcs for day 364 and 365 of 2002.

7.4.2 P-code Ionospheric Delay

Generally, from the pure mathematical sense, the ionosperic delay can be expressed as the difference of both P-code pseudoranges:

$$P_I = P_2 - P_1 \approx d_{ion} \tag{7.1}$$

Figure 7.11 illustrates the P-code ionospheric delay on day 364 and 365 of 2002.

7.4.3 P-code Noise

After the system errors have been removed from the GPS measurements, the positional accuracy is determined by the measurement noise and geometry only. The measurement noise includes the signal noise, hardware noise and multipath effect. In this chapter, the noise of both P_1 and P_2 were inspected using the following expression [*Zhou, et al.*, 2003]:

$$PM_{1t} = \left(P_{1_{t+1}} - P_{1_t}\right) - \lambda_1\left(L_{1_{t+1}} - L_{1_t}\right),$$
$$PM_{2t} = \left(P_{2_{t+1}} - P_{2_t}\right) - \lambda_2\left(L_{2_{t+1}} - L_{2_t}\right) \qquad t = 0, 1, 2\ldots \tag{7.2}$$

Here λ_1 = 0.1903 metres for the frequency of f_1 (1575.42 *MHz*), and λ_2 = 0.2442 metres for the frequency of f_1 (1227.60 *MHz*). PM_{1t} and PM_{2t} mainly contain receiver noise and multipath errors. The standard deviations of the observations P_1 and P_2 are given as:

$$\sigma_{P1} = \sqrt{\frac{\sigma^2_{PM_1}}{2}}, \qquad \sigma_{P2} = \sqrt{\frac{\sigma^2_{PM_2}}{2}} \tag{7.3}$$

Due to possible variation of atmospheric conditions between epochs, (δ_{p_1} and δ_{p_c} are conservative estimates to the standard deviation for the measurements P_1 and P_c).

Figure 7.12 illustrates P_1 ranging noises against the elevations for the Day 364, 2002 (upper) and Day 008, 2003 (lower), respectively. The overall P_1 range RMS values for the three data sets are 1.44m, 1.66m respectively. The RMS values are estimated excluding the P_1 ranging noises greater than 15 metres, which are 0.16%, 0.32% of total in the two cases.

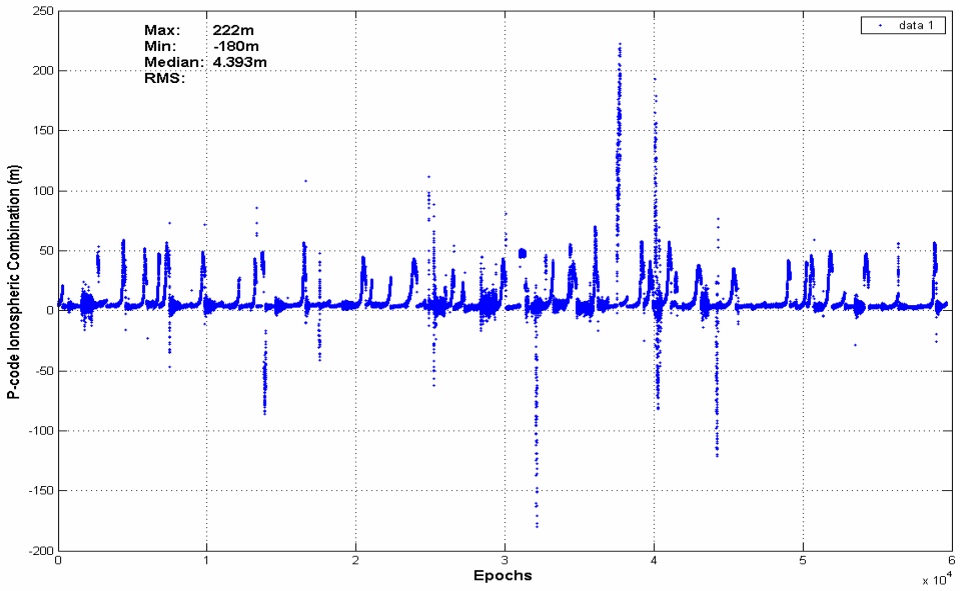

Figure 7.11 P-code ionospheric combinations for all satellites on day 364 and 365 of 2002.

Figure 7.13 is the histogram of the P_1 ranging errors for the period of Day 083 to Day 086, 2003, showing a good normal distribution nature. The threshold of ± 5m was set for both RMS estimation and follow-up orbit estimation.

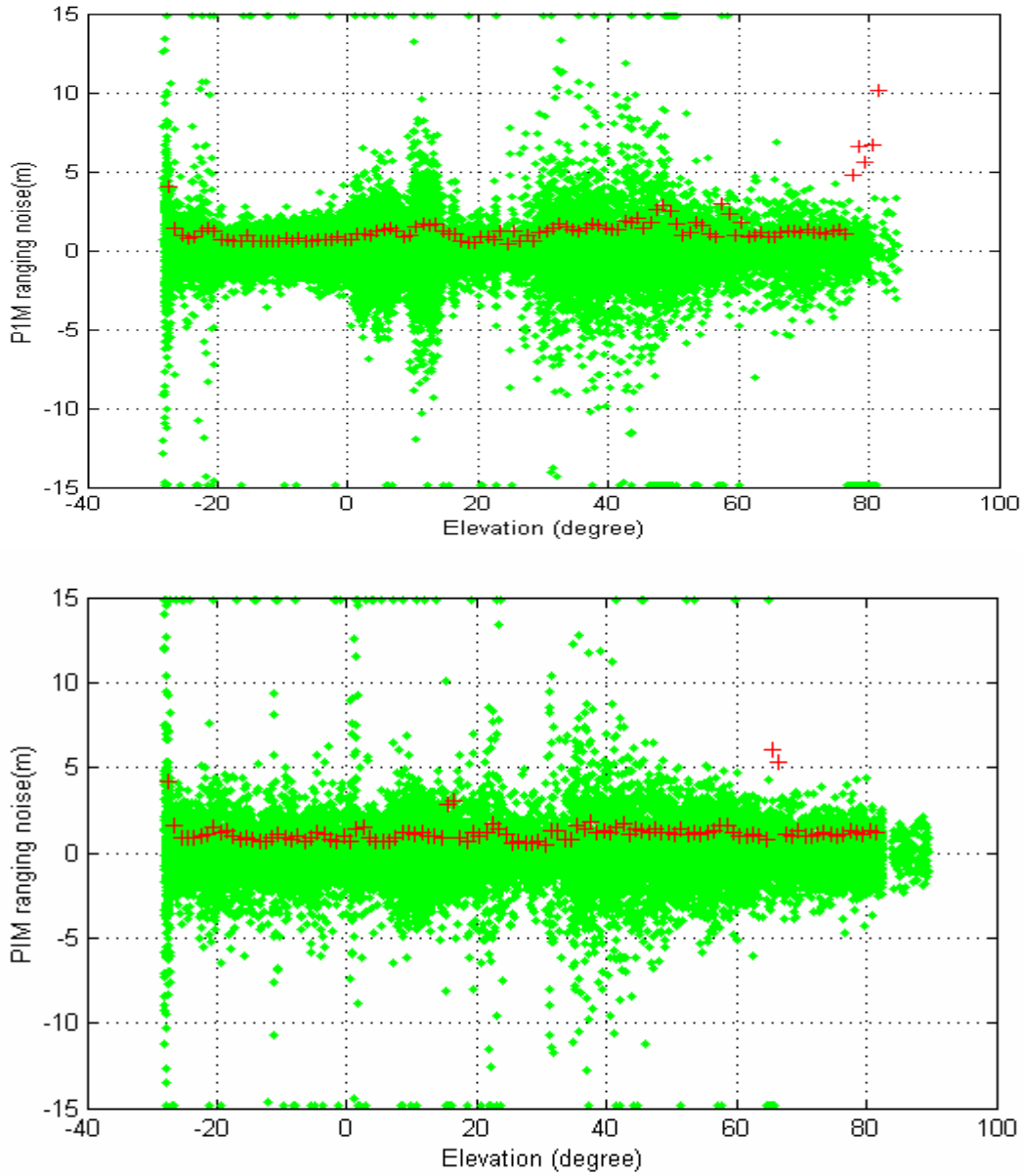

Figure 7.12 Illustration of P_1 ranging noises against the elevation for the Day 364, 2002 (upper) and Day 008, 2003 (lower), respectively. The overall P_1 range RMS values for the two data sets are 1.44m and 1.66m respectively.

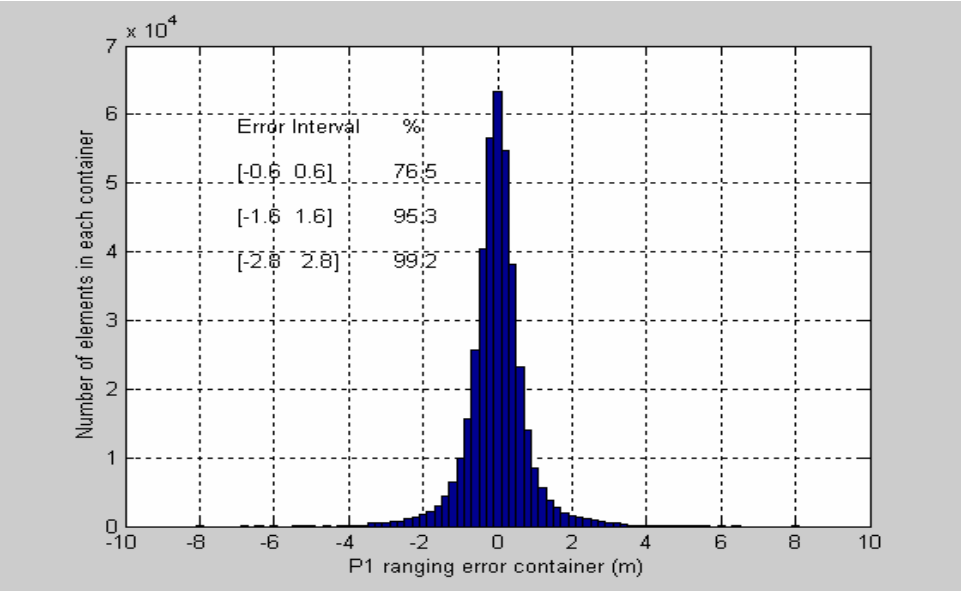

Figure 7.13 Histogram of the P_1 ranging errors on day 364 and 365 of 2002, showing their good normal distributed nature.

Table 7.3 compares the RMS values from different satellite missions and FedSat data sets of different days against elevation angle. It is observed that the GPS data with elevation angle below 10 degrees are much noisier than those with higher elevation angles for CHAMP and SAC-C missions where flight data for orbit determination were collected using an up-looking antenna. In the FedSat case, we have viewed the following instead:

- The overall RMS uncertainty/noise level of two FedSat data sets is constantly 3 to 5 times higher than these for CHAMP and SACC data;
- The data with elevation angle below -27 degrees is much noisier than those above -27 degrees;
- The ranging noise level for negative elevation is not necessary higher than those for positive elevation;
- The overall noise level of P_1 code measurements in the three FedSat data sets is about 1.6m showing a consistent data quality.

We also found that there are some big jumps in the P_1, P_2, P_c measurements of raw RINEX data file. This jump happens to every satellite observed. We assumed this is due to the receiver clock jump and can not be grouped to the P_1, P_2, P_c errors; there

is a 9000km clock jump in this instance. From another point of view, we can see that there are big clock errors in FedSat GPS receiver sometimes.

Table 7.3 Summary of the RMS values from different satellite missions and FedSat data sets of different days against elevation angles.

Mission	Receiver	Day	All Data	0<Elev.<10	10<Elev.<20	Elev.>25
CHAMP	BlackJack	3 days	0.53	0.93	0.64	0.42
SAC-C	TurboRogue III	3 days	0.32	0.73	0.46	0.17
Topex	Motorola Monarch	3 days	0.34	0.38	0.38	0.33
		Day		**Elev.<-27**	**-27<Elev.<0**	**Elev.>0**
FedSat	BlackJack	364, 2002	1.44	4.19	1.00	1.56
FedSat	BlackJack	008, 2003	1.66	4.06	0.93	1.98

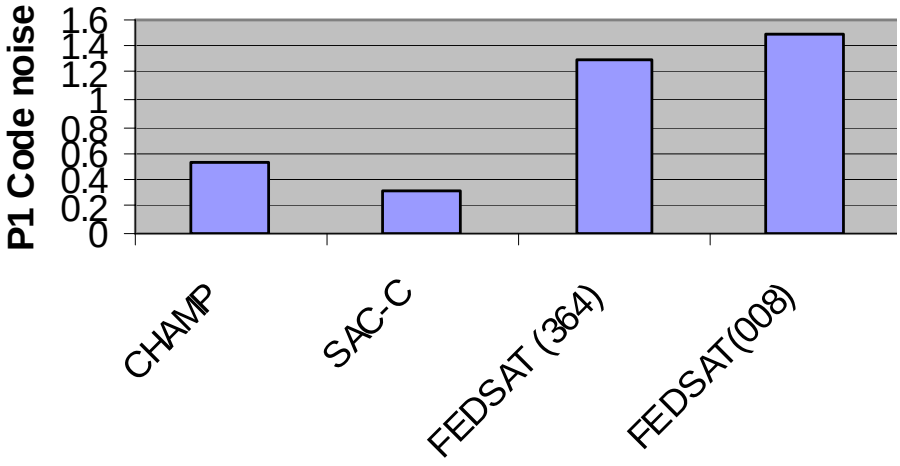

Figure 7.14 FedSat code noise on day 364 and 365 of 2002 compared with SACC and CHAMP.

7.5 FedSat Onboard Navigation Solution (ONS) and Single Point Positioning (SPP)

The FedSat onboard navigation solutions (ONS) are computed by the Blackjack receiver with all satellites in view, regardless of negative and positive elevations. Suffering from the large code noise and poor satellite geometry as indicated above, the FedSat ONS is expected to be much worse than the ONS in other missions.

To evaluate the FedSat ONS solutions, we perform two types of comparisons:

- with independently computed single point positioning (SPP) solutions from the code measurements, to understand the consistence; and
- with FedSat orbit filtering solutions, computed with the QUT FODT software as described in the next section

Figure 7.15 compares the ONS and SPP 3D RMS values with respect to the FODT solutions for a period of 1050 seconds (105 epochs, ONS were given at 10 seconds), showing the consistence between the two solutions under normal observational conditions. It appears that the SPP solutions are more robust against some outlying code measurements. Under the worst geometry (large PDOP), both ONS and SPP solutions suffer from the outlying code measurements.

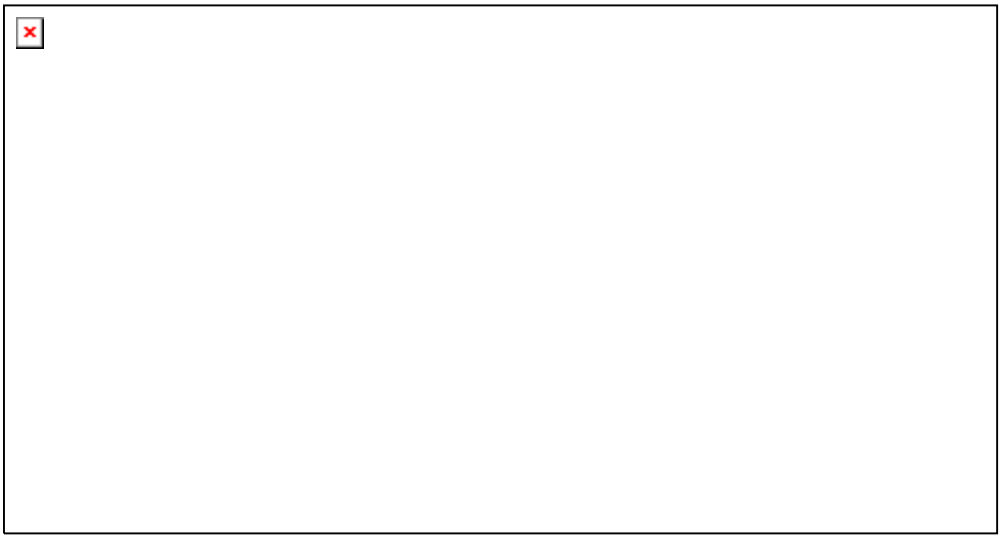

Figure 7.15 Comparison of the ONS and SPP 3D RMS values with respect to the FODT solutions.

Figure 7.16 plots the histogram of the ONS 3D positional errors, which indicates a long-tale normal distraction of the ONS positional errors. According to this histogram, the 1δ of 3D error is less than 40m. However, the 3D orbit errors with the 95, 97, and 99 percentiles reach 200m, 400m and 800m respectively. Statistical analysis based on the ONS errors falling within 95 percentile shows a 3D RMS of 57m, with means values of 9.3, -0.7, and –8.3m for the *x*, *y*, and *z* components respectively. Figure 7.17 is a scatter plot for the ONS positional errors within the range of ± 200 m.

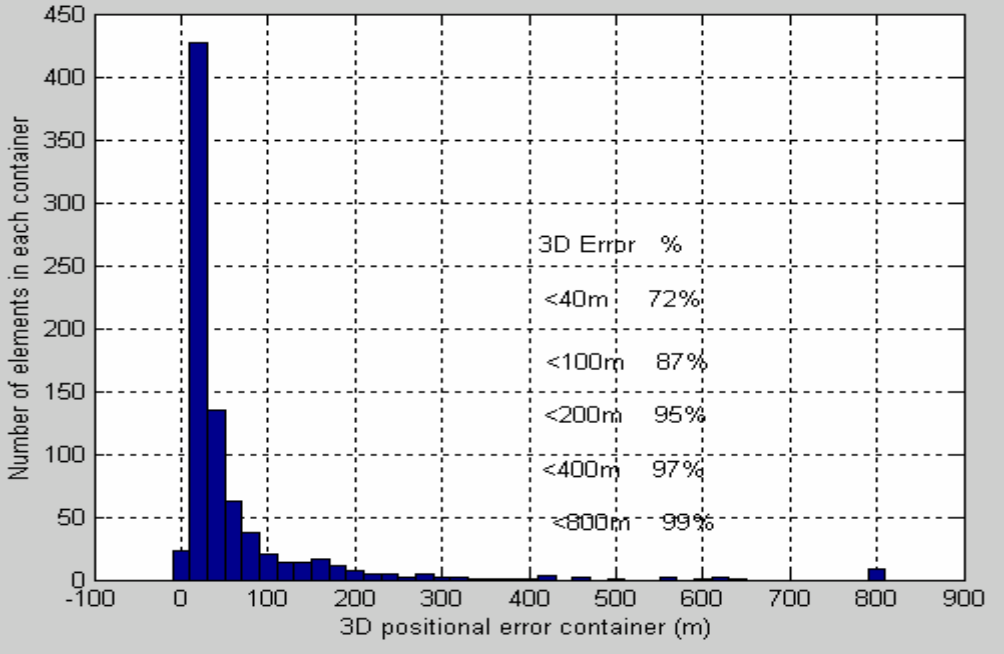

Figure 7.16 Histogram of the ONS 3D positional errors, indicating a long-tale normal distraction of the ONS positional errors.

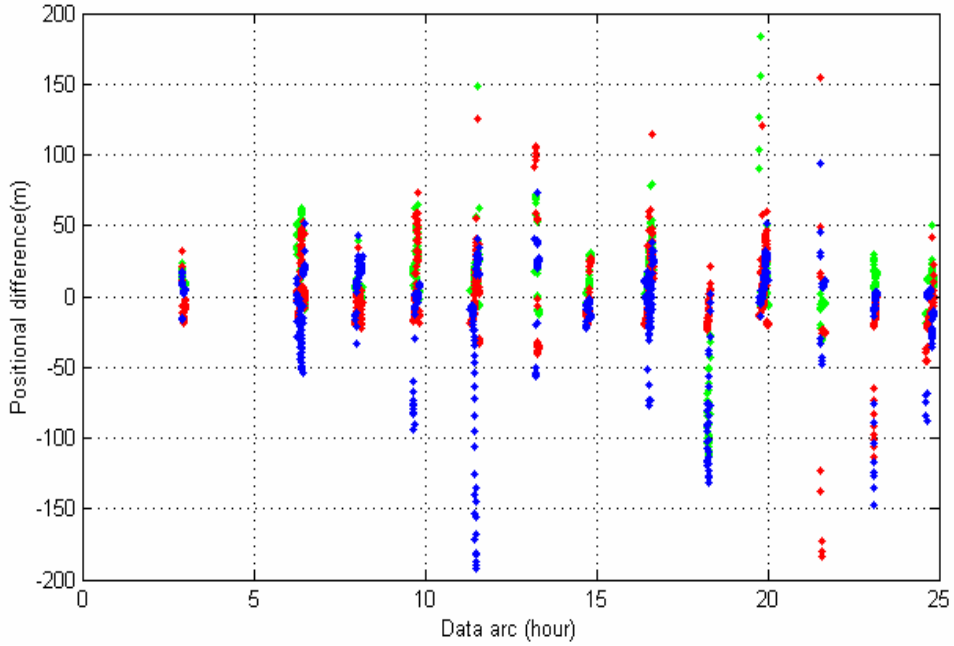

Figure 7.17 FedSat ONS positional error scattered within the range of ± 200m. An overall 3D RMS value based on the error of this range is estimated at 57m, which is about three times of the CHAMP ONS 3D RMS value.

7.6 Orbit Determination for Ground Ka-Band Tracking

7.6.1 Introduction

FedSat is a low Earth orbiting micro-satellite, which conducts space science, communications, Earth remote sensing and engineering experiments. The satellite flies the BlackJack spaceborne GPS receiver to compute its position and velocity for routine tracking operations, platform engineering needs (time keeping), as well as scientific experiments such as orbit determination (OD) and GPS occultation studies. Of all the above applications, the most restrict engineering need is specified by the Ka-Band tracking, requiring a pointing accuracy of 0.03°. As shown in Figure 7.18, the allowed orbit error Δr is approximately expressed as the function of the pointing error $\Delta\beta$, elevation angle β, and altitude of the orbit:

$$\Delta r = \Delta\beta \frac{\pi}{180} \rho(\beta) \tag{7.4}$$

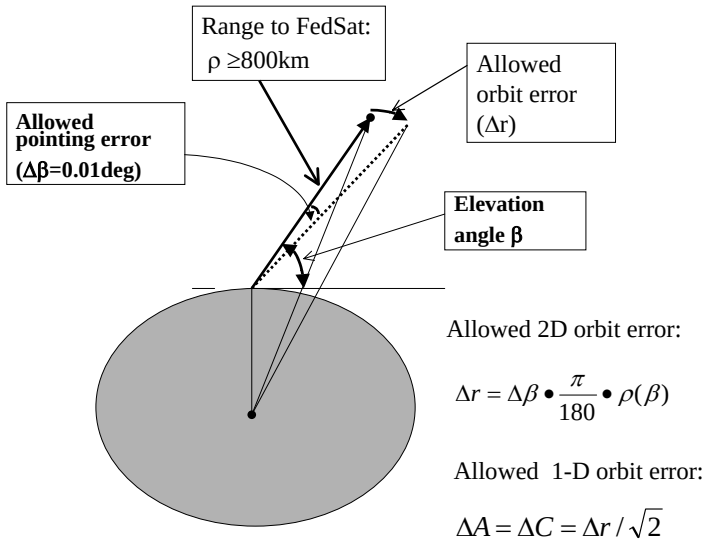

Figure 7.18 The accepted orbit error expressed as the function of the pointing error $\Delta\beta$, elevation angle β, and altitude of the orbit for FedSat ground-based Ka-band tracking.

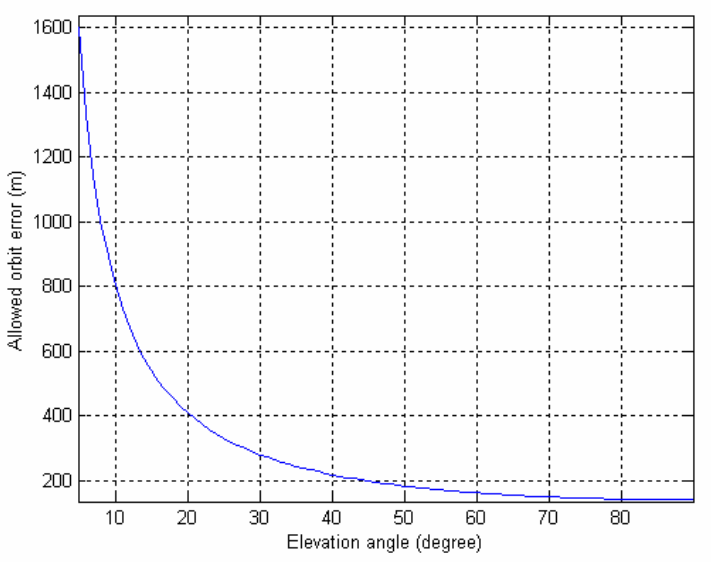

Figure 7.19 Accepted orbit error with respect to elevation angle.

Figure 7.19 plots the allowed orbit error against the elevation angle. It is observed that the most restricted orbit accuracy is required where the satellite passes over the zenith direction, $\beta = 90^{\circ}$. For the case of FedSat orbit, the requirement will be $\Delta r = 140\,\text{m}$. Only the errors in along-track and cross-track will affect the pointing accuracy. The accuracy requirement for each direction is

$$\Delta A = \Delta C = 139/\sqrt{2} \approx 100\,\text{m} \tag{7.5}$$

7.6.2 OD Processing Strategy in QUT Ground Base Station

To satisfy the Ka-Band tracking demand, an automatic OD processing system has been developed in CRCSS QUT node. It was established around November 2002 by Willam Kellar and the author. From the launch date to May 2003, the system has been thoroughly tuned and automatically running since then. The system includes two parts: GPS data acquisition / decoding and OD processor. Based on the accuracy and time requirements, the OD processor was configured as the following:

Table 7.4 Ground OD data processing strategies for Ka-band tracking.

Orbit force modeling	
Earth Gravity Model	JGM-3, 50x50
Third body gravity	Sun & moon, all planets except pluto
Planet ephemerides	JPL DE405
Solar pressure	Direct effect
Atmospheric density model	MSIS 86
Pression / Nutation	IAU1976 / IAU 1980 (with corrections)
Polar motion	IERS bulletin B
GPS Data Processing modeling	
P code noise threshold	5m
GPS ephemerides	IGS ultra rapid solution
Carrier phase smoothing	15 minutes arc length
GPS Data processing mode	Ionosphere free P code with single difference
Estimation Strategy	
Filtering arc / Prediction arc	1~2 days / 2~4 days
Parametre estimation	8 (6 state vector, drag and solar pressure coefficients)
Orbit representation method	Chebyshev polynomial, 25minute segment

Under the operation mode, every pass of GPS data is downloaded as soon as the data is available at the FedSat Control Centre. Meanwhile all the needed ephemerides data, solar activity data, geomagnectic data and IERS data are downloading by a robot program. OD processor will be launched after enough GPS data were successfully collected and decoded. Usually, the OD solution will be available within one day and will be placed on a restrict access ftp server for CRCSS community engineering and scientific usage.

7.6.3 OD Results

Orbit determination and prediction was performed for day 30-December, 2002 to 2-January, 2003. Figure 7.20 is the comparison between Filtered orbit and onboard navigation solutions, showing some large uncertainties of a thousand metres in the navigation solutions, as the filter solution is a smooth orbit, which may have a systematic error growth, but no irregularities. Figure 7.21 compares the orbit determination result with results from SAC-C and CHAMP. Figure 7.22 shows the orbit four days prediction result compared with the onboard navigation solution (ONS).

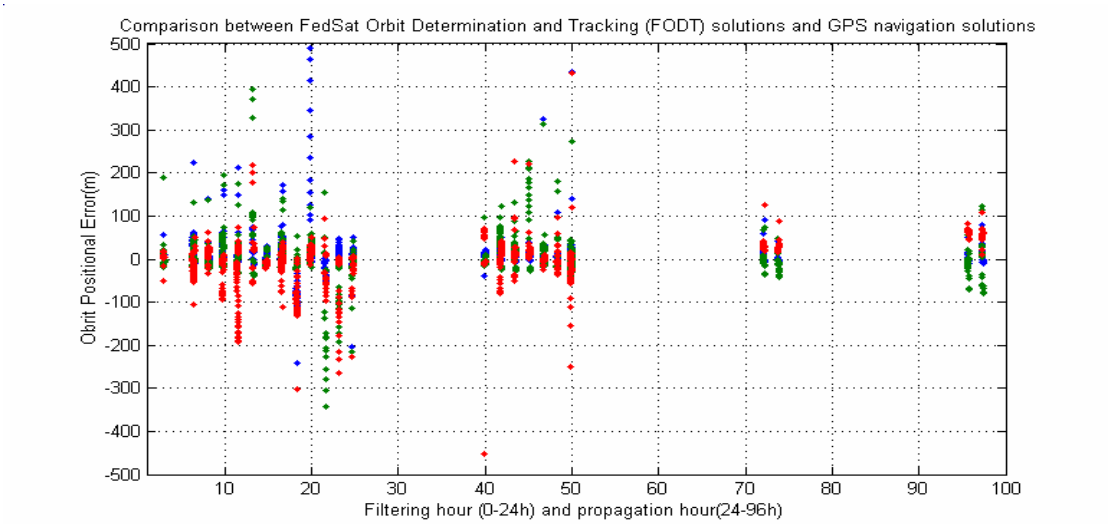

Figure 7.20 Comparison between the FedSat FODT and FedSat ONS solutions over the filtering orbit of 24h (2:50,364 to 2:49 365, 2002) and the propagation orbit from 40h to 98h (Days 001,002 & 003, 2003).

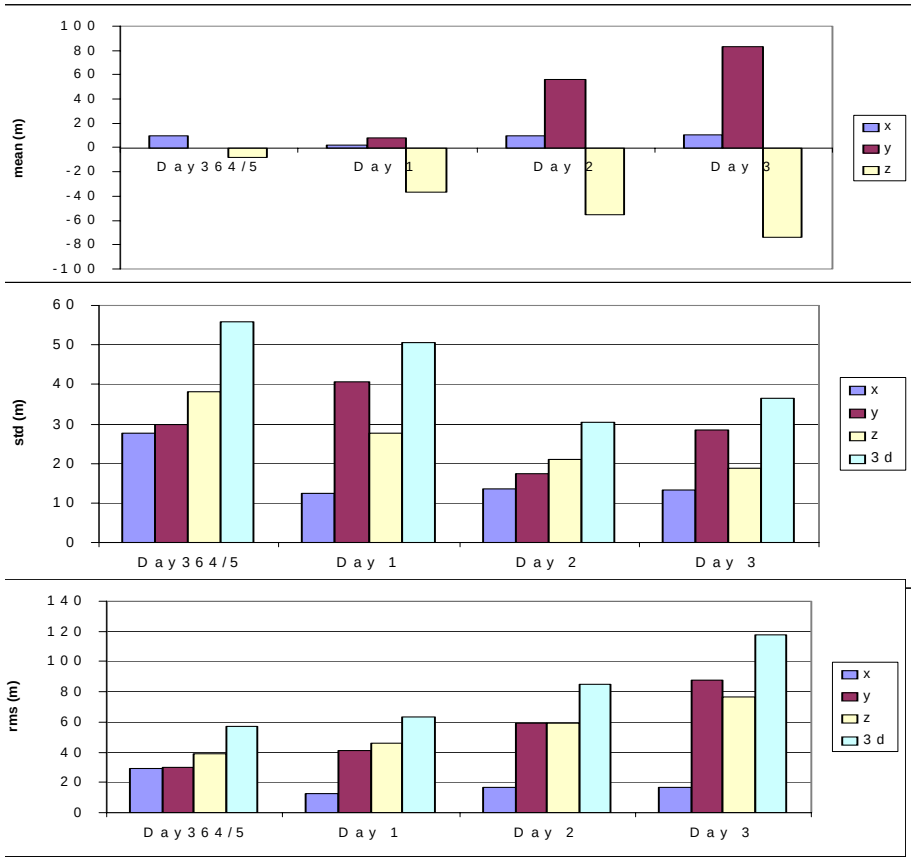

Figure 7.21 Illustration of mean, standard deviation (STD) and RMS values over the filtered orbit (Day 364/5, 2002) and predicted orbit on Days 001, 002 and 003, 2003.

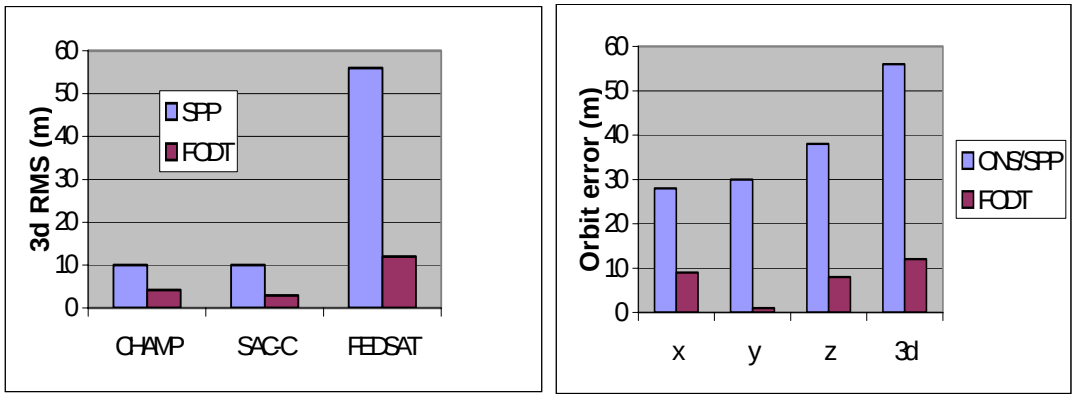

Figure 7.22 FedSat Orbit filtering results compared with SAC-C and CHAMP.

Figure 7.20 compares between the FedSat FODT solutions and FedSat ONS solutions over the filtering orbit of 24h (02:50, Day 364 to 02:49, Day 365, 2002) and the propagation orbit period from 40h to 98h (Days 1 ~ 3, 2003). The results show the agreement of ±120m with the ONS solutions at the end of the propagation period of 72 hours. Figure 7.21 compares the mean, standard deviation (STD) and RMS values of the filtering orbit for Day 364 of 2002 and the propagation orbits on Day 1, Day 2 and Day 3 of 2003. Figure 7.22 compares the filtering and ONS results between FedSat and SAC-C/CHAMP. According to these figures, we have obtained the following observations:

- The STD values do not grow with the extension of the propagation arc from Day 1 to Day 3; the mean values show a steady growth when the prediction arc extends from Day 365 to Day 3;
- The mean values basically reflect the filtering and/or propagation uncertainties, while the STD values reflect the uncertainties of the ONS solutions. If this is the case, we may indicate that with the given data sets analyzed, the FODT filtered orbit errors are in the order of ±10m in each component, while the predicted orbit errors in each component will be in the order of ±20m, ±60m and ±80m for 24 hours, 48 hours and 72 hours forward, respectively

7.6.4 Covariance Analysis of Data Set 08403~08703

For the data sets collected in the period of Day 83 to 87, we apply strict quality control procedures to excluding all the possible outlier measurements. For instance,

the P_1 measurements with associated P_{1M} errors beyond the thresholds of ±7.07m (5m for P_1) were excluded before entry to orbit estimation. FODT is run to produce the filtered orbits for each day separately, and propagate the filtered orbit of the first day (Day 83) 96 hours forward. Figure 7.23 shows the difference between the prediction orbits from Day 83 and the filtered orbits over each day from 084 to 087. It can be clearly seen that the predicted orbit errors fall in the ranges of ±30m, ±70m, ±120m and ±240m for the first, second, third and forth day, respectively.

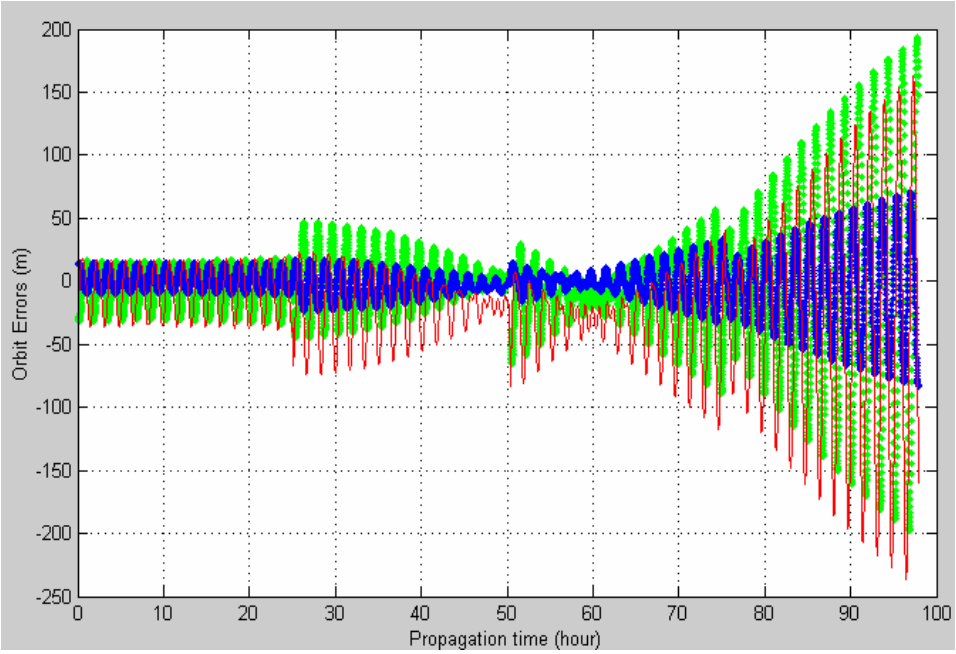

Figure 7.23 Difference between the prediction orbits from the end of day 083 of 2003 and the filtered orbits over each day from 84 to 87 of 2003.

7.7 FedSat Short-arc Processing

7.7.1 Introduction

Normally, the FedSat orbit determination solution of previous strategies comes out within one-day latency. This is sufficient for the Ka-Band ground tracking because we normally predict the orbit into the future about 2~4 days. But for some other applications that need ultra rapid orbit solution with high precision, previous method is not enough. These applications usually require metre level accuracy within several hours' latency.

Based on the short-arc techniques in the Chapter six, a short-arc processor was designed to generate a rapid orbit solution. Basically, the orbit modeling and GPS data processing strategy are the same as the long arc one except:

- Orbit modeling: for the short-arc processing, the GPS measurement number is far less than the long arc one, it is not safe to estimate the osculate parametres like the drag coefficient if the GPS measurements are not precise and outlier-free enough. Otherwise the solution will fail due to wrong orbital parametre estimation. On the other hand, it is also very safe to ignore some osculate orbital parametres because the orbit propagate error due to modeling error is limited in short-arc. In the FedSat short-arc filtering case, the solar pressure and drag coefficients are fixed in the filtering process. We used the two values as:

  $$C_{drag} = 0.002 \quad \text{and} \quad C_{solar} = 0.0008$$

  Thus, only six state vectors are estimated in the short-arc filtering. This will make the solution more stable.
- GPS data processing: First, the SPP pre-processing is not carried out in the short-arc processing due to the time limit. Second, only broadcast ephemerides is used instead of IGS precise ones. This will greatly reduce the latency, but not reduce the precision too much.

There are two ways to configure the short-arc processor. The first one is to process every short-arc separately. Due to the Duty Cycle operation mode of FedSat, we usually process one or two 15 minutes arcs in a short-arc processing, which is about one or two hours. After every single pass of data is downloaded, the processor can be launched and the solution will be available in minutes. The orbit prediction of several hours can be made from the filtering results. In this way, the solution can be available within tens minute latency.

Another strategy comes from the idea of “Sliding-window processing”. Firstly, a longer arc of data, for instance, around 6 ~ 8 hours, is processed. As soon as a set of new 15 minutes data comes, a new data arc is formed by deleting the oldest 15 minutes data. In this way, the filter will result in more stable accuracy solution and

longer prediction, but the latency will be around 1 ~ 2 hours due to longer processing time.

7.7.2 Experiment Description and Results

The short-arc experiments were carried out on day 364 and 365 of 2002. The arc length details in these two days have been given in Figure 7.10. Figure 7.24 gives the short-arc filtering results and compared with SPP. The 3D positional RMS was given. All the results were compared with 24h long arc OD results.

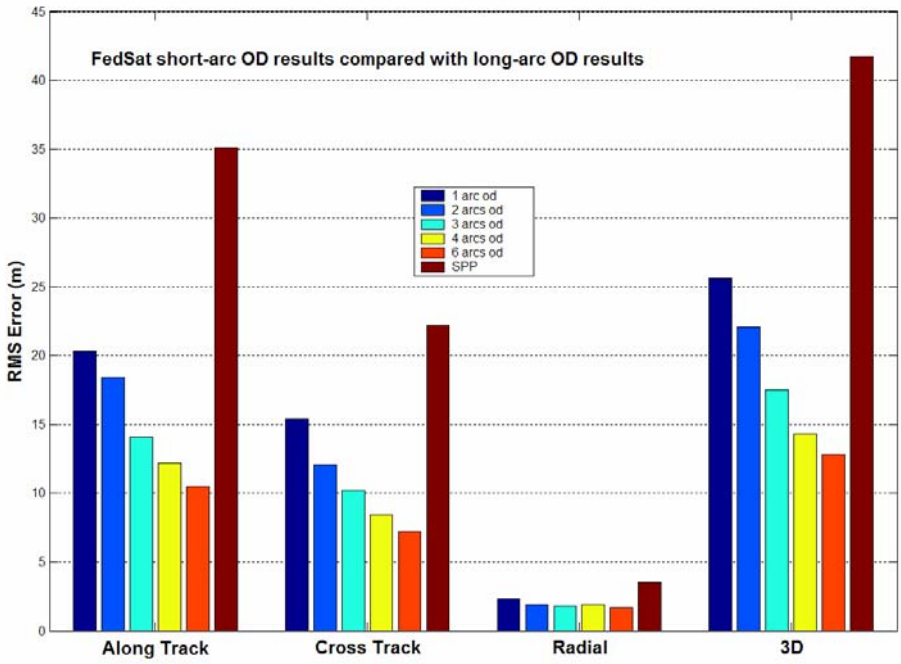

Figure 7.24 Comparison of shot-arc OD results with long-arc OD.

7.8 Ground-based Autonomous Orbit Determination System

7.8.1 Introduction

Although the previous ground orbit determination system has been running smoothly and generating a reasonable solution for some engineering projects, a more comprehensive precise orbit determination system is proposed. The new autonomous system is to provide the FedSat orbit solution at sub-metre level for scientific and engineering applications. Based on current work, this system was expected to be in operation in 2006.

7.8.2 Automation

One of the most important goals of this system is the automation. This not only means it can automatically download, edit and process data but also means that it can automatically generate different OD strategies based on the data quality and OD performance analysis. The system will be running on a Windows XP server. After initial launch, it should continuously work without any human interference. The main automation features include:

- Automatically downloading real time GPS data; daily broadcast ephemerides data, IGS data and sun flux data; monthly IERS data, geomagnetic data; yearly JPL planetary DE405 data.
- Automatically generating all the configuration files for each OD modules based on current data set analysis.
- Automatically running each OD modules, and also can stop and restart the whole system itself.
- Automatically presenting the result in different formats and generate some simple text/graphic reports based on different requirements.
- Automatic error reporting and logging. This includes process log and email alert functions. The main results and error message can be emailed to the persons who are in charge.

7.8.3 Combined OD Strategy

Generally, the system will generate ultra-rapid, rapid and final orbit filtering solutions using different strategies. In addition, a PPP solution also will be generated for ultra-rapid backup solution and analysis purpose. Another layer of this solution tier is a SGP4 one, it will be generated based on the analysis of several batches of final solutions. It aims to provide a long-term backup solution in case no measurements data are available. The system also will predict the orbit for one or two weeks using the final solution.

Not all the solutions will be generated at every processing; it depends on the application requirement and different processing situation. A set of options will be implemented to let the system know what strategy it should use.

7.8.4 Accuracy and Stability

For the final solution, sub-metre or even decimetre level accuracy is expected. It will be used for some high precision applications. For rapid solution, metres to sub metres accuracy can be achieved. For ultra rapid and PPP, metres accuracy is the achievable. For the SGP4 model, hopefully, hundreds metres to kilometers of accuracy can be achievable for a several months arc.

The system is more stable because it can generate multiple solutions based on different and independent algorithms.

7.8.5 OD Strategies

The basic filtering scheme is to process 30 hours GPS data using current OD processing techniques, the beginning and ending three hours are used for covariance analysis. The middle 24 hours solution is used as a rapid solution. Seven consecutive rapid solutions are collected; the overlapped arcs are analyzed to generate a smoothing function. After that, a smoother is performed for the seven days' data to generate the final solution.

The ultra-rapid solution is generated using the "sliding-window short-arc" filtering technique introduced in Chapter 6. Normally the processing data arc is around 4 ~ 6 hours, and the update frequency is every single pass (around 15 ~ 20 minutes). This ultra-rapid solution can be available in 2 ~ 4 hours.

Precise Single Point Positioning (PPP) solution is generated after a single set of GPS observation data and the IGS ephemerides are available, the time latency should be around 1~2 hours. Usually, the accuracy of PPP for FedSat is worse than other missions, such as SACC, but a 3D RMS of 6 ~ 7 metres is still achievable with

precise PPP model. If only broadcast ephemerides are used, the latency should be within half hour and the 3D RMS accuracy can be around 10 metres.

For SGP4 model, a separate least square filter is used to generate the two line elements. Only final solutions are used in the filter for accuracy reasons. Because the limits of SGP4 model itself, the orbit propagation accuracy is only at several hundred metres. But it is very simple in computation because it is an analytical model and can be used for a very long arc, such as one or two months. The following figures illustrate these OD strategies. Figure 7.25 illustrates the details of different OD strategies.

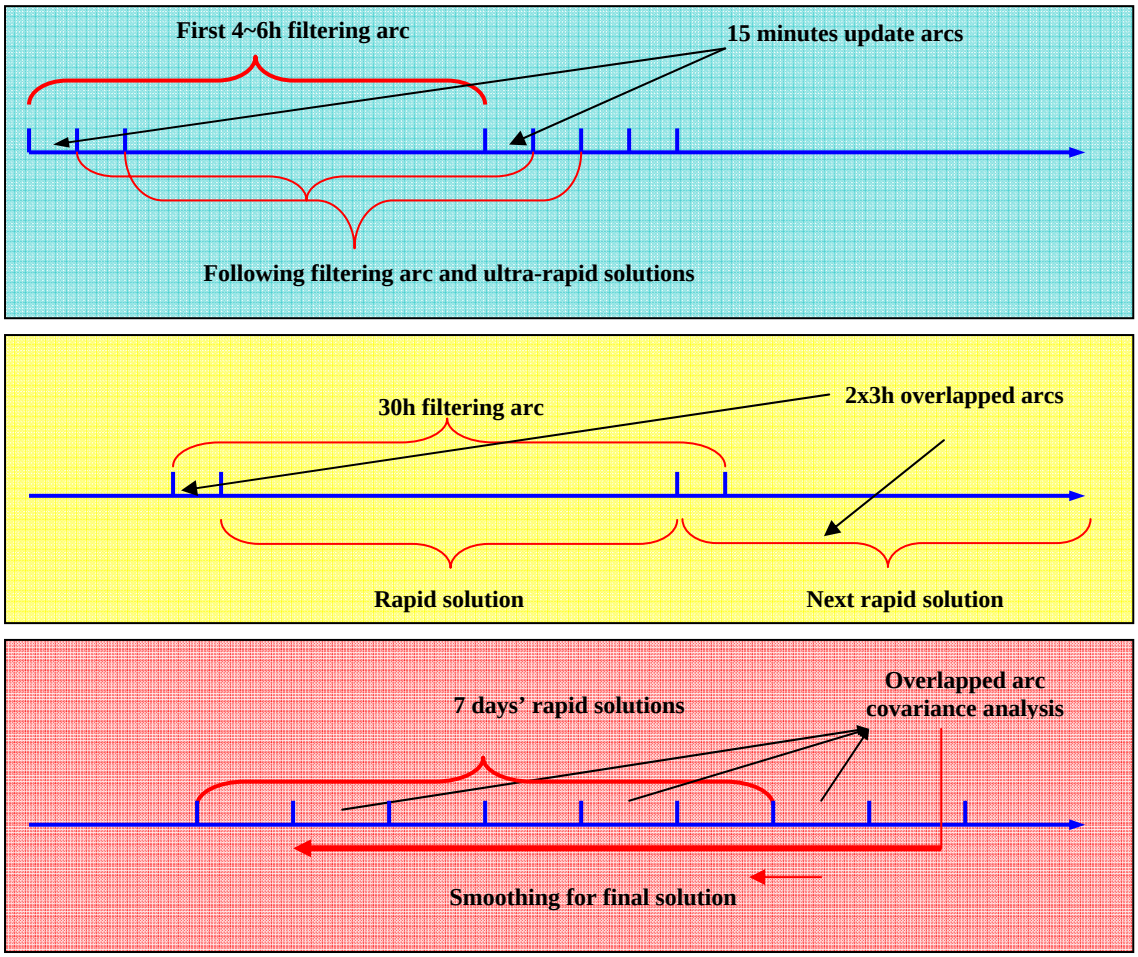

Figure 7.25 Ultra-rapid solution, rapid solution and final solution concepts.

7.8.6 System Structure

This system will be gradually constructed based on current autonomous orbit determination system. Figure 7.26 illustrates the system structure.

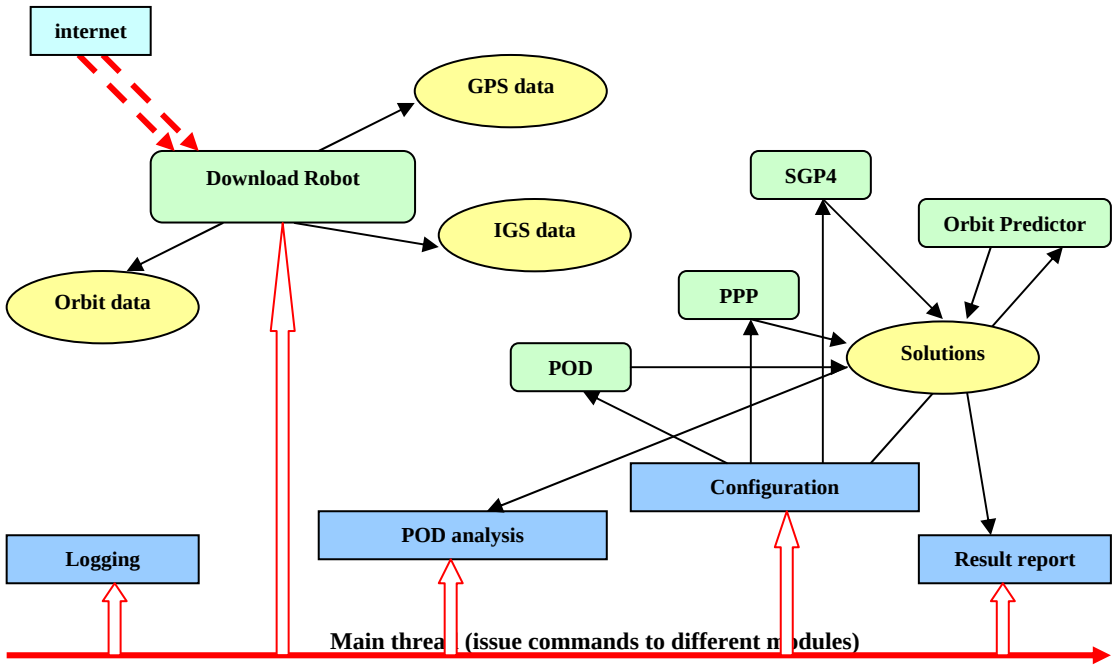

Figure 7.26 Ground-based autonomous precise orbit determination system structure.

7.9 Summary

The research effort has been made towards the establishment of autonomous orbit determination system for FedSat. Based on the experiment results, we have the following findings:

- The FedSat GPS data quality is three times worse than these achieved with data from other satellites missions with an up-looking antenna.
- FedSat onboard navigation solutions have shown large uncertainties and irregularities: although a RMS accuracy of 56m was achieved, it was often with errors ranging from a few to several hundreds and thousands of metres.
- Filtering processing over the 24 hours arc on 30, December 2002 provides a convergent estimation for drag parametre, thus resulting in the orbit positional errors of ± 120 m in the end of the propagation period of 72 hours. With the fixed drag parametre, the prediction errors reach 1.6km in the end of

120 hours (Day 8 of 2003). The result met the requirement of Ka-band ground tracking project.

- The autonomous OD system in QUT has demonstrated the ability to provide tens of metres of FedSat orbit accuracy in half-day delay.
- Preliminary short-arc orbit determination has been validated using FedSat data; the results show the potential to process data in near-real time. The short-arc filtering can generate 20 metres accuracy solution using 2~4 revolutions data, which contains a data arc of 20 to 40 minutes.

With the poor quality of data collected under poor observation conditions, the preliminary OD results are reasonable. Further research effort can be made combine the SLR and two line elements data into a current processing system, metre level accuracy can be expected with this multi-data-source system. Furthermore, the system should have the ability to provide different accuracy solution in near-real time and post-processing modes.

Chapter 8
Conclusions and Recommendations

8.1 Summary of Research Contributions

Onboard GPS orbit determination is promising technique for enabling advanced space engineering and scientific applications. Metre to sub-metre 3D position accuracy is now possible in real or near-real time. In this thesis we have systematically studied the models and algorithms for GPS-based onboard orbit determination, and demonstrated various results using different experiments with flight GPS data. The research has addressed some scientific and engineering challenges in onboard orbit determination, and provided efficient technical strategies and solutions to these problems.

This thesis focuses on the onboard orbit determination techniques and the proposed onboard orbit determination algorithms were successfully validated using real onboard GPS data collected from Topex/Poseidon, CHAMP and SAC-C satellites.

8.1.1 Orbit Dynamical Models

Onboard computing power is always limited. Therefore the orbit dynamic models are often simplified in current onboard orbit determination systems. As a result, achievable orbit accuracy has been limited to several to tens of metres. In this research a systematic study of orbital dynamic model simplification has been made for onboard computing. It includes Earth gravity model truncation, simplified solar & lunar ephemerides, simplified atmospheric density model, celestial parametre interpolation and integral equation integrator. All of these techniques together greatly reduce the computing burden while retaining metre level orbit integration accuracy. Furthermore, the Earth gravity acceleration approximation method was

studied and implemented. A pseudo-centre grid with appropriate interpolation functions replaced the traditional recursive algorithm. Consequently the computional burden is equivalent to that of a 5×5 gravity model retaining the accuracy of a 70×70 model. At the cost of a few additional Mbytes storage, which is not a problem for most onboard spacecraft systems.

8.1.2 Orbit Estimation

A Kalman filter can theoretically generate orbit solutions from epoch-to-epoch in real time with GPS measurements. The problem is that the stability of the solution cannot be easily brought under control. In other words, although theoretically a Kalman filter is ideal for onboard OD processing, in practice it is hard to balance between different noise and biases in the models and observations. Hence, the results may be easily affected by measurement outliers, causing the solution to diverge. Furthermore, the Kalman filter takes several hours of data to obtain a converged solution, which is quite long for many applications. On the other hand the traditional long-arc least squares estimation can give stable solutions, but it requires many observations and long processing time, as well as precise orbit models for good orbit accuracy. In this study, a short-arc least squares filter with sliding-window processing was developed, implemented and tested to assure stable solutions while keeping the computing time short. In addition, the short-arc technique can tolerate dynamic orbital modelling errors, providing good orbit accuracy without the need for precise orbit models.

Based on experiments using SAC-C data, the following comments can be made:

- With a data arc as short as 30 minutes, a 3D position RMS error of 2.5m and 3D velocity RMS error of 5mm/s can be achieved with 5 minutes latency. The solution is more stable than that of a traditional Kalman filter, and it doesn’t require any initialization process (which is around 4~6 hours for a typical Kalman filter). Furthermore, the computional burden is comparable to Kalman filter processing.
- With a data arc of 1~2 hours, a 3D position RMS error of 1m and 3D velocity RMS error of 2mm/s can be achieved in 10 ~ 20 minutes latency. The radial

component position accuracy was 40cm, which is adequate for some applications. The accuracy is approaching that of ground-based long-arc OD, though with much less computional burden.

8.1.3 Quality Control and Improvement of Onboard GPS Data Processing

The quality of onboard GPS measurements and navigation solutions is often worse than those obtained on the ground due to the harsh observation conditions in space. As a consequence, great care has to be taken to ensure improvement of the measurement quality by having reliable outlier detection algorithm for code measurements. In addition, if we take the GPS measurements at every sample epoch of 1~10 seconds directly, the nominal orbit and partial derivations need to be generated at these epochs, which in turn results in a heavy computional burden (as well as large onboard memory storage). To improve this situation, an optimal GPS data processing scheme was implemented that included a simple recursive outlier detection modules, a closed-form single point positioning algorithm (without need of initial coordinates to increase onboard autonomy), and a sliding-window phase smoothing algorithm to generate clean and compacted GPS measurements (further savings of storage and efficient onboard orbit estimation).

The major results from the analysis and numerical studies can be summarized as follows:

- We found that the best SPP result was achieved with 10 ~ 20 minutes of data smoothing. For sliding-window smoothing, the results are basically the same as with different window sizes, such as 1/2/5 minutes. Thus the 5 minutes window size with 10 ~ 20 minutes smoothing is a good choice for onboard processing.
- The closed-form SPP algorithm generates positioning solutions with tens of metres of error. This accuracy can be achieved for 83% of measurements. Furthermore, the error is smaller than 10 *km* for 99% of measurement, which is still a good initial estimate for the subsequent orbit filtering process.

8.1.4 Ground-based FedSat Orbit Determination Software System

Development and implementation of an orbit determination software system is a very challenging engineering task. Based on the same preliminary software at the CRCSS, a comprehensive GPS-based orbit determination software system has been developed as part of this PhD research effort. This software not only provides a technical platform for testing and implementation of the proposed new models and algorithms, but also leads to an operational orbit determination system for ground-based near-real time orbit determination for the FEDSAT satellite launched in 2002. The system generates FEDSAT orbit solution with half-day latency on an operational basis. This autonomous FedSat orbit determination system has also supported the scientific missions of FEDSAT within the CRCSS community, such as Ka-band tracking and GPS atmosphere studies.

The major results from the analysis and numerical studies are:

- The FedSat GPS data quality is approximately three times worse than data from other satellite missions with an up-looking antenna. The FedSat onboard navigation solutions have shown large uncertainties and irregularities, and although an RMS accuracy of 56m was achieved, it was often with errors of a few hundreds and even thousands of metres.
- The autonomous OD system at QUT has demonstrated the ability to provide tens of metres FedSat orbit accuracy with half-day delay.

8.2 Scope and Limitation of the Research, Future Directions

This research focuses on software aspects of onboard GPS orbit determination problem. As the computation will need to take time to complete after each data output, strictly speaking this is a near-real time solution. However, by the use of prediction the system can provide real time precise orbit knowledge to cover the delay due to the computation, which can be several to tens of minutes in length. In addition, although the techniques have been thoroughly tested using real LEO GPS data, additional efforts are needed to implement the algorithms into a real hardware platform. Issues of computing speed, memory usage and power consumption must be re-visited from the point of view of software and hardware engineering. To reach an

optimal performance revisions to the proposed methods are also required addressing the actual computing system. Apart from this, suggestions for future research are:

- The computational burden of the Earth gravity acceleration method can be further improved. The storage penalty of 2.5 Mbytes is still not optimal. There are savings available in simply using more latitude bands (e.g. smaller incremental changes in $\Delta\lambda$). An investigation of other functional forms is planned, including continued fractions, in an effort to reduce the number of coefficients to be stored.
- The research in extrapolation of Earth polar motion parametres was limited. Further efforts should be made in this area, as this will improve the orbit propagation accuracy and reduce the data upload frequency to the satellite.
- This research is based on dual-frequency GPS measurements. Further research effort can be made to implement a solution with single-frequency GPS receivers.
- A ground-based autonomous orbit determination is proposed in this dissertation. With the innovative combination of short-arc GPS orbit determination, long-arc GPS orbit determination, GPS precise single point positioning and SGP4 filter; the system can automatically generate multi-layer orbit determination solutions. However, more research effort is needed to implement it as an operational system.

References

Abel, J. S., J.W. Chaffee (1991). "Existence and Uniqueness of GPS Solution". IEEE Transactions on Aerospace and Electronic System, Vol. 27, 952-955.

Abramowitz, M., I. A. Stegun (1992). "Handbook of Mathematical Functions", U.S. Dept. of Commerce, 1992. An electrical version can be found at: http://www.convertit.com/Go/ConvertIt/Reference/AMS55.ASP.

Ashby, N., B. Bertotti (1986). "Relativistic Effects in Local Inertial Frames". Phys. Rev. D, 34 (8), 1986. p2246.

Ashkenazi. V, W. Chen, C.J. Hill, T. Moore, University of Nottingham; D. Fortune, D. Stanton, European Systems Ltd.; N. Shave, Defense Evaluation and Research Agency, Farnborough (1997). "Real-time Autonomous Orbit Determination of LEO Satellites Using GPS", Proceedings of ION GPS-97, Kansas City, Missouri, U.S.A., 16-19 September, 1997. 755-762.

Bancroft, S. (1985). "An Algebraic Solution of the GPS Equations", IEEE Transactions on Aerospace and Electronic Systems Vol. 21, 56-59.

Barlier, F., C. Berger, J.L. Falin, G. Kocharts, G. Thuiller (1977). "A Thermospheric Model Based on Satellite Drag Data", Aeronomica Acta A-No. 185.

Battin, R.H., G.M. Levine (1970). "Application of Klman Filtering Techniques to the Apollo Program". Chap. 14 in Leondes C. T. (ed.); Theory and Application of Kalman Filtering, NATO Advisory Group for Aerospace Res. Develop., AGARDograph 139, 1970.

Bertiger, W.I., T.P. Yunck (1990). "The Limits of Direct Satellite Tracking with GPS", Navigation Vol. 37, 65-79.

Bertiger, W.I., Y.E. Bar-Sever, E.J. Christernsen, E.S. Davis, et al. (1994). "GPS Precise Tracking of TOPEX/POSEIDON: Results and Implications" J. Geophys. Res., TOPEX/POSEIDON Special Issue Vol. 99(C12), 24,449-24,464.

Bertiger, W.I., B. Haines, D. Kunag, M. Lough, S. Lichten, R. Muellerschoen, Y. Vigue, S.C. Wu (1998). "Precise Real Time Low Earth Orbiter Navigation with GPS", Proceedings of ION GPS-98, Nashville Convention Centre, Nashville, Tennessee, U.S.A., 15-18, September 1998, 1927-1936.

Bisnath, S., R.B. Langley (1996). "Assessment of the GPS/MET TurboStar GPS Receiver for Orbit Determination of a Future CSA Micro/Small-Satellite Mission". Final report by the Department of Geodesy and Geomatics Engineering, University of New Brunswick, Frederiction. N. B. for the Directorate of Space Mechanics, Space Technology Branch of the Canadian Space Agency, St-Hubert, Que. under Public Works and Government Services Canada Contract No. 9F011-5-0651/001/XSD, July, 188-198.

Bisnath, S., R.B. Langley (2001). "GPS Phase-Connected, Precise Point Positioning of Low Earth Orbiters", Poster Presented at GNSS 2001, 8-11 May 2001, Seville, Spain.

Bisnath, S., R.B. Langley (2002). "CHAMP Orbit Determination with GPS Phase-Connected, Precise Point Positioning". Proceedings of the First CHAMP Science Meeting, Potsdam, Germany, 22-25 January 2002. 59-64.

Bruinsma, S. L., G. Thuillier (2000). "A Revised DTM Atmospheric Density Model: Modeling Strategy and Results". EGS XXV General Assembly, Session G7, Nice, France.

Campbell J. K., S.P. Synnott, G.J. Bierman (1983). "Voyager Orbit Determination at Jupiter". IEEEE Transactions on Automatic Control, AC-28, 256-268.

Chaffee, J., J. Abel (2001). "On the Exact Solutions of Pseudorange Equations". IEEE Transactions on Aerospace and Electronic Systems Vol. 30, No. 4, 1021-1030.

Chao, B.F. (1985). "Predictability of the Earth's Polar Motion". Bull. Geod. 59, 81-93.

Chen, W. (1998). University of Nottingham, Notingham, UK, Personal Communication.

Chiaradia, A.P.M, H.K. KugaKUGA, A.F.B.A Prado (1992). "Autonomous Artificial Satellite Orbit Determination in Real-Time Using Single Frequency GPS Measurements". Reunião da Sociedade Astronômica Brasileira, 2002, Florianópolis. Boletim da Sociedade Astronômica Brasileira. São Paulo : Instituto Astronômico e Geofísico da USP, 2002. 31-31.

Clynch, J. R., D. S. Coco (1986). "Error Characteristics of High Quality Geodetic GPS Measurements: Clocks, Orbits, and Propagation Effects". Proceedings of the 4th International Geodetic Symposium on Satellite Positioning, University of Texas at Austin, Austin, Texas, U.S.A., 28 April-2 May, 1986. 539-556.

Collins, J.T, R.T. Conger (1994). "MANS-Autonomous Navigation and Orbit Control for Communications Satellites", Proceedings of the 15th AIAA International Coomunications Satellite Systems Conference, San Diego, California, U.S.A., 28 February-3 March, 1994.

Collins, J. P, R.B. Langley (1999). "Possible Weighting Schemes for GPS Carrier Phase Observations in the Presence of Multipath", Contract Report for the United States Army Corps of Engineers Topographic Engineering Center, No. DAAH04-96-C0086 / TCN 98151, March, 1999. p33~ (Available online at: http://gauss.gge.unb.ca/papers.pdf/acereport99.pdf).

Colombo, O. L. (1986). "Ephemeris Errors of GPS Satellites", Bulletin Geodesique 60, 64-84.

Colombo, O. L. (1989). "The Dynamics of Global Positioning System Orbits and the Determination of Precise Ephemerides". Journal of Geophysical Research Vol. 94, No. B7, 9167-9182.

Cruickshank, D.R. (1998). “Genetic Model Compensation: Theory and Applications”. PhD Thesis, Aerospace Engineering Sciences, University of Colorado, Boulder, Colorado, U.S.A., 1998.

Cubbedge, S., T. Higbee (1994). "Design, Integration, and Test of a GPS Receiver on an Inertially Pointed Satellite: a Case Study". Proceedings of ION GPS-94, Institute of Navigation, Salt Lake City, Utah, U.S.A., 20-23 September 1994, 1701-1710.

Elyasberg, P., B. Kugaenko, V. Synitsyn, M. Voiskovsky (1972). “Upper Atmospheric Density Determination from the COSMOS Satellite Deceleration Results”. Space Research, Vol. XII.

Enderle, W., Y. Feng, N. Zhou (2003). “Orbit Determination of FedSat based on GPS Receiver Position Solution”. Proceedings of AIAC 2003, Brisbane, Australia, July 2003.

Euler, H.-J., C.C. Goad (1991). “On Optimal Filtering of GPS Dual Frequency Observations without Using Orbit Information”. Bulletin Geodesique Vol 65(2), 1991, 130-143.

Farr, J. E. (1979). “Space Navigation Using the Navstar Global Positioning System”. Rocky Mountain Guidance and Control Conference, American Astronautical Society, Keystone, Colorado, U.S.A., 24-28 February 1979. p27.

Feng, Y. (1998). “A Semi-Dynamic Approach to Precise Orbit Determination with GPS Data of an Onboard Receiver and a Regional Tracking Network”. Proceedings of ION GPS-98, Nashville Convention Center, Nashville, Tennessee, U.S.A., 15-18 September 1998, 1529-1535.

Feng, Y. (1999). “FedSat Orbit Determination: Duty Cycle Operations and Orbit Accuracies”. Proceedings of ION GPS-99, Nashville Convention Center, Nashville, Tennessee, U.S.A., 14-17 September 1999. 445-450.

Feng, Y. (2000). “An Efficient Orbit Integrator/Filter for GPS-based Precise LEO Autonomous Navigation”. The Proceedings of IEEE PLANS 2000, 13-16 March 2000, San Diego, California, U.S.A., 2000. 317-324.

Feng, Y. (2001). “Alternative Orbit Integration Algorithm for GPS-based precise LEO Autonomous Navigation”. Journal of GPS Solutions Vol. 5, No 2, Fall 2001. 1-11.

Feng, Y., N. Zhou, W. Enderle (2003). “FedSat Orbit Determination Strategies and Results from the Daily Flight GPS Measurements”. Proceedings of ION GPS-2003. Oregon Convention Centre, Portland, Oregon, U.S.A., September 2003. 2248-2254.

Feng, Y., N. Zhou, W. Enderle (2003). “Demonstration of the First FedSat Orbit Determination Results with Daily GPS Flight Code Observations”. Proceedings of 10th Australian International Aerospace Congress, Brisbane, Australia, 29 July - 1 August, 2003.

Feng, Y., N. Zhou, W. Enderle (2003). “FedSat Orbit Determination: Results From Daily GPS Flight Code Observations”. Proceedings of SatNav 2003, Melbourne, Australia, 22-25 July 2003.

Gibson, L. R. (1983). “A Derivation of Relativistic Effect in Satellite Tracking”. Technical Report 83-85, NSWC, Dahlgren, Virginia, U.S.A., April, 1983.

Gill.E, O. Montenbruch, H. Kayal (2001). “The BIRD Satellite Mission as a Milestone Toward GPS-based Autonomous Navigation”. Navigation Vol.48, No.2, Summer 2001. 69-75.

Goad, C.C., D.G. Brzezinska, M. Yang (1996). “Determination of High Precision GPS Orbits Using Triple Differencing Technique”. J. Geodesy Vol. 70(11), 655-662.

Goad, C.C., M. Yang (1997). “A New Approach to Precision Airborne GPS Positioning for Photogrammetry”. Photogrammetric Engineering and Remote Sensing Vol. 63(9), 1067-1077.

Gold, K., W.I. Bertiger, T.P. Yunck, S.C. Wu, R. Muellerschoen, G. Born, K. Larson (1994a). “A Study of Real Time Orbit Determination for the Extreme Ultraviolet Explorer”. A95-22921 05-32, Navigating the Earth and Beyond; Proceedings of the Institute of Navigation’s 1994 National Technical Meeting, San Diego, California, U.S.A., 24-26 January 1994.

Gold, K., A. Reichert, G. Born, W.I. Bertiger, S.C. Wu, T.P. Yunck (1994b). "GPS orbit determination in the presence of Selective Availability for the Extreme Ultraviolet Explorer". Proceedings of ION GPS-94, Institute of Navigation, Salt Lake City, Utah, U.S.A., 20-23 Sept., 1994, 1191-1199.

Gore, A. (Vice President of the United States) (1999). “New Global Positioning System Modernization Initiative”, The White House, Office of the Vice President, Contact (202) 456-7035, Public Announcement on the Global Positioning System, Washington, DC, January 25, 1999.

Goodyear, W.H. (1965). “A General Method of Variation of Parameters for Numerical Integration”. The Astronomy Journal Vol. 70(5). 524-526.

Gottzein, E, W. Fichter, A. Jablonski, O. Juckenhőfel, M. Mittnacht, C. Műller, M. Surauer (2000). “Challenges in the Control and Autonomy of Communications Satellites”. Control Engineering Practice Vol. 8(4), 409-427.

Grafarend, E., J. Shan (1997a). “Close-form Solution of P4P or the Three Dimensional Resection Problem in terms of Möbius Barycentric Coordinates”. J. Geodesy Vol.71, 217-231.

Grafarend, E., J. Shan (1997b). “Close-form Solution of the Twin P4P or the Combined Three Dimensional Resection-Intersetion Problem in terms of Möbius Barycentric Coordinates”. J.Geodesy Vol.71, 232-239.

Hajj, G., E.R. Kursinski, W.I. Bertiger, S. Leroy, L. Romans, J.T. Schofield (1995). "Sensing the Atmosphere from a Low-Earth Orbiter Tracking GPS: Early Results and Lessons from the GPS/MET Experiment". Proceedings of the ION GPS-95,

Institute of Navigation, Palm Springs, California. 12-15, September, 1995. 1167-1174.

Halain, J. P., T. Welter, P. Francken et al. (1998). "Performance of Least Squares and Kalman Filter Algorithms for Orbit Determination using Single- and Multi-Station Tracking of Geostationary Satellites". Advances in the Astronautical Sciences Vol. 100, Spaceflight Dynamics, AAS98-368, 835-847.

Han, S. (1997). "Ambiguity Recovery for Long-Range GPS Kinematic Positioning". Navigation, Journal of Institute of Navigation Vol. 44, Number 2, 1997, 257-266.

Hart, R.C., K.R. Hartman, A.C. Long, T. Lee, D.H. Oza (1996). "Global Positioning System (GPS) Enhanced Orbit Determination Experiment (GEODE) on the Small Satellite Technology Initiative (SSTI) Lewis Spacecraft". Proceedings of ION GPS-96, Kansas City Convention Centre, Kansas City, Missouri, U.S.A., 17-20, September 1996, A97-20826 04-32.

Hart, R.C., A.C. Long, T. Lee (1997a). "Autonomous Navigation of the SSTI/Lewis Spacecraft Using the Global Positioning System (GPS)". Proceedings of the Flight Mechanics Symposium 1997, Greenbelt, Maryland, U.S.A., 19-21 May 1997, A97-32176 8-18.

Hart, R.C., S. Truong, A.C. Long, T. Lee, J. Chan, D.H. Oza (1997b). "GPS Navigation Initiatives at Goddard Space Flight Center Flight Dynamics Division". Proceedings of the AAS/AIAA Space Flight Mechanics Conference, Huntsville, Alabama, U.S.A., 10-12, February 1997, A97-35251 9-12.

Hartinger, H., F. K. Brunner (1999). "Variance of GPS Phase Observations: the Sigma-ε Model". GPS Solution Vol. 2(4), Spring, 35-43.

Hatch, R. (1982). "The Synergism of GPS Code and Carrier Measurements". Proceedings of the Third International Geodetic Symposium on Satellite Doppler Positioning, DMA, NOS, Las Cruces, New Maxico, U.S.A., 8-12 February, Physical

Science Laboratory, New Mexico State University, Las Cruces, New Mexico, U.S.A., Vol. 2, 1213-1232.

Hedin, A.E. (1991). "Extension of the MSIS Thermosphere and Exosphere with Empirical Temperature Profiles". J. Geophys Res. Vol. 96, 1159-1172.

Hedin, A.E., E.L. Fleming, A.H. Manson, F.J. Schmidlin, S.K. Avery, Clark, R.R, S.J. Franke, G.J. Fraser, T. Tsuda, F. Vidal, R.A. Vincent (1996). "Empirical Wind Model for the Upper, Middle and Lower Atmosphere". Journal of Atmospheric and Terrestrial Physics Vol.58, 1421-1447.

Heiskanen, W.A., H. Moritz (1967). "Physical Geodesy". W.H. Freeman and Company, San Francisco and London.

Herman, J. (1998). "General Description of the TLEGEN Software for Two-Line Elements Generation". FDS-GEN-1030, Issue 1.0, DLR Oberpfaffenhofen.

Herring, T.A., B.A. Buffertt, P.M. Mathews, I.I. Shapiro (1991). "Forced Nutations of the Earth: Influence of Inner Core Dynamics 3. Very Long Interferometry Data Analysis". J. Geophys Res. Vol. 96, 8252-8273.

Holdridge, D.B. (1967). "An Alternate Expression for Light Time Using General Relativity". JPL Space Program Summary 37-48, III, 2-4.

Hoots, F.R., R.L. Rochrich (1980). "Models for Propogation of NORAD Element Sets". Project Spacecraft Report No. 3, Aerospace Defense Command, United States Air Force, December 1980.

Hujsak, R. S. (1996). "Gravity Acceleration Approximation Functions". Advances in the Astronautical Sciences Vol. 93, Part.1, 335-349.

Hurst, K., "GIPSY-OASIS II". 26 August 1998,
UNAVCO, http://www.unavco.ucar.edu/processing/gipsy/, Last visited in October, 2004.

Hydraulics Laboratory, http://hydraulicslab.ucsd.edu/gps/gpsMay2000.html, Last visited in October, 2004.

Ichikawa, T., K. Ninomiya, S. Kumagai, M. Mistutak (1995). "Experimental Results of Using the GPS for SFU Onboard Navigation". Proceedings of the ION GPS-95, Institute of Navigation, Palm Springs, California, U.S.A., 12-15, September 1995, 573-577.

IERS Conventions 1996 (1996). "IERS Technical Note 21". McCarthy, D.D. (Ed.), Observatorie de Paris, July, p95.

IGS, 2004. "IGS product overview". http://igscb.jpl.nasa.gov/components/prods.html, Last visited in December, 2004.

Jacchia, L.G., (1971). "Revised Static Models of the Thermosphere and Exosphere with Empirical Temperature Profiles". SAO Report No. 332, May 5, 1971.

Jacchia, L.G. (1977). "Thermospheric Temperature Density, and Composition: New Models". SAO Report No. 375, Rep., 375. March 15, 1977.
Kaplan, E.D. (1996). "Understanding GPS: Principles and Applications". Artech House, Boston, Maryland.

Kalman, R.E. (1960). "A New Approach to Linear Filtering and Prediction Problems". J. Basic Eng. Vol. 82, 35-45.

Kalman, R.E., Bucy, R.S. (1961). "New Results in Linear Filtering and Prediction Theory". J. Baic Eng. Vol. 83D, 95-108.

Kaula, W.M. (1996). "Theory of Satellite Geodesy". Blaisdell, Waltham, Mass.

Kawano, I., M. Mokuno, T. Kasai, T. Suzuki (1999). "First Autonomous Rendezvous Using Relative GPS Navigation by ETS-VII". Proceedings of ION GPS-99, Nashville Convention Center, Nashville, Tennessee, U.S.A., 14-17 September, 1999. 393-400.

King-Hele, D.G. (1964). “Theory of Satellite Orbits in an Atmosphere”. London: Butterworths.

King-Hele, D.G. (1976). “Analysis of the Orbit of 1970-114F in Its Last 20 Days”. Planet. Space Sci. Vol. 24(1), 1-16.

Klepczynski, W.J. (1996). “GPS for precise time and time interval measurement, In Global Positioning System: Theory and Applications Volume II”. AIAA, Washington, D.C., U.S.A., 461-480.

Koskela, P. E. (1967). “Astrodynamics Analysis for the Advanced Orbit / Ephemeris Subsystem”, Aeronutronic Publication U-4180, Philco-Ford Corporation, September 1, 1967.

Kuang, D., Y.E. Bar-Sever, W.I. Bertiger, S. Desai, B.J. Haines, B.A. Iijima, G. Kruizinga, T. Meehan, L. Romans (2001). “Precise Orbit Determination for CHAMP using GPS Data from BlackJack Receiver”. Proceedings of ION National Technical Meeting 2001, Long Beach, California, U.S.A., January, 2001. 762-770.

Langley, R.B. (1997). “GPS Receiver System Noise”. GPS World Vol. 8(6), 40-45, 1997.

Lee, T., A.C. Long (1999). “GPS Enhanced Orbit Determination Experiment (GEODE) Mathematical Specifications Version 4”, CSC-96-932-05R0UD0, Goddard Space Flight Center, Flight Dynamics Division, Greenbelt, Maryland, January 1999.

Lichten, S., R. Mullerschoen, J. Srinivasan, U. Lindqwister, T. Munson, S.C. Wu, B. Haines, J.Guinn, L. Young (1995a). “An Automated Low-Earth Orbit Determination System with High Accuracy Real-Time Capability”, A95-415011 11-32, 1995 National Technical Meeting Proceedings, Anaheim, California, U.S.A., 18-29, January 1995. 611-619.

Lichten, S., Y. Bar-Sever, W.I. Bertiger (1995). "GIPSY-OASIS II: A High Precision GPS Data Processing System and General Satellite Analysis Tool". Technical Report, Jet Propulsion Laboratory, Pasadena, California, U.S.A..

Lieske, J.H., T. Lederle, W.Fricke, and B. Morando (1977). "Expressions for the Precession Quantities Based upon the IAU (1976) System of Astronomical Constants". Astronomy and Astrophysics Vol. 58, 1-16.

Lieske, J.H. (1979). "Precession Matrix Based on IAU 1976 System of Astronomical Constants". Astronomy and Astrophysics Vol. 73, 282-284.

Lightsey, E.G. (1996). "Spacecraft Attitude Control Using GPS Carrier Phase". Global Positioning System: Theory and Applications Volume II. (Eds.) B.W. Parkinson, J.J. Spilker Jr., P. Axelrad, P. Enge, AIAA, Washington, D.C., U.S.A., 1996. 461-480.

Liu, L. (2000). "Orbit Theory of Spacecraft". Defense Industrial Publication, China. 419-450.

Long, A.C., J.O. Cappellari, C.E. Velez, A.J. Fuchs (1989). "Mathematical Theory of the Goddard Trajectory Determination System". Goddard Space Flight Center, FDD/522-89/001, Greenbelt, Maryland, U.S.A..

Lopes, R.V., H.K. Kuga (1997). "ORBEST – A GPS Navigation Solution Algorithm Without DOP Analysis". A97-35251 09-12, Proceedings of the AAS/AIAA Space Flight Mechanics Conference, Huntsville, Alabama, U.S.A., 10-12 February 1997. 153-166.

McCarthy, J.J., S. Rowton, D. Moore, D. Pavlis, S.B. Luthcke, L. Tsaoussi (1993). "GEODYN II Systems Description". NASA Goddard Space Flight Center, Greenbelt Maryland, U.S.A., 1993.

McDonald, K.D. (2002). “The Modernization of GPS: Plans, New Capabilities and the Future Relationship to Galileo”. Journal of Global Positioning Systems Vol. 1(1), 1-17.

Mehlen, C. (ALCATEL), D. Laurichesse (CNES) (2000). “Real-time GEO Orbit Determination Using TOPSTAR 3000 GPS Receiver”. Proceedings of ION GPS-2000, Salt Palace Convention Centre, Salt Lake City, Utah, U.S.A., 19-22 September, 2000. 1985-1994.

Melbourne, W.G. (1985). “The Case for Ranging in GPS Based Ceodetic Systems”. Poceedings 1st International Symposium on Precise Positioning with the Global Positioning System, U.S. Department of Commerce, Rockville, Maryland, U.S.A., 1985, 373-386.

Milliken, R.J., C.J. Zoller (1978). “Principle of Operation of NAVSTAR and System Characteristics”. Navigation Vol. 25, 95-106.

Minkler, G., J. Minkler (1993). “Theory and Application of Kalman Filtering”. Magellan Book Co., 1993.

Mitchell, S., Jackson, B., S. Cubbedge, T. Higbee (1996). "Innovation: Navigation Solution Accuracy from a Spaceborne GPS Receiver". GPS World Vol. 7. No. 6, 42, 44, 46-48, 50.

Montenbruck, O. (1989). “Practical Ephemeris Calculations”. Springer Verlag, Heidelberg, 1989.

Montenbruck, O., E. Gill (1996). “Orbit Determination of the MIR Space Station using MOMSNAV GPS Measurement”, 20th International Symposium on Space Technology and Science, 11th International Symposium on Space Flight Dynamics, 96-c53, Gifu, Japan, May 19-25, 1996.

Montenbruck, O., T. Pfleger (2000). “Astronomy on the Personal Computer”. Springer Verlag, Heidelberg, 4th Edition. 2000.

Moyer, T.D. (1981). "Transformation from Proper Time on Earth to Coordinate Time in Solar System Barycentric Space-Time Frame of Reference, Part 1 & 2". Celestial Mechanics Vol. 23, 33-56, 57-68.

Muellerschoen, R., S. Litchen, U. Lindqwister, W.I. Bertiger (1995). "Results of An Automated GPS Tracking Systems in Support of Topex/Poseidon and GPSMet". Proceedings of the ION GPS-95, Institute of Navigation, Palm Springs, California, U.S.A., 12-15, September 1995, 183-193.

Munjal, P., W. Feess, M.P.V. Ananda (1992). "A Review of Spaceborne Applications of GPS". Proceedings of the ION GPS-92, Albuquerque Convention Center, Albuquerque, Washington DC. 16-18, U.S.A., September, 1992. 813-823.

Nerem, R.S., F.J. Lerch, J.A. Marshall, et al. (1994). "Gravity Model Development for TOPEX/POSEIDON: Joint Gravity Models 1 and 2". Journal of Geophysical Research Vol. 99, 24421-24447.

Nicastri, E. (1992). "Progress To-Date -- Vision for the Future". Small Satellite Technologies and Applications II, Proceedings of SPIE Vol. 169, Ed. B.J. Horais. The International Society for Optical Engineering, Orlando, Florida, U.S.A., 112-130. 21-22 April, 1992.

NIMA, 1999 (1999). National Imagery Transmission Format Version 2.1, National Imagery and Mapping Agency (NIMA), Bethesda, Maryland, U.S.A..

Oza, D.H., T.L. Jones, M. Hodjatzadeh, M.V. Samii, et al. (1991). "Evaluation of TDRSS-User Orbit Determination Accuracy Using Both Least-Squares and Sequential Methods". 3rd International Symposium on Space Flight Dynamics, Darmstadt, Germany, 30 September – 4 October, 1991. 411-419.

Potti, J., J.C. Carmona, P. Bernedo, P. Silvestrin (1995). "An Autonomous GNSS-Based Orbit Determination System for Low-Earth Observation Satellites". Proceedings of ION GPS-95, The Institute of Navigation, Palm Springs, California, U.S.A., 2-15 September 1995, 173-182.

Pradines, D., J.P. Berthias, C. Jayles, F. Nouel (1993). "Real-Time Orbit Determination with DORIS Onboard of SPOT4", IAF, International Astronautical Congress, 44th, Graz, Austria, October 1993, 16-22.

Press, W.H., S.A. Teukolsky, W.T. Vettering, B.P. Flannery (1992). "Numerical Recipes in FORTRAN". University Press, 1992.

Robert, J. (1988a). "Multivariate Interpolation of Large Sets of Scattered Data". ACM Transactions on Mathematical Software Vol. 14, No. 2, June 1988. 139-148.

Robert, J. (1988b). "Algorithm 661, QSHEP3D: Quadratic Shepard Method for Trivariate Interpolation of Scattered Data". ACM Transactions on Mathematical Software Vol. 14, No. 2, June 1988. 151-152.

Schutz, B.E., B.D. Tapley (1980). "Orbit Accuracy Assessment for Seasat". J. Astron. Sci. Vol. 28, No. 4, October-December, 1980. 371-390.

Schutz, B.E., B.D. Tapley, R.J. Eanes, M.M. Watkins (1988). "Earth Rotation from Lageos Laser Ranging". Bureau International De L'Heure (BIH) Annual Report, July, 1988. D51-D56.

Schutz, B., P.A.M. Abusali, C. Schroeder, B.D. Tapley, et al. (1995). "GPS Tracking Experiment of a free-flyer Deployed from Space Shuttle". Proceedings of the ION GPS-95, Institute of Navigation, Palm Springs, California, U.S.A., 12-15, September 1995, 229-235.

Seidelmann, P.K. (1982). "1980 IAU Theory of Nutation: The Final Report of the IAU Working Group on Nutation". Celestial Mechanics Vol. 27, 79-106.

Shum, C.K., J.C. Ries, B.D. Tapley, P. Escudier, E. Delaye (1986). "Atmospheric Drag Model for Precise Orbit Determination". CSR-86-2, Center for Space Research, The University of Texas of Austin, 1986.

Soop, E.M. (1983). "Introduction to Geostationary Orbits". ESA SP-1053, 1983.

Spaceborne GPS Mission Directory,
http://gauss.gge.unb.ca/grads/sunil/missions.htm, Last visited in December, 2004.

Spardley, L.H. (1993). "Real-time Differential GPS with 20 to 50 cm Accuracies". A94-20628 04-32, Evolution through Integration of Current and Emerging Systems; Proceedings of the ION GPS-93 National Technical Meeting, San Francisco, California, U.S.A., 20-22 January 1993. 409-414.

Spilker, J.J. (1978). "GPS Signal Structure and Performance Characteristics", Navigation Vol.25. No.2, Summer, 1978. 121-146.

Standish, E.M. (1998). "JPL Planetary and Lunar Ephemerides DE405/LE405". JPL Interoffice Memorandum, IOM 312. F-98-048, August 26, 1998.

Tapley, B.D., B.E. Schutz, R.J. Eanes (1985). "Station Coordinates, Baselines and Earth Rotation From Lageos Laser Ranging: 1976-1984". J.Geophys Res. Vol. 90, 1985. 9235-9248.

Tapley, B.D., J.C. Ries (1987). "Orbit Determination Requirements for TOPEX". Proc. AAS/AIAA Astrodynamics Specialist Conference, Kalispell, Montana, U.S.A., 10-13 August, 1987. 87-429.

Tapley, B.D., J.C. Ries, G.W. Davis, R.J. Eanes, B.E. Schutz, C.K. Shum, M.M. Watkins. (1994). "Precision Orbit Determination for TOPEX/POSEIDON". J. Geophys. Res., TOPEX/POSEIDON Special Issue, 99, No. C12, 24383-24404.
Tapley, B.D., M.W. Watkins, J.C. Ries, (1996). "The Joint Gravity Model 3". Journal of Geophysical Research Vol. 101, 28029-28049.

Teunissen, P., B. Twilley, M. Hendy, D. Zwartz (1999). "Monitoring Isostatic Rebound in Antarctica Using Continuous Remote GPS Observations". GPS Solutioin Vol.2 (3), Winter, 1999. 70-75.

Tu, K.C. (1990). “Precise Real-time Orbit Determination for Application to GPS Differential Positioning”. Ph.D. Thesis, Aerospace Engineering Sciences, University of Colorado, Boulder, Colorado, 1990.

Unwin, M.J. (1993). “The PoSAT Microsatellite GPS Experiment”. Proceedings of the ION GPS-93, Institute of Navigation, Salt Lake City, Utah, U.S.A., 22-24 September, 1993. 811-817.

Unwin, M.J., M.N. Sweeting (1994). “First Results from PoSAT-1 GPS Experiment”. Proceedings of the ION GPS-94 National Technical Meeting, Institute of Navigation, San Diego, California, U.S.A., 24-26 January 1994, 413-420.

Unwin, M.J., M.N. Sweeting (1995). “A Practical Demonstration of Low Cost Autonomous Orbit Determination Using GPS”. Proceedings of the ION GPS-95, Institute of Navigation, Palm Springs, Califonia, U.S.A., 12-15 September 1995, 579-587.

Van Dierendonck, A.J., P. Fenton, T. Ford (1992). “Theory and Performance of Narrow Correlator Spacing GPS Receiver”. Proceedings of the ION GPS-92 National Technical Meeting, San Diego, California, U.S.A., 27-29 January 1992 pp. 115-124.

Van Flandern, T.C., K.F. Pulkkinen (1979). “Low Precision Formulae for Planetary Positions”. Astrophysical Journal Supplement Series Vol. 41, November 1979. 391-411.

Van Leeuween, A., L. Carrier (1997). “The Global Positioning System and Its Applications in Spacecraft Navigation”. Navigation Vol. 26, 1997. 204-221.

Vermeer, M. (1997). “The Precision of Geodetic GPS and One Way of Improving It”. J.Geodesy Vol. 71, Springer-Verlag, 1997. 240-245.

Wahr, J. M. (1981). “The Forced Nutations of an Elliptical, Rotating, Elastic, and Oceanless Earth”. Geophys, J.R. Astron. Soc. Vol. 64, 1981. 705-727.

Webb, F., J. Zumberge (1995). “An Introduction to GIPSY-OASIS II”. JPL D-11088. California Institute of Technology, 1995.

Wu, S.C., T.P. Yunck, C.L. Thornton (1991). “Reduced Dynamic Technique for Precise Orbital Determination of Low Earth Satellites”. Journal of Guidance, Control and Dynamics Vol. 14, No.1 1991, 24-30.

Wübbena, G. (1985). “Software Developments for Geodetic Positioning with GPS Using TI 4100 Code and carrier Measurements”. Proceedings First International Symposium on Precise Positioning with the Global Positioning System, U.S. Department of Commerce, Rockville, Maryland, 1985, 403-412.

Yang, M. (1995). “New GPS Measurement Modeling Techniques of Orbit Determination and Precise Kinematic Positioning”. Department Report No.431, Department of Geodetic Science and Surveying, The Ohio State University, Columbus, Ohio, U.S.A., 1995.

Yunck, T.P. (1996). “Orbital Determination, Global Positioning System: Theory and Applications, Volume II”. Published by AIAA, 559-592.

Yunck, T.P. (2002). “An Overview of Atmospheric Radio Occultation”. Journal of Global Positioning Systems Vol. 1, No. 1, 2002, 58-60.

Zhou, N., Y. Feng (2002a). “Robust Filtering Techniques Using Simplified Dynamic Models for Onboard Spacecraft Orbit Determination”. Proceedings of 2002 International Symposium on GPS/GNSS, Wuhan University, China, 6-8 November 2002. 45-53.

Zhou, N., Y. Feng (2002b). “Short-Arc Batch Estimation for GPS-Based Onboard Spacecraft Orbit Determination”. Journal of Global Positioning Systems Vol. 1, No2, 2002, 106-112.

Zhou, N., Y. Feng, E. Werner (2002c). "Robust Filtering Techniques for Autonomous Spacecraft Orbit Determination". Proceedings of ION GPS 2002, Oregon Convention Centre, Portland, Oregon, U.S.A., 15-18 September, 2002.

Zhou, N., Y. Feng (2002d). "Methods and Preliminary Test Results of Orbit Improvement and Prediction". Publications on GPS 2001: Cooperative Research Centre for Satellite Systems Technical Memorandum 03/02, 15-25.

Zhou, N., Y. Feng, W. Enderle (2003). "A Short-Arc Batch Estimation Strategy Towards Decimetre Level GPS-Based Onboard LEO Orbit Determination". Proceedings of ION GPS-2003. Institute of Navigation, Portland, Oregon, U.S.A., 9-12 September 2003. 2264-2270.

Appendix A

An analytical solution of state transition matrix considering only the two-body forces, this is the computation formulae for the **H** in Equation (3.42):

$$\left.\begin{aligned} h &= 1-\frac{GM}{r_0}S_2 \\ g &= (t-t_0)-GMS_3 \\ \dot{h} &= -\frac{GM}{r\cdot r_0}S_1 \\ \dot{g} &= 1-\frac{GM}{r}S_2 \end{aligned}\right\} \qquad \text{(A-1)}$$

where

$$\left.\begin{aligned} r_0 &= \sqrt{x_0^2+y_0^2+z_0^2} \\ \dot{r}_0^2 &= \dot{x}_0^2+\dot{y}_0^2+\dot{z}_0^2 \\ R_0 &= x_0\dot{x}_0+y_0\dot{y}_0+z_0\dot{z}_0 \\ r &= \sqrt{x^2+y^2+z^2} \\ &= r_0\cdot S_0+R_0\cdot S_1+GM\cdot S \end{aligned}\right\} \qquad \text{(A-2)}$$

Define:

$$\left.\begin{aligned} \alpha &= \dot{r}_0^2-\frac{2GM}{r_0} \\ a &= -\frac{GM}{\alpha},\ n=\sqrt{\frac{GM}{a^3}} \\ E_0 &= (t-t_0)\frac{\sqrt{-\alpha}}{a} \\ \beta &= \frac{E_0}{\sqrt{-\alpha}} \end{aligned}\right\} \qquad \text{(A-3)}$$

Then for i =0,1,2 and 3, S_i can be computed as:

$$\left.\begin{aligned} S_0 &= \cos(E_0), S_1 = \frac{\sin(E_0)}{\sqrt{-\alpha}} \\ S_2 &= \frac{S_0-1}{\alpha}, S_3 = \frac{S_1-\beta}{\alpha} \end{aligned}\right\} \qquad \text{(A-4)}$$

Update E_0 with E, the true anomaly angle:

$$E = n(t-t_0)+(1-\frac{r_0}{a})\sin(E_0)-\frac{R_0}{na^2}[1-\cos(E_0)] \qquad \text{(A-5)}$$

Iteration is needed for the computation of E.

To express the partial derivatives for time t , the transcendental functions

$$\left.\begin{aligned} S_4 &= \frac{\left(S_2 - \beta^2/2\right)}{\alpha} \\ S_5 &= \frac{\left(S_3 - \beta^3/6\right)}{\alpha} \end{aligned}\right\} \tag{A-6}$$

of β are used to determine the function:

$$U = S_2(t - t_0) + GM\left(\beta S_4 - 3S_5\right) \tag{A-7}$$

Also, the accelerations are:

$$\ddot{x} = -GM\frac{x}{r^3}, \quad \ddot{y} = -GM\frac{y}{r^3}, \quad \ddot{z} = -GM\frac{z}{r^3} \tag{A-8}$$

$$\ddot{x}_0 = -GM\frac{x_0}{r_0^3}, \quad \ddot{y}_0 = -GM\frac{y_0}{r_0^3}, \quad \ddot{z}_0 = -GM\frac{z_0}{r_0^3} \tag{A-9}$$

The following solution for the 36 partial derivatives is completely general for the elliptic case:

$$\begin{bmatrix} \frac{\partial x}{\partial x_0} & \frac{\partial x}{\partial y_0} & \frac{\partial x}{\partial z_0} \\ \frac{\partial y}{\partial x_0} & \frac{\partial y}{\partial y_0} & \frac{\partial y}{\partial z_0} \\ \frac{\partial z}{\partial x_0} & \frac{\partial z}{\partial y_0} & \frac{\partial z}{\partial z_0} \end{bmatrix} = \begin{bmatrix} h & 0 & 0 \\ 0 & h & 0 \\ 0 & 0 & h \end{bmatrix} + U\begin{bmatrix} \dot{x} \\ \dot{y} \\ \dot{z} \end{bmatrix}\begin{bmatrix} \ddot{x}_0 & \ddot{y}_0 & \ddot{z}_0 \end{bmatrix} +$$

$$\begin{bmatrix} x & \dot{x} \\ y & \dot{y} \\ z & \dot{z} \end{bmatrix}\begin{bmatrix} -\frac{\dot{h}S_1 + (h-1)/r_0}{r_0} & -\dot{h}S_2 \\ \frac{(h-1)S_1}{r_0} & (h-1)S_2 \end{bmatrix}\begin{bmatrix} x_0 & y_0 & z_0 \\ \dot{x}_0 & \dot{y}_0 & \dot{z}_0 \end{bmatrix}$$

$$\begin{bmatrix} \frac{\partial x}{\partial \dot{x}_0} & \frac{\partial x}{\partial \dot{y}_0} & \frac{\partial x}{\partial \dot{z}_0} \\ \frac{\partial y}{\partial \dot{x}_0} & \frac{\partial y}{\partial \dot{y}_0} & \frac{\partial y}{\partial \dot{z}_0} \\ \frac{\partial z}{\partial \dot{x}_0} & \frac{\partial z}{\partial \dot{y}_0} & \frac{\partial z}{\partial \dot{z}_0} \end{bmatrix} = \begin{bmatrix} g & 0 & 0 \\ 0 & g & 0 \\ 0 & 0 & g \end{bmatrix} - U\begin{bmatrix} \dot{x} \\ \dot{y} \\ \dot{z} \end{bmatrix}\begin{bmatrix} \dot{x}_0 & \dot{y}_0 & \dot{z}_0 \end{bmatrix} +$$

$$\begin{bmatrix} x & \dot{x} \\ y & \dot{y} \\ z & \dot{z} \end{bmatrix}\begin{bmatrix} -\dot{h}S_2 & -(\dot{g}-1)S_2 \\ (h-1)S_2 & gS_2 \end{bmatrix}\begin{bmatrix} x_0 & y_0 & z_0 \\ \dot{x}_0 & \dot{y}_0 & \dot{z}_0 \end{bmatrix}$$

$$\begin{bmatrix} \frac{\partial \dot{x}}{\partial x_0} & \frac{\partial \dot{x}}{\partial y_0} & \frac{\partial \dot{x}}{\partial z_0} \\ \frac{\partial \dot{y}}{\partial x_0} & \frac{\partial \dot{y}}{\partial y_0} & \frac{\partial \dot{y}}{\partial z_0} \\ \frac{\partial \dot{z}}{\partial x_0} & \frac{\partial \dot{z}}{\partial y_0} & \frac{\partial \dot{z}}{\partial z_0} \end{bmatrix} = \begin{bmatrix} \dot{h} & 0 & 0 \\ 0 & \dot{h} & 0 \\ 0 & 0 & \dot{h} \end{bmatrix} + U \begin{bmatrix} \ddot{x} \\ \ddot{y} \\ \ddot{z} \end{bmatrix} \begin{bmatrix} \ddot{x}_0 & \ddot{y}_0 & \ddot{z}_0 \end{bmatrix} +$$

$$\begin{bmatrix} x & \dot{x} \\ y & \dot{y} \\ z & \dot{z} \end{bmatrix} \begin{bmatrix} -\dot{h}\left[\frac{S_0}{rr_0} + \frac{1}{r^2} + \frac{1}{r_0^2}\right] & -\frac{\dot{h}S_1 + (\dot{g}-1)/r}{r} \\ \frac{\dot{h}S_1 + (h-1)/r_0}{r_0} & \dot{h}S_2 \end{bmatrix} \begin{bmatrix} x_0 & y_0 & z_0 \\ \dot{x}_0 & \dot{y}_0 & \dot{z}_0 \end{bmatrix}$$

$$\begin{bmatrix} \frac{\partial \dot{x}}{\partial \dot{x}_0} & \frac{\partial \dot{x}}{\partial \dot{y}_0} & \frac{\partial \dot{x}}{\partial \dot{z}_0} \\ \frac{\partial \dot{y}}{\partial \dot{x}_0} & \frac{\partial \dot{y}}{\partial \dot{y}_0} & \frac{\partial \dot{y}}{\partial \dot{z}_0} \\ \frac{\partial \dot{z}}{\partial \dot{x}_0} & \frac{\partial \dot{z}}{\partial \dot{y}_0} & \frac{\partial \dot{z}}{\partial \dot{z}_0} \end{bmatrix} = \begin{bmatrix} \dot{g} & 0 & 0 \\ 0 & \dot{g} & 0 \\ 0 & 0 & \dot{g} \end{bmatrix} - U \begin{bmatrix} \ddot{x} \\ \ddot{y} \\ \ddot{z} \end{bmatrix} \begin{bmatrix} \dot{x}_0 & \dot{y}_0 & \dot{z}_0 \end{bmatrix} +$$

$$\begin{bmatrix} x & \dot{x} \\ y & \dot{y} \\ z & \dot{z} \end{bmatrix} \begin{bmatrix} -\frac{\dot{h}S_1 + (\dot{g}-1)/r}{r} & -\frac{(\dot{g}-1)S_1}{r} \\ \dot{h}S_2 & (\dot{g}-1)S_2 \end{bmatrix} \begin{bmatrix} x_0 & y_0 & z_0 \\ \dot{x}_0 & \dot{y}_0 & \dot{z}_0 \end{bmatrix}$$

(A-10)

Appendix B

The following directory chronologically lists the space missions that have included a GPS receiver or receivers for any number of reasons. The directory is not an all-inclusive listing of spaceborne GPS missions flown, but is rather a comprehensive directory of missions that have been cited in scientific literature. Mission descriptions, the capacity that the GPS receiver or receivers are used in, the model of GPS receiver, references citing the mission relevant hyperlinks to mission home pages or other related sites can be found in Spaceborne GPS website [*Spaceborne GPS mission directory*, 2004].

Launch Date	**Mission**	**Receiver(s)**
July 1982	Landsat4	GPSPAC
March 1984	Landsat5	GPSPAC
July 1991	ORBCOMM-X	--
June 1992	EUVE	GPSDR
August 1992	TOPEX/Poseidon	GPSDR
numerous flights	Space Shuttle	TANS
June 1993	RADCAL	TANS Quadrex
July 1993	ORFEUS-SPAS-1	Alcatel/SEL
September 1993	PoSat-1	TANS
February 1994	OREX	GPSDR
March 1994	DARPASAT	AST-V
May 1994	TAOS/STEP-0	AST-V
May 1994	STEP-2	AST-V
August 1994	APEX	TANS Vector
November 1994	CRISTA-SPAS	TANS Vector
(1992 and 1994)	COMET	Ashtech SB24
January 1995	Faisat-1	--
March 1995	SFU	GPSR
April 1995	ORBCOMM-FM1	TANS II
April 1995	ORBCOMM-FM2	TANS II
April 1995	OrbView-1 (formerly MicroLab-1)	TurboStar

August 1995	FASat-Alfa	TANS
September 1995	Wake Shield Facility-02	TurboStar
September 1995	Skipper	TANS II
January 1996	GADACS / SPARTAN OAST Flyer	Two TANS Vectors
May 1996	GANE / STS-77	TANS
May 1996	MSTI-3	Viceroy
May 1996	MOMS-2P	Viceroy
November 1996	HETE	SEXTANT
November 1996	Wake Shield Facility-03	TurboStar
February 1997	HALCA (formerly MUSES-B)	GPS
March 1997	Zeya	GPS and GLONASS
August 1997	OrbView-2 (formerly SeaStar)	redundant Viceroys
August 1997	SSTI Lewis	Two Tensors
September 1997	Faisat-2v	--
September 1997	IRS-1D	--
October 1997	Falcon Gold	TIDGET
October 1997	YES (sub-satellite of TEAMsat satellite)	TANS II
November 1997	ETS-VII	--
December 1997	Equator-S	Viceroy
December 1997	EarlyBird	Vector and Viceroy
February 1998	GFO	Four TurboStars
February 1998	Globalstar	Tensor
February 1998	SNOE	MicroGPS
July 1998	FASat-Bravo	TANS II
July 1998	TMSat-1	SGR-10
October 1998	SEDSat-1	G12
October 1998	ARD	--
November 1998	International Space Station	--
December 1998	SAC-A	--
January 1999	ORSTED	TANS, TurboStar
February 1999	ARGOS	--
February 1999	SUNSAT	TurboStar
April 1999	UoSAT-12	SGR-20
April 1999	Ikonos-1	Rockwell C/A code

April 1999	ABRIXAS	TANS II
May 1999	IRS-P4 (OceanSat)	--
June 1999	QuikSCAT	2 Viceroys
September 1999	SRTM	AstroNav
September 1999	JAWSAT	TANS Vector
late 1999	AMSAT Phase 3D	Two TANS Vectors
1999	STRV-C	AstroNav
1998	ARISTOTELES	--
1998	TechSAT-II	--
1997 and 1998	EOS-A and EOS-B	--
1998	TSX-5	two TANS Vectors
1999	SAC-C	Lagrange, Tensor, AstroNav
1999	QuickBird	2 Viceroys
late '90s	European Polar Platform	--
late '90s	RAMOS	--
1999	Gravity Probe B	2 Vectors
December 1999	CHAMP	AstroNav
summer 1999	OSEM	Tensor or TANS Vector
May 2000	Jason-1	AstroNav
August 2000	VCL	AstroNav
2000	BIRD	Rockwell Collins
2001	MetOp-1	ESA GNSS receiver
June 2001	GRACE	AstroNav
December 2002	FedSat-1	JPL BlackJack
July 2001	ICESat	AstroNav
late 2001	BOLAS	--
February 2003	Columbus Laboratory	--
March 2003	ESA/ATV	Tensor
2004	STEP	AST-V
--	NASA/STV	Mayflower receiver
-	Spartan Lite	GEC Plessey Chipset
-	Orbit Maneuvering Vehicle and Orbit Transfer Vehicle	--

-	MEDSAT	--
2000	STENTOR	--
-	CESAR	--